ARMY RESEARCH OFFICE
AND
AIR FORCE OFFICE OF SCIENTIFIC RESEARCH

DISTRIBUTION STATEMENT A
Approved for Public Release
Distribution Unlimited

2002
CONTRACTORS MEETING
IN
CHEMICAL PROPULSION

20030923 166

AFRL-SR-AR-TR-03-

0347

REPORT DOCUMENTATION PAGE

Public reporting burden for this collection of information is estimated to average 1 hour per response, including the time for reviewing instruc data needed, and completing and reviewing this collection of information. Send comments regarding this burden estimate or any other aspe this burden to Department of Defense, Washington Headquarters Services, Directorate for Information Operations and Reports (0704-0188) 4302. Respondents should be aware that notwithstanding any other provision of law, no person shall be subject to any penalty for failing to comply with a collection of information if it does not display a currently valid OMB control number. PLEASE DO NOT RETURN YOUR FORM TO THE ABOVE ADDRESS.

1. REPORT DATE (DD-MM-YYYY)	2. REPORT TYPE	3. DATES COVERED (From - To)
19-06-2002	Technical	01-06-2001 - 31-05-2002

4. TITLE AND SUBTITLE
(U) Army Research Office and Air Force Office of Scientific Research 2002 Contractors Meeting in Chemical Propulsion

5a. CONTRACT NUMBER

5b. GRANT NUMBER

5c. PROGRAM ELEMENT NUMBER
61102A, 61102F

6. AUTHOR(S)
David M. Mann and Julian M. Tishkoff

5d. PROJECT NUMBER

5e. TASK NUMBER

5f. WORK UNIT NUMBER

7. PERFORMING ORGANIZATION NAME(S) AND ADDRESS(ES)

Army Research Office
Research Triangle Park NC
27709-2211

Air Force Office of Scientific Research
Arlington VA 22203-1977

8. PERFORMING ORGANIZATION REPORT NUMBER

9. SPONSORING / MONITORING AGENCY NAME(S) AND ADDRESS(ES)
AFOSR/NA
801 North Randolph Street
Room 732
Arlington VA 22203-1977

10. SPONSOR/MONITOR'S ACRONYM(S)

11. SPONSOR/MONITOR'S REPORT NUMBER(S)

12. DISTRIBUTION / AVAILABILITY STATEMENT
Approved for public release; distribution is unlimited

13. SUPPLEMENTARY NOTES

14. ABSTRACT

Abstracts are given for 6.1 basic research in chemical propulsion sponsored by the Army Research Office and the Air Force Office of Scientific Research

15. SUBJECT TERMS
Flames, Propulsion, Gas Turbines, Diesel Engines, Scramjets, Pulse Detonation Engines, Hydrocarbon Fuels, Diagnostics, Spray, Droplet, Supercritical Fluids, Turbulence, Combustion

16. SECURITY CLASSIFICATION OF:			17. LIMITATION OF ABSTRACT	18. NUMBER OF PAGES	19a. NAME OF RESPONSIBLE PERSON
a. REPORT	b. ABSTRACT	c. THIS PAGE			Julian M. Tishkoff
Unclassified	Unclassified	Unclassified	UL	191	19b. TELEPHONE NUMBER (include area code) (703) 696-8478

ARMY RESEARCH OFFICE
AND
AIR FORCE OFFICE OF SCIENTIFIC RESEARCH

DISTRIBUTION STATEMENT A
Approved for Public Release
Distribution Unlimited

2002
CONTRACTORS MEETING
IN
CHEMICAL PROPULSION

ARO/AFOSR Contractors' Meeting in Chemical Propulsion
TABLE OF CONTENTS

ARO/AFOSR CONTRACTORS MEETING

IN

CHEMICAL PROPULSION

Dayton OH
12-14 June 2002

WEDNESDAY, 12 JUNE

1:00 - 1:15	AFOSR Combustion and Diagnostics Program – Julian Tishkoff
1:15 - 1:30	Army Research Office Overview - David Mann
Topic: Diagnostics	
1:30 - 2:00	Experimental and Computational Characterization of Combustion Phenomena James Gord, AFRL/PR
2:00 - 2:30	Advanced Diagnostics for Reacting Flows Ronald K. Hanson, Stanford University
2:30 - 3:00	Simultaneous Measurements of Species Concentrations, Temperature, and Flow Velocity in a Flame Rajendra Gupta, University of Arkansas
3:00 - 3:30	BREAK
3:30 – 4:00	Cross-Plane Laser Imaging of Premixed Turbulent Combustion Processes Frederick Gouldin, Cornell University
4:00 - 4:30	Planar Image Particle Analyzer for Whole Field Spray Applications Cecil F. Hess, MetroLaser, Inc.
4:30 - 5:00	Sub- and Supercritical Evaporation and Combustion of a Moving Droplet George Gogos, University of Nebraska
5:00 - 7:30	DINNER
7:30 - 9:30	DISCUSSION – Future Gas Turbine Technology – The DOD Integrated High Performance Turbine Engine Technology (IHPTET)

	And Versatile Affordable Advanced Turbine Engine (VAATE) Programs
9:30	BREAK

THURSDAY, 13 JUNE

8:15 - 8:30	Announcements
8:30 - 9:00	Soot Morphology in Unsteady Counterflow Diffusion Flames William Roberts, North Carolina State University

Topic: Atomization and Sprays

9:00 - 9:30	Center of Excellence in Propulsion Systems at the Engine Research Center Patrick V. Farrell, University of Wisconsin-Madison
9:30 - 10:00	Ramjet Research Thomas A. Jackson, AFRL/PR
10:00 - 10:30	BREAK
10:30 - 11:00	Large-Eddy Simulations of Supercritical Multicomponent Mixing Layers Josette Bellan, Jet Propulsion Laboratory
11:00 - 11:30	Nonlinear Distortion and Disintegration of Conical Liquid Sheets at High Pressures William A. Sirignano, University of California, Irvine
11:30 - 12:00	Drop-Gas Interactions in Dense Sprays G. M. Faeth, University of Michigan
12:00 - 1:30	LUNCH
1:30 - 4:30	Air Force Research Laboratory Combustion Research Facilities Tour

FRIDAY, 14 JUNE

Topic: Fuel Chemistry

8:00 - 8:30	Advanced Supercritical Fuels/Supercritical Combustion Tim Edwards, AFRL/PR
8:30 - 9:00	Fuels Combustion Research: Supercritical Fuel Pyrolysis M. J. Wornat, Princeton University
9:00 - 9:30	Experimental and Detailed Numerical Studies of Fundamental Flame Properties of Gaseous and Liquid Fuels Fokion Egolfopoulos, University of Southern California
9:30 - 10:00	BREAK
10:00 – 10:30	Development and Optimization of a Comprehensive Kinetic Model of Hydrocarbon Fuel Combustion Hai Wang, University of Delaware

Topic: Ignition/Extinction

10:30 – 11:00	The Chemistry Controlling Ignition of Hydrocarbons and Their Mixtures at High Pressures Nicholas Cernansky, Drexel University
11:00 – 11:30	Chemical Kinetic Characterization of Autoignition and Combustion of Diesel and JP-8 Kalyanasundaram Seshadri, University of California, San Diego
11:30 - 1:00	LUNCH
1:00 - 1:30	Shock Tube Measurements of Ignition Processes in Diesel-Related Fuels and Additives Ronald K. Hanson, Stanford University
1:30 - 2:00	Autoignition and Burning Speeds of JP-8 Fuel at High Temperatures and Pressures Mohamad Metghalchi, Northeastern University
2:00 - 2:30	Stabilization and Blowout of Gaseous and Spray Jet Flames Kevin Lyons, North Carolina State University
2:30 - 2:45	BUSINESS SESSION - Contractors in Dr. Mann's Program Only
2:45 - 3:15	BUSINESS SESSION - Contractors in Dr. Tishkoff's Program Only
3:15	ADJOURN

AFOSR SPONSORED RESEARCH IN COMBUSTION AND DIAGNOSTICS

PROGRAM MANAGER: JULIAN M. TISHKOFF

AFOSR/NA
801 North Randolph Street, Room 732
Arlington VA 22203-1977

SUMMARY/OVERVIEW: The Air Force Office of Scientific Research (AFOSR) program in combustion and diagnostics currently is focused on five areas of study: high-speed propulsion, turbulent combustion, diagnostics, supercritical fuel behavior, and plasma-enhanced combustion. An assessment of major research needs in each of these areas is presented.

TECHNICAL DISCUSSION

AFOSR is the single manager for Air Force basic research, including efforts based on external proposals and in-house work at the Air Force Research Laboratory (AFRL). Combustion and Diagnostics is assigned to the AFOSR Directorate of Aerospace and Materials Sciences along with programs in rocket and space propulsion, fluid and solid mechanics, and structural materials.

Interests of the AFOSR Combustion and Diagnostics subarea are given in the SUMMARY section above. Many achievements can be cited for these interests, yet imposing fundamental research challenges remain. The objective of the program is publications in the refereed scientific literature describing significant new understanding of multiphase turbulent reacting flow. Incremental improvements to existing scientific approaches, hardware development, and computer codes fall outside the scope of this objective.

The Combustion and Diagnostics subarea reflects a new Air Force commitment to support space science and technology. Accordingly, the research in this subarea will address research issues related to chemical propulsion for all Air Force aerospace missions, including combined cycle propulsion for access to space. This program will complement related research activities in space propulsion and energetic materials.

The primary focus of research in turbulent combustion is the creation of computational modeling tools for combustor designers that are both computationally tractable and

quantitatively predictive. This research has been directed in two areas: the formulation of augmented reduced chemical kinetic mechanisms for the combustion of hydrocarbon fuels and the development of subgrid-scale models for large eddy simulation of turbulent combustion.

Future airbreathing and chemical rocket propulsion systems will require propellants to absorb substantial thermal energy, raising their temperatures to supercritical thermodynamic conditions. Understanding and controlling fluid properties at these conditions will be crucial for avoiding thermal degradation and for optimizing subsequent processes within the combustor. Research has focused on the role of supercritical transport in the thermal destabilization of hydrocarbon fuel prior to combustion and on primary and secondary fuel breakup under transcritical and supercritical conditions.

Plasma research is one of six AFOSR Theme topics selected for support beginning in Fiscal Year 2001. The focus primarily is on the utilization of plasmas for ignition and flame stabilization in scramjets; however, the extension of this technology to other modes of chemical propulsion and energy conversion also is of interest. The theme research will be supplemented by research coordinated between universities and small businesses under the Department of Defense Small Business Technology Transfer (STTR) Program. The Air Force also supports related research activity in Russia under the Air Force Research Laboratory International Research Initiative. The Theme and Russian research activity will be presented as part of a Weakly Ionized Gas Dynamics Workshop at the 31st AIAA Aerospace Sciences Meeting and Exhibit in January 2003.

Decisions on support for research proposals are based on scientific opportunities and technology needs. Researchers interested in submitting proposals should contact Dr. Tishkoff for information on time constraints associated with proposal evaluations. Further information on research interests and proposal preparation can be found on the AFOSR web site, http://www.afosr.af.mil. The availability of funds places a major constraint on program redirection and growth. Figure 1 shows the recent trend of funding for basic research in combustion and diagnostics from Air Force and DOD sources. Informal inquiries for new research are encouraged throughout the year. Formal proposals should be submitted by 1 April for peer review by the National Research Council.

The purpose of this abstract has been to communicate AFOSR perceptions of research trends to the university and industrial research communities. However, communication from those communities back to AFOSR also is desirable and essential for creating new research opportunities. Therefore, all proposals and inquiries for fundamental research are encouraged even if the content does not fall within the areas of emphasis described herein. Comments and criticisms of current AFOSR programs also are welcome.

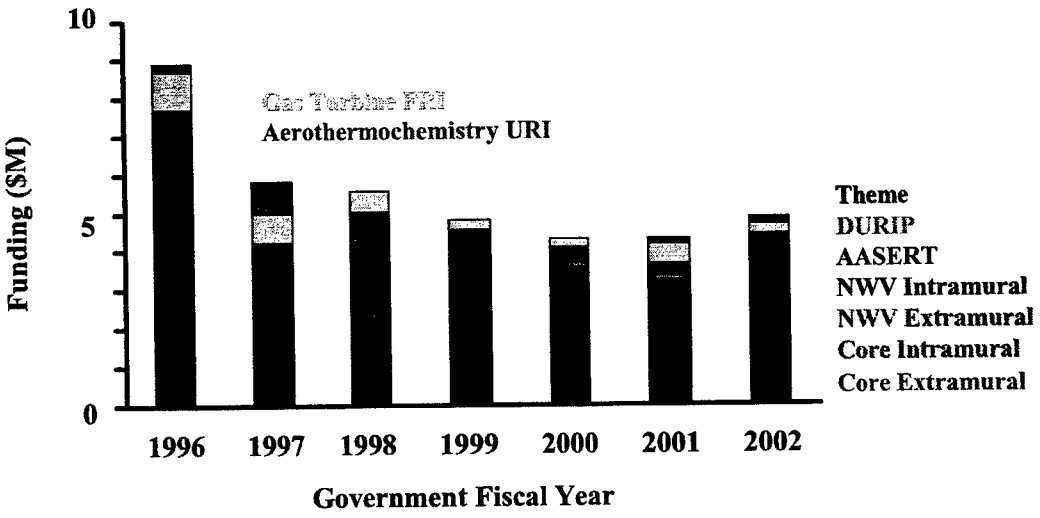

Figure 1. AFOSR Funding for Combustion and Diagnostics

The Army Research Office Program in Propulsion and Energetics

David M. Mann
Mechanical and Environmental Sciences Division
US Army Research Office

The Army is on a fast-paced path to transformation. That transformation involves the development of new classes of fighting vehicles, the Future Combat System, which are lighter and more mobile, while maintaining the levels of lethality and survivability offered by today's systems, e.g. the M1 Abrams tank. Over the years, propulsion and energetics research has played a vital part in providing the options for the development of the new systems. Research in future years will yield breakthroughs that will enable new capabilities.

The Army transformation has re-emphasized the need for lightweight, high power density, high efficiency engines for air and ground vehicles. The ARO Propulsion program continues to focus on optimizing the combustion processes in diesel and gas turbine engines. Fundamental to that optimization is understanding and developing predictive models for the controlling mechanisms and processes. Particularly important research areas are fuel injection and fuel-air mixing dynamics, ignition, combustion and heat transfer. In order to be applicable to the environments of advanced engines, it is vitally important to address these areas in the appropriate parameter space of temperature, pressure and turbulence level. Ultimately the goal is to combine the detailed understanding of combustion with active control techniques, capable of optimization of engine performance under all conditions and engine health monitoring.

Projectile and missile propulsion is the focus of the ARO Energetics program. The emphasis is on the development of higher energy systems, both through the utilization of current energetic materials under higher loading conditions and through the development of higher energy/output energetic materials. In the first instance, fixed volume systems, such as gun and missile combustion chambers, can deliver higher energies if higher charge densities (guns) or more compact combustors (liquid fueled missiles) are used. Here the challenges are the ignition and heat release dynamics at high density. In the second instance, the Army is exploring the potential of nano-scale energetic materials to provide higher energy and higher power for propulsion and explosive uses. In this new field, emphasis is being placed on the preparation and characterization of novel nanostructures and on understanding their reactivity.

Details on submitting proposals to ARO may be found on the ARO web site, www.aro.army.mil. The site contains the Broad Agency Announcement for the ARO and other Army Research Laboratory Directorates' research efforts. Prospective offerors to ARO are encouraged to informally discuss their research ideas with the appropriate ARO program manager prior to submitting a formal proposal.

EXPERIMENTAL AND COMPUTATIONAL CHARACTERIZATION OF COMBUSTION PHENOMENA

AFOSR Task No. 02PR01COR

Principal Investigator: James R. Gord

Air Force Research Laboratory
AFRL/PRTS Bldg 490
1790 Loop Rd N
Wright-Patterson AFB OH 45433-7103

SUMMARY/OVERVIEW

Propulsions systems represent a substantial fraction of the cost, weight, and complexity of Air Force aircraft, spacecraft, and other weapon-system platforms. The vast majority of these propulsion systems are powered through combustion of fuel; therefore, the detailed study of combustion has emerged as a highly relevant and important field of endeavor. Much of the work performed by today's combustion scientists and engineers is devoted to the tasks of improving propulsion-system performance while simultaneously reducing pollutant emissions. Increasing the affordability, maintainability, and reliability of these critical propulsion systems is a major driver of activity as well. This research effort is designed to forward the scientific investigation of combustion phenomena through an integrated program of fundamental combustion studies, both experimental and computational, supported by parallel efforts to develop, demonstrate, and apply advanced techniques in laser-based/optical diagnostics and modeling and simulation.

TECHNICAL DISCUSSION

While this AFOSR-funded program involves numerous ongoing investigations, just a few recent advances are described in this abstract. Some specific ongoing activities that have been reviewed during recent AFOSR/ARO Contractors Meetings but are not discussed at length in this abstract include: 1) development of a mid-infrared, ultranarrowband, doubly-resonant optical parametric oscillator for spectroscopy and line-of-sight absorption measurements of various target species, including carbon monoxide at ~2.3 μm, 2) studies of combustion in impulsively initiated vortex rings with emphasis on application to the design and development of vortex-based ignition schemes, and 3) the development of terahertz-radiation ("T-ray") systems for combustion studies in the far infrared. New work is presented in test-cell diagnostics, collaborative studies of vortex/flame interactions with French colleagues, triple-pump coherent anti-Stokes Raman scattering (CARS), and frequency-mixing-based diode-laser sensors. Also cited are two emerging collaborations that show great promise: 1) application of picosecond time-resolved laser-induced fluorescence spectroscopy (PITLIFS) in test cells at Wright-Patterson Air Force Base (WPAFB) with Prof. Norm Laurendeau and the Purdue University team and 2) diode-laser based measurements of temperature and water concentration in a pulsed-detonation engine (PDE) at WPAFB with Prof. Ron Hanson and the Stanford University team.

Development and Application of Practical Diagnostics for Test-Cell Applications. In the past year, numerous optical diagnostics have been applied to studies of advanced combustors, including a trapped-vortex combustor (TVC) and an ultra-compact combustor/inter-turbine

burner (UCC/ITB); a PDE; and particulate-mitigating fuel additives. Recent work with molecular-emission spectroscopy, high-speed digital imaging, and laser-induced incandescence (LII) is highlighted here.

Active control of the fuel/air ratio is an important goal of advanced combustor development. Local fuel/air ratios in combustors reflect the complex dynamics of fuel atomization and fuel/air mixing. These processes directly impact the operating efficiency of combustors. Molecular-emission spectroscopy offers promise as a monitor suitable for active control. Changes in local fuel/air ratios are manifested as variations in local combustion chemistry that yield fluctuations in the local concentration of key radical species. We have acquired molecular-emission spectra in various combustors, including a UCC/ITB, a PDE, and a Hencken burner, to assess the use of such spectra for determining the local fuel/air ratio. Molecular emission from the combustion intermediates OH, CH and C_2 has been collected in a time-averaged mode. In addition, time-resolved OH emission has been collected at fixed wavelengths. These data are being correlated with combustor operating parameters to enhance our understanding of the underlying combustion chemistry while providing design feedback for our combustor engineers.

These molecular-emission measurements are complemented by qualitative studies of unsteady combustion processes achieved through high-speed digital imaging of flame luminosity. Improved fuel-air mixing and subsequent flame propagation are essential for enhanced combustor performance. Highly intermittent, three-dimensional combustors are difficult to study with single-frame, laser-based imaging. We are evaluating the diagnostic utility of high-speed digital imaging in various advanced combustors at WPAFB, including a single swirl-cup combustor, a TVC, and a PDE. Imaging rates up to 63,000 frames-per-second and exposure times as low as 10 μs surpass the capabilities of conventional high-speed photography and provide new insights into phenomena such as soot formation, flame morphology at elevated pressures, and deflagration-to-detonation transition. In addition we are exploring the use of high-speed digital imaging for coherent-structure velocimetry (CSV) to enable time-resolved studies of flame-structure/fluid-dynamics interactions in unsteady, turbulent reacting flowfields.

In concert with an Air Force program designed to study the effects of additives on particulate production, we have accomplished planar LII measurements in a JP-8-fueled, single swirl-cup combustor with a central nozzle. Single-shot LII images of the soot exhibit localized high concentrations with varying spatial and temporal behavior. High-speed luminescence images reveal a similarly complex soot structure driven by local fluid and chemical behavior. Averages of the single-shot images have been utilized to assess the impacts of laser fluence, camera gate and delay settings, and global equivalence ratio on the LII signal. Most importantly, these single-shot and averaged LII measurements have been used to evaluate the performance of numerous particulate-mitigating fuel additives under development by the Fuels Branch (AFRL/PRTG) at WPAFB.

Continuing Collaborative Studies of Vortex/flame Interactions with École Centrale Paris and ONERA. Ongoing work in this area has been expanded to include experimental and computational studies of vortex/flame interactions in two-phase counterflow diffusion flames. Initial studies of multiple-vortex interactions that involve the collision of two vortices at the counterflow-flame location have been accomplished as well. Computational and experimental visualization of such multiple-vortex events is depicted in Fig. 1. Recent numerical simulations of flame interactions involving "micro" vortices (millimeter-sized) and "large" vortices (centimeter-sized) have provided some important insights regarding non-adiabatic flame temperatures observed during vortex/flame interactions.

Vortex-induced flame wrinkling and extinction represent fundamental turbulent flame phenomena that must be understood for the development of accurate numerical models. In our continuing work, we have achieved repeatable flame wrinkling and extinction using a two-phase

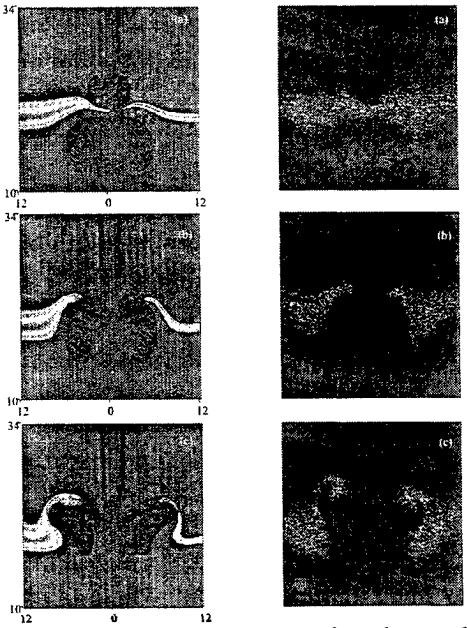

Figure 1. Computational and experimental visualization of a multiple-vortex/flame interaction. A larger vortex impinges from the air (bottom) side, while a smaller vortex impinges from the hydrogen (top) side.

counterflow diffusion flame and a piston-actuated vortex. Planar laser-induced fluorescence (PLIF) of CH has been used to mark the flame front, and particle-image velocimetry (PIV) has been used to obtain information about the flowfield. The phase-correlated CH PLIF and PIV results demonstrate that flame extinction occurs within one millisecond after the vortex begins to wrinkle the flame. Velocity measurements show that a five-fold increase in the fuel-side peak strain rate occurs during this extinction process. In addition to flame wrinkling and extinction, the effects of fuel equivalence ratio, droplet seeding, and PAH fluorescence on the CH PLIF signal have been studied.

Previous experimental and numerical studies have demonstrated that local flame temperatures can range significantly above or below the adiabatic flame temperature during micro (millimeter-size)-vortex/flame interactions. Such large excursions in temperature do not occur in large (centimeter-size)-vortex/flame interactions. To identify the physical mechanisms responsible for generating these super- or sub-adiabatic flame temperatures, numerical studies have been conducted for micro-vortex/flame interactions in a H_2/air counterflow diffusion flame. Contrary to expectations, preferential diffusion between H_2 and O_2 and geometrical curvature are not found to be the mechanisms responsible for generating these variations in local flame temperature. This is revealed in part through a simulation with identical diffusion coefficients for H_2 and O_2 that yields super- or sub-adiabatic flame temperatures during the micro-vortex/flame interaction. It appears that the Lewis number and the reactant-limiting characteristics of the micro-vortices are responsible for the observed behavior of the flame temperature. The magnitude of the temperature excursions depends on the value of the Lewis number. Propagation of the flame into the micro-vortex suggests that the amount of reactant carried by the micro-vortex is insufficient to feed the flame with fresh reactant during the entire vortex/flame-interaction process. While Lewis number governs the pre-heating or dilution of the reactant, the reactant-limited micro-vortex drives the generation of super- or sub- adiabatic flame temperatures by transporting the affected reactant into the flame zone at a different location—typically, to the flame near the head of the vortex. Conversely, in a large-vortex/flame interaction, the flame wraps around the outer perimeter of the vortex and remains there with sufficient inflow of fresh reactant to maintain it throughout the interaction process. In this case, the flame is unaffected by the Lewis number.

Triple-Pump Coherent Anti-Stokes Raman Scattering (CARS) for Simultaneous Measurements of Temperature and Multiple Species Concentrations. Working in close collaboration with Prof. Bob Lucht and his diagnostics team at Texas A&M University, we recently developed and demonstrated a triple-pump CARS system for simultaneous measurements of temperature and multiple species concentrations with high spatial and temporal resolution. Our triple-pump CARS approach employs four laser beams to generate CARS signals near two distinct wavelengths. Temperature and relative concentrations of the target species (with respect to N_2) are extracted by fitting the measured CARS spectra in each wavelength region. For the proof-of-concept measurements, CARS signals from N_2/O_2 and

N_2/H_2 pairings were collected. Single-shot and time-averaged measurements were performed in an atmospheric-pressure H_2/air diffusion flame. Representative spectra are depicted in Figs. 2 and 3. Demonstration of this measurement capability in a practical combustor rig at WPAFB is scheduled for this summer.

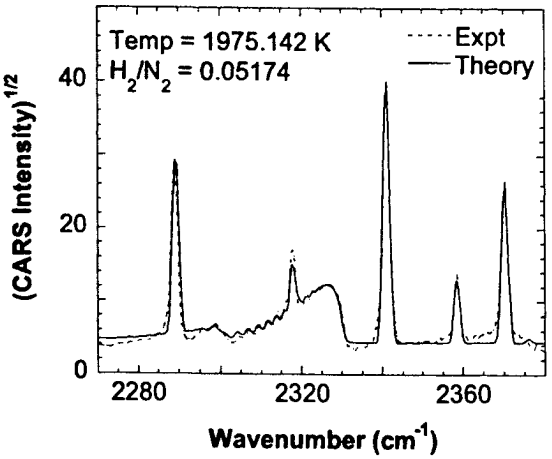

Figure 2. H_2/N_2 CARS signal obtained near 437 nm in a H_2/air diffusion flame (fuel-rich side).

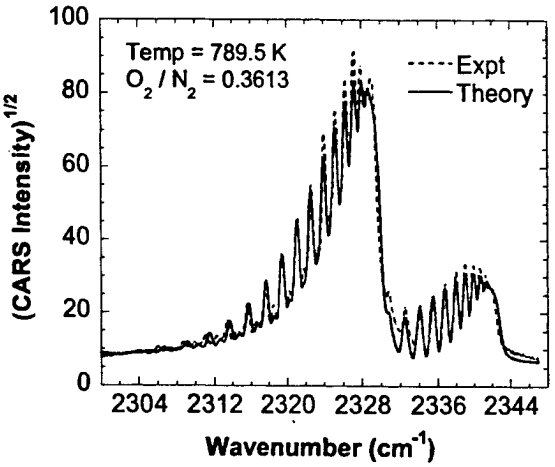

Figure 3. N_2/O_2 CARS signal obtained near 491 nm in a H_2/air diffusion flame (fuel-lean side).

Absorption Sensors in the Ultraviolet and Mid-Infrared Based on Diode-Laser Frequency-Mixing Schemes. Two all-solid-state continuous-wave (cw) laser systems, one for ultraviolet absorption measurements of nitric oxide (NO) and another for mid-infrared absorption measurements of carbon monoxide (CO), have been developed and demonstrated in collaboration with the Texas A&M group as well. In the NO system, the single-mode tunable output of a 10-mW, 395-nm external-cavity diode laser (ECDL) is sum-frequency mixed with the output of a 115-mW, frequency-doubled, diode-pumped cw Nd:YAG laser in a beta-barium borate (BBO) crystal to produce ~40 nW of tunable cw radiation at 226.8 nm. The wavelength of the 395-nm ECDL is scanned over NO absorption lines to produce a fully resolved absorption spectrum. Initial results with mixtures of NO and N_2 in a room-temperature gas cell suggest an NO detection limit of 0.2 ppm per meter path length based on a demonstrated absorption sensitivity of $2x10^{-3}$. Representative data are presented in Fig. 4.

In the CO system, the single-mode, tunable output of a 70-mW, 860-nm ECDL is difference-frequency mixed with the output of a 550-mW diode-pumped cw Nd:YAG laser in a periodically-poled lithium-niobate (PPLN) crystal to produce ~1 μW of tunable cw radiation at 4.5 μm. The wavelength of the 860-nm ECDL is scanned over a CO absorption line to produce a fully resolved absorption spectrum. Both the NO and CO sensors will be employed for measurements in the exhaust of a well-stirred reactor at WPAFB during the coming summer. Comparisons with computational predictions and physical-sampling-probe measurements are planned.

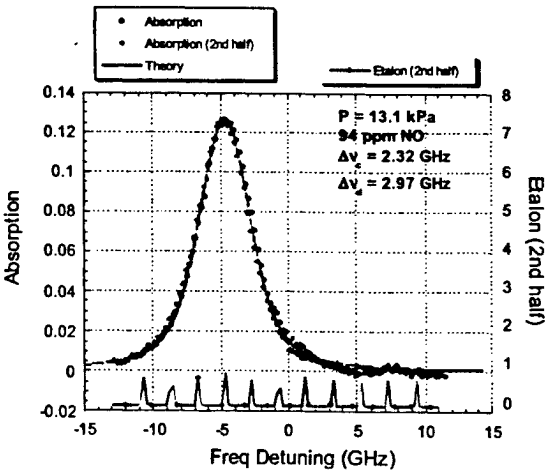

Figure 4. NO absorption spectrum of the $P_2(10)$ and $^PQ_{12}(10)$ overlapped absorption lines.

ADVANCED DIAGNOSTICS FOR REACTING FLOWS

AFOSR Contract No. 01-1-0145

Principal Investigator: Ronald K. Hanson

Mechanical Engineering Department
Stanford University, Stanford, California 94305-3032

SUMMARY/OVERVIEW:

The goal of this research is to develop advanced laser-based diagnostics for non-intrusive measurements relevant to air-breathing combustion. The program emphasizes spectrally-resolved absorption using cw tunable IR lasers and planar laser-induced fluorescence (PLIF) using pulsed IR and UV laser sources. Detailed below is progress on several diagnostic concepts: ketone tracers for PLIF imaging; IR PLIF for imaging IR-active gases; LIF at high pressure; wavelength-multiplexed strategies for fuel sensing; new concepts for wavelength-agile diode laser sensing; and a rapid kinetic spectrograph for shock tube studies. Also reported are high-temperature absorption measurements of CO_2, which have significant implications for UV-based combustion diagnostics, and initial work to explore shock tube and laser diagnostic techniques for studies of plasma-based ignition of combustion.

TECHNICAL DISCUSSION:

Ketone Photophysics for Quantitative PLIF Diagnostics

PLIF research on ketones is focused on fundamental photophysical experiments to quantify absorption and relative strength of fluorescence as a function of temperature, pressure, and excitation wavelength. Additionally, we model the photophysical behavior, enabling predictive capability for a broad range of conditions, and we use our fundamental understanding to guide development of PLIF techniques that measure relevant parameters in practical flowfields.

A database containing a variety of tracers is motivated by the need for a variety of physical properties (e.g. boiling points, diffusion coefficients) that match relevant fuels. Our PLIF-tracer database now contains measured absorption and fluorescence properties up to 1000 K and 16 atmospheres for acetone and 3-pentanone, in addition to an acetone photophysical model that allows extrapolation beyond current experimental data. (Adapting the model to 3-pentanone looks quite promising and is currently under way.) Utilizing our fundamental understanding of the photophysics, we have developed and optimized schemes for simultaneous, two-dimensional measurements of temperature and tracer-concentration in unsteady flows [see publication 1].

IR PLIF using Vibrational Transitions

Important combustion species such as CO_2 and CO do not have accessible, single-photon, electronic transitions outside the vacuum-UV. However, we have shown previously that the distribution of these species can be determined by LIF using vibrational transitions in the infrared [2]. IR PLIF is different from traditional UV/Vis PLIF because excited vibrational levels have much longer radiative lifetimes than excited electronic systems, and there are often multiple mechanisms for vibrational relaxation. For instance, in a flame, vibrationally excited

CO_2 undergoes extremely fast near-resonant vibrational transfer with H_2O (V-V transfer). Since the rates of V-V transfer vary greatly depending on the molecule and the conditions, evaluating vibrational LIF excitation schemes requires detailed analysis of the signal quantum yield.

We have recently performed detailed model calculations for CO and CO_2 LIF schemes [3,4]. For molecules like CO, which has relatively slow vibrational relaxation, linear excitation produces a signal with straightforward interpretation [3]. By contrast, the fast vibrational transfer of excited CO_2 with H_2O produces a quantum yield which has a very strong variation with gas composition for linear infrared LIF of CO_2. However, for CO_2, this can be mitigated with saturated excitation that overcomes the V-V transfer, resulting in a quantum yield that varies slowly with gas composition. Saturated excitation of LIF from hot CO_2 in flames thus appears feasible using the high power available in pulsed CO_2 lasers [4].

Quantitative LIF of NO at High Pressure

LIF of native NO is useful for understanding pollutant production, and LIF of seeded NO is an attractive means to measure instantaneous temperature and velocity fields. However, at pressures above a few bar, spectral broadening produces interference LIF from O_2, especially in lean systems. In the past year we have evaluated strategies previously proposed for excitation of NO A-X in the (0,0) band [5]. O_2 interference has been characterized for stoichiometries between 0.83 and 1.2 and pressures up to 60 bar. In addition, we have recommended a new strategy for the measurement of temperature from the ratio of LIF signals obtained from exciting a high and a low rotational energy feature. PLIF temperature measurements are shown in Fig. 1 for the burned gases in our premixed high-pressure flame facility for a methane/air flame seeded with 300 ppm NO. Using these temperature distributions, we have demonstrated the first quantitative PLIF measurement of NO in the burned gases of high pressure flames [6]. In addition to O_2 interference, the variation in collisional quenching with gas composition and temperature, and the effects of laser attenuation have been investigated.

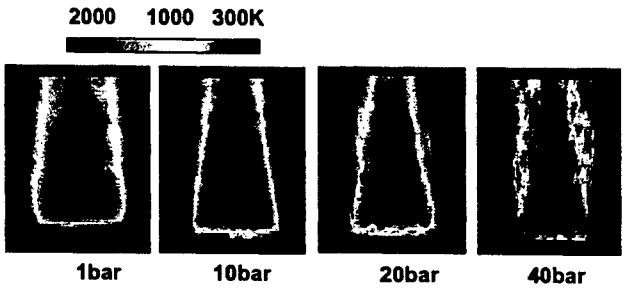

Figure 1. Temperature in the burned gases of a premixed methane/air flame from the ratio of PLIF images of NO.

Two-Phase Fuel Diagnostics by Wavelength-Multiplexing

Research is underway to develop a rapid-response diagnostic for simultaneous measurements of line-of-sight-averaged fuel droplet size, droplet volume fraction, and fuel vapor concentration. Laser diagnostics for monitoring both vapor and liquid droplets are complex in that: 1) the vapor of most liquid fuels has diffuse spectral features which cannot be covered by the rapid tuning range of existing lasers [7], and 2) vapor absorption and droplet extinction of the probe beam are usually coupled. Our initial approach is a sensor based on wavelength-multiplexing of five laser beams: three are used to measure droplet size (Sauter Mean Diameter) based on transmission

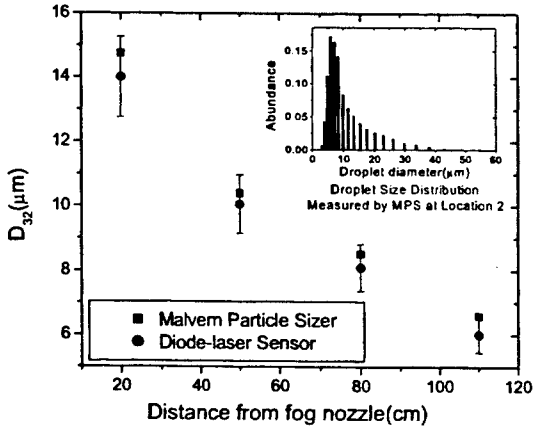

Figure 2. Comparison of droplet size measured with diode-laser senor and with Malvern Particle Sizer. Inset shows droplet size distribution measured by MPS 50 cm from the fog nozzle. From [8].

measurements; the other two are used to monitor vapor concentration based on differential absorption [8]. Successful initial results in a laboratory-scale ethanol spray, shown in Fig. 2, motivate further work and applications of this technique in propulsion systems.

Rapid Sensing of Temperature and Pressure by Spectrally-Resolved Absorption

Studies of advanced propulsion systems call for non-intrusive measurements under extreme conditions. Spectrally resolved absorption provides a powerful tool for such problems. Here we report a diagnostic based on cesium absorption that yields measurements of detonated-gas temperature and pressure histories spanning 2000 – 4000 K and 0.5 – 30 atm, with microsecond time response. We exploit the wavelength-scanning agility offered by an 852 nm vertical cavity surface-emitting laser (VCSEL), scanned at megahertz rates over a 10 cm^{-1} spectral window encompassing the spectral structure of the D_2 transition of atomic Cs. The trial application of this diagnostic is to a C_2H_4/O_2-filled pulse detonation engine [9,10]. Fig. 3 shows the good agreement between pressure measured spectroscopically and by transducer and compares measurements with a simulation from the Naval Research Laboratory.

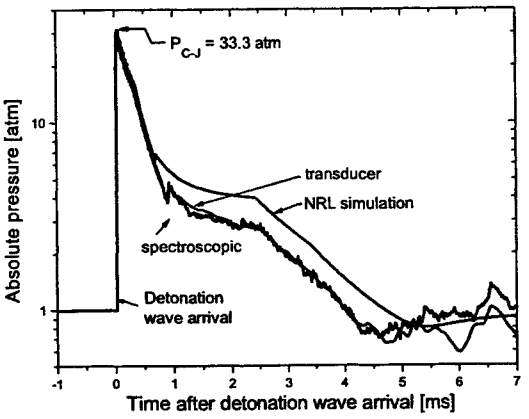

Figure 3. Pressure histories in a pulse detonation tube filled with stoichiometric C_2H_4/O_2 measured by spectrally resolved absorption, piezoelectric transducer, and by simulation. From [10].

This diagnostic strategy exhibits several advantages for applications in practical propulsion systems. First, the extremely strong absorption of Cs and the broad-wavelength scanning ability of the VCSEL make this sensor very robust. Second, the microsecond time response is attractive for studies of highly transient propulsion flows. Finally, this sensor offers the opportunity for off-wall pressure measurements.

Two other diode-laser diagnostics based on rapid broad-tuning have been developed. The first utilizes a VCSEL laser to measure O_2 absorption near 760 nm, allowing determination of the temperature distribution in a non-uniform region [11]. The second diagnostic utilizes an external heating source to achieve rapid, broad scans (~20 cm^{-1}) near 1.4 μm [12]. This should enable measurements of water vapor spectra and temperature in combustion gases at high pressure, where normal diode-laser techniques can fail due to scan-range limitations.

Kinetic Spectrograph

We have developed a UV absorption kinetic spectrograph for the identification and investigation of stable and transient species at high temperatures. With this new diagnostic, we have measured broad absorption spectra (190-300 nm) at 10 μs intervals in shock tube experiments. By first quantifying the absorption spectra of these species and then using this information to track their concentration in time, we have identified primary decomposition and oxidation pathways for large fuel molecules, and we have built a database for the time-histories of these species in shock-heated mixtures.

Implications of Absorption of Hot CO_2 on Ultraviolet Combustion Diagnostics

Measurements using our new kinetic spectrograph have revealed strong UV absorption by hot CO_2. Since CO_2 is UV-transparent at room temperature it has traditionally been neglected as

a source of interference in UV combustion diagnostics. However, we now realize that neglecting laser attenuation due to hot CO_2 can lead to large errors in such measurements [13,14].

Absorption cross-sections were measured in shock-heated CO_2 and H_2O between 900 and 3050 K, for wavelengths between 190 and 320 nm [13]. An empirical fit to the temperature-dependent absorption spectra provides a corrective tool for UV combustion diagnostics, and this has been applied to NO-LIF measurements in engines [14]. Such corrections are large enough that we think combustion diagnosticians using wavelengths under 250 nm need to consider absorption by hot CO_2, especially in large scale and/or high-pressure combustors.

Shock Tube Studies of Plasma Ignition

We have begun to investigate the use of shock tubes and spectroscopic diagnostics in the study of the chemistry and flow dynamics of plasma-assisted ignition. The shock tube provides a spatially-uniform combustion volume with well-defined conditions and excellent optical access. Diagnostics of interest include spectrally-resolved absorption and PLIF imaging.

AFOSR-SPONSORED PUBLICATIONS:

1. Thurber, M.C. and Hanson, R.K. "Simultaneous Imaging of Temperature and Mole Fraction Using Acetone Planar Laser-induced Fluorescence," *Experiments in Fluids*. **30**, 93-101 (2001).
2. B.J. Kirby and R.K. Hanson, "Imaging of CO and CO_2 using Infrared Planar Laser Induced Fluorescence," *Proceedings of the Combustion Institute* **28**, 253-259 (2000).
3. B.J. Kirby and R.K. Hanson, "Linear Excitation Schemes for IR Planar-Induced Fluorescence Imaging of CO and CO_2," *Applied Optics* **41**, 1190-1201 (2002).
4. B.J. Kirby and R.K. Hanson, "CO_2 Imaging with Saturated Planar Laser-Induced Vibrational Fluorescence," *Applied Optics* **40**, 6136-6144 (2001).
5. W.G. Bessler, C. Schulz, T. Lee, J.B. Jeffries, R.K. Hanson, "Strategies for laser-induced fluorescence detection of nitric oxide in high-pressure flames: I. A-X (0,0) excitation," *Applied Optics*, (2002) in press.
6. W.G. Bessler, C. Schulz, T. Lee, D.-I. Shin, M. Hofmann, J.B. Jeffries, J. Wolfrum, R.K. Hanson, "Quantitative NO-LIF Imaging in High-pressure Flames," *Appl. Phys. B*, submitted, May, 2002.
7. Ma, L., Jeffries, J. B., Romo, E. A., and Hanson, R. K., "Two-phase Fuel Measurements Using a Diode-laser Sensor", *41st Aerospace Sciences Meeting, Jan. 2003,* submitted 5/2002.
8. Ma, L., Sanders, S. T., Jeffries, J. B., and Hanson, R. K., "Monitoring and Control of a Pulse Detonation Engine Using a Diode-Laser Fuel Concentration and Temperature Sensor," *Proceedings of the Combustion Institute,* **29** (2002) in press.
9. Sanders, S. T., Mattison, D. W., Jeffries, J. B., and Hanson, R. K., "Sensors for High-Pressure, Harsh Combustion Environments Using Wavelength-Agile Diode Lasers", *Proceedings of the Combustion Institute,* **29** (2002) in press.
10. Sanders, S. T., Mattison, D. W., Ma, L., Jeffries, J. B., and Hanson, R. K., "Wavelength-Agile Diode-Laser Sensing Strategies For Monitoring Gas Properties in Optically Harsh Flows: Application in Cesium-Seeded Pulse Detonation Engine", *Optics Express,* submitted 4/2002.
11. Sanders, S. T., Wang, J., Jeffries, J. B., and Hanson, R. K., "Diode-Laser Absorption Sensor for Line-of-Sight Gas Temperature Distributions", *Applied Optics*, **40,** 4404 (2001).
12. Sanders, S. T., Mattison, D. W., Jeffries, J.B., and Hanson, R K., "Rapid Temperature-Tuning of a 1.4 μm Diode Laser with Application to High-Pressure H_2O Absorption Spectroscopy", *Optics Letters,* **26**, 1568 (2001).
13. C. Schulz, J.D.Koch, D.F. Davidson, J.B.Jeffries, R.K. Hanson, "Ultraviolet Absorption Spectra of Shock-Heated Carbon Dioxide and Water between 900 and 3050 K," *Chemical Physics Letters*, **355** 82-88(2002).

14. C. Schulz, J.B. Jeffries, D.F. Davidson, J.D. Koch, J. Wolfrum, R.K. Hanson, "Impact of UV Absorption by CO_2 and H_2O on NO LIF in High-Pressure Combustion Applications," *Proceedings of the Combustion Institute*, **29** (2002) in press.

MEASUREMENT OF ABSOLUTE OH CONCENTRATION AND TEMPERATURE IN A FLAME BY PHOTOTHERMAL DEFLECTION SPECTROSCOPY

ARO Grant Number DAAG55-98-1-0278

Principal Investigator: R. Gupta

Department of Physics
University of Arkansas
Fayetteville, AR 72701

SUMMARY/OVERVIEW

We have demonstrated that *absolute* minority species concentrations and temperature can be measured *simultaneously* in a flame by the photothermal deflection spectroscopy technique. OH concentration and temperature profiles in a fuel-rich flame have been measured. The measured values have been verified by independent measurements by other techniques. The ultimate goal of these experiments is to measure another parameter, the flow velocity, simultaneously with the absolute concentration and temperature.

TECHNICAL DISCUSSION

We are engaged in experiments to demonstrate that photothermal deflection spectroscopy (PTDS) technique can be used to measure absolute species concentration, temperature, and flow velocity in a flame. As a first step, we have measured two of the three parameters, that is, the absolute OH-concentration and temperature simultaneously.

In this technique, a laser beam, tuned to one of the absorption lines of the species of interest, is absorbed by the species. Most of the absorbed optical energy quickly appears in the thermal modes of the flame gases, thereby changing its refractive index. This change in the refractive index is detected by the deflection of a probe laser beam (1). The deflection amplitude yields the absolute species concentration. The temporal evolution of the signal yields the diffusion time, which is proportional to the temperature. If a significant fluid flow exists, the flow velocity can be measured by placing the probe beam slightly downstream from the pump beam and measuring the time-of-flight of the heat pulse (2).

Figure 1 shows the burner used in this work. Premixed methane and air with an equivalence ratio of $\varphi = 1.63$ was used. A conical flame, about 5 cm in diameter at the base and about 6 cm in height, was produced. The experimental arrangement is shown in Figure 2. $Q_1(8)$ line of OH at 309.243 nm was excited by a frequency-doubled dye-laser. The laser pulses were about 7-ns in duration and we used about 12 μJ of energy/pulse. For absolute measurements, it is important that the optical transition not be saturated and every attempt was made to ensure this. The probe beam was provided by a cw HeNe laser. The deflection of the probe beam was detected by a

position-sensitive detector (a quadrant detector used in conjunction with a difference amplifier) and the data were observed on a digital oscilloscope

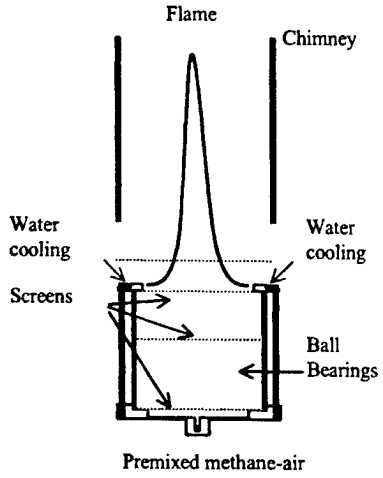

Fig 1: A sketch of the burner used in this work

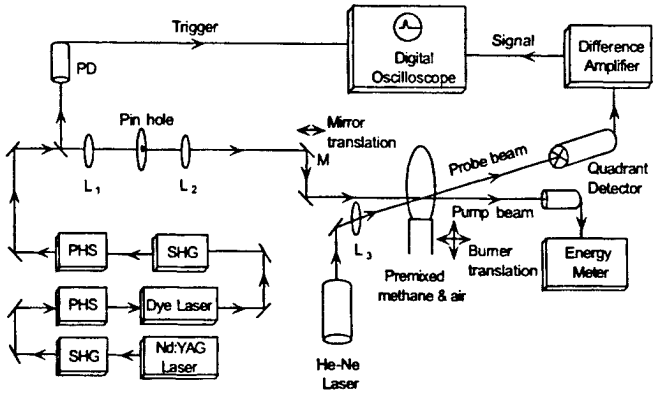

Fig 2:Schematic diagram of the apparatus

Figure 3 shows typical data. The deflection of the probe beam (in micro-radians) is plotted against time. Zero of the time-axis corresponds to the instant of laser pulse (assumed to be a δ-function) firing. The probe beam deflects at the instant of laser firing, and gradually returns to its original position on the time scale of thermal diffusion from the laser-irradiated region. The flow velocity of the flame gases had a negligible effect on the PTDS signals in this particular flame.

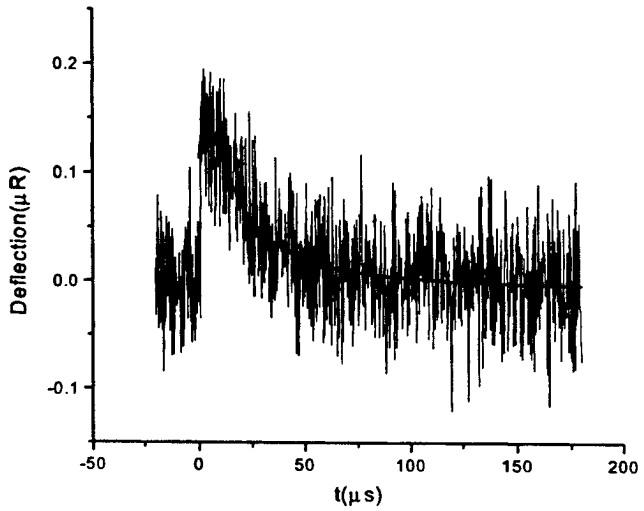

Fig 3: A typical PTDS signal

The amplitude of the signal depends on the absorption of the laser beam, which is a measure of the OH density. The quenching rates in OH are much faster than the radiative decay rate (3), thus we can assume that most of the optical energy appears in the thermal modes of the flame

gases. This allows us to determine the absolute concentrations. Unlike LIFS, we use collisions to our advantage. We do not need to know what the collision rate is, as long as we know that it is much faster than the radiative rate. An analysis of the temporal shape of the signal yields the thermal diffusivity of the laser-irradiated region. The temperature of the flame is determined from the measurement of the thermal diffusivity (4).

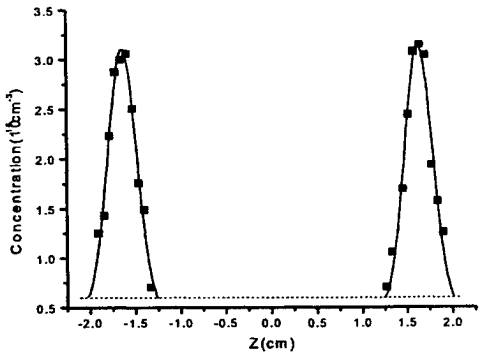

Fig 4: OH concentration profile in our flame

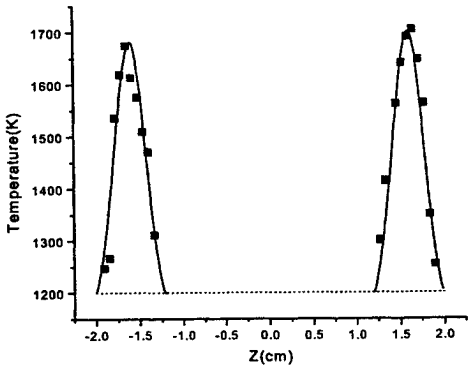

Fig 5: OH temperature profile in our flame

Figure 4 shows the absolute OH-concentration profile in this flame, obtained from the analysis of PTDS data. The OH density peaks near the outer rim due to air-entrainment in this fuel-rich flame. Zero of the abscissa corresponds to the center of the burner. The dotted line corresponds to the current limit-of-detection in our experiment. Figure 5 shows the temperature profile of the same flame, also obtained by the analysis of the PTDS data.

Further experiments were conducted to determine the reliability of our concentration and temperature measurements. At one point, z = -1.72 cm, the temperature was also measured by a measurement of the Boltzmann distribution (5) among the rotational sublevels of OH ($Q_1(3)$-$Q_1(10)$). The temperature, T = 1600±70 K, agrees with the value T = 1655±100 K obtained by the Boltzmann method within the uncertainties of the two measurements. In order to check the reliability of our concentration measurements, a McKenna flat-flame burner was used. This burner has a very uniform concentration profile in the horizontal direction, and the optical path-length is sufficiently long that a reliable concentration measurement using the direct absorption measurement can be performed. The PTDS measurements of the concentration agreed with those obtained by the direct absorption measurements within few percent (6). Therefore, we are quite confident of our concentration and temperature measurements.

We are currently engaged in experiments to measure absolute concentration, temperature, and flow velocity measurements in a flame with significant flow velocity.

REFERENCS

1. See for example, R.Gupta, chapter 3 in *Photothermal Investigation of solids and fluids*, Ed. J.A.Sell (Academic Press, New York, 1989)
2. R. Gupta, Chapter 8 in *Photothermal Investigation of solids and fluids*, Ed. J.A.Sell (Academic Press, New York, 1989)
3. M.Köllner, P.Monkhouse, J.Wolfrum, *Chem.phys. Lett.* 168, 355(1990)

4. Y.Li and R.Gupta, *Applied Physics. B.*, Accepted for publication, 2002
5. See, for example, A.C.Eckbreth, *Laser Diagnostics for Combustion Temperature and Species,* (Abacus Press, Cambridge, MA, 1988)
6. Y.Li and R.Gupta, to be submitted to *J. Appl.Phys.*.

CROSSED-PLANE LASER IMAGING OF PREMIXED TURBULENT COMBUSTION PROCESSES

DAAD19-99-1-0324
F. C. Gouldin

Cornell University, Ithaca, NY 14853

OVERVIEW

The objective of this research is to measure, using crossed-plane imaging, flamelet normal vectors and the instantaneous thermal structure of flamelets in premixed turbulent flames. Data for surface normal vectors can be used to calculate important quantities such as Σ, the flamelet surface density, a quantity that is proportional to the mean rate of product formation per unit volume, $\langle w \rangle$. Flamelet thermal structure data can be used to estimate the constant of proportionality between $\langle w \rangle$ and Σ. Instantaneous flamelet normals have been measured in three dimensions using crossed-plane imaging via laser tomography and planar laser induced acetone fluorescence. The evolution of flamelet wrinkling in the downstream direction in V-flames has been measured. Crossed-plane Rayleigh imaging has been developed to measure temperature gradients and other thermal quantities within flamelets.

TECHNICAL DISCUSSION

Under previous ARO support, crossed-plane tomography was developed to measure directly all three components of the instantaneous surface normal vector. Mie scattering by silicon oil droplets from two, pulsed-laser light sheets is recorded by ICCD cameras. Because the droplets evaporate at approximately 650 K, scattered light marks regions of reactants, and the boundary between light and dark regions in an image marks where the flamelet intersects the laser light sheet. For crossed-plane tomography two sheets are aligned perpendicular to each other, and their horizontal line of intersection is the measurement line. Where the flamelet crosses this line, lines tangent to the flamelet surface are found in each light sheet and their cross product defines the instantaneous flamelet normal direction.

In the past several years we have used the concept of crossed-plane tomography to measure normal vectors in laboratory V-flames [1-3] and in a research spark ignition engine [4]. During the past year we have explored the use of single plane tomography for quantifying, under special circumstances, the magnitude of surface wrinkling. In addition, we have extended the concept of crossed-plane imaging to crossed-plane Rayleigh imaging for temperature and are using this technique to quantify the flamelet's instantaneous thermal structure. Finally we are working to combine crossed-plane tomography with stereo particle imaging velocimetry (SPIV) to measure components of flamelet strain and curvature imposed by the reactant flow.

Single Plane Imaging

Flamelet normal measurements in V-flames and in a research spark ignition engine [1-4] suggest that the probability density function (pdf) of the flamelet normal has a universal form. When the

normal vector is defined in spherical coordinates with a polar angle ϕ, an azimuthal angle θ ($\underline{N}(\phi,\theta)$), and the polar axis aligned normal to mean progress variable, <c>, constant surfaces (parallel to the surface normal, $\underline{N}_{<c>}$), the pdf is given by

$$P(\phi,\theta)d\Omega = C\exp(-(\phi/\varsigma)^2)\sin\phi d\phi d\theta . \quad (1)$$

$d\Omega$ is a differential solid angle and equals $\sin\phi d\phi d\theta$; C is a normalization constant.

In crossed-plane tomography one measures $\underline{N}$ where the surface crosses the measurement line, and hence the data are weighted by the probability that a surface of a given orientation crosses this line; the data are crossing-weighted [3]. The crossing-weighted pdf has the form

$$P_c(\phi,\theta)d\Omega = C'|\cos\beta|\exp(-(\phi/\varsigma)^2)\sin\phi d\phi d\theta , \quad (2)$$

where β is the acute angle between $\underline{N}$ and the measurement line.

Equation (1) shows that all values of θ are equally probable. This symmetry means that we can extract the value of ζ from single plane imaging data provided that the image plane contains $\underline{N}_{<c>}$. Consider the case of a V-flame with tomography data taken in a vertical imaging plane that is perpendicular to the stabilizer rod. A normal to the flamelet curve in the vertical plane is the projection of $\underline{N}$ onto the image plane. Data for the orientation of this projection, in the form of the angle, α, between the projection and a η line that is locally parallel to $\underline{N}_{<c>}$ (Figure 1), can be taken along η. Through numerical analysis based on (2) it can be shown that the crossing weighted pdf of α is fit by

$$P_c(\alpha)d\alpha = C^*|\cos\alpha|\exp(-(\alpha/\gamma)^2)d\alpha, \quad (3)$$

and that there is a one to one relationship between the fit parameters γ and ζ, Figure 2.

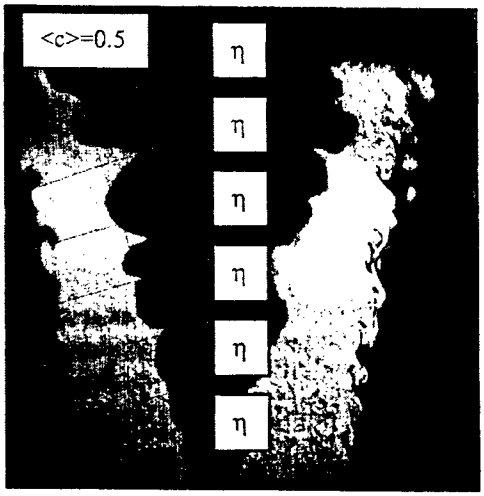

Figure 1. Image of V-flame showing six representative η lines and the <c> = 0.5 contour.

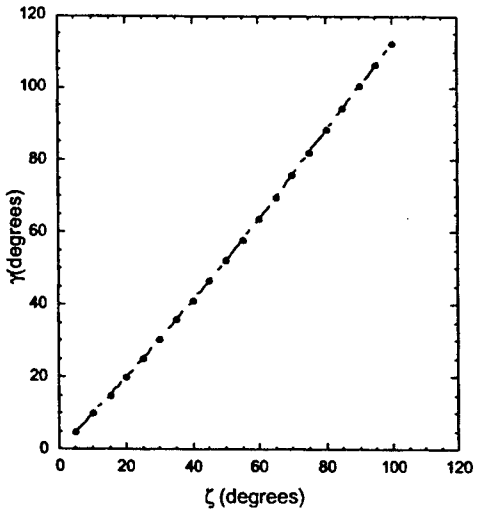

Figure 2. Plot of 2-D fit parameter γ versus the 3-D fit parameter ζ found by numerical analysis.

To exploit this relationship we have taken single plane data from 7 different V-flames in order to quantify the change in flamelet wrinkling with downstream distance. In each flame between a 1000 and 2000 images were taken, and data for α along six different η lines (Figure 1) were obtained. Pdfs were constructed from the data taken along individual η lines for each flame condition, and values of γ were obtained by fitting (3) to the pdfs. The γ values were then used to find ζ, for different downstream locations. It was found that over the measurement region, ζ increases linearly with distance and that the rate of increase depends on the turbulent intensity scaled by the laminar flame speed and other factors [5].

Crossed-Plane Rayleigh Imaging

Rayleigh scattering from molecules is proportional to the molecular number density, n, and for lean premixed methane-air flames the constant of proportionality is a weak function of c. Consequently, 2-D Rayleigh imaging can be used to measure 2-D distributions of n and temperature, T. In turn crossed-plane Rayleigh imaging can be used to measure instantaneous temperature and temperature gradient vectors along the measurement line with very high spatial and temporal resolution (< 0.2 mm and < 50 nsec). From a single image plane two of the three components of the gradient can be calculated. With crossed-plane imaging, the third component is calculated in the orthogonal plane along the line of intersection of the two imaging planes.

We have made crossed-plane Rayleigh measurements in a turbulent V-flame; $\Phi = 0.7$; U = 3 m/s; u'/U = 7% and $u'/S_L^0 = 1$. Image data were obtained using a pulsed Nd:YAG laser and two thermoelectrically cooled, intensified CCD cameras. The laser output was split into two laser beams, and to avoid interference due to simultaneous scattering from both beams a delay loop was used to separate in time the arrival at the burner of light in the two image planes. The two cameras exposures were controlled by gating the intensifiers. Images were stored on disk for later analysis that consisted of spatial smoothing to reduce the influence of shot noise and, through calibration, determination of the temperature field. Along the measurement line the components of the temperature gradient are obtained by fitting to polynomials the temperature variation in three orthogonal directions and differentiating.

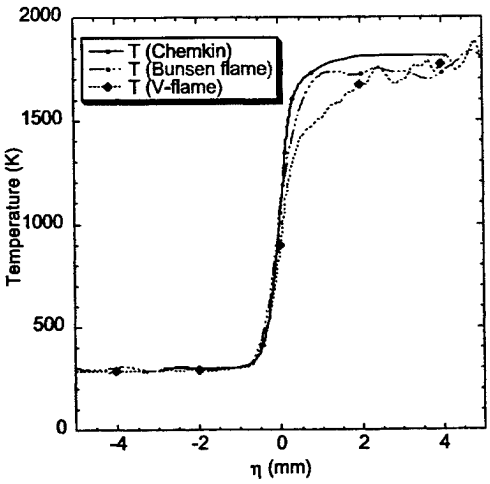

Figure 3. Comparisons of temperature profiles obtained from Rayleigh imaging of laminar V- and Bunsen flames and from calculation.

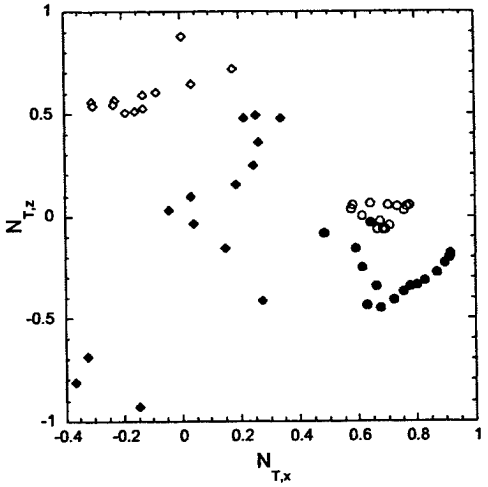

Figure 4. $N_{T,x}$ versus $N_{T,z}$ along the measurement line from four different realizations. The view is of the tip of $\underline{N}_T$ sighting down the measurement line.

To evaluate the influence of noise, vertical plane measurements were made on laminar V- and Bunsen flames and the results compared to calculations of an unstretched laminar flame with the same equivalence ratio, Figure 3. It can be seen that for temperatures below about 1500 K the agreement between measurements and calculation are quite good. The largest source of noise in these measurements is shot noise, and therefore the signal to noise ratio declines with increasing temperature. This trend is evident in Figure 3 where noise becomes apparent above 1500 K. At high temperature there is a systematic difference between calculation and the V-flame profile and, to a lessor extent, between the calculation and the

Bunsen results. The V-flame difference is surprisingly large. It is repeatable from laser shot to laser shot, from day to day and for different flow velocities and for different mixture ratios. Our conjecture is that flow induced stretch due to acceleration in the product gases is the cause of the "dip" seen in the temperature profile. Support for this conjecture is found in the Bunsen flame data where no dip is seen. In V-flames, product gases are confined to the V, and streamlines are curved upward, while in Bunsen flames product gases are free to expand.

Based on the results of asymptotic analysis, Peters has proposed a three layer structure for premixed flames – the preheat zone, the inner and the oxidation layers [7]. The oxidation layer lies on the product side of the other layers and is where CO is oxidized. For laminar V-flames we suggest that stretch extends from the combustion products into the oxidation layer and slows CO oxidation causing the "dip". The stretch is caused by the acceleration of combustion products confined to the center of the V-flame, a confinement not present in a Bunsen flame.

Crossed-plane Rayleigh data can be used to obtain a number of quantities along the measurement line, y, the line of intersection between the two laser sheets. These quantities include $T(y)$, $\nabla T(y)$, isothermal surface normals ($\underline{N}_T = \nabla T(y)/|\nabla T(y)|$), and the isothermal surface density (Σ_T). As an example, plots of the z versus the x components of $\underline{N}_T$ are presented in Figure 4. For some realizations the normals are nearly co-linear indicating little perturbation of the flamelet structure, while in other realizations there is large variation.

Summary and Future Work

Crossed-plane tomography has been developed to measure instantaneous flamelet surface normals and data obtained in several V-flames and a SI engine indicate a universal form for the surface normal pdf. This form has been used to extract from 2-D imaging data the 3-D fit parameter as a function of downstream distance in seven different flames. The data show that the fit parameter grows linearly with distance. The concept of crossed-plane imaging has been extended to Rayleigh imaging and data along the measurement line for T, ∇T, $\underline{N}_T$, and Σ_T have been obtained in a single flame.

Planned future work includes single plane measurements and additional crossed-plane Rayleigh imaging measurements in three different burners: V-flame, Bunsen flame and swirl-flow burners. The goal of the measurements is to determine the influences of flame configuration and turbulence levels on flamelet wrinkling and the thermal structure. In addition, the plan is to combine SPIV with crossed-plane tomography. The SPIV image plane will be vertical and the two tomography planes will be at ±45 degrees with respect to the vertical. Three lines of intersection between the imaging planes are formed. Velocity data in reactants will be obtained in the vertical plane, and flamelet normals will be obtained at flamelet crossing points along the three intersection lines. From these data components of the flamelet surface curvature tensor and the reactant flow velocity normal to the surface will be estimated and used to help quantify flow imposed strain and reaction sheet curvature.

References

1. D. C. Bingham, F. C. Gouldin, D. A. Knaus, *Proc. Comb. Inst.* **27**: 77-84, 1998.
2. D. A. Knaus, F. C. Gouldin, *Proc. Comb. Inst.* **28**: 367-373, 2000.
3. D. A. Knaus, F. C. Gouldin, D. C. Bingham, *Comb. Sci. Tech.*, **174**: 101-134, 2002.
4. D. A. Knaus, F. C. Gouldin, P. C. Hinze, P. C. Miles, *SAE Trans.***108**, Paper No.1999-01-3543, 1999.
5. S. S. Sattler, F. C. Gouldin, D. A. Knaus, to appear in *Proc. Combust. Inst.* **29** (2002).
6. N. Peters, *Turbulent Combustion*, Cambridge University Press, 2000.

PLANAR IMAGE PARTICLE ANALYZER FOR WHOLE FIELD SPRAY APPLICATIONS

SBIR Program (Grant/Contract No.DAAD19-01-C-0011)

Principal Investigators(s): Cecil Hess, Jan Burke, and Dave Weber, MetroLaser
Volker Kebbel, BIAS, Bremen, Germany

MetroLaser, Inc., 2572 White Road, Irvine, CA 92614-6236 (chess@metrolaserinc.com)
BIAS, Klagenfurter Straße 2, D-28359 Bremen, Germany

SUMMARY/OVERVIEW

The purpose of this work is to develop a whole field measurement technique that is capable of simultaneously sizing multiple transparent droplets on a plane from scattered light features that are independent of laser beam intensity and obscuration. Last year we reported the first droplet size results obtained with digital holography. This year we discuss some of the requirements of the technique to measure sprays and some of the tradeoffs associated with fringe analysis versus image analysis.

TECHNICAL DISCUSSION

Light scattered by reflection and refraction from droplets immersed in a laser sheet is recorded holographically on a CCD chip and subsequently reconstructed mathematically. The reconstruction may be realized at any convenient plane thus giving the user flexibility in signal analysis. The first paper based on the holographic technique was presented in Lisbon (Hess, 1998.) Other related research in this area is based on photographic recordings of interference patterns, which typically limit the applications to sparsely populated sprays (Glover, 1995). Cylindrical optics has also been used to compress the images in one dimension and thus increase the number density capability (Maeda, 2000). Digital holography (Kreis, 1997, Kebbel, 1999) expands the capability of the technique to a third dimension thus giving the user the option to mathematically reconstruct the object at a convenient plane. For the present application the object consists of scattering features from droplets, which can be reconstructed at a plane where particle overlapping can be avoided or filtered out.

The technique is called Planar Image Particle Analyzer (PIPA). The general configuration of PIPA is given in **Figure 1**. A laser sheet illuminates the particles and their scattered light (object beam) is collected by a receiver of f-number (f/#) placed at a collection angle θ. A beamsplitter mixes the reference beam with the object beam to form the hologram.

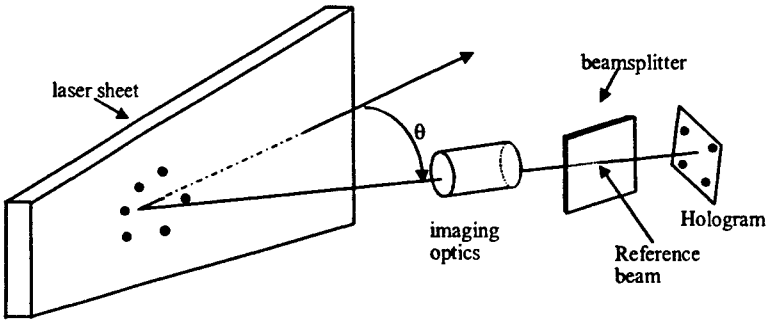

Figure 1. Schematic of PIPA.

Each of the transparent droplets immersed in the laser sheet will scatter light that is refracted and reflected thus yielding either a fringe pattern (*fringe mode*; defocused particle images) or two distinctive spots (*spot mode*; focused particle images) for each particle. The fringe count or fringe frequency and/or the separation between the two spots yield the droplet size. Because of the 3-D capability of holography, one can choose to reconstruct the scattered light to show either the fringe pattern or the two spots, depending on the resolution of the recording medium and filtering requirements, to avoid the overlapping of particle images.

To record holograms requires the introduction of a reference beam. The angle between the object and reference beams is limited by the resolution of the recording media (in the case of a CCD by the pixel pitch) according to the following relationship:

$$\textbf{2 x film resolution or pixel pitch} = \frac{\lambda}{2\sin\left(\frac{\theta_{max}}{2}\right)}. \qquad (1)$$

For $\lambda = 0.694$ μm and pixel pitch = 6.8 μm, $\theta_{max} = 0.051$ rad. This represents the most significant limitation of the technique since, with current technology, it limits the field of view or the minimum droplet size. However, CCDs continue to advance both in number of pixels and in reduced pixel size. Therefore, the limitation will be less significant in the future.

In PIPA, particle images appear as two point light sources that are separated by approximately 90% of the particle diameter. If the resolution of the recording medium is not adequate to record two closely spaced spots, the measurement strategy can shift to recording the scattered light away from the image plane where the light emanating from the two spots interferes to produce a fringe pattern. Thus, at an out–of–focus plane, the particles appear as a fringe pattern. Size information can subsequently be obtained from the fringe frequency. With photography, one can only record and examine one measurement plane at the time. The problem of measuring the out–of–focus plane with photography is that for high particle concentration, the areas corresponding to individual particles overlap, making the fringe analysis difficult at best and impossible under some conditions.

Reconstruction of Digital Holograms at the Scheimpflug Angle

In order to avoid the overlap of wavefronts from different droplets, the images of all the droplets should come to a focus in the same plane. This minimizes the image size and reduces overlapping. This condition may be obtained by tilting the CCD to the Scheimpflug angle as shown in **Figure 2.**

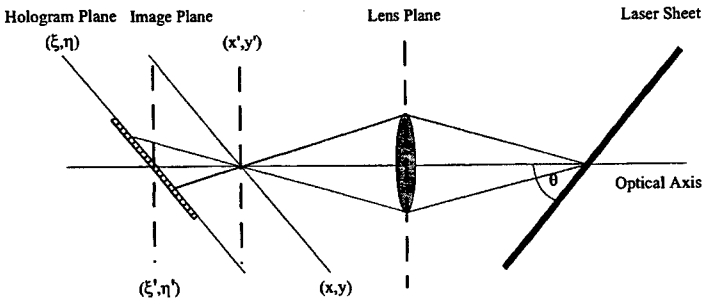

Figure 2. Recording geometry of digital holograms at the Scheimpflug angle.

Tilting the CCD reduces the effective pixel size in one dimension and a numerical reconstruction of the wavefront in the image plane leads to distortions of the wavefront if a conventional reconstruction algorithm is used. To accurately reconstruct the images we need to consider the tilt of the hologram in the reconstruction algorithm in order to prevent the distortions.

The basis for the numerical reconstruction of holograms is the Rayleigh-Sommerfeld diffraction formula:

$$b(x,y)=\frac{1}{i\lambda}\iint h(\xi,\eta)r(\xi,\eta)g(x,y,\xi,\eta)\cos\Theta\, d\xi d\eta \tag{2}$$

with

$$g(x,y,\xi,\eta)=\frac{exp\{ik\rho\}}{\rho} \tag{3}$$

and

$$\rho=\sqrt{d^2+(\xi-x)^2+(\eta-y)^2}\ . \tag{4}$$

Here $h(\xi,\eta)$ is the recorded hologram, $r(\xi,\eta)$ represents the reference wave field and k denotes the wave number. Due to the small angles between the hologram normal and the rays from the hologram to the image points, the obliquity factor cos Θ normally can be set cos Θ = 1.

For a proper reconstruction according to **Figure 2**, the impulse response function $g(x', y', \xi', \eta')$ has to be modified with respect to a conventional reconstruction. This is performed by applying a coordinate transformation defined by the angles of rotation θ and φ:

$$\begin{aligned}\xi'-x' &= (\xi-x)\cdot\cos(\varphi)\\ \eta'-y' &= (\eta-y)\cdot\cos(\theta)+(\xi-x)\cdot\sin(\varphi)\cdot\sin(\theta)\\ d' &= d-(\xi-x)\cdot\cos(\theta)\cdot\sin(\varphi)+(\eta-y)\cdot\cos(\theta)\end{aligned} \tag{5}$$

If this transformation is applied, the impulse response function contains spatial frequencies which cannot be resolved by the given raster. This effect is generated by the additional (linear) factors in the transformation of the distance d. If this linear phase factor is neglected, the tilted plane can be reconstructed.

In the reconstruction algorithm this transformation can be performed to the pixel size of the CCD-target. This approach was tested using holograms of a USAF resolution chart. During data acquisition the CCD-target was tilted in order to fulfill the Scheimpflug condition.

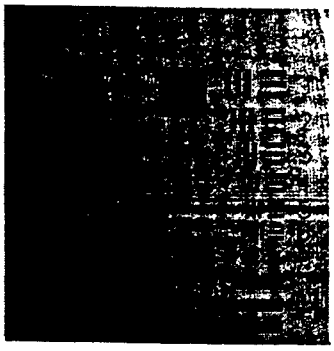

Figure 3. Numerical reconstruction using coordinate transformation.

Note how in **Figure 3** the horizontal as well as the vertical lines are in focus thus demonstrating the validity of the procedure. In the coordinate transformation a linear phase factor is neglected. This can lead to a systematic error in the result. Its influence as well as that of the reconstructed pixel size has to be investigated in the future. The transformation can be applied in the Fresnel as well as in the convolution approach but it is simpler in the latter, because the original pixel sizes are the same

in the hologram and the reconstruction plane. Data corresponding to a stream of monodisperse droplets collected with digital holography at the Scheimpflug angle is shown in **Figure 4**.

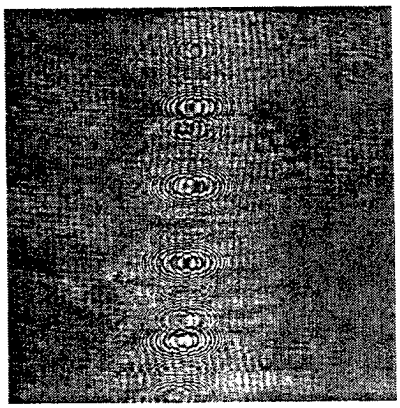

Figure 4. Particle images recorded under the Scheimpflug condition; camera tilted about vertical axis by 50° versus optical axis.

It can clearly be seen how the particle images (their hexagonal shape comes from a variable iris) are now elongated in the x direction. The reconstruction of these holograms has to account for the different effective pixel dimensions in x and y direction, since these introduce a pronounced astigmatism. A coordinate transformation is applied to rectify this effect; reconstructions with and without the correction can be seen in **Figure 5**.

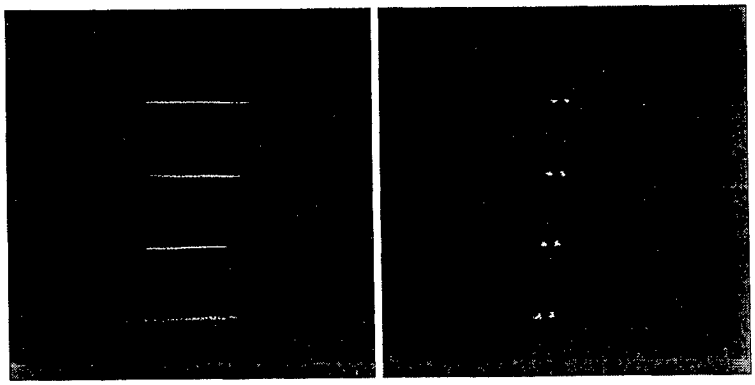

Figure 5. Digital intensity reconstructions from the hologram of Figure 6 at a distance of 12.3 cm from the CCD plane. Left: without correction (note the focus of vertical component). Right: with correction.

Without the correction, the vertical focus is at 12.3 cm and the horizontal focus at 31 cm from the CCD plane; with the correction applied, all the particles now come to a focus in the same plane.

If the correction is omitted, the vertical compression of the particles can be advantageously used to eliminate vertical overlapping of particle images, while the horizontal fringes are still present for evaluation. This has been achieved by Maeda, *et al.* (2000) with the use of a cylindrical lens; in the case of digital holography, no additional optical components are necessary. Besides exploiting the astigmatism, it is also possible to use a digital filtering technique to overcome the overlapping of particle images and background noise.

REFERENCES

Glover, A., Skippon, S., and Boyle, R., (1995) "Interferometric Laser Imaging for Droplet Sizing: A Method for Droplet-Size Measurement in Sparse Spray Systems", Applied Optics, Vol. 34, No. 36, pp. 8409-8421.

Hess, C.F., (1998) *"Planar Particle Image Analyzer"*, presented at 9th International Symposium on Application of Laser Techniques to Fluid Mechanics, July 13-16, 1998, Lisbon, Portugal.

Kebbel, V., Adams, M., Hartmann, H.J., and Jüptner, W., (1999) "Digital Holography as a Versatile Optical Diagnostic Method for Microgravity Experiments", *J. of Meas. Sci Technology*, 10, pp. 893-899.

Kreis, T. and Jüptner W., (1997) "Principles of Digital Holography" (Akademie Verlag series in Optical Metrology 3) *ed. W. Jüptner and W. Osten* (Berlin: Akad. Verl.) pp. 353-363.

Maeda, M., Kawaguchi, T., Hishida, K., (2000) "Novel Interferometric Measurement of Size and Velocity Distributions of Spherical Particles in Fluid Flows", Meas. Sci. Technol. 11, L13-L18.

SUB- AND SUPER-CRITICAL EVAPORATION AND COMBUSTION OF A MOVING DROPLET

DAAD 19-99-1-0116

Principal Investigator: George Gogos

University of Nebraska-Lincoln
303 Canfield Administration Bldg
Lincoln, NE 68588-2618

SUMMARY: We are conducting a comprehensive computational study of fuel droplet evaporation and combustion in sub- and super-critical ambient conditions under forced convection. An experimentally validated model for a moving spherical droplet that undergoes combustion has been developed. Multicomponent mass diffusion, which moved predictions closer to experimental data, and transient effects have been examined. With respect to high pressure and high temperature droplet vaporization, we have attempted to include deformation of a moving droplet. Our previous axisymmetric code (in spherical coordinates) is not convenient to handle droplet deformation. We developed a new 2-D code in cylindrical coordinates for that purpose. At this point, the new code predicts results in agreement with experimental data (and with our previous code) when we turn off droplet deformation (low Weber numbers).

TECHNICAL DISCUSSION: Two major aspects of droplet evaporation/combustion have been studied and are discussed below.

I. Numerical Simulation of Droplet Combustion Under Forced Convection. Starting with our validated axisymmetric quasi-steady code for the combustion of a moving droplet, we have made the following two major changes to the code:

a) We have relaxed the assumption that all binary diffusion coefficients have the same value. The current code allows for different multicomponent diffusion coefficients. Preliminary results have only recently been obtained.

b) We have relaxed the quasisteady assumption. The current transient code can predict, for example, how a moving droplet with a wake flame configuration, transitions to a droplet surrounded by an envelope flame, as the droplet decelerates due to the drag it experiences. These two changes are presented in more detail below.

a). Numerical Simulation of Droplet Combustion in a Forced Convection Environment; Multicomponent Diffusion Coefficients (with Dr. Daniel N. Pope). Over the past few years, a quasi-steady numerical model has been developed to investigate fuel droplet combustion under forced convection in a low pressure zero-gravity environment [1]. The gas-phase solution was obtained using the axisymmetric equations of mass, species, momentum, and energy conservation in spherical coordinates. Droplet internal circulation was accounted for by solving the axisymmetric momentum equations for the liquid phase. The gas and liquid phase were solved iteratively and coupled via the interfacial conservation equations. A staggered grid was

adopted and the governing equations were discretized using the finite volume [2] and SIMPLEC [3] methods.

Two key assumptions used in the quasi-steady model were; (1) a one-step overall reaction was used to describe combustion, and (2) all binary diffusion coefficients were assumed to be equal. The values for the activation energy, and oxygen and fuel concentration exponents in the finite-rate kinetics were adopted from Westbrook and Dryer [4]. The pre-exponential factor was determined by comparison of numerical results with experimental data [5] for extinction velocity. For n-heptane, a pre-exponential factor three times that of Westbrook and Dryer [4] was selected. The assumption of a single binary diffusion coefficient (along with neglecting pressure and thermal diffusion) results in Fick's Law for the diffusion velocity of each species. The binary diffusion coefficient for the fuel and oxidizer was used in the code and was evaluated as a function of the local temperature. Despite the use of these assumptions, the numerical predictions were in qualitative agreement with experimental results from the literature [1].

It has been shown that for quasi-one-dimensional diffusion flames, the structure and extinction of the flame depends on the different diffusional transport rates of fuel and oxidizer in the "inner" and "outer" flame zones [6]. A more accurate description of the diffusion velocity for each species is required to model this effect. The governing equation for the diffusion velocity of each species, assuming that pressure and thermal diffusion are negligible, is the Stefan-Maxwell equation. This equation, when written for each species, gives an equation set that is linearly dependent. To solve this problem, one of the equations in the equation set is replaced by the constraint equation $\sum Y_i V_i = 0$, where Y_i and V_i are the mass fraction and diffusion velocity of the i^{th} species and the sum is taken over all species. The direct solution of the resulting set of equations at each grid point would be computationally prohibitive for the current axisymmetric (2-D) case. Simplified treatments [7-10] and approximations [11] have been proposed in the literature to reduce the computational requirements. A new method has been developed and incorporated in the quasi-steady code. This new method uses Fick's Law with a different multicomponent diffusion coefficient for each species (see method V in [9]) to define the diffusion part of the convection/diffusion flux in the finite volume form of the species conservation equations. The approximate diffusion velocity given by Fick's Law is then corrected to an exact value by iteratively solving (using Gauss-Seidel) the Stefan-Maxwell equations subject to the constraint equation. This approach gives an exact solution with much fewer mathematical operations than a direct solution would require.

Initial testing of the quasi-steady code with multicomponent diffusion coefficients has been conducted using a one-step overall chemical reaction. As noted previously, the original code required a pre-exponential factor of three times that of Westbrook and Dryer [4] to match experimental data for the extinction of n-heptane droplets [5]. The new code, which uses a multicomponent diffusion formulation, uses the same kinetics (including the pre-exponential factor) as Westbrook and Dryer [4] to match the experimental data [5]. Additional testing of the new code is currently being conducted.

b). Numerical Model for Droplet Combustion in a Forced Convection Environment; Transient Effects (with Dr. Daniel N. Pope and graduate student Kun Lu) This part of our research has focused on the development of a numerical model to study the flame transition during fuel droplet combustion under forced convective environment. Based on our quasi-steady numerical model, which utilized staggered numerical grid and neglected heat transfer to droplet interior [1], a transient code has been developed to model droplet combustion in a forced convection, zero-gravity environment. A colocated numerical grid, one-step overall chemical

kinetics and a single diffusion coefficient to describe the mass diffusion were used in the transient model.

The transient code was used to investigate combustion of n-heptane droplets in air at atmospheric pressure. The investigation included two scenarios: suspended droplet combustion with blowing air (which is to simulate droplet combustion experiments) and moving droplet combustion (which is more close to the conditions in practical combustion systems). The initial droplet diameter (D_0 = 0.5 mm) and initial droplet temperature (T_0 = 297 K) were fixed, the ambient temperature (T_∞) and initial droplet velocity ($U_\infty(0)$) or "blowing" velocity (U_∞) were varied. Results have been obtained for suspended droplet combustion with initial Reynolds numbers of 10, 25, 50 and 100 at an ambient temperature of 1000 K. For moving droplet combustion, tests were conducted for Reynolds numbers of 10, 25, 50, 75, and 100 and ambient temperatures of T_∞ = 800 K, 1000 K, and 1200 K (Re = 10, 25 and 50).

Numerical results indicate that at the same ambient temperature, the Reynolds number determines the flame configuration that forms during droplet ignition for both suspended and moving droplets. In both cases, an envelope flame was formed during droplet ignition for a low initial Reynolds number (such as Re = 10), and a wake flame was observed at higher Reynolds numbers (such as Re = 50). In the suspended droplet combustion case, the wake flame configuration was observed throughout the droplet lifetime, while for the moving droplet case, as the initial wake flame gradually approached the droplet, an envelope flame might eventually be formed due to deceleration of the droplet. Reynolds number not only determines the flame configuration, but also affects the initial flame location (ignition location). The results for moving droplet combustion indicated that both initial Reynolds number and ambient temperature affect the ignition location. A high initial Reynolds number tended to make the droplet ignite further away from the droplet in the downstream direction. For higher ambient temperatures, the flame tended to initiate at locations closer to the droplet.

II. Evaporation of a Deformable Fuel Droplet under a Forced Convective Environment (with Dr. Hongtao Zhang and graduate student Yuan Shi). Over the past few years, an evaporation model of a moving spherical droplet has been developed for high pressure and high temperature environments [12, 13]. This model is only available at low Weber numbers ($We \leq 1$) due to the assumption that the fuel droplet is spherical. At intermediate Reynolds numbers the Weber number may be large enough to cause droplet deformation. A more complex evaporation model of a moving fuel droplet which includes droplet deformation is needed for the detailed understanding of the dynamics and evaporation process of moving fuel droplets under high pressure and high temperature environments. Our previous axisymmetric code (in spherical coordinates) is not convenient to handle droplet deformation. Over this past year we developed a new 2-D code in cylindrical coordinates to be able to handle droplet deformation.

A non-orthogonal, algebraically generated grid system was chosen. This choice was motivated by computational economy because it simplified the task of repeated grid regeneration dictated by the constantly changing free surface shape. The non-orthogonal coordinates are defined with the η-coordinate direction following the radial lines and the ξ-coordinate direction following the 'tangential' lines. In the liquid phase, all lines radiated from a common origin at the midpoint of the original spherical droplet, and terminated at points distributed around the liquid/gas interface. In the gas phase the radial lines emerged from the same points that defined the termini of the liquid-grid radial lines at the liquid/gas interface, and extended to predetermined points along a fixed outer boundary. The first section adjacent to the liquid/gas interface was made at Δ_1=0.01, and other each subsequent sections were increased by a fixed

flare rate k ($\Delta_{j+1} = k\,\Delta_j$) to yield the appropriate total radial line length so that it terminated at the desired far field boundary.

The gas and liquid phase solutions are obtained by solving the axisymmetric unsteady equations of mass, species, momentum, and energy conservation in cylindrical coordinates, using a colocated grid. These equations are coupled via the conservation equations at the interface and are solved iteratively. Variable properties in the gas and liquid phase are calculated using appropriate high pressure correlations. The effect of gravity is neglected. The finite-volume [14] and SIMPLEC [15] methods are used to discretize the governing equations in the computational domain. Real gas effects are modeled using the Peng-Robinson equation of state with the appropriate binary interaction coefficient and transport and thermodynamic properties as recommended by Reid et al. [16].

At this point, the new code predicts results in agreement with experimental data (and with our previous code) when we "turn off" droplet deformation (low Weber numbers). Further debugging is needed to be able to handle droplet deformation which becomes important at higher Weber numbers.

References

1. D. N. Pope, *Numerical Simulation of Convective Fuel Droplet Vaporization and Combustion in a Low Pressure Zero-Gravity Environment*, Ph.D. Dissertation, University of Nebraska-Lincoln, Lincoln, Nebraska, 2001.
2. S. V. Patankar, *Numerical Heat Transfer and Fluid Flow*, Hemisphere Publishing Corp., New York, 1980.
3. J. P. Van Doormaal and G. D. Raithby, *Numerical Heat Transfer*, 7:147 (1984).
4. C. K. Westbrook and F. L. Dryer, *Comb. Sci. and Tech.*, 27:31 (1981).
5. S. Okajima and S. Kumagai, *Proc. Combust. Inst.*, 19:1021 (1982).
6. S. H. Chung and C. K. Law, *Comb. Flame*, 52:59 (1983).
7. R. B. Bird, W. E. Stewart and E. N. Lightfoot, *Transport Phenomena*, John Wiley and Sons, Inc., 1960.
8. F. A. Williams, *Combustion Theory*, 2nd ed., The Benjamin/Cummings Publishing Company, Inc., 1985.
9. T. P. Coffee and J. M. Heimerl, *Comb. Flame*, 43:273 (1981).
10. J. D. Ramshaw, *J. Non-Equilib. Thermodyn.*, 15:295 (1990).
11. E. S. Oran and J. P. Boris, *Prog. Energy Comb. Sci.*, 7:1 (1981).
12. H. Zhang, Evaporation of a Spherical Moving Fuel Droplet over a Wide Range of Ambient Pressure within a Nitrogen Environment, Ph.D. Dissertation, University of Nebraska-Lincoln, Nebraska, 2000.
13. H. Zhang, and G. Gogos, Droplet Evaporation within a Zero Gravity High Pressure and High Temperature Convective environment, *Proc. of International Conference on Power Engineering*, Vol. 2, pp. 1613-1620, October 8-12, 2001, Xi'an, China.
14. S. V. Patankar, *Numerical Heat Transfer and Fluid Flow*, Hemisphere Publishing Corporation, New York, 1980.
15. J. P. Van Doormaal, and G. D. Raithby, *Numerical Heat Transfer* 7:147 (1984).
16. R. C. Reid, J. M. Prausnitz, and B. E. Poling, *The Properties of Gases and Liquids (4th ed)*, McGraw-Hill, Inc., New York, 1987.

SOOT MORPHOLOGY IN UNSTEADY COUNTERFLOW DIFFUSION FLAMES

Grant/Contract Number DAAD19-00-1-0429

Principle Investigator: William L. Roberts

North Carolina State University
Box 7910, Dept of Mechanical Engineering
Raleigh, NC 27695-7910

SUMMARY/OVERVIEW:

Particulate matter emission from Diesel engines can be considerable due to the predominance of the diffusion controlled combustion phase. These soot particles have a much stronger thermal signature compared to gas phase products and the temporal behavior of this signature is a function of the morphology of the soot. It is, therefore, important to understand, and eventually control, not only the soot volume fraction of the particulate matter but also its morphology. The goal of this research project is to measure the morphology of soot formed in unsteady diffusion flames non-intrusively to gain understanding of the processes dictating its formation and morphology.

TECHNICAL DISCUSSION

Thermophoretic sampling has been used to examine the morphology of soot in laminar co-flow ethylene-air diffusion flames [1-4]. This intrusive technique may not be suitable to unsteady or turbulent flames and the ability to measure the morphology of soot non-intrusively is highly desirable. Most non-intrusive techniques rely on laser scattering and extinction measurements, LII, or a combination of both. LII has been shown to be successful at spatially and temporally resolved soot volume fraction measurements, but is very limited in its ability to resolve morphology. Measurements of scattering and extinction in diffusion flames in a variety of combustion systems can be found in [5-8].

Even though a primary soot spherule is on the order of 30-50 nm in diameter, well within the Rayleigh regime, the scattering intensity from soot is observed to be highly dependant on the scattering angle, making simple Rayleigh theory unusable. The agglomerated particle may be two orders of magnitude larger in size (in at least one dimension), and thus fitting within the Mie regime. SEM/TEM images of the soot agglomerates show them to have a fractal like structure. Rayleigh-Debye-Gans / polydisperse fractal aggregate (RDG/PFA) theory has been shown to accurately predict the angular dependence on the laser scattering. This technique has been used to successfully measure morphology in simple laminar and turbulent axisymmetric diffusion flames by Koylu [8].

However, in spite of the considerable amount of research that has been done, there is a limited amount of soot morphology data in diffusion flames generated using this technique available in the literature. The data that does exist is primarily at 45~75% of the flame height in axisymmetric flames. At this flame location, good agreement has been shown with this technique and intrusive sampling and subsequent SEM/TEM imaging. To determine all six morphological parameters, a large number of scattering measurements at different angles (~>10) must be taken. The interpretation of the data is not straightforward; the data reduction process involves several assumptions that strongly influence the results, especially in regions where soot concentration is low.

Although many-angle scattering is a more precise and comprehensive approach, it is difficult to apply to transient or turbulent flames. If the fractal nature of the soot and the distribution of spherules per agglomerate is assumed to be known, the number of measurements can be reduced to three; an extinction measurement and scattering measurements at two different angles. The most restrictive assumption is that the fractal dimension, D_f, is constant. This approximate approach has achieved some success, as presented by Koylu [9] and De Luliis [10]. The data presented is very limited, however. One of the goals of this research is to determine the range of applicability of this approximate approach.

One of the primary objectives of this research is to measure soot morphology in an unsteady counterflow diffusion flame burner as a function of initial strain rate and imposed oscillation frequency and amplitude. LII measurements in this flame have shown very large fluctuations in the soot volume fraction throughout the oscillation for some operating conditions, and relative insensitivity at other operating conditions. The unsteady CFDF is described in detail in DeCroix and Roberts [11], along with soot volume fraction results obtained via LII at various initial strain rates and imposed oscillations for propane-air flames.

The typical experimental apparatus required for soot morphology measurements at a point is relatively simple: an argon ion laser is focused to a point inside the flame; extinction measurements are made using a photodiode and scattering measured with a PMT. The scattering/extinction system is calibrated using Rayleigh scattering from nitrogen. Figure 1 shows the measured soot volume fraction and calculated fractal dimension as a function of height using this RDG/PFA technique in an ethylene air co-flow flame. This data is taken along the centerline of the flames. As seen in this figure, the soot volume fraction is reasonably large from about 45% to 75% of the flame height. This is the region of the flame where the majority of experimental data is available in the literature. Although there is considerable disagreement on the exact value of the fractal dimension, the range of D_f for soot generated in these laminar diffusion flames is 1.6 to about 1.8 in the region of maximum soot volume fraction. As seen in this figure, the measured D_f agrees with these accepted values only over a narrow range. The reason the measurement fails is most likely due to a combination of factors, including very limited agglomeration of spherules low in the flame, and large measurement error due to the low soot volume fraction.

It is important to understand where in the flame the fractal dimension is known and constant because one of the assumptions in reducing the many-angle requirement to a two-angle approach is knowledge of this parameter. In the laminar co-flow flame, the region of applicability is relatively easy to define, but in the counterflow geometry and turbulent flames in general, this will not be as straightforward. In the unsteady counterflow flame, it may be especially problematic. Current work is aimed at understanding the applicability of the two-

angle soot morphology approach to flame geometries other than the co-flow flame, and within the co-flow flame at other flame locations.

To extend the RDG/PFA method from a point measurement to a planar measurement, and thus making it more applicable to transient and turbulent flames, a number of changes to the optical set up are required. To generate sufficient scattering intensity in a plan, the argon ion laser is replaced with a Nd:YAG, and the PMT is replaced with a pair of ICCD cameras, and the photo diode is replaced with a video camera; the optical layout is shown in Fig. 2. To avoid laser induced incandescence, the Nd:YAG is run in long pulse mode, with a pulse length of approximately 400 μs. The absence of incandescence interference has been verified experimentally. Algorithms to analyze the scattering images and interpret soot morphology are currently being developed.

References:

1. R.A. Dobbins and C. M. Megaridis, "Morphology of Flame Generated Soot as Determined by Thermophoretic Sampling," Langmuir 3, 254-259 (1987)
2. C. M. Megaridis and R.A. Dobbins, "Soot Aerosol Dynamics in a Laminar Ethylene Diffusion Flame," Proc. of Comb. Instit. Vol. 22 1988, pp.353-362.
3. C. M. Megaridis and R.A. Dobbins, "Comparison of Soot Growth and Oxidation in Smoking and Non-Smoking Ethylene Diffusion Flames," Combust. Sci. Tech., 66, 11-116 (1989)
4. C. M. Megaridis and R.A. Dobbins, "Morphology Description of Flame-Generated Materials," Combust. Sci. Tech., 71, 95-109 (1990)
5. R. Puri, T.F. Richardson, R. J. Santoro, and R. A. Dobbins, "Aerosol Dynamic Processes Of Soot Aggregates In A Laminar Ethane Diffusion Flame," Combust. Flame 92, 320-333 (1993).
6. R. J. Santoro, Semerjian, H.G., and Dobbins, R.A., "Soot Particle Measurements in Diffusion Flames," Combust. Flame 51:203-218 (1983).
7. C. R. Shaddix and K. Smyth, "Quantitative Measurements of Enhanced Soot Production in a Flickering Methane/Air Diffusion Flame," Combust. Flame 99:723-732 (1994).
8. U. O. Koylu, "Quantitative Analysis of In Situ Optical Diagnostics for Inferring Particle/Aggregate Parameters in Flames: Implications for Soot Surface Growth and Total Emissivity," Combust. Flame 109:488-500 (1996).
9. U. O. Koylu, "A Simple Two-Angle Laser-Scattering Technique For Characterization of Soot in Flames," Chem. Phy. Proc. Comb. 1999, pp.324-327.
10. S. De Luliis, F. Cigoli, S. Benecchi, and G. Zizak, "Determination of Soot Parameters by a Two-Angle Scattering-Extinction Technique in an Ethylene Diffusion Flame," Applied Optics 37, pp.7865-7874 (1998)
11. M. E. DeCroix and W. L. Roberts, "Transient Flow Field Effects on Soot Volume Fraction in Diffusion Flame," Combust. Sci. & Tech., Vol. 160, pp. 165-190 (2000)

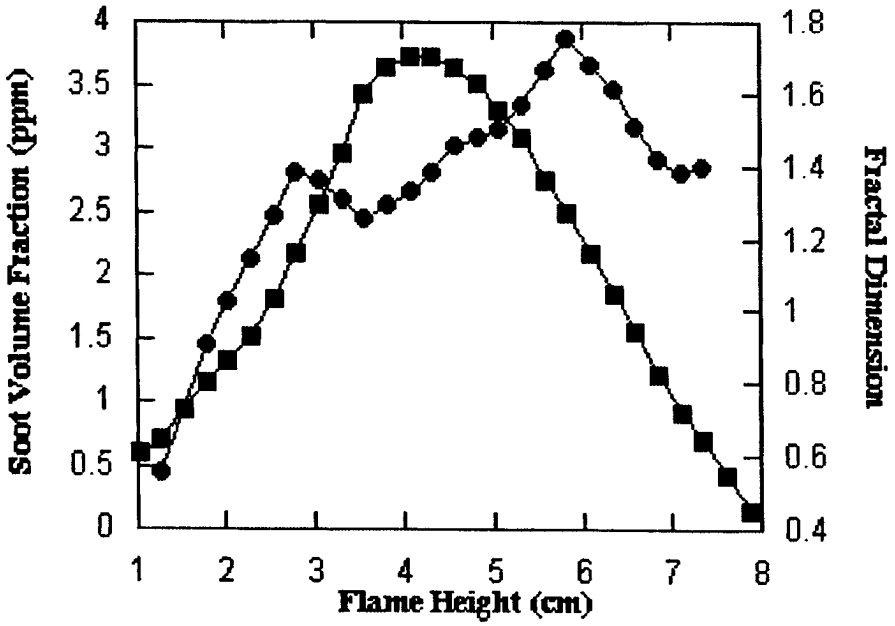

Figure 1. Soot volume fraction (from extinction measurements) and fractal dimension, D_f, (from multi-angle scattering and RDG/PFA analysis) as a function of flame height in an ethylene-air laminar co-flow diffusion flame as derived.

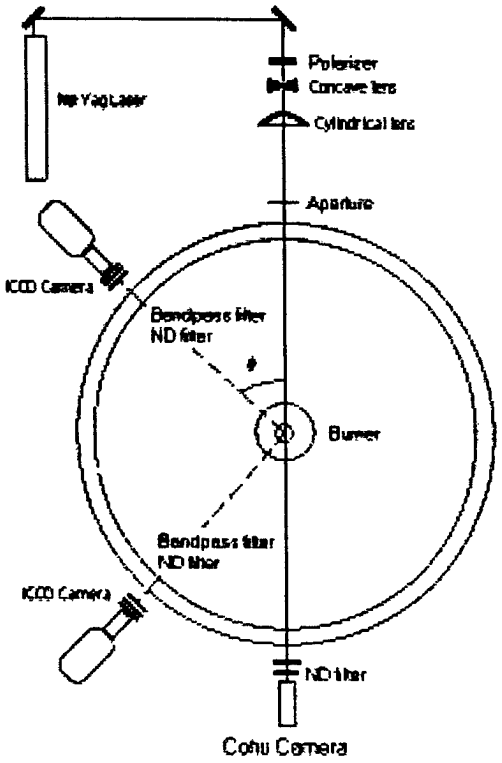

Figure 2. Optical layout for 2-D RDG/PFA soot morphology measurements. Nd:YAG is run in long pulse mode to avoid laser induced incandescence.

CENTER OF EXCELLENCE FOR PROPULSION SYSTEMS AT THE ENGINE RESEARCH CENTER

(DAAD19-00-1-0487)

Principal Investigator(s): P. V. Farrell, D. Foster, J. Ghandhi, J. Moskwa, R. Reitz, C. Rutland

Engine Research Center
Department of Mechanical Engineering
University of Wisconsin-Madison
1500 Engineering Drive
Madison, WI 53706

SUMMARY/OVERVIEW:

This program is intended to address current and future powertrain issues of interest to the Army and its suppliers. The focus of the program is on diesel engine powertrain power density, performance, fuel economy, and related emissions and control issues. A goal of the work is to provide fundamental research results that will allow future Army vehicles to have a smaller size powertrain with increased power, reduced fuel consumption, minimal emission signature, and increased reliability and durability.

TECHNICAL DISCUSSION

The specific goals of this program are to: develop and apply the means to measure transient engine characteristics with an emphasis on high power density engine configurations; develop research-based modeling of combustion process and overall powertrain system behavior so these models can be applied to future engine design and operation; and explore the fundamental relationships among engine performance (power, bsfc), emission quantity (g/kw-hr), and detailed emission characteristics (e.g. particulate size distribution).

This program is a joint effort among the UW-Madison Engine Research Center, the UW-Madison Powertrain Control Research Lab (PCRL), UW-Madison Civil Engineering and the State of Wisconsin Hygiene Laboratory, Michigan Technological University (MTU), and the University of Minnesota (UMinn).

Due to the limited space in this abstract, outlines of some of the projects in this program will be given.

Transient Spray Measurements

This project is aimed at developing and applying a method for making transient measurements of engine performance, primarily for smaller displacement high-speed diesel engines. Future Army powertrains may employ smaller displacement, higher speed engines which can provide higher power density output for smaller and lighter future vehicles, with a potential for improved fuel economy as well.

Under development at the University of Wisconsin are a high bandwidth hydrostatic engine dynamometer, high data rate diagnostics, and a format for evaluating engine control

inputs in light of real-time engine data. At MTU, the focus is on developing piston measurement systems that can accurately describe the state of the piton, which is often a limit in pushing towards higher power density.

In preparation for transient engine experiments, a series of experiments were performed in spray chamber tests of fuel sprays using PIV looking at entrained gas velocities [1] (see fig. 1) and Exciplex fluorescence [2] to measure vapor phase equivalence ratio and temperatures as seen in fig. 2. In-cylinder measurements will use somewhat simpler optical techniques, including visible light photography and infra-red imaging. The results shown in figs. 1 and 2 and the publications that describe them provide some evidence of the extent of the liquid and vapor phases of a high-pressure fuel spray in a high temperature environment.

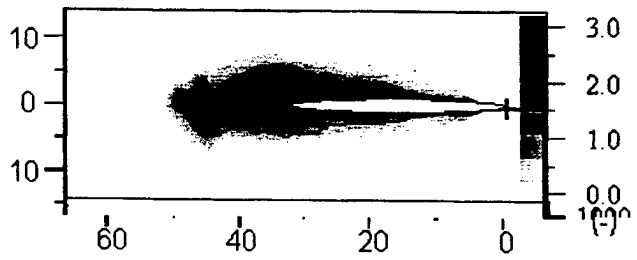

Figure 1. PIV measurements of air entrainment

Figure 2. Equivalence and temperature measurements, 1300 μs ASOI, 1000K

Engine Simulation and Powertrain Modeling and Emissions Predictions:

The goals of this part of the program include development of new models for better prediction of engine behavior, improving the speed and usability of the current KIVA code, investigating optimization strategies, and developing ways to evaluate the robustness of simulation codes. To illustrate some of the progress in these areas, two projects are briefly described below.

"Chamber Geometry Parameterization and Automated KIVA Grid Generation for Optimization" by David Wickman and Rolf Reitz

A flexible 6-parameter combustion chamber geometry parameterization and automated KIVA grid generation technique has been developed. The goal of this grid generation technique is to have the flexibility to create a very large range of bowl shapes and sizes, using a minimum number of parameters, while retaining very similar grid resolution and structure. The grid quality and resolution are preserved by using a novel blocking structure in the bowl region, where each vertical column of cells is a block. An initial optimization has been started using the KIVA-GA code. The measure of design fitness was based on NOx, particulate matter, CO, and unburned HC emissions, and BSFC. Results of the optimization are shown in fig. 3, which presents the maximum merit function curve.

Figure 3 and 4 present soot vs. NOx+HC and BSFC vs. NOx+HC, respectively, for many of the simulation cases performed in the optimization. Also shown in the figures are target value boxes representing the mandated emissions and target fuel consumption levels for this class of engines.

"Large Eddy Simulation for Diesel Engine Simulations" by Sergei Chumakov and Christopher Rutland

A new class of LES subgrid models based on the Dynamic Structure (DS) approach are being developed for use in diesel engine CFD simulations. The DS approach was developed at the ERC (Pomraning and Rutland, 2002) and shows excellent potential for LES simulations in complex flows. Current efforts are focused on scalar modeling. In this context, the DS approach uses a vector model coefficient and a scaling term based on a sub-grid mixing term. The vector coefficient is obtained from the dynamic approach. The sub-grid mixing term is based on the sub-grid scalar variance and is obtained from a transport equation.

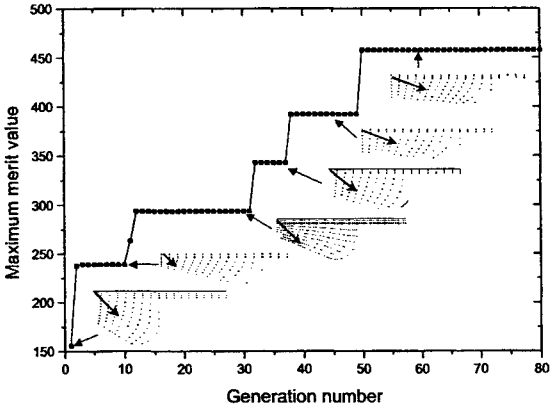

Figure 3: Maximum merit function curve for the small-bore engine optimization study. Also shown are the chamber geometries and spray angle corresponding to the major merit value changes.

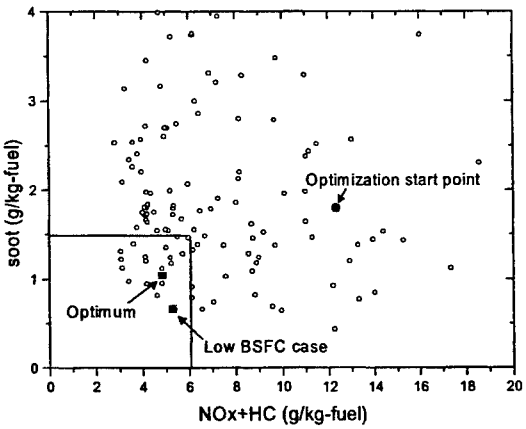

Figure 4: Soot vs. NOx+HC .

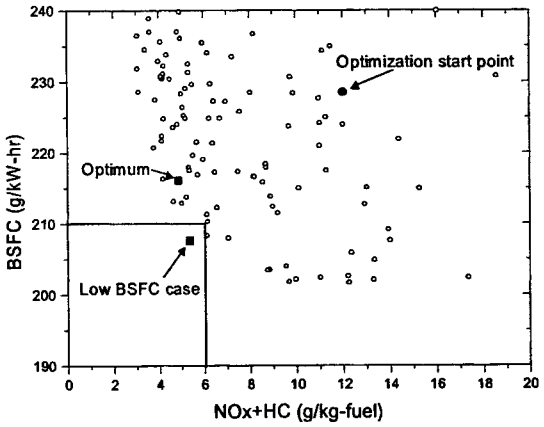

Figure 5: BSFC vs. NOx+HC .

Within the DS approach, the primary modeling closures required for scalars are the scalar flux in the mean equation and the scalar dissipation. in the sub-grid transport equation. Figure 6 shows the overall scalar field in both a DNS and the corresponding LES simulation. The excellent agreement extends to growth rates of the scalar field, profiles of the mean scalar, and downstream self-similarity of the mean scalar profile.

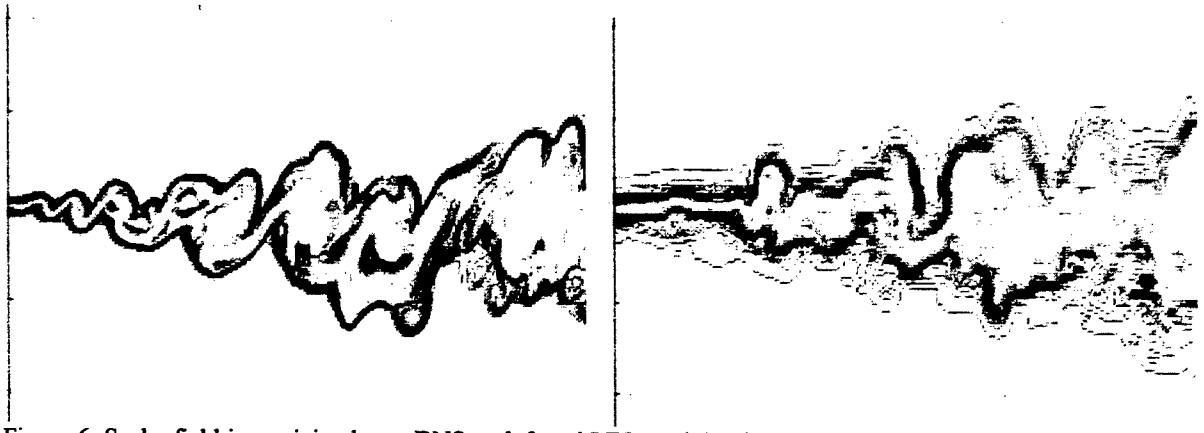

Figure 6: Scalar field in a mixing layer. DNS on left and LES on right. Growth rates and mean profiles of the scalar field show excellent agreement (inlet Re = 200 based on vorticity thickness).

Detailed Chemical Characterization of Diesel Engine Exhaust:

This task has three objectives: development of methods that integrate advanced air pollution sampling and analysis techniques with state of the art engine research facilities; investigate the effects of changes in engine design and operating conditions, lubricants and fuels on the physical and chemical properties of emissions; use these data to gain an enhanced understanding of the phenomena that limit engine performance through constraints on operating in order to meet emission regulations.

Samples of results to date are shown in figs. 7 and 8. Figure 7 shows emission results for each of 8 speed/load operating modes for a single-cylinder version of a Cummins N14 DI diesel engine operating on standard (350 ppm sulfur) fuel. Figure 8 shows particulate size distributions for each of the 8 mode from a scanning particle mobility analyzer.

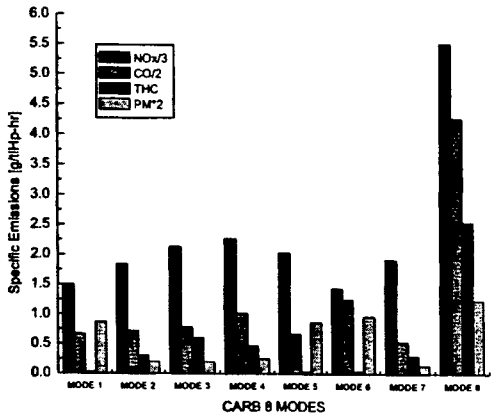

Figure 7: Emissions results for 8 mode tests on Cummins N14 engine.

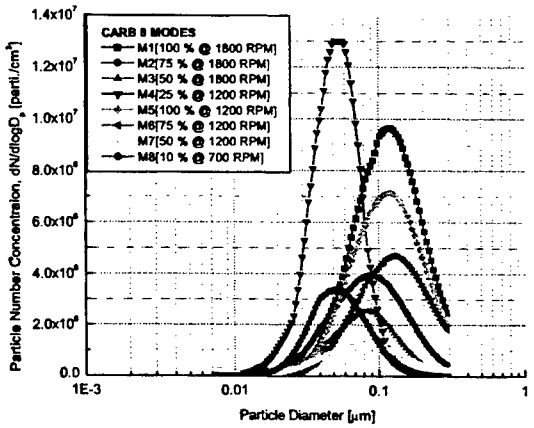

Figure 8: Particulate size for 8 mode tests on Cummins N14 engine

REFERENCES:

1. D. Rhim and P. V. Farrell " " SAE Paper 2001-000000 (2001).

2. T. Kim, " Quantitative 2-D Fuel Vapor Concentration Measurements in an Evaporating Diesel Spray Using the Exciplex Fluorescence Method", Ph. D. Thesis, UW-Madison, 2001.

3. E.Pomraning, C.J.Rutland, "Dynamic One-Equation Nonviscosity Large-Eddy Simulation Model," AIAA Journal, 40 (4), pg. 689-701 (2002).

TITLE: AERATED-LIQUID INJECTION – INTERNAL FLOWS AND FAR-FIELD CHARACTERISTICS

AFOSR TASK 2308BW

Principal Investigators: Thomas A. Jackson
Mark R. Gruber

Aerospace Propulsion Office
Propulsion Directorate
Air Force Research Laboratory
Wright-Patterson AFB OH 45433

SUMMARY/OVERVIEW

Our investigation of an aerated liquid injected into a high-speed cross-flow continues. In the context of a hydrocarbon fuelled scramjet the fuel is used to keep the propulsion system in thermal equilibrium. Over the Mach 4 to 8 speed range the fuel changes phase and composition, prior to injection into the combustor. During engine start the fuel will be a liquid and the internal airflow will be at Mach 2. Rapid distribution of the fuel within the high-speed engine airflow, and rapid atomization of the liquid are critical for successful ignition. Aerating the liquid has been useful in increasing liquid momentum flux, resulting in greater penetration of the high-speed core flow from a flush-wall injector. As expected the aeration also accelerates the atomization of the liquid. Our understanding of the relevant break-up processes and the near field characteristics of the spray plume remain qualitative. Recent studies have focused on the flows within the injector, as the two-phase injectant is established, on the penetration of the aerated liquid into the cross-flow, and on the far field characteristics of the resulting fuel plume. These aspects are the focus of this discussion.

TECHNICAL DISCUSSION

We postulated that under certain conditions the mixed flow through a fuel injector is characterized by a central flow of gas surrounded by a co-flowing liquid sheath. As the gas-liquid ratio is increased the liquid sheath thins and accelerates at constant liquid flow. The resultant hollow, liquid tube has a correspondingly higher momentum and penetrates further into the high-speed cross-flow. This heuristic model of the injection process has been confirmed by images extracted from a transparent injector[1], designed to evaluate the critical features of the aerated liquid injector. Figure 1(a) depicts the process; Figure 1(b) is a schematic of the transparent injector used to study the internal flow. The injector is modular, permitting changes in the method by which air is added to the liquid, the stand-off distance between aerating tube and the nozzle contraction, the injector length to "diameter", and the contraction angle. The nozzle cross-section at the exit plane is square, sized to approximate an axi-symmetric injector. This constraint forces the gas-liquid mixing section and transition contraction to be rectangular in cross-section. This compromise in geometry has not posed a problem.

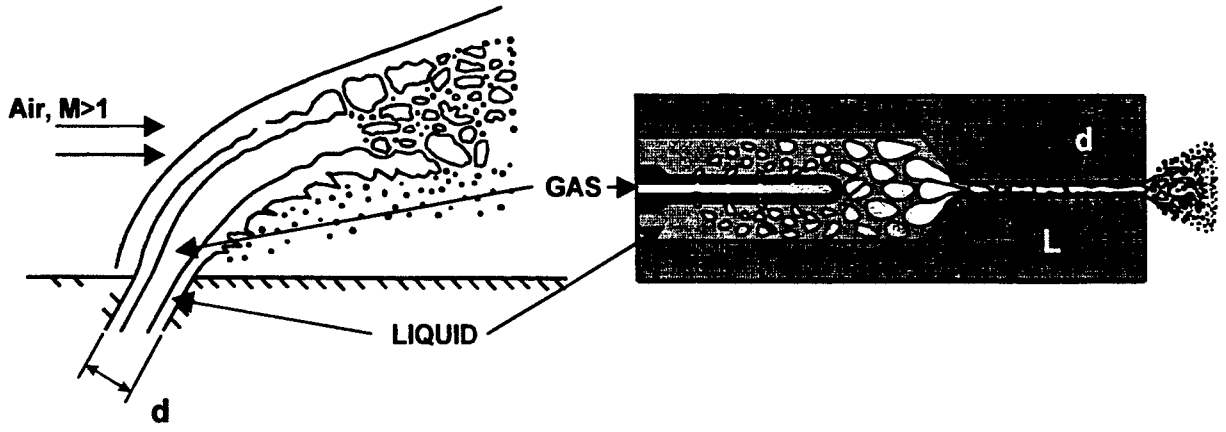

Figure 1 Aerated liquid injection (a) Concept; (b) Transparent Injector

In work reported two years ago in this forum we observed that at low gas loadings the two-phase flow was unsteady, oscillating between pure liquid injection and full, aerated injection. Above some critical value of gas loading the injector steadied into the full, aerated liquid mode. The injector nozzle had a length to discharge diameter of 2.4. The split image in Figure 2 illustrates this situation. Each image pair is of the same event. With the high magnification two separate images are required to capture the mixing chamber, the full injector length of 20 L/d, and the exit plane. The image pairs are of identical geometries and liquid flow rates, differing only in the gas-liquid ratio. The upper images capture approximately the first 2.5 L/d's of the nozzle. At lower gas-liquid loading the gas bubbles begin to coalesce, but large volumes of gas remain separated in the nozzle passage. If the discharge plane is located at this short L/d, the resulting spray is unsteady, alternating between pure liquid and aerated. As the gas loading is increased the gas bubbles completely coalesce within a short distance. The two-phase mixture begins to look like a continuous gaseous core surrounded by a thinning liquid sheath. Given additional length between the mixing chamber and discharge plane, even a mixture with low gas-liquid loading will transition to a co-annular flow. The full length of the nozzle in these images is 20 nozzle diameters. Our axi-symmetric nozzles with L/d of 20 exhibit only mono-modal behavior at all gas-liquid loadings.

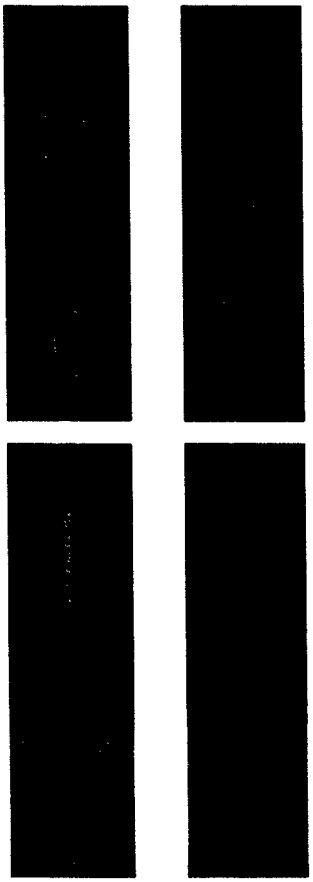

Figure 2 Photographs of the internal structures of aerated-liquid jets. Discharge: 2x2 mm; nozzle length: 40 mm; liquid flow rate: 0.38 l/min; GLR = 0.32% (left) and 1.24% (right).

While enhanced atomization is a prime motivator for this effort, the distribution of liquid into the high-speed cross-flow is of equal importance. To date quantitation of the spray has been limited to the post-secondary break-up regime. Single component, phase Doppler particle analyzer measurements are taken typically 100 injector diameters downstream[2,3]. We have also used this technique to revisit the penetration height of an aerated spray in cross-flows. Consistent with many past studies on pure liquid injectors we have measured spray height through shadow photography, using light transmittance through the spray as a discriminator of the spray boundary. We've also measured penetration height with the phase Doppler instrument, defining

the boundary when the measured liquid volume flux falls below 0.01 cc/s/cm2. Correlations for penetration height for the two measurement approaches are[4]

From shadowgraph images,

$$(h - h_0)/d_0 = 0.59\, q_0^{0.33}\, (x/d_0)^{0.45}\, (GLR)^{0.49}\, M^{-0.56} \qquad (1)$$

And, from phase Doppler measurements,

$$(h - h_0)/d_0 = 0.9\, q_0^{0.34}\, (x/d_0)^{0.39}\, (GLR)^{0.46}\, M^{-0.64} \qquad (2)$$

Where h is the height from the injection plane; d is the injector orifice diameter; q is the jet-to-free stream momentum flux ratio; x is the axial distance downstream of the injector; GLR is the gas-liquid mass ratio; and, M is the free stream Mach number. The subscript "0" refers to the non-aerated case.

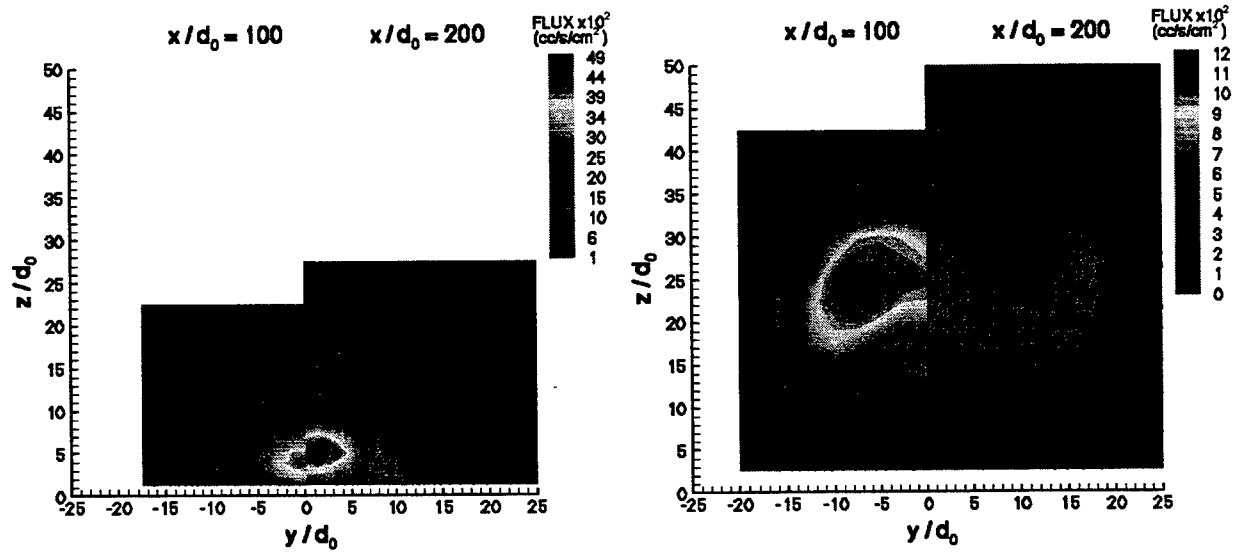

(a) GLR = 0%

(b) GLR = 4%

Figure 3 Liquid volume flux. Injectant: water, d_0 = 1.0 mm, L/d_0 = 20, M = 0.3, q_0 = 0.3

At positions x/d_0 = 100 and 200, Figure 3 depicts the measured volume flow of liquid spray plumes from an injector with no aeration and 4% aerating gas. The cross-flow is at M = 0.3. It is apparent that aeration dramatically improves penetration of the spray and transverse spreading of the plume. This is consistent with the lower mean droplet size of the aerated plume relative to that of the pure liquid, with smaller droplets more quickly accelerating to the surrounding gas velocity. Perhaps a more interesting feature is the comparison of spray penetration heights for an aerated spray at nearly the same flow conditions as those of Figure 3. In Figure 4 the penetration into the Mach 0.3 flow is assessed by shadow photography and by the phase Doppler techniques. The imaging approach is more sensitive to number density than to droplet size, missing larger droplets in the spray perimeter. The difference in the two techniques is 20% of the spray volume, with a measured height difference of over 40%.

Preliminary conclusions of the recent work on aerated injection in high-speed cross-flows are:

(1) Behavior of the aerated liquid is a strong function of the structure of the two-phase flow within the discharge passage.
(2) Steady, aerated behavior can be obtained with sufficient nozzle L/d or with high gas-liquid ratio
(3) Aerating the liquid increases spray penetration, the rate of atomization, and the transverse dispersion of the liquid.
(4) Image-based measurements under-predict the spray penetration

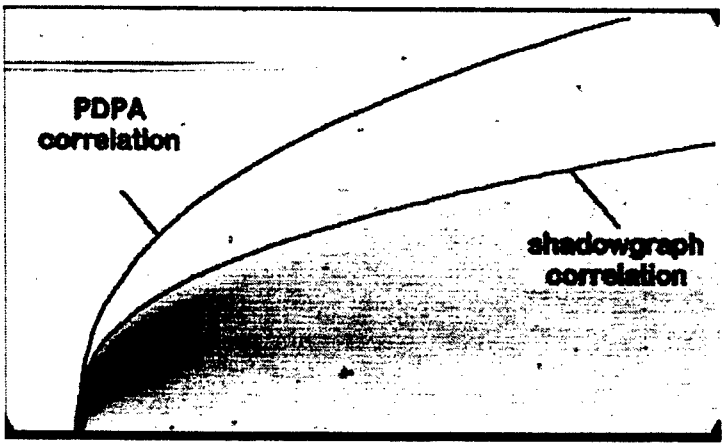

Figure 4 Spray penetration height correlations using shadow graphs and phase Doppler measurements. Injectant: water, d_0 = 1.0 mm, q_0 = 5, GLR = 4%, M = 0.3

tend to

Quantitation of the near-spray region continues with a focus on both holographic imaging and simulation.

References:

1. Lin, K.-C., Kennedy, P.J., and Jackson, T.A., "Structures of internal flow and the corresponding spray for aerated-liquid injectors," AIAA Paper 2001-3569, July 2001
2. Lin, K.-C., Kennedy, P.J., and Jackson, T.A., "Spray structures of aerated-liquid jets in subsonic crossflows," AIAA 2001-0330, January 2001
3. Lin, K.-C., Kennedy, P.J., and Jackson T.A., "Structures of aerated-liquid jets in high-speed crossflows," AIAA 2002-3178, to be presented June 2002
4. Lin, K.-C., Kennedy, P.J., and Jackson, T.A., "Penetration heights of liquid jets in high-speed crossflows," AIAA 2002-0873, January 2002.

LARGE EDDY SIMULATIONS OF SUPERCRITICAL MULTICOMPONENT MIXING LAYERS

(Contract Number: AFOSR-ISSA-00-0012)
(ARO Proposal Number 41116-EG)
Principal Investigator: Dr. Josette Bellan

Jet Propulsion Laboratory
California Institute of Technology
4800 Oak Grove Drive
MS 125-109
Pasadena, Ca 91109-8099

SUMMARY/OVERVIEW:

The objective of this study is the fundamental understanding of fuel disintegration and mixing in a supercritical environment (relative to the fuel) in order to determine parameter regimes advantageous to mixing. The approach is based on developing a model of a supercritical, turbulent jet mixing with surrounding fluid. The method is one that combines the modeling of supercritical fluids with a systematic development based on the Large Eddy Simulation (LES) approach. This systematic development includes a consistent protocol based upon Direct Numerical Simulations (DNS) for developing a Subgrid Scale Model (SGS) appropriate to supercritical fluids, rather than choosing in an ad hoc manner an existing SGS model developed under assumptions inconsistent with supercritical fluid behavior. This SGS model will be used in the LES of a supercritical turbulent jet.

TECHNICAL DISCUSSION

During the current year our activities focused on several aspects of supercritical mixing layers for the purpose of understanding the physics as a precursor to further Subgrid Scale modeling.

(i) A linear inviscid stability analysis for real gas was conducted with the goal of finding other forcing wavelengths that perhaps promote quicker transition, therefore minimizing computational costs. The results of the stability analysis and the ensuing simulations were documented in Okong'o and Bellan, 2001. Two-dimensional (2D) stability results showed that the unstable growth rates for the compressible flow are smaller at all wavenumbers than the equivalent growth rates found from an incompressible analysis; also, the most unstable wavelengths occurred at smaller wavenumbers with increasing density stratification. 2D mixing layer simulations showed that at the same initial mean flow conditions the solution is virtually independent of the excitation wavelength. This observation raised the alluring prospect of finding the shortest streamwise compressible unstable wavelength at which rollup and pairing could be obtained in three-dimensional (3D) simulations; for such a wavelength, the size of the domain could be reduced (since it is four times the perturbation wavelength) leading to a reduced number of grid points for the same resolution. However, in contrast with the 2D problem where for each wavelength there is a single eigenvalue (i.e. propagation speed), in 3D it was found that additional to the wavelength of the perturbation, the angle of the wave direction in the streamwise-spanwise plane must be specified as well. To minimize the wavelength of the

spanwise perturbation, it was shown that one must maximize the angle representing the direction of the perturbation. For the purpose of applications to 3D flow simulations, this implies that shorter wavelengths in the streamwise direction are counter balanced by the need to use a longer wavelength in the spanwise direction. Therefore, to avoid enlarging the spanwise domain size, the heuristic approach of using non-eigenfunction perturbations was adopted and simulations conducted for five shear layer were compared; for each of these simulations the streamwise domain size was four times the perturbation wavelength and the calculation was initiated with four vortices leading after two pairings to an ultimate vortex. Among these five simulations, two layers (differing by the value of the initial Reynolds number) were excited with the incompressible most unstable wavelength. The third and fourth layers (differing by the value of the initial Reynolds number) were excited with the shortest compressible unstable wavelength from the 2D stability analysis and the same amplitudes as the first two layers. The fifth layer was excited with the shortest compressible unstable wavelength from the two-dimensional stability analysis and a larger amplitude of the 3D excitation. Examination of the momentum thickness, the product thickness, the positive spanwise vorticity, the enstrophy and the momentum-thickness-based Reynolds number, Re_m, showed that only three of these five layers achieved transition, and the expectation of reduced CPU time for the layer perturbed with the shortest compressible unstable wavelength did not materialize. Global evolution and contour plots showed that the inability of transition achievement by two of the layers perturbed with the shortest compressible unstable wavelength is due either to the inability of the formed small scales to produce substantial vorticity or to the early formation of small scales and vorticity production which destroy the coherence of the ultimate vortex preventing its growth and initiating its decay.

Transitional states obtained with different perturbation wavelengths had different global and detailed characteristics, and therefore such simulations were recommended for enlarging the database necessary to extract turbulence models utilizable in the mathematical description of turbulent spatial flows.

(ii) To determine the influence of the perturbation wavelength on the transitional state characteristics, comparisons of the HDGM regions composition was performed for two transitional states described in (i) above. The results were reported in Okong'o and Bellan, 2002a, 2002b. The mass fraction of the heavy species in the HDGM region seems independent on the perturbation wavelength indicating that this feature might persists for spatial mixing layers. Additionally, for all layers it was found that the assumed-PDF representation of supercritical turbulence by Gaussian or K-density functions is inappropriate. Moreover, to determine the influence of the identity binary species pair on the results, comparisons were also performed between this C_7H_{16}/N_2 system and results from similar simulations performed for the O_2/H_2 system. The conclusion is that the qualitative aspect of the results is maintained independent of the identity of the binary species system, but that the quantitative features (with the exception of the mass fraction composition of the HDGM regions) are subject to change. This finding is consistent with the dissipation being dominated by mass flux effects, which are species dependent.

(iii) Area production in supercritical turbulent fluids was investigated as related to fluid disintegration and the results will be documented in Okong'o and Bellan, 2002c. The interest was in examining production in a coordinate system attached to fronts moving with the relative velocity between the front and the flow. A database of turbulent transitional states obtained from Direct Numerical Simulation of supercritical mixing layers encompassing two binary-species systems, and two wavelength initial perturbations for each species system was interrogated. The results showed that while locally area may be created or destroyed, on average area is always created. Moreover, area creation is larger in the lighter fluid region (see Table 1 and Fig. 1); a smaller initial density stratification yields a larger area production (see Table 1 and Fig. 1); the

area creation is uncorrelated with the momentum thickness based Reynolds number at the transitional state (see Table 1 and Fig. 1); and smaller wavelength initial perturbations lead to enlarged area creation (see Table 1 and Fig. 1). This last observation represents an initial step towards the control of area production. The preponderant influence of the strain related term motivated the development of the conservation equation for the strain-rate/conserved-scalar-gradient tensorial product, and the examination of its budget. For all layers, strain and convection effects lead to production of area, whereas rotational and species mass flux effects destroy it; while viscous effects are negligible, pressure gradient effects can either produce or destroy area. Strong pressure-gradient-related RMS were found for the species-system that shows considerable departures from perfect gas and ideal mixture behavior, and were shown to be the manifestation of the strong pressure/density coupling through the equation of state. The findings regarding the manifestations of mixture non-ideality and pressure-to-density coupling in determining the area production highlight the importance of real gas thermodynamics in the modeling of supercritical turbulent reactive/non-reactive flows.

(iv) Turbulence aspects of two different binary-species systems were compared and documented in Bellan et al. 2002. The density gradient magnitude non-dimensionalized by the initial value based on conditions at the boundary between the two species revealed that regions of high density-gradient magnitude are stronger but narrower for C_7H_{16}/N_2 than for O_2/H_2 at transition. This was attributed to the reduced solubility and to the mixture non-ideality when compared to the O_2/H_2 system. Since a sharp density stratification is very effective at damping turbulent eddies, we have identified thermodynamic processes (i.e. solubility and mixture ideality) that affect turbulent development. Confirmation of the importance of thermodynamic processes in supercritical turbulence came from inspection of the irreversible entropy production (i.e. the dissipation) for the two binary species systems; we previously showed that the locations of maximum dissipation occur within the high density-gradient magnitude regions. The maximum dissipation level is larger for the O_2/H_2 layer consistent with the lower turbulence levels detected from the global analysis, this being attributed to the wider regions of high density-gradient magnitude. However, the largest dissipation is located for the O_2/H_2 layer within regions originating from the distortion of the original density stratification boundary, and for the C_7H_{16}/N_2 layer within regions created through mixing. This difference is traced to the larger solubility and the near mixture-ideality of the O_2/H_2 that creates relatively weak high density-gradient magnitude regions through mixing, and therefore these regions induce a relatively weak dissipation.

1. Okong'o, N. and Bellan, J., Direct Numerical Simulation of a transitional supercritical mixing layer: heptane and nitrogen, in press in the *Journal of Fluid Mechanics*, 2002a

2. Okong'o, N. and Bellan, J., Temporal linear stability analysis and numerical simulations of real gas two- and three-dimensional mixing layers, submitted for publication to *Physics of Fluids,* 2001

3. Okong'o, N. and Bellan, J., Characteristics of Supercritical Transitional Temporal Mixing Layers, Proceedings IUTAM Symposium on Turbulent Mixing and Combustion, Kingston, Canada, June 3-6 2001, Pollard and Candel (eds), Kluwer Academic Publ., Dortrecht, 2002b

4. Okong'o, N. and Bellan, J., Area production in supercritical, transitional mixing layers, to be submitted for publication, 2002c

5. Bellan, J., Okong'o, N. and Harstad, K., Aspects of supercritical turbulence: Direct Numerical Simulation of O2/H2 and C7H16/N2 temporal mixing layers, presented at the JANNAF Meeting, April 8-12, Destin, Florida, 2002

Case label	Heavier/Lighter Fluid	$\varsigma_1/N_{y,0}$	Amplitude F_{3D}	Specified Re_0	Resulting Re_m

HN500	C_7H_{16}/N_2	7.29	0.05	500	1250
HN800	C_7H_{16}/N_2	4.57	0.05	800	1256
OH550	O_2/H_2	10.35	0.025	550	1513
OH750	O_2/H_2	7.29	0.05	750	1507

Table 1. Initial conditions of the simulations and value of the momentum-thickness-based Reynolds number, Re_m, at transition. In all simulations $M_{c,0} = 0.4$, $\delta_{\omega,0} = 6.859 \times 10^{-3}$ m and $F_{2D} = 0.1$. For the C_7H_{16}/N_2 layers, $\rho_2/\rho_1 = 12.88$, $p_r = 2.22$ ($p_0 = 60$atm), $T_2 = 600$K, $T_1 = 1000$K and $((\rho_2 U_2)/(\rho_1 U_1)) = 5.277$; for the O_2/H_2 layers, $\rho_2/\rho_1 = 24.40$, $p_r = 2.01$ ($p_0 = 100$atm), $T_2 = 400$K, $T_1 = 600$K and $((\rho_2 U_2)/(\rho_1 U_1)) = 5.001$.

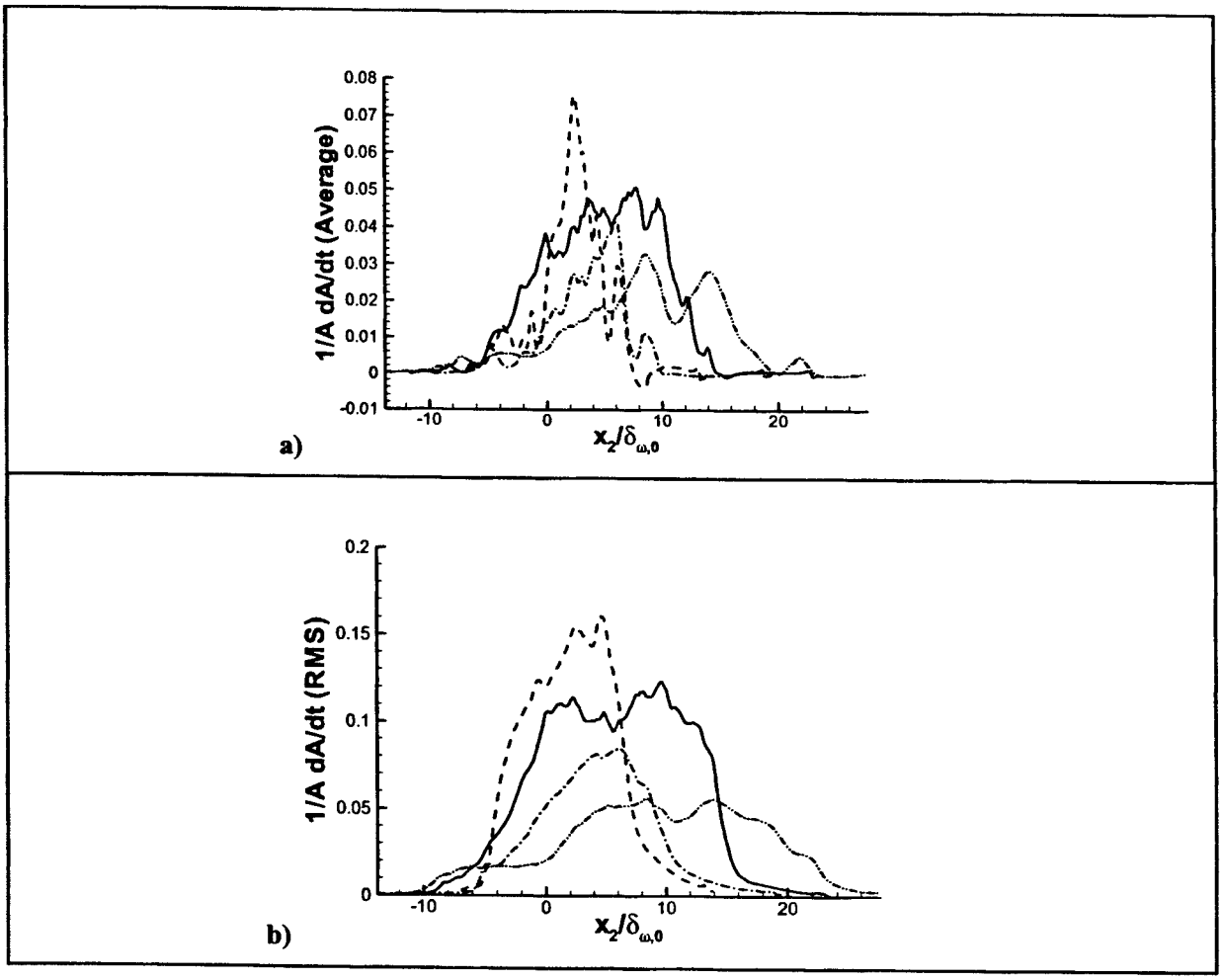

Figure 1. (1/A)(dA/dt) in a coordinate system attached to fronts moving with the relative velocity between the front and the flow; (a) average and (b) RMS, both calculated in (x_1,x_3) homogeneous planes for all layers listed in Table 1: HN500 (——), HN800 (– – –), OH750 (– τ – τ –), OH550 (– ττ – ττ –). x_1, x_2 and x_3 are the streamwise, cross-stream and spanwise coordinates.

NONLINEAR DISTORTION AND DISINTEGRATION OF CONICAL LIQUID SHEETS AT HIGH PRESSURE

ARO Grant/Contract No. DAAD19-99-1-0204

PRINCIPAL INVESTIGATOR:

W.A. Sirignano

Department of Mechanical and Aerospace Engineering
University of California
Irvine, CA 92697

SUMMARY/OVERVIEW:

Previous studies of planar liquid sheets have been extended to the analysis of liquid films discharging from a two-dimensional twin-fluid atomizer. Sinuous (anti-symmetric) and dilational (symmetric) film distortion have been analyzed and evaluated. Furthermore, an analysis of the dynamic stretching of a two-dimensional liquid film has been conducted in order to better understand the process of film rupture due to the effects of inertia, surface tension, viscosity and long range intermolecular forces. Finally, a linear analysis of three-dimensionally distorting swirling annular liquid films has been performed in order to provide guidance for the studies of nonlinearly distorting swirling annular and conical sheets with three-dimensional disturbances. Comparison between linear and nonlinear results for the annular case quantifies the influence of nonlinear effects on film distortion and film breakup.

AUTHORS W.A. Sirignano C. Mehring

TECHNICAL DISCUSSION

Planar Liquid Film Discharging From Twin-Fluid Atomizer

A thin liquid film is injected from a two-dimensional slit-nozzle located in the symmetry plane of a two-dimensional twin-fluid atomizer. See Fig.1. The liquid film is impacted on both sides by gas-jets discharging from two inlet ports angled with respect to the film discharge plane at an angle α. Both liquid film and gas streams are injected into a two-dimensional channel. For the analysis, the coordinate system is fixed to the nozzle exit with the $y-$axis located within the film discharge plane and the $x-$axis coinciding with the symmetry plane of the atomizer. For the spatially developing semi-infinite liquid film, capillary waves generated by the impacting gas jet do not reach the outflow boundary of the computational domain during the computation.

The specification of liquid-phase boundary conditions at the nozzle exit follows previous work by the authors [1]. Gas-phase velocity components normal to solid-walls have been set to zero; Parallel outflow conditions have been specified within the gas-phase. Gas-jet injection at the two gas-jet inlet ports has been specified, in general, according to $u_{g;1,2}(t) = \sum_{n=0}^{\infty} u_{g;0} \sin^2 [\pi(\frac{t}{T_p} - (2n + n_{\theta;1,2}))]$ for $(2n + n_{\theta;1,2}) < \frac{t}{T_p} < (2n + 1 + n_{\theta;1,2})$ and $u_{g;1,2}(t) = 0$ otherwise. This pulsing sequence, i.e. one gas pulse of time period T_p followed by a 'resting-period' T_p without gas flow is subsequently described as the base-case pulsation. Here T_p denotes the pulse period and subscripts 1 and 2 refer to the lower and upper gas jets, respectively. A gas-jet pulse of period T_p at either inlet ports is followed by an equal-time period where there is no pulse for that particular port. Parameters $n_{\theta;1,2}$ describe any time delay or phase-shift in the pulsing of the gas jets at the lower (1) and upper (2) injection ports. In this analysis $n_{\theta;1} = 0$ always, whereas $n_{\theta;2}$ ranged from 0 to 1. Note that gas jet pulsation with $n_{\theta,1} = n_{\theta,2} = 0$ will always result in dilational film deformation whereas $n_{\theta,1} = 0$ and $n_{\theta,2} = 1$ will generate initially (predominantly) sinuous film distortions.

After nondimensionalization [2] the following (nondimensional) flow parameters have to be considered: (1) The ratio of maximum gas jet momentum to liquid film momentum $\mathrm{M} = \rho_g u_{g,0}^2 s/(\rho_l u_l^2 h)$, (2) the nondimensional square of the film injection velocity or liquid-phase Weber number $\mathrm{We}_l = \rho_l u_l^2 h/\sigma$, (3) the

gas-to-liquid density ratio ρ_g/ρ_l, and three geometric parameters, i.e. the gas jet injection angle α, as well as s/h and H/h denoting the ratios of gas-jet inlet port width or discharge channel width to the thickness of the undisturbed liquid film, respectively. Here, the parameters M and α have been replaced by $M_{\parallel} = M\cos\alpha$ and $M_{\perp} = M\sin\alpha$ representing the maximum values of the gas jet components parallel and perpendicular to the undisturbed liquid film. The former is relevant for the initial generation of film disturbances, while the latter can cause amplification of an existing disturbance through Kelvin-Helmholtz wave growth.

Fig. 2 shows a sinusoidally distorting liquid film subject to the forcing conditions (described earlier) imposed onto the gas jet inlet velocities $u_{g;1}$ and $u_{g;2}$. Plug flow has been assumed at both gas jet outlets. Here, both lower and upper gas jet pulsations are out-of phase so that $n_{\theta,1} = 0$ and $n_{\theta,2} = 1$, the base-case pulsation. Parameters for this base case are $\mathrm{M}_{\parallel} = \mathrm{M}_{\perp} = 1$, $\rho = \rho_g/\rho_l = 0.0012$, $\mathrm{We}_l = 10$ and $s/h = H/h = 10$. For this case, film rupture is predicted after approximately $t^* = 16$ at a location of $x/h \approx 45$. For the similar case but dilationally gas-jet pulsing, i.e. $n_{\theta,1} = n_{\theta,2} = 0$, the energy provided by the impacting gas jets and base-case pulsation is insufficient to break the film, the latter being stabilized by surface tension. This stabilizing effect is overcome if the energy flux imposed onto the film by the gas jets is increased. In Fig. 3 the gas jet pulses of period T_p follow immediately upon each other without a 'resting-period' resulting in film rupture at $x/h = 106.5$ after $t^* = 25$.

At constant gas-to-liquid jet momentum ratio, higher ambient pressure conditions, i.e. higher gas-to-liquid density ratios, will affect film distortion and disintegration only through changes in the film dynamics or interface dynamics via the unsteady Bernoulli equation. The latter determines the gas pressure at the interfaces in dependence on the instantaneous gas-phase velocity potential. If the ambient pressure or gas-to-liquid density ratio is increased while keeping the gas- and liquid-phase velocities constant, film distortion is determined by the described interface dynamics directly but also indirectly through the changed gas-phase momentum influx which will affect the force balance at the interfaces. Fig. 4 shows the same case as in Fig. 2 at an earlier time together with the results obtained for a tenfold increase in gas-to-liquid density ratio but with the same gas-to-liquid jet momentum ratio. For the larger density ratio case, larger sections of the discharging liquid film are being deflected by the impacting gas jets and film rupture time is greatly reduced. Rupture or rather film tearing occurs before the development of a wave structure on the discharging film. A similar behavior is observed if gas and liquid injection velocities are kept constant rather than the momentum ratio.

The density-ratio effects described above are identical in the limit where the gas-jet-momentum influx is reduced to zero. In that case, i.e. for a liquid film moving through a quiescent gas, linear (and also nonlinear) theory shows that (temporal) growth rates of unstable sinuous (and dilational) waves present on the liquid film increase with increasing density ratio at fixed liquid Weber number. The described analysis of the twin-fluid atomizer configuration also included parametric studies considering variations in the various other problem parameters. In addition, the studies also included the consideration of an underlying continuous gas-flow onto which gas-jet modulations were superimposed. Film modulation via pulsed gas-jets was compared to direct film modulation via velocity modulation of the liquid film itself. See Ref. [2].

Dynamic Film Stretching

A previously derived model for two-dimensionally distorting thin liquid films in a void at zero gravity has been extended by including viscous effects and long-range intermolecular forces into the reduced field-equations and boundary equations. Using the extended model, the dynamic stretching of a thin liquid film subject to equal but opposite pulling velocities at both ends was investigated. Due to the existing symmetry, we analyze only one half of the film. The film is initially undisturbed with $\delta(0 < x < l_\circ, t = 0) = \delta_\circ$ and $u(0 < x < l_\circ, t = 0) = 0$, where $2l_\circ$ is the initial total length of the film. Boundary conditions in the plane of symmetry at $x = 0$ for $t \geq 0$ are given by $(\partial\delta/\partial x) = 0$ and $u = 0$. The pulling velocity $u_p(t)$ at $x = l(t) = u_p(t)\,t$ was assumed to increase smoothly from 0 to a maximum steady value $u_\circ$ according to $u(x = l(t), t) = u_p(t) = u_\circ\,[1 - \cos(2\pi t/T_p)]$. The film thickness δ at the pulling end was assumed to be fixed, i.e. $\delta(x = l(t), t \geq 0) = \delta_\circ$. Numerical solutions were carried out after introducing the following coordinate transformation: $\eta = \frac{x}{l(t)}$ and $\tau = t$. where $2\,l(t)$ denotes the instantaneous total film length. Furthermore, intermolecular forces were not included in this first analysis. Several distinct film topologies

have been identified depending on liquid Weber number $We = \rho u_\circ^2 \delta_\circ / \sigma$ and Reynolds number $Re = u_\circ \delta_\circ / \nu$, i.e., the magnitude of the stretching rate (end velocity) compared to signal propagation rates through the liquid via capillary waves and viscous action.

Fig. 5 shows the variation of film thickness with time for the case with $We = 1$ and $Re = 100$. The nondimensional length $l_b^* = l_b/\delta_\circ$ at which the film ruptures is 2.45, with rupture occuring after nondimensional time $\tau_b^* = \tau_b/(\delta_\circ/u_\circ) = 1.95$. We observe the formation of a liquid wedge at the pulling end. Also, capillary waves initially generated at the pulling end propagate into the film leading to an absolute maximum in the film thickness at $\eta = x/l = 0$ before and at the time of film break-up.

As the Weber number is decreased (at fixed Reynolds number) the pulling velocity decreases with respect to the capillary wave velocity. Accordingly, the time scale for the exchange of information along the liquid film is significantly smaller than the time scale associated with the generation of film disturbances due to the accelerating film. Consequently, a distinct liquid wedge at the pulling end is no longer formed. As the film stretches over a longer period of time without rupture, the film thickness at $\eta = 0$ continuously decreases at later times and its maximum value is reached at the pulling end. On the other hand, as the Weber number is increased (at fixed Reynolds number), the effects of film thinning by film stretching are not communicated fast enough towards the film center, such that at the point of film rupture the center of the film remains essentially undisturbed.

As Reynolds number is decreased at fixed Weber number, propagation of information from the pulling end into the film is increasingly determined by viscous diffusion. At small Reynolds numbers, the film thickness has a local maximum at the centerline whose value continuously decreases as time (or stretching) progresses. For small Weber number and small Reynolds number, a long thin liquid filament or band of "uniform" thickness is formed with a well-defined film wedge located at the pulling end. Filament pinching occurs at its transition into this film wedge.

Three-Dimensionally Distorting Linear and Nonlinear Annular Films

In order to guide the analysis of nonlinearly distorting annular (and conical) three-dimensionally distorting liquid films, a linear spatial analysis of swirling three-dimensional annular liquid films has been conducted. Analogous to previous analyses of planar semi-infinite liquid films, derivation of the corresponding dispersion relation and subsequent evaluation of group velocities associated with the different wavenumber solutions provided information on energy propagation on the three-dimensionally linear distorting film and on the appropriate number of boundary conditions to be specified at the film discharge location if non-axisymmetric modes are considered. Growth rates in dependence of modulation frequency showed that for large Weber numbers, the instability range decreases with increasing circumferential wave number n. In fact, for large enough n-values no instability exists. See Fig. 6. The maximum growth rate increases with decreasing Weber number. Also, as the Weber number decreases, the instability range of non-axisymmetric modes ($n \neq 0$) increases and might become larger than for the n=0 case. However, the maximum growth rate is (as for the larger Weber number cases) still observed for the axisymmetric case. For small Weber numbers and small enough $n-$values, the instability range of non-axisymmetric modes is larger than for the $n = 0$ case.

Comparison between linear and nonlinear theory shows that for the considered unstable "dilationally" modulated annular films, the nonlinear growth rate for axisymmetric $n = 0$ modulations is about 56 percent larger than the linear prediction. Comparison between nonlinear numerical solutions for axisymmetric and non-axisymmetric (n=3) cases also showed that, the increase of the maximum film thickness is approximately the same in both cases while the decrease of the minimum thickness (at the same downstream location) is larger for the non-axisymmetric case. Linear analysis also predicts that the wave angle $-k/n$ for unstable "dilational" waves decreases with increasing n at fixed ω, and that the magnitude of the wave angle increases linearly with ω at fixed n (except for small ω).

References

[1] Mehring, C. and Sirignano, W. A., 1999, "Nonlinear capillary wave distortion and disintegration of thin planar liquid sheets," *J. Fluid Mech.*, Vol. 388, pp. 69–113.

[2] Mehring, C. and Sirignano, W. A., 2000, "Liquid film disintegration from twin-fluid atomizers," submitted to *Physics of Fluids* .

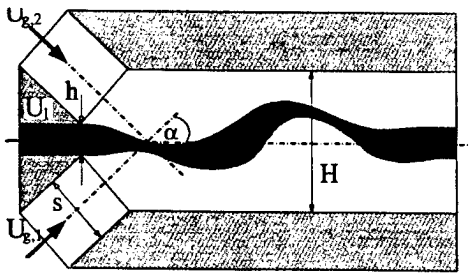

Figure 1: Twin-fluid atomizer configuration.

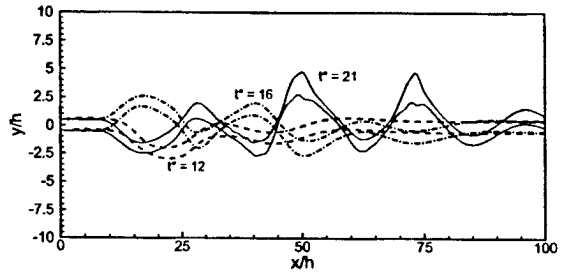

Figure 2: Sinuous film distortion and rupture due to out-of-phase modulated impacting gas jets.

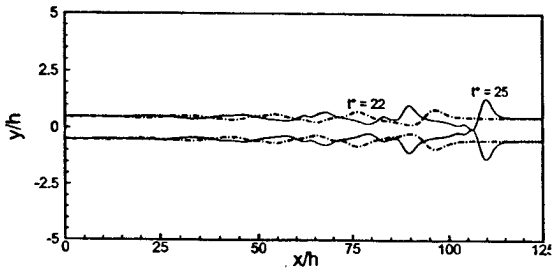

Figure 3: Dilational film distortion and rupture due to in-phase modulated impacting gas jets.

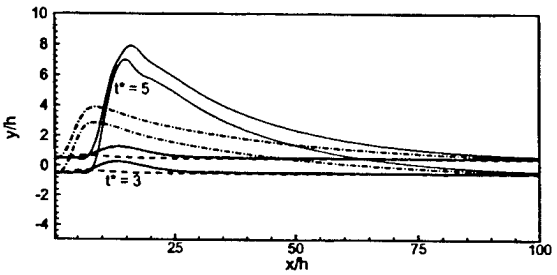

Figure 4: Comparison, between sinuous film distortion and rupture at low and elevated pressures, i.e. for ρ_g/ρ_l = 0.0012 (dash, dot), 0.012 (dash-dot,solid).

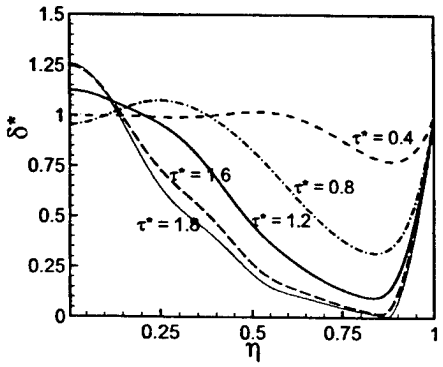

Figure 5: Temporal evolution of film thickness for film stretching at We = 1, Re = 100.

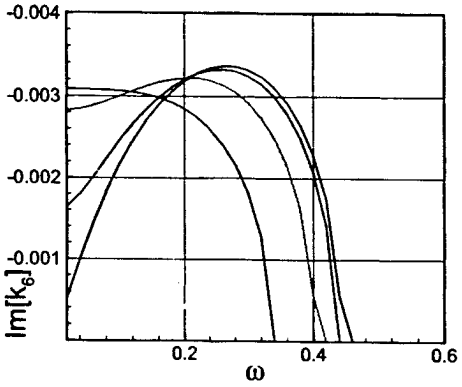

Figure 6: Linear spatial growth rates for axisymmetric ($n = 0$) and non-axisymmetric ($n \neq 0$) unstable "dilational" waves on swirling annular films (black: n=0, red: n=1, green: n=2, blue: n=3, yellow: n=4).

DROP/GAS INTERACTIONS OF DENSE SPRAYS

(AFOSR Grant No. F49620-02-1-0074)

Principal Investigator: G. M. Faeth

Department of Aerospace Engineering
The University of Michigan
3000 François-Xavier Bagnoud Bldg.
Ann Arbor, Michigan 48109-2140, U.S.A.

SUMMARY/OVERVIEW:

Turbulence generation and liquid breakup are being studied due to their relevance to dense combusting sprays found in propulsion systems. Turbulence generation is the main source of turbulence in dense sprays; it consists of drop (particle) wake disturbances embedded in a turbulent interwake region. Both regions involve unusual flows that have received little attention in the past: the particle (drop) wakes are laminar-like turbulent wakes that are observed for intermediate Reynolds number spheres in turbulent environments; the turbulent interwake region consists of isotropic turbulence in the little-studied final decay period. Earlier work found the properties of these flows for monodisperse particle (drop) flows; current work is considering their properties for more practical polydisperse particle (drop) flows.

Primary and secondary liquid breakup are important because they are rate-controlling processes of dense sprays and fix initial conditions of dilute sprays. Earlier experiments at large liquid/gas density ratios have shown that breakup of round nonturbulent liquid jets in crossflows is remarkably similar to secondary breakup of drops, that secondary drop breakup should be treated as a rate process, and has provided the needed temporal properties of secondary drop breakup. Current experiments are considering the breakup properties of round nonturbulent liquid jets in crossflow at large liquid/gas density ratios, whereas, current time-dependent numerical simulations are seeking liquid breakup properties for both processes, emphasizing small liquid/gas density ratios that are difficult to address using experiments.

TECHNICAL DISCUSSION

TURBULENCE GENERATION. Early studies showed that turbulence generation by particles (drops) involved particle wakes embedded in a turbulent interwake region (Parthesarathy and Faeth 1990; Mizukami et al. 1992). Wu and Faeth (1993,1994,1995) subsequently showed that the wakes behaved like laminar wakes but with fast mixing due to the presence of turbulence (commonly referred to as "laminar-like turbulent wakes"). Subsequently, Chen et al. (2000) and Chen and Faeth (2000,2001) considering monodisperse particle flows showed that the turbulent interwake region consisted of isotropic turbulence in the rarely observed final-decay period defined by Batchelor and Townsend (1948). Current work of Lee et al. (2002) seeks to extend these observations to the turbulent interwake region of more practical polydisperse particle flows, using wake-discriminating laser velocimetry.

Chen and Faeth (2001) developed an analogy between grid-generated isotropic turbulence and particle-generated isotropic turbulence, when both were in the final-decay period. This yielded a very useful correlation between relative turbulence intensities in the streamwise and cross-stream directions, ($\overline{u}'$ and $\overline{v}'$)/U_p, where U_p is the mean velocity of the particles relative to the gas, and the dimensionless rate of dissipation of mechanical energy of the particles, D.

During the present investigation, mixing rules were developed to extend these ideas to polydisperse particle flows, based on dissipation weighting for each particle size group. The resulting correlations are illustrated in Fig. 1: results for both monodisperse and polydisperse particle flows are seen to correlate the same way, the correlation also effectively handles different sized particles, and finally the correlation correctly indicates that relative turbulence intensities are proportional to the square root of the dimensionless dissipation factor, providing considerable insight concerning the nature of turbulence generation.

Current experiments involve conditional (wake discriminating) measurements of energy spectra and characteristic length scales for the turbulent interwake region of polydisperse particle flows. Results obtained thus far are illustrated in Fig. 2, where the ratio of the streamwise integral scale, L_u, to the dissipation (Taylor) scale, λ, is plotted as a function of the turbulence Reynolds number, Re_λ, for both conventional isotropic turbulence in the initial-decay period along with the results of Chen and Faeth (2001) and the present investigation concerning isotropic turbulence in the final-decay period. Notably, unlike conventional turbulence where L_u/λ increases as Re_λ increases, turbulence in the final-decay period behaves just the opposite because the turbulence is sparse and has rates of dissipation that are orders of magnitude larger than conventional turbulence. Nevertheless, the generality of the results seen in Fig. 2 provides encouragement that effective models of the properties of interwake turbulence, and thus turbulence generation, can be developed: current work is seeking information along these lines.

LIQUID BREAKUP. Past experimental studies have established the temporal properties of secondary drop breakup (Chou and Faeth 1997; Chou et al. 1997; Dai and Faeth 2001; Faeth 1996; Hsiang and Faeth 1992,1993,1995) and have initiated studies of round nonturbulent liquid jet breakup in crossflow (Mazallon et al. 1999), both at large liquid/gas density ratios. Current work is considering these processes using numerical simulations and emphasizing small liquid/gas density ratios that are difficult to address by experiments, see Aalburg et al. (2002a,b) for detailed descriptions of this work.

Current work has emphasized drop deformation and secondary breakup when subjected to shock-wave disturbances. Figure 3 is a typical result, giving predicted and measured normalized deformation as functions of Weber numbers (We, the ratio of drag to surface-tension forces) and Ohnesorge numbers (Oh, the ratio of liquid-viscous to surface-tension forces), which is the classical approach for correlating these properties due to Hinze (1955). The predictions are excellent at small Oh but overestimate We at large Oh because the Reynolds numbers of the simulations are small compared to the measurements; calculations to correct this deficiency are in progress and suggest excellent agreement between measurements and predictions for the range where they can be compared. Another useful result shown in Fig. 3 is that the drop breakup limit corresponds to a maximum deformation of 60%, providing a computationally tractable way to estimate breakup properties that won't be computationally tractable for some time to come.

Similar to earlier findings concerning the breakup of liquid jets in crossflow (Aalburg et al. 2002a), the Hinze (1955) plot did not provide a useful treatment of effects of liquid/gas density and viscosity ratios on breakup. A better approach was to account for liquid viscous effects directly by plotting the ratio of drag/liquid-viscous forces, $We^{1/2}/Oh$, as a function of the ratio of surface-tension/liquid-viscous forces, $1/Oh$. These results are illustrated in Fig. 4 where measurements and predictions are in excellent agreement. Finally, a new effect is observed, where increasing drag coefficients as Reynolds numbers decrease as the Stokes regime is approached, increases drop resistance to deformation and breakup.

Current work involves additional simulations to better match conditions of the calculations to existing measurements and to investigate broader ranges of breakup parameters. In addition, measurements of round nonturbulent liquid jet breakup in crossflow, similar to past measurements of secondary drop breakup, have been initiated.

REFERENCES

Aalburg, C.M. et al., (2002a) *Int. J. Multiphase Flow*, submitted.
Aalburg, C.M. et al.(2002b) *AIAA J.*, in preparation.
Batchelor, G.K. and Townsend, A.A. (1948) *Proc. Roy. Soc. (London)* 193A, 539.
Chen, J.-H. and Faeth, G.M. (2000) *AIAA J.* 38, 995.
Chen, J.-H. and Faeth, G.M. (2001) *AIAA J.* 39, 180.
Chen, J.-H. et al. (2000) *AIAA J.* 38, 636.
Chou, W.-H. and Faeth, G.M. (1997) *Int. J. Multiphase Flow* 24, 889.
Chou, W.-H. et al. (1997) *Int. J. Multiphase Flow* 24, 651.
Dai, Z. and Faeth, G.M. (2001) *Int. J. Multiphase Flow* 27, 217.
Faeth, G.M. (1996) *Proc. Combust. Inst.* 26, 1593.
Hinze, J.O. (1955) *AIChE J.* 1, 289.
Hsiang, L.-P. and Faeth, G.M. (1992) *Int. J. Multiphase Flow* 18, 635.
Hsiang, L.-P. and Faeth, G.M. (1993) *Int. J. Multiphase Flow* 19, 721.
Hsiang, L.-P. and Faeth, G.M. (1995) *Int. J. Multiphase Flow* 21, 545.
Lee, K. et al. (2002) *AIAA J.*, in preparation.
Mazallon, J. et al. (1999) *Atom. Sprays* 9, 291.
Mizukami, M. et al. (1992) *Int. J. Multiphase Flow* 18, 397.
Parthesarathy, R.M. and Faeth, G.M. (1990) *J. Fluid Mech.* 220, 485.
Wu, J.-S. and Faeth, G.M. (1993) *AIAA J.* 31, 1448.
Wu, J.-S. and Faeth, G.M. (1994)*AIAA* . 32, 535.
Wu, J.-S. and Faeth, G.M. (1995) *AIAA J.* 33,171.

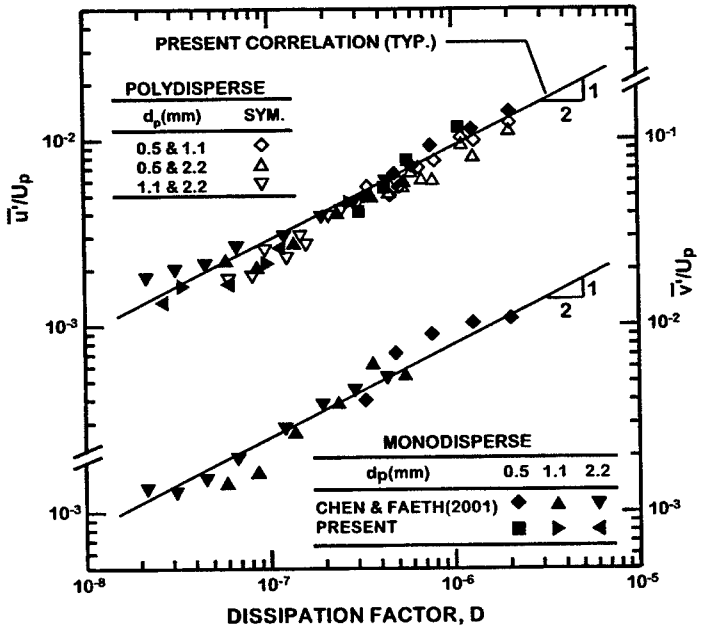

Fig. 1 Relative turbulence intensities as a function of the dissipation factor for the turbulent inter-wake region. From Lee et al. (2002).

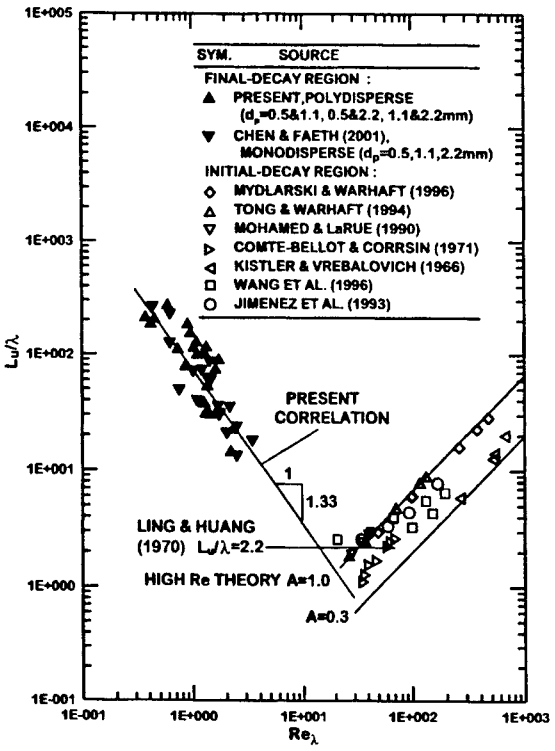

Fig. 2 Integral/dissipation length scale ratios as a function of turbulence Reynolds number. From Lee et al. (2002).

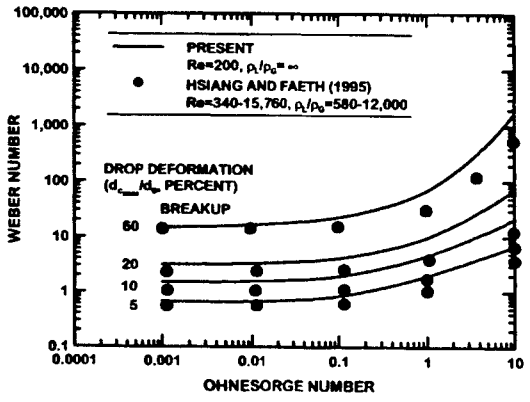

Fig. 3 Deformation and breakup regime boundaries for drops subjected to shock-wave disturbances in the classical Hinze(1955) coordinate. From Aalburg et al. (2002b)

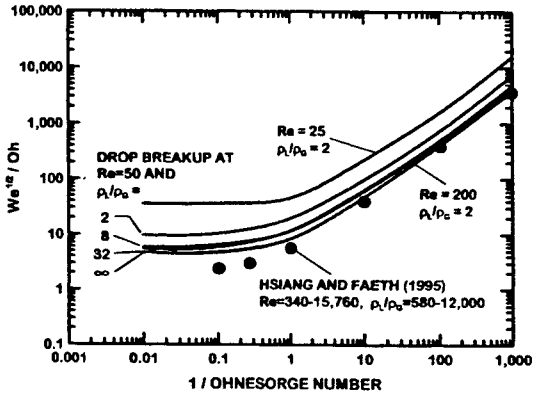

Fig. 4 Breakup regime boundaries for drops subjected to shock-wave disturbances in the revised coordinate. From Aalburg et al. (2002b)

ADVANCED SUPERCRITICAL FUELS

LRIR 93PR02COR

Principal Investigators: Tim Edwards, Chris Bunker, Tom Jackson

Air Force Research Laboratory
AFRL/PRTG Bldg 490
1790 Loop Rd N
Wright Patterson AFB, OH 45433-7103

SUMMARY/OVERVIEW:

Increases in aircraft and engine performance are increasing the heat load being transferred into an aircraft's primary coolant--the fuel. This research is aimed at understanding the limitations of operation of fuel heated to 480 C (900 F) and beyond. Important issues are expected to be thermal stability, injection/combustion properties, and fuel characterization [1].

TECHNICAL DISCUSSION

A key barrier to the use of fuels at supercritical temperatures (>~750 F) is thermal-oxidative deposition. A pseudo-detailed kinetic mechanism continues to be refined in two areas: fuel-surface interactions and deposition-enhancing trace fuel species characterization. As described in last year's abstract, recent innovative measurements at WPAFB have shown a stronger role for metal surfaces in fuel autoxidation behavior. Modeling of this behavior indicates a surface role in fuel hydroperoxide decomposition [2]. The role of trace sulfur and other heteroatomic species is being investigated using extraction of polar species [3]. Ultimately, it would be desirable for modeling purposes to be able to characterize deposition-enhancing species in fuels with a single parameter. Earlier efforts to use the fuel sulfur content were less than ideal, since other heteroatomic species were neglected, such as oxygen and nitrogen-containing impurities. Also, fuel sulfur is roughly equally divided between reactive sulfides/disulfides and relatively inert thiophenes/benzothiophenes [4].

Another key barrier to the use of fuels as coolants, especially for scramjets, is the variation in fuel properties as a function of fuel temperature (which becomes a function of mission time). Current hydrocarbon-fueled scramjets suffer from poor combustion behavior with liquid fuels, so the injection and combustion behavior of fuels as the fuel transitions from liquid to vapor is under active investigation. A key concern is condensation as supercritical (T,P) fuels are injected through choked orifices into combustion chambers at subcritical pressures. Expansion of supercritical fuels through turbopumps also raises condensation concerns. This continues to be of concern at higher temperatures as the fuel is thermally cracked during use as a coolant and the composition changes. Mixture effects have been looked at initially with methane/ethylene mixtures. The entropy-pressure diagram for one of the methane/ethylene mixtures is shown in Fig. 1 with two isentropic expansion paths illustrated. The path originated at a temperature close to the critical point can readily penetrate into the two-phase region during isentropic expansion while the other path initiated at a temperature away from the critical point may exhibit an idea gas expansion. Injection conditions representative to both isentropic paths are qualitatively demonstrated in Figure 2. An opaque jet image, possibly with condensation occurring within the jets, was observed when the jet is injected at a reduced temperature close to

unity. The supercritical methane/ethylene jet can also undergo an ideal-gas-like expansion with both barrel shock and Mach disk visible inside the jets when injected at a high reduced temperature. To further illustrate the condensation phenomenon, Fig. 3 demonstrates the internal structures of supercritical methane/ethylene jets inside a transparent injector. An abrupt boundary indicating the onset of two-phase transition is located inside the injector for the jet injected at a temperature close to critical temperature. Homogeneous condensation, which is prompted through rapid expansion to reach a metastable supersaturation state and can produce a large quantity of droplet nuclei almost spontaneously, is believed to be the mechanism. The evaluations of ethylene/sulfur hexafluoride (SF_6) will be carried out during the subsequent research activities, in order to see whether representative mixing phenomena of JP-7 can be simulated with a large difference in molecule weight.

The increased demands being placed on fuel (higher performing aircraft and engines generating greater quantities of heat) and the apparent downward trend in the quality of petroleum feed stocks has made the development of field-level, fuel-quality diagnostics a priority. Studies of the application of multivariate analysis to large scale gas chromatographic data sets is continuing with the focus being on rapid analysis using a fast-GC (under five minute separation) method [5,6]. As shown in Figure 4, high quality chromatographic traces are achieved using a specialized column and instrument method. Analysis of the principle fuel components shows good fuel identification capability (Figure 5). Sensors based on long-period-grating (LPG) technology are being developed for the identification of specific compounds in fuel [7,8]. The current sensor design uses carboxymethyl cellulose as a Cu^{2+}-sensitive binding layer (Figure 6). Exposure of the sensor to solutions containing Cu^{2+} results in significant and quantifiable changes in the spectral response (Figure 7). Continuing efforts will be focused on developing fuel specific layers targeting important additives [9-12].

Our understanding of the properties of hydrocarbon-based supercritical fluids as models for supercritical aviation fuel has been furthered by investigations of two-component systems [13]. Data obtained using pyrene as a probe of local solvent strength in hexane-toluene fluids verifies the well-known solute-solvent phenomenon (Figure 8) and indicates the possibility of enhanced solute-solute interactions (Figure 9). Efforts are on-going to model the observed behaviors using a combination of quantum mechanical and Monte Carlo computational techniques. Two review articles have been published in this area [14,15].

[1] Edwards, T., Meyer, M., "Propellant Requirements for Future Aerospace Propulsion Systems," AIAA-2002-3870, July 2002.

[2] T. Doungthip, J. Ervin, T. Ward, T. Williams, S. Zabarnick, "Surface Deposition Within Treated and Untreated Stainless Steel Tubes Resulting from Thermal-Oxidative Degradation of Jet Fuel," *ACS Petrol. Chem. Div. Preprints* **2002**, *47*, in press..

[3] S. Zabarnick, R. Striebich, K. Straley, and L. Balster, Solid Phase Extraction Analysis of Polar Species in Jet Fuel," *ACS Petrol. Chem. Div. Preprints* **2002**, *47*, in press.

[4] Link, D. D., Minus, D. M., Striebich, R. C., Rothenburger, K. S., Baltrus, J. P., "The Analysis of Total and Speciated Sulfur in Aviation Turbine Fuels," *ACS Petrol. Chem. Div. Preprints* **2002**, *47*, in press.

[5] Rozenzhak, S. M.; Striebich, R. C.; Bunker, C. E. "Development of a High-Speed Jet-Fuel Diagnostic System Using Gas Chromatography and Principal Component Analysis" *ACS Petrol. Chem. Div. Preprints* **2002**, *47*, in press.

[6] Striebich, R. C., "Fast Gas Chromatography for Middle-Distillate Aviation Turbine Fuels," *ACS Petrol. Chem. Div. Preprints* **2002**, *47*, in press.

[7] Widera, *J.;* Reich, *R. F.;* Pacey, *G. E.;* Puckett, *S. D.;* Bunker, *C. E.;* Gord, J. R. "Long-Period-Grating Fiber-Optic Sensors for Smart Nozzle Development. Evaluation of a Commercial Cu^{2+} Sensor" *ACS Petrol. Chem. Div. Preprints* **2002**, *47*, in press.

[8] Widera, J.; Cox, J. A.; Pacey, G. E.; Bunker, C. E.; Gord, J. R. "Developing Analytical Techniques for 'Smart Nozzle' Technology" 27th Annual Dayton-Cincinnati Aerospace Science Symposium, Dayton, OH, March 5, 2002.

[9] Harruff, B. A.; Bunker, C. E. "Luminescence Study of CdS Nanoparticles: Observation of a Photolytic Passivation Effect" 27th Annual Dayton-Cincinnati Aerospace Science Symposium, Dayton, OH, March 5, 2002.

[10] Phelps, D. K. "Application of Gibbs Ensemble Monte Carlo to Calculations of Phase Equilibria in Jet Fuel" 27th Annual Dayton-Cincinnati Aerospace Science Symposium, Dayton, OH, March 5, 2002.

[11] Phelps, D. K. "Molecular Dynamics Study of Reverse Micelle Formation in Fuel" *ACS Petrol. Chem. Div. Preprints,* **2002**, *47*, in press.
[12] Bunker, C. E.; Meyer, T. R.; Brown, M.; Katta, V. R.; Zweifel, D. A.; Sun, Y.-P.; Gord, J. R.; Harruff, B. A. "Micro to Nano—Small Research for Fuels and Combustion" in *Surf. Eng.: Sci. Tech. II*, 131st The Minerals, Metals & Materials Society, Seattle, WA, Feb. 2002.
[13] Bunker, C. E., Harruff, B. A.; Zweifel, D. A.; Rabe, M. R.; Gord, J. R. "Solute-Solvent and Solute-Solute Interactions in Two Component High-Temperature, High-Pressure Supercritical Fluids" *ACS Petrol. Chem. Div. Preprints* **2002**, *47*, in press.
[14] Bunker, C. E., Rollins, H. W., Sun, Y.-P., "Fundamental Properties of Supercritical Fluids," Chapter 1 of Supercritical Fluid Technology in Materials Science and Engineering-Syntheses, Properties, and Applications, Y.-P. Sun, ed., Marcel Dekker, Inc., New York, 2002.
[15] Sun, Y.-P., Rollins, H. W., Bandara, J., Meziani, J. M., Bunker, C. E., "Preparation and Processing of Nanoscale Materials by Supercritical Fluid Technology," Chapter 13 of Supercritical Fluid Technology in Materials Science and Engineering-Syntheses, Properties, and Applications, Y.-P. Sun, ed., Marcel Dekker, Inc., New York, 2002.

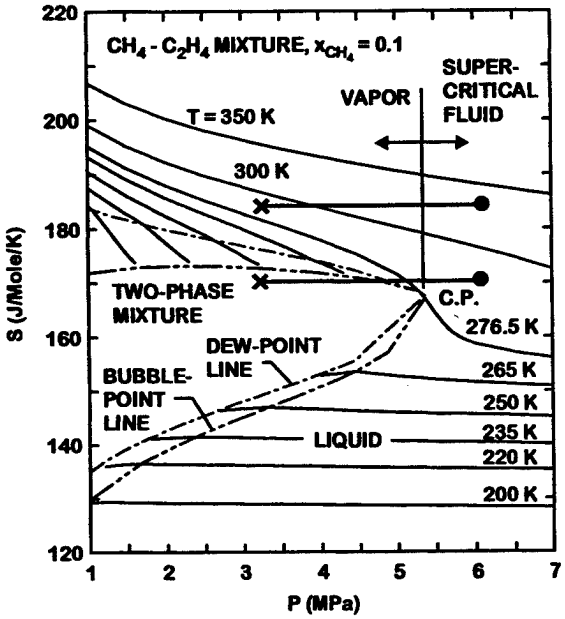

Fig. 1 Isentropic expansion paths in an entropy-pressure phase diagram for the methane/ethylene mixture with x_{CH4}=0.1.

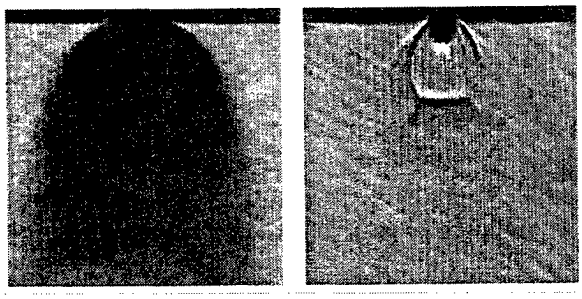

P_{inj}/P_c	1.16	1.15
T_{inj}/T_c	1.03	1.23
P_{inj}/P_{chm}	36.7	35.7

Fig. 2 Shadowgraph images for supercritical methane/ethylene jets at various injection temperatures. x_{CH4}=0.1 and d=1.0 mm.

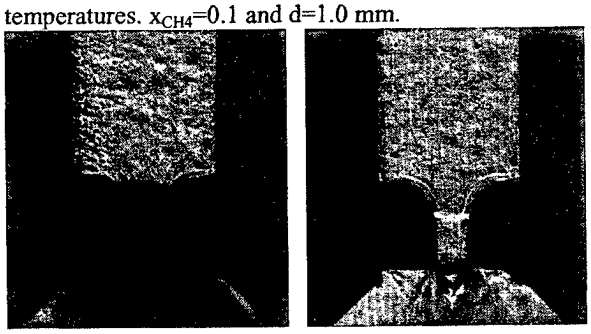

P_{inj}/P_c	1.04	1.03
T_{inj}/T_c	1.00	1.08
P_{inj}/P_{chm}	32.5	35.7

Fig. 3 Shadowgraph images for supercritical methane/ethylene jets using a transparent injector.

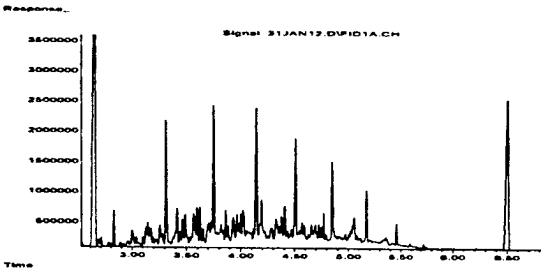

Figure 4. Representative gas chromatogram of Jet A collected with the fast-GC method.

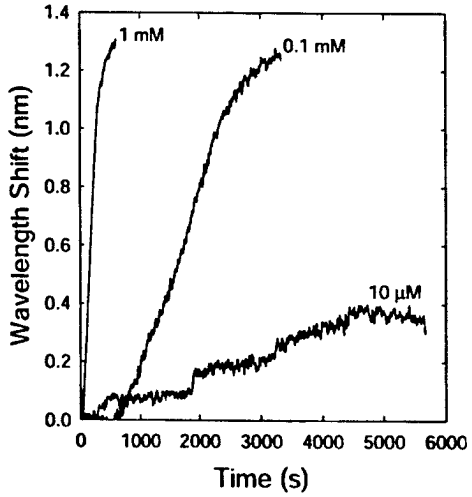

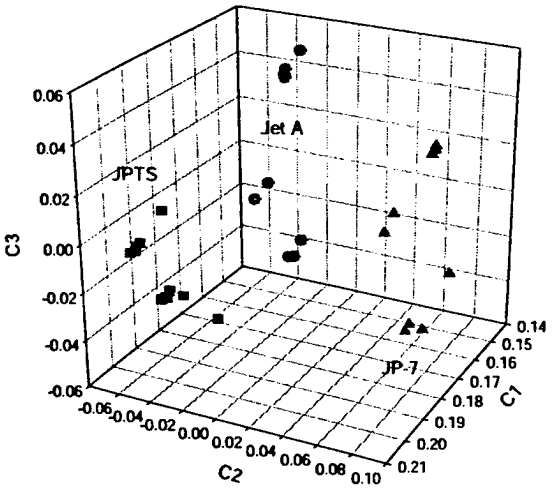

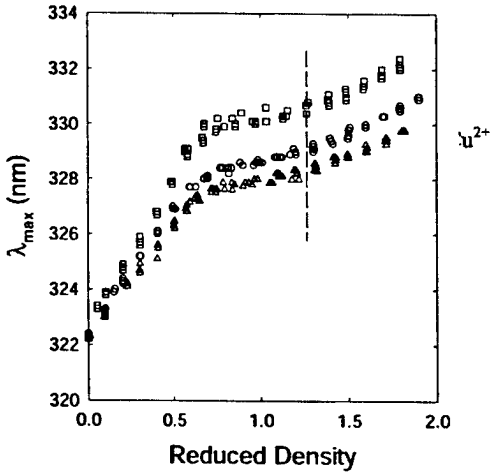

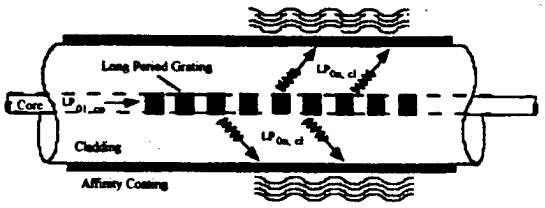

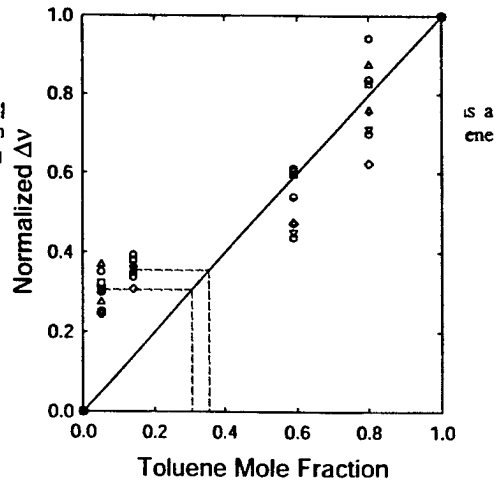

Figure 6. Schematic representation of the LPG fiber sensor.

FUELS COMBUSTION RESEARCH: SUPERCRITICAL FUEL PYROLYSIS

AFOSR Grant No. F49620-00-1-0298
Principal Investigator: Mary Julia (Judy) Wornat

Princeton University
Department of Mechanical and Aerospace Engineering
Princeton, New Jersey 08544

SUMMARY/OVERVIEW

The fuels used in the next generation of hypersonic aircraft [1] will have to operate under very high pressures (beyond the critical pressures of most hydrocarbons) and will have to sustain very high heat loads in order to meet aircraft cooling requirements. Potential candidates for meeting these stringent cooling requirements are "endothermic" fuels, fuels that can undergo a controlled heat-absorbing chemical reaction (e.g., dehydrogenation) prior to combustion. Critical to the development of the fuel systems in these aircraft is an understanding of the fuel pyrolysis reaction mechanisms under the conditions that the fuels will be operating. Of particular interest are the reactions leading to polycyclic aromatic hydrocarbons (PAH), which can serve as precursors to fuel-line deposits, a problem of critical importance to avoid, for safe aircraft operation. In order to better elucidate the mechanisms and kinetics of the reactions of endothermic fuel pyrolysis and PAH formation under supercritical conditions, supercritical pyrolysis experiments are being conducted, under the present research program, with model fuels, over a range of supercritical pressures and temperatures. The model fuels include two endothermic fuels, methylcyclohexane and decalin, as well as toluene and heptane, hydrocarbons representative of the aromatic and aliphatic components of jet fuels. The reaction products are analyzed by high-pressure liquid chromatography with diode-array ultraviolet-visible absorbance detection (HPLC/UV), an isomer-specific technique ideally suited for the analysis of PAH [2]. It is anticipated that the results from this study will provide information of critical importance to the design and development of fuel systems for high-speed aircraft.

AUTHORS: M. J. Wornat, E. B. Ledesma, P. G. Felton, J. A. Sivo, and N. D. Marsh

TECHNICAL DISCUSSION

Pyrolysis experiments have been conducted with toluene (critical temperature 319 °C, critical pressure 41 atm) at temperatures up to 585 °C, pressures up to 100 atm, and residence times up to 550 sec. Collection and analysis of the toluene reaction products from these experiments reveals that increases in pyrolysis temperature, pressure, and/or residence time bring about increases in PAH formation, in terms of both the yields of the products formed as well as their molecular sizes.

Because of the complexity of the mixture of aromatics produced in the toluene experiments, both gas chromatography/mass spectrometry (GC/MS), for the lower-ring-number species, and HPLC/UV, for the higher-ring-number species, are employed in the product analyses. Component identifications are made by matching chromatographic retention times and MS and/or UV spectra with those of authentic reference standards, several of which have been specially synthesized for these purposes. The structures of the 26 unequivocally identified PAH products of supercritical toluene pyrolysis are presented in Figure 1, an HPLC chromatogram of the products from pyrolysis at 535 °C, 100 atm, and 550 sec. (The large unlabelled peaks in the 12- to 20-minute retention time range correspond to toluene dimers, which are better resolved by GC and not included in the product structures of Figure 1.) As shown in Figure 1, four classes of PAH are represented among

the supercritical toluene pyrolysis products: 15 benzenoid PAH (those with only six-membered rings), 4 fluoranthene benzologues (those with an internal five-membered ring), 2 indene benzologues (those with a five-membered ring containing a methylene carbon), and 5 methylated PAH. Noticeably absent from the supercritical toluene pyrolyisis products are cyclopenta-fused PAH and ethynyl-substituted PAH, two classes of PAH produced by a variety of other fuels but under subcritical pyrolysis conditions [2-4]. The absence of these two classes of products suggests that mechanisms other than acetylene-addition (widely applicable in subcritical pyrolysis environments [3]) are responsible for PAH growth in supercritical pyrolysis systems.

Of particular note in Figure 1 are the four very large PAH of 8, 9, and 10 fused aromatic rings—benzo[*a*]coronene, benzo[*pqr*]naphtho[*8,1,2-bcd*]perylene, naphtho[*8,1,2-abc*]coronene, and ovalene—none of which have ever before been identified as products of toluene pyrolysis or as products of supercritical pyrolysis of any fuel. The UV spectral matches confirming the identifications of two of these large PAH are displayed in Figures 2 and 3. It should be noted that it is rare for any of these large PAH to be observed in fuel products—partly because few researchers are in possession of the specially synthesized reference standards [5] necessary to identify these species and partly because formation of these large PAH requires extreme conditions. For example, one of the only other cases in which the large PAH ovalene has been shown [6] to be produced is from subcritical fuel-rich combustion of naphthalene/ethylene mixtures at 1375 °C. The fact that the monocyclic fuel toluene can produce the 10-ring ovalene at a temperature of only 535 °C points to the huge effect of the supercritical conditions on facilitating the formation of large PAH, precursors to solid deposits. In fact, supercritical toluene pyrolysis experiments at 585 °C (just 50 °C higher than the condition corresponding to Figure 1) result in repeated plugging of the reactor, due to solid deposit formation.

The yields of all of the PAH of Figure 1 are extremely dependent on both pyrolysis temperature and pressure. For example, toluene pyrolysis at the same conditions of Figure 1, except a temperature 55 °C lower, results in aromatics of only up to two rings and in much lower yields. The effects of pyrolysis pressure are illustrated for various individual PAH of 3 to 10 rings in Figures 4-7. As demonstrated in these figures, PAH yields increase continuously with pressure, rising particularly dramatically at pressures above the critical pressure of 41 atm. This exponential dependence on pressure is followed by all the PAH, including those not shown in Figures 4-7. Figures 4-7 also illustrate that for a given pressure, PAH yield generally decreases as the number of rings increases—a trend demonstrated by supercritical methylcyclohexane pyrolysis and generally characteristic of pyrolytic molecular growth processes [7]. A result peculiar to high-pressure toluene pyrolysis is illustrated in Figure 4. Unlike results observed for toluene at atmospheric pressure [8], Figure 4 reveals that in the supercritical toluene experiments, yields of anthracene exceed those of its isomer phenanthrene. A similar finding is reported by Colket and Seery [9] for toluene pyrolysis at 10 atm. Both of these $C_{14}H_{10}$ PAH can result from the combination of toluene and benzyl radical, as illustrated in Figure 8 (adopted and extended from Colket and Seery [9]). The observed dominance of anthracene over phenanthrene suggests that at high pressures, union of the benzyl radical to an aryl site of toluene (top pathway of Figure 8) is preferred over union at the benzyllic site (bottom pathway). This observation on the relative yields of the $C_{14}H_{10}$ PAH illustrates the importance of pressure in determining reaction pathway.

Because toluene is both an aromatic component of jet fuel and a dehydrogenation product of the endothermic fuel methylcyclohexane, the results from the supercritical toluene experiments—the formation of very large PAH solid-deposit precursors, the extreme sensitivity of PAH yield to temperature and pressure, and the evidence that different mechanisms are governing PAH growth in supercritical environments compared to subcritical ones—are of particular importance with regard to the prevention of fuel-line fouling in high-speed aircraft.

The above results were discussed, in part, during the Principal Investigator's visit to the Wright-Patterson Air Force Research Laboratory in February, 2002.

REFERENCES

1. Edwards, T., "USAF Supercritical Hydrocarbon Fuels Interests," AIAA Paper 93-0807 (1993).
2. Wornat, M. J., Ledesma, E. B., and Marsh, N. D., "Polycyclic Aromatic Hydrocarbons from the Pyrolysis of Catechol (*ortho*-Dihydroxybenzene), a Model Fuel Representative of Entities in Tobacco, Coal, and Lignin," *Fuel* 80:1711-1726 (2001).
3. Wornat, M. J., Vernaglia, B. A., Lafleur, A. L., Plummer, E. F., Taghizadeh, K., Nelson, P. F., Li, C.-Z., Necula, A., and Scott, L. T., "Cyclopenta-Fused Polycyclic Aromatic Hydrocarbons from Brown Coal Pyrolysis," *Proceedings of the Combustion Institute* 27:1677-1686 (1998).
4. Wornat, M. J., Vriesendorp, F. J. J., Lafleur, A. L., Plummer, E. F., Necula, A., and Scott, L. T., "The Identification of New Ethynyl-Substituted and Cyclopenta-Fused Polycyclic Aromatic Hydrocarbons in the Products of Anthracene Pyrolysis," *Polycyclic Aromatic Compounds* 13: 221-240 (1999).
5. Fetzer, J. C., and Kershaw, J. R., "Identification of Large Polycyclic Aromatic Hydrocarbons in a Coal Tar Pitch," *Fuel* 74:1533-1536 (1995).
6. Lafleur, A. L., Taghizadeh, K., Howard, J. B., Anacleto, J. F., and Quilliam, M. A., "Characterization of Flame-Generated C_{10} to C_{160} Polycyclic Aromatic Hydrocarbons by Atmospheric-Pressure Chemical Ionization Mass Spectrometry with Liquid Introduction via Heated Nebulizer Interface," *Journal of the American Society of Mass Spectrometry* 7:276-286 (1996).
7. Ledesma, E. B., Marsh, N. D., Sandrowitz, A. K., and Wornat, M. J., "Global Kinetic Rate Parameters for the Formation of Polycyclic Aromatic Hydrocarbons from the Pyrolysis of Catechol," submitted to *Energy & Fuels* (2001).
8. Badger, G. M. and Spotswood, T. M., "The Formation of Aromatic Hydrocarbons at High Temperatures, Part IX. The Pyrolysis of Toluene, Ethylbenzene, Propylbenzene, and Butylbenzene," *Journal of the Chemical Society* 1960: 4420-4427 (1960).
9. Colket, M. B., and Seery, D. J., "Reaction Mechanisms for Toluene Pyrolysis," *Proceedings of the Combustion Institute* 25:883-891 (1994).

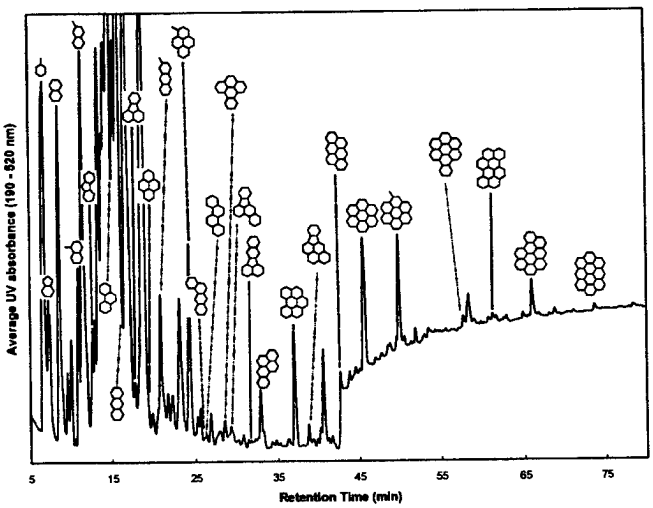

Figure 1. HPLC chromatogram of products of toluene supercritical pyrolysis at 535 °C and 100 atm. Identified components from left to right, are: toluene, indene, naphthalene, 1-methylnaphthalene, 2-methylnaphthalene, fluorene, phenanthrene, anthracene, fluoranthene, pyrene, 2-methylanthracene, 1-methylpyrene, benz[*a*]anthracene, chrysene, benzo[*e*]pyrene, benzo[*b*]fluoranthene, benzo[*k*]fluoranthene, benzo[*a*]pyrene, benzo[*ghi*]perylene, indeno[*1,2,3-cd*]pyrene, anthanthrene, coronene, 1-methylcoronene, benzo[*a*]coronene, benzo[*pqr*]naphtho[*8,1,2-bcd*]perylene, naphtho[*8,1,2-abc*]coronene, ovalene.

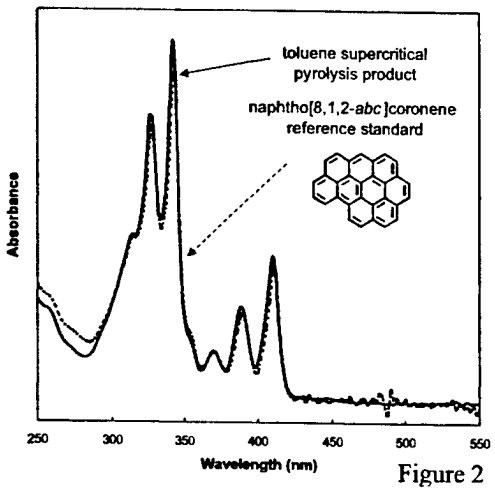

Figure 2

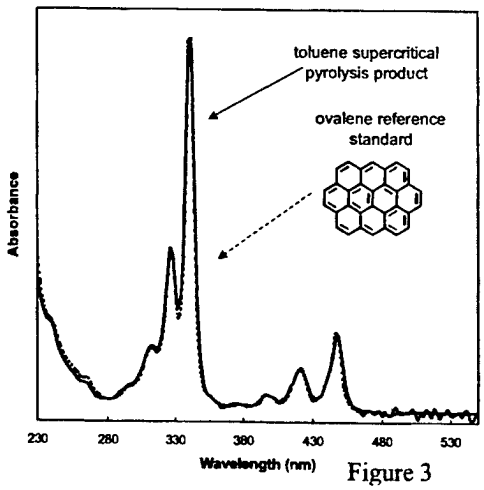

Figure 3

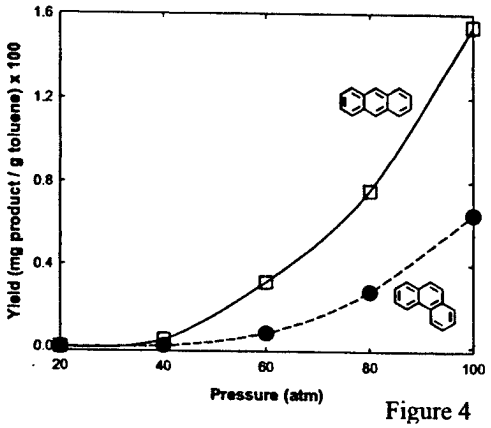

Figure 4

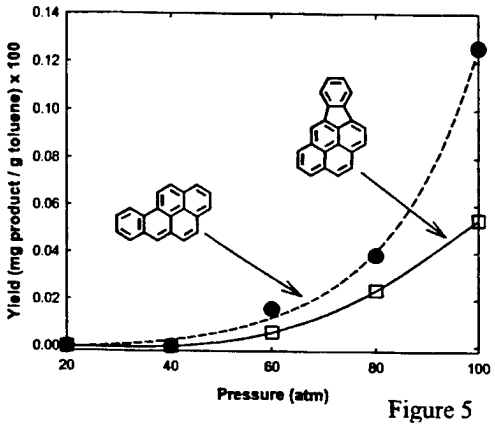

Figure 5

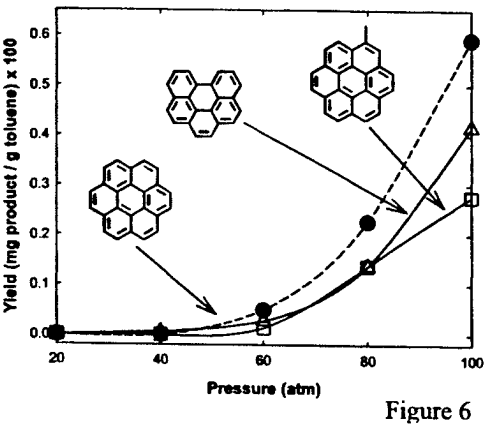

Figure 6

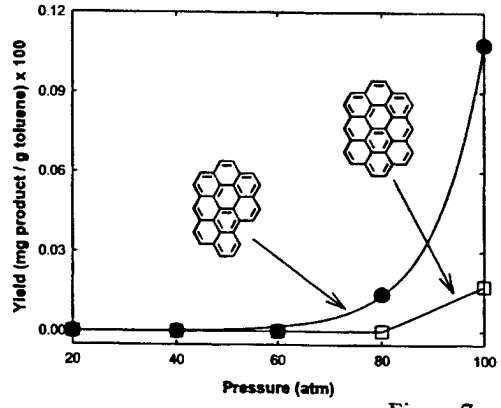

Figure 7

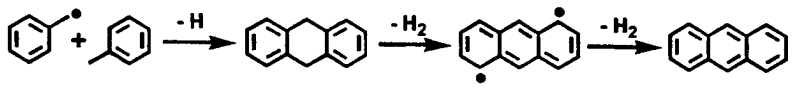

anthracene formation

Figure 8

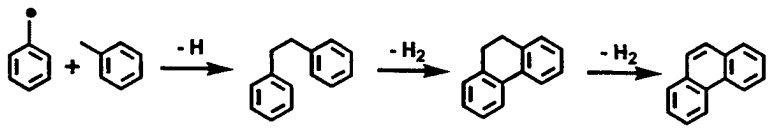

phenanthrene formation

EXPERIMENTAL AND DETAILED NUMERICAL STUDIES OF FUNDAMENTAL FLAME PROPERTIES OF GASEOUS AND LIQUID FUELS

AFOSR Grant F49620-02-1-0002

FOKION N. EGOLFOPOULOS
Department of Aerospace & Mechanical Engineering
University of Southern California
Los Angeles, California 90089-1453

Summary/Overview

The main goal of this research is to provide fundamental data on the dynamic behavior of laminar flames for a wide range of conditions. The parameters considered include the fuel type, equivalence ratio, flame temperature, pressure, and combustion mode. The experimental data will constitute a basis for partially validating the combustion chemistry of a large number of fuels ranging from hydrogen to gaseous and liquid hydrocarbons. Emphasis will be given to kinetics regimes that have not been systematically probed in past flame studies and/or in which current knowledge of combustion chemistry appears to be inadequate.

Technical Discussion

The accurate knowledge of the chemical kinetics mechanisms of hydrocarbon fuels is essential for the design of the next generation of air-breathing engines operating at speeds and altitudes that are noticeably greater compared to the ones currently achieved. State-of-the-art knowledge of hydrocarbon oxidation chemistry is limited to that of H_2 and CH_4. For example, the GRI-3.0 mechanism [1] closely predicts a wide range of flame properties for H_2 and CH_4 mixtures with air, especially at high temperatures. However, even for H_2 and CH_4 their oxidation kinetics at low temperatures have not been systematically probed in previous flame studies. The oxidation kinetics of higher carbon hydrocarbons are subjected to significant uncertainties even at the C_2-level [*e.g.* 2]. Furthermore, systematic flame studies of liquid hydrocarbons at high pressures are limited.

This research is both experimental and numerical. The experimental measurements focus on the determination of global flame properties such as laminar flame speeds and extinction strain rates, and a number of innovations are introduced. For example, while propagation and extinction are typically treated as high-temperature phenomena for hydrocarbons, their kinetics are also probed at low temperatures. This is achieved by adding small amounts of hydrocarbons to ultra-lean and/or highly diluted hydrogen flames. Such flames can be sustained at temperatures as low as 900 K, a regime of interest to hydrocarbon ignition. Such additions are expected to noticeably affect the reactivity of hydrogen flames. The experiments include gaseous as well as liquid fuels such as hydrocarbons in the C_5 to C_{12} range. Of interest will be the kinetics of such liquid fuels at high pressures for which their vapor pressures may be exceeded. To overcome this challenge, it is proposed that small amounts of liquid fuels be added to CO/air flames in order to noticeably accelerate the rate of CO oxidation. Thus, results for pressures up to 10 atm can be obtained. The final innovation includes constant flame temperature experiments for a given fuel and pressure and variable fuel concentration. This can be achieved by controlling the ratio of O_2 to N_2 in the oxidizer. Thus, any kinetics deficiencies of sufficiently off-stoichiometric mixtures are not masked behind the uncertainties associated with reduced values of global flame properties. This is the case when the flame temperature is also reduced with stoichiometry.

The experiments are performed in the opposed-jet configuration and through the use of a recently developed Correlation Image Velocimetry (CIV) technique. Laminar flame speeds, S_u^o, are determined at the point of transition from a planar to a Bunsen flame as proposed by Vagelopoulos and Egolfopoulos [3] (VE98). The use of CIV allows for the determination of the instantaneous velocity field just before the transition initiates. Thus, the instantaneous strain rate, K, and the attendant S_u^o can be *directly* measured. The extinction strain rate, K_{ext}, is also measured *directly* by reducing the fuel flow rate rather than increasing the strain rate; the latter procedure also requires extrapolations. The experiments are modeled by using detailed description of molecular transport, chemical kinetics, and thermal radiation. The chemical kinetics schemes tested include the GRI-3.0 mechanism [1] including C_1-C_3 hydrocarbon kinetics as well as a mechanism developed by Wang and coworkers [4] including C_1-C_6 hydrocarbon kinetics.

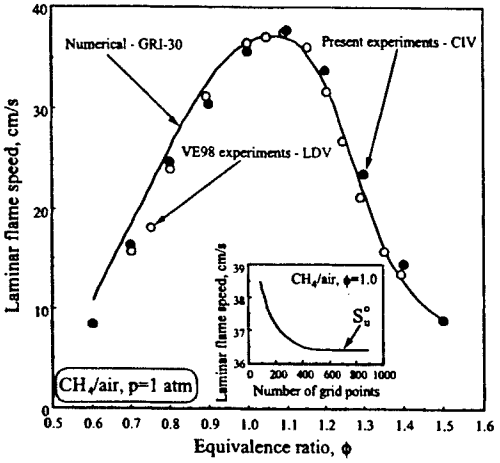

FIG. 1. Comparisons between the present experimental S_u^o data for atmospheric CH_4/air mixtures with those of VE98 and predictions using the GRI30 mechanism.

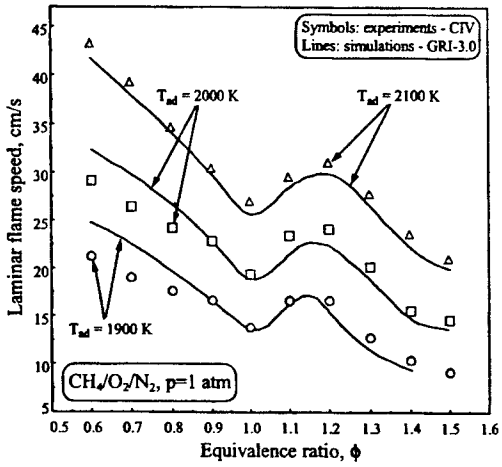

FIG. 2. Variation of experimental and predicted S_u^o with ϕ and flame temperature for atmospheric $CH_4/O_2/N_2$ mixtures.

Figure 2 compares the present S_u^o's and those determined in VE98 with LDV for CH_4/air mixtures at various ϕ's [5]. The two sets of data are in close agreement, which is an independent validation of the accuracy of the CIV-derived data. The numerically determined S_u^o's are also shown in Fig. 2 and close agreement can be seen in general; inset depicts the dependence of the predicted S_u^o on the number of grid points used in the simulations. Note, however, that there is a systematic overprediction of the experimental S_u^o's as the mixture becomes progressively leaner.

The discrepancies between experimental and predicted S_u^o for very lean mixtures have not attracted proper attention, as the observed differences of 1-2 cm/s are typically considered to lie within experimental uncertainties. This is because as ϕ decreases, S_u^o decreases as a result of the flame temperature reduction. Thus, if S_u^o is to be used for validating chemical kinetics for a wide range of ϕ's, the proper way to do it is by keeping the flame temperature constant as ϕ changes so that concentration effects are isolated from that of temperature [6].

Figure 2 depicts experimental and predicted S_u^o's for $CH_4/O_2/N_2$ mixtures as functions of ϕ, keeping the adiabatic flame temperature, T_{ad}, constant [5] by modifying the relative O_2/N_2 free-stream concentrations; T_{ad} was determined by equilibrium calculations. For all three T_{ad}'s investigated i.e. 1900, 2000, and 2100 K, S_u^o exhibits a non-monotonic behavior. For $\phi < 1$ mixtures, S_u^o increases as ϕ decreases. Species consumption and sensitivity analyses showed that as ϕ decreases the rate of the main branching reaction $H + O_2 \rightarrow OH + O$ (R1) is enhanced as the O_2 concentration increases for the same T_{ad}. For $\phi > 1$ mixtures, S_u^o first increases and then decreases as ϕ increases. S_u^o increases because the O_2 concentration increases relatively to N_2 in order to maintain the same T_{ad}. Thus, the rate of R1 is enhanced. Subsequently, the mixture reactivity is reduced as the CH_4 concentration increases to the point that it effectively scavenges H radicals through reaction $CH_4 + H \rightarrow CH_3 + H_2$ (R2) competing, thus, for H radicals with R1 whose rate is reduced. As a result the burning rate is also reduced.

Comparing the experimental and predicted S_u^o's, it can be seen that there is a close agreement for near-stoichiometric and rich flames. It is interesting, however, that while for lean flames the agreement is very close for $T_{ad} = 2100$ K, for the lower T_{ad}'s the experiments are noticeably over-predicted by the simulations. The observed discrepancies are greater than the experimental uncertainty, which has been determined to be less than 3%.

Extinction data have been and are currently derived for fuel-lean mixtures of air with H_2, CH_4, C_2H_6, C_2H_4, C_2H_2, C_3H_8, and C_3H_6 by utilizing both the symmetric, twin-flame configuration as well as the single flame configuration that results by counterflowing a mixture against an air jet. This is essential in order to maintain the K_{ext} values below approximately 550 s^{-1} that the existing CIV system can reliably measure, while varying ϕ. Thus, the twin-flame configuration is more appropriate for lower ϕ's while single-flames are can be used with higher ϕ's. Given that we have been able to *directly* measure the K_{ext} values, we largely focus on using K_{ext}'s for model validation. This is because, there is always a small but finite uncertainty associated with the determination of S_u^o's, either because of the presence of residual stretch or the need of using fitting formulas to extract S_u^o. Additionally, at ultra-low strain rates instabilities can develop on the flame surface for Le < 1 flames such as lean H_2/air. Apparently this is not the case for highly strained flames. Figures 3 through 8 depict experimental and numerical K_{ext}'s for single, lean premixed CH_4/air, C_2H_6/air, C_2H_4/air, C_2H_2/air, C_3H_8/air, and C_3H_6/air flames. The inability of the GRI-30 mechanism to predict K_{ext}'s other than CH_4 and C_2H_6 flames is apparent and in agreement with a previous study [2]. The Wang mechanism is currently tested against the C_2H_2/air, C_3H_8/air, and C_3H_6/air data.

REFERENCES

1. Bowman, C.T., Frenklach, M., Gardiner, W.R. & Smith, G. 1999 "The GRI 3.0 Chemical Kinetic Mechanism." http://www.me.berkeley.edu/gri_mech/.
2. Egolfopoulos, F.N., & Dimotakis, P.E., *Combust. Sci. Tech.* **162**, pp. 19-36, (2001).
3. Vagelopoulos, C.M. & Egolfopoulos, F.N. *Proc. Combust. Inst.* **27**: 513-519 (1998).
4. Wang, H., Personal Communications (2002).
5. Dong, Y., Vagelopoulos, C.M., Spedding, G.R. & Egolfopoulos, F.N. *Proc. Combust. Inst.* **29**, in press (2002).
6. Zhu, D.L., Egolfopoulos, F.N. & Law, C.K. *Proc. Combust. Inst.* **22**: 1537-1545 (1988).

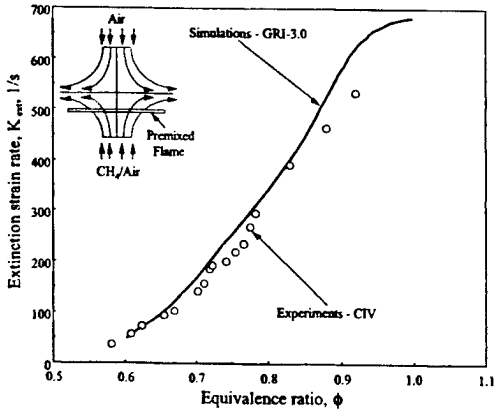

Fig. 3. K_{ext}'s for single CH_4/air flames

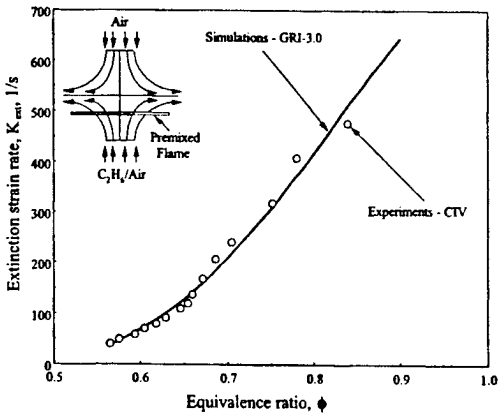

Fig. 4. K_{ext}'s for single C_2H_6/air flames

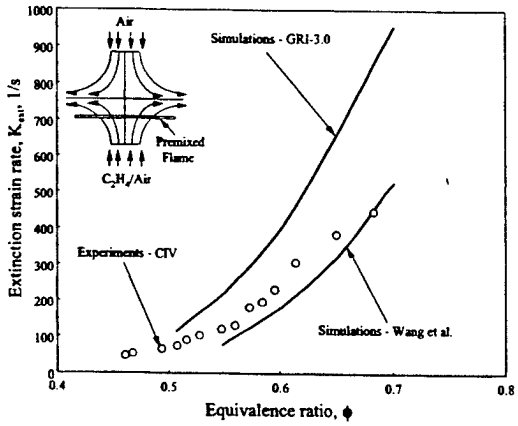

Fig. 5. K_{ext}'s for single C_2H_4/air flames

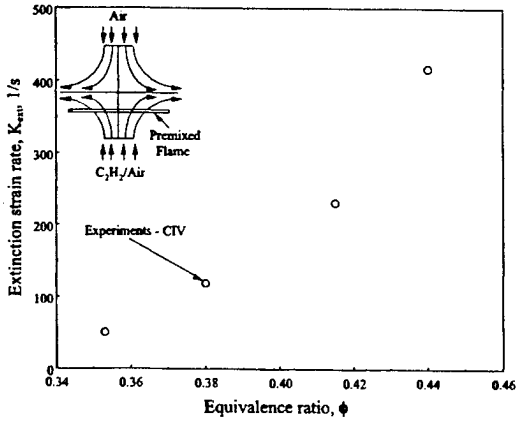

Fig. 6. K_{ext}'s for single C_2H_2/air flames

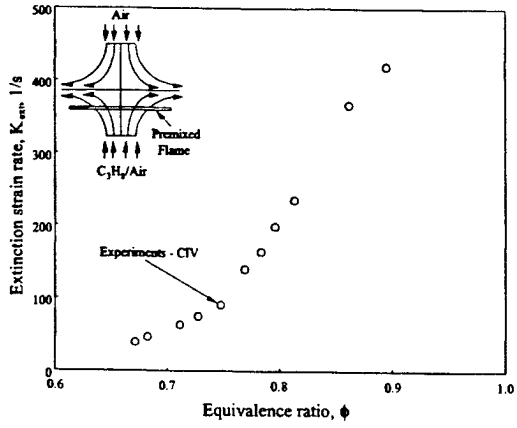

Fig. 7. K_{ext}'s for single C_3H_8/air flames

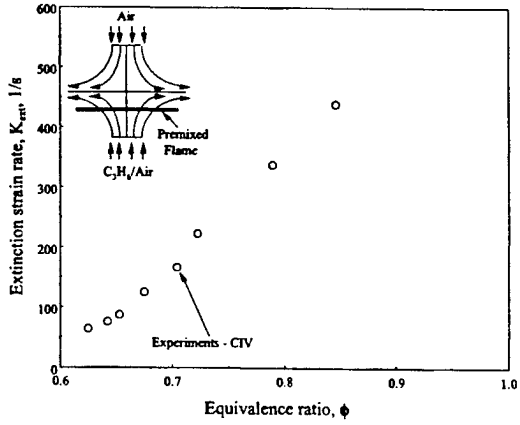

Fig. 8. K_{ext}'s for single C_3H_6/air flames

DEVELOPMENT AND OPTIMIZATION OF A COMPREHENSIVE KINETIC MODEL OF HYDROCARBON FUEL COMBUSTION

(Grant/Contract Number F49620-01-1-0144)

Principal Investigator: Hai Wang

Department of Mechanical Engineering
University of Delaware, Newark, DE 19716

SUMMARY/OVERVIEW

The objective of this research program is to develop a comprehensive, predictive, and detailed kinetic model of hydrocarbon combustion for aeropropulsion simulations. During the reporting period progress has been made in a number of areas, including (1) a first-principle calculation for the diffusion coefficients of H-He, H_2-He, H-H_2, and H-Ar, (2) a round of complete revision of a comprehensive mechanism for C_1-C_4 fuel combustion developed over the last four years, (3) the development of a new response surface method for mechanism optimization. The three projects represent the two key ingredients that are necessary for the success of the overall research program: (a) an accurate physico-chemical property database for combustion kinetics, and (b) a unified and optimized kinetic model for higher aliphatic and aromatic fuel combustion.

TECHNICAL DISCUSSION

1. A First-Principle Calculation for the Diffusion Coefficients of H-He, H_2-He, H-H_2, and H-Ar

Recently, Law and coworkers reported the laminar flame speeds of H_2-O_2-He mixtures in the pressure range of 1 to 20 atm. They showed that the flame speeds were severely over-predicted using the chemical reaction model of Mueller *et al.* and the SANDIA transport database, and the discrepancy becomes larger at higher pressures. Our sensitivity analysis showed that the laminar flame speed is sensitive not only to key reaction rate parameters, but it is equally sensitive to the binary diffusion coefficients of pairs like H-He, H-H_2, and H_2-He.

Prompted by the above study, we undertook the present work with the aim of providing more accurate binary diffusion coefficients for pairs important to the H_2-O_2-He flames. We carried out first-principle calculations for the diffusion coefficients of H-He, He-H_2, and H-H_2, over a wide temperature range. A similar calculation was performed for the diffusion coefficient of H-Ar.

Chapman-Enskog theory was used to obtain the binary, atom-atom diffusion coefficients in terms of the collision integral. The collision integrals were directly calculated by numerical integration using the literature potential functions for H-He and H-Ar. Second-order correction to the diffusion coefficient was made. For He-H_2 and H-H_2, we considered the influence of internal degrees of freedom on the scattering process and consequently the diffusion coefficients. The scattering problem was solved using the Close-Coupling method, which transforms the time-independent Schrödinger equation into a set of coupled second-order differential equations. These equations were integrated to obtain the scattering *S*-matrix. The energy-dependent cross-sections were then calculated from the *S*-matrix elements, and the diffusion cross-section was

obtained by thermally averaging the energy-dependent cross-sections with a Boltzmann weighting factor and summing the contribution from each rotational transition.

Literature potential energy functions were carefully evaluated against various cross section data from molecular beam experiments and against our own quantum chemical CCSD(T)/aug-cc-PV*Z calculations. Reliable potential energy functions were then chosen for the computation of diffusion coefficients. Table 1 presents the diffusion coefficients, computed for H-He, H-Ar, and $H-H_2$ and compared to data directly measured for these pairs. The computed diffusion coefficients were found to be in good agreement with the data. Figures 1-3 show comparisons of the present calculations with those predicted by the Sandia TRANFIT and DRFM compilations. It is seen that the DRFM and TRANFIT predictions differ markedly from our first-principle results at high temperatures.

Using the H-He, $He-H_2$, and $H-H_2$ diffusion coefficients calculated above, we recomputed the flame speeds of H_2-O_2-He mixtures. The flame speeds were compared to the experimental data of Law and coworkers and those computed using the Sandia TRANFIT database. Figure 4 shows that no improvements were made for the prediction using the new diffusion coefficients. However, the remaining uncertainty can now be safely attributed to reaction kinetics.

Our study demonstrated that a semi-empirical approach to estimate the diffusion coefficient used by the TRANFIT and DRFM packages might not be adequate for a quantitative prediction of basic flame properties such as the laminar flame speed. Rather, the diffusion coefficients of many key pairs will have to be closely examined, case by case, to ensure the accuracy of these coefficients at high temperatures. The above results are reported in Refs. 1 and 2.

2. Revision of a Comprehensive Mechanism for C_1-C_4 Fuel Combustion

The work just discussed convinced us that there is a critical need at this time to re-evaluate the kinetic pathways and reaction rate parameters in our C_2-C_4 fuel combustion mechanism. The project described in this section was motivated by the concern that a reaction mechanism capable of predicting the combustion properties of hydrocarbon fuels must also be able to predict the most basic hydrogen combustion data. In addition, much of hydrogen and C_{1-2} chemistry in our existing reaction mechanism was based on the GRI-Mech. Some of the kinetic parameters used in the GRI-Mech is becoming outdated as a wealth of new kinetic and thermochemical data have been made available in recent years. For this reason, we carried out a comprehensive review and evaluation of recent literature kinetic data. A significant portion of the reaction mechanism has been updated. A new version of the reaction mechanism will be made available shortly.

3. Development Of a New Response Surface Method for Mechanism Optimization

The optimization of a large reaction mechanism requires the minimization of an objective function given by the least squares differences of the computed and experimental flame responses. During minimization, thousands of least squares calculations are required. Direct flame solution to obtain flame response renders the optimization expansive and in most cases, prohibitive. To solve this problem, solution mapping was developed and used, for example, in the optimization of the GRI-Mech. In this method, a kinetic response surface is developed for each optimization target η, which expresses the target value as a simple function of reaction rate parameters. Usually, this response surface is expressed as a second-order polynomial,

$$\eta = a_0 + \sum_i^L a_i x_i + \sum_i^L \sum_{j \geq i}^L a_{ij} x_i x_j , \qquad (1)$$

where L is the number of active rate parameters in that target, and x is the rate parameter k normalized by the uncertainty factor f, $x=\ln(k/k_0)/\ln(f)$, so when $x=0$, k is equal to the base rate parameter, k_0. Coefficients a were usually evaluated by regression of a factorial test. The

factorial design method may become prohibitively expansive when L is large. The full factorial design requires 2^L+2L+1 numerical experiments. Fractional factorial design reduces the number of required numerical experiments at the expense of accuracy. For a flame-speed response surface with L=13, a $2^{13-4}+2\times13+1$ fractional factorial design requires 539 flame speed computations Therefore the development of response surfaces for flame speed can be a formidable task, and is usually a time hindrance during model optimization.

We developed a new method which is capable of producing a response surface at better than 1/10 of CPU cost with an accuracy which is comparable, if not better than, that from a factorial design analysis. This method is based on local sensitivity coefficients readily obtainable from available flame codes. Specifically, a combustion response was expanded about $\mathbf{x}$=0. Comparing the terms in the Taylor expansion with eq. (1), we obtained expressions directly relating coefficients a_i with the first-order sensitivity coefficients, and a_{ij} with the second-order sensitivity coefficients, which were obtained by finite differencing the first-order sensitivity coefficients. The method proposed herein requires only $2L+1$ local sensitivity calculations, compared to $2^{L-M}+2L+1$ flame computations. Furthermore, these calculations also yield the third-order x_i^3 and $x_i^2x_j$ terms.

Table 1 presents a comparison of the CPU costs and the mean, RMS, and maximum errors of representative response surfaces obtained by the sensitivity method and by fractional factorial design. It is seen that our sensitivity method yields 95 and 99% CPU savings for the two sample cases, yet the quality of the response surfaces is as good as those obtained with the factorial design method. Figure 5 presents a 45° angle diagonal plot of flame speeds predicted by response surfaces versus those from computational experiments. It is seen that the quality of the response surface obtained by the sensitivity method is excellent.

An automated computational code was developed for response surface analysis. The utility of this computational tool is obvious, in that it could reduce months of time devoted to response surface construction during mechanism optimization to a matter of few days.

PUBLICATIONS AND CONFERENCE PRESENTATIONS (May 2001 – April 2002)

1. Middha, P., Yang, B., and Wang, H. "A first-principle calculation of the binary diffusion coefficients pertinent to kinetic modeling of hydrogen-oxygen-helium flames," *Proceedings of the Combustion Institute*, in press.
2. Yang, B., Middha, P. and Wang, H. "A theoretical study of binary diffusion coefficients of H-He and H-Ar at high temperatures," in *Chemical and Physical Processes of Combustion*, 2001 Fall Technical Meeting of the Eastern States Section of the Combustion Institute, Hilton Head, SC, December 2001, pp. 202-205.
3. Hirasawa, T., Sung, C. J., Joshí, A., Yang, Z., Wang, H. and Law, C. K. "Determination of laminar flame speeds of fuel blends using digital particle image velocimetry: ethylene, *n*-butane, and toluene flames," *Proceedings of the Combustion Institute*, in press.
4. Wang, H. "A new mechanism for initiation of free-radical chain reactions during high-temperature, homogeneous oxidation of unsaturated hydrocarbons: ethylene, propyne, and allene," *International Journal of Chemical Kinetics* **33**, pp. 698-706 (2001).
5. Law, C. K., Sung, C. J., Wang, H. and Lu, T. F. "On the development of detailed and reduced chemical reaction mechanisms for aeropropulsion modeling," *40th AIAA Aerospace Sciences Meeting and Exhibit*, Reno, Nevada, January 14-17, 2002, paper AIAA-2002-0331.
6. Davis, S. G., Wang, H. and Tsang, W. "A theoretical study of the reactions on the C_2H_3O potential energy surfaces: kinetics of C_2H_2+OH → products and the unimolecular dissociation of the vinoxy radical," Fifth International Conference on Chemical Kinetics, Gaithersburg, MD, July, 2001.

Table 1. Comparison of experimental and computed diffusion coefficients (cm^2/s) at 298 K and 1 atm.

Pair	Computed	Experimental	Pair	Computed	Experimental
H-He	2.22	$2.2 \pm 0.1, 2.7 \pm 0.1, 2.9 \pm 0.7$	H-Ar	1.35	$1.4 \pm 0.2, 1.4 \pm 0.1, 1.3 \pm 0.2,$
$H-H_2$	2.15	$2.1 \pm 0.1, 2.4 \pm 0.3, 2.2 \pm 0.2$			$1.5 \pm 0.3, 1.61 \pm 0.4$

Table 2. CPUs and absolute errors (cm/s) of sample flame-speed response surfaces.

	methane-air $\phi = 0.98, L = 10$		propane-air $\phi = 1.2, L = 13$	
Method[a]	1	2	1	2
Number[b] of runs	21(S)	85(F)	27(S)	539(F)
Relative CPU	0.05	1.00	0.01	1.00
Mean error	0.2	0.3	0.5	0.3
RMS error	0.2	0.3	0.6	0.3
Maximum error	0.5	0.7	1.0	0.9

[a] (1) sensitivity method; (2) 2^{L-4} fractional factorial design. [b] "F" denotes the number of flame calculations. "S" denotes the number of sensitivity runs.

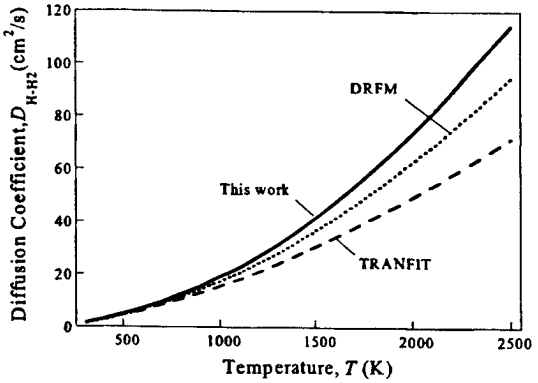

Figure 2. Comparison of $H-H_2$ diffusion coefficient computed in the present work with those predicted by Sandia TRANFIT and DRFM.

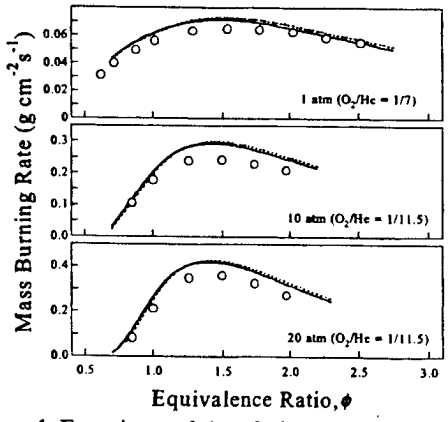

Figure 4. Experimental (symbols, Law and coworkers) and computed mass burning rate of H_2-O_2-He mixtures. Solid lines: computed with the Sandia TRANFIT database; dotted lines: computed with the diffusion coefficients of the present study.

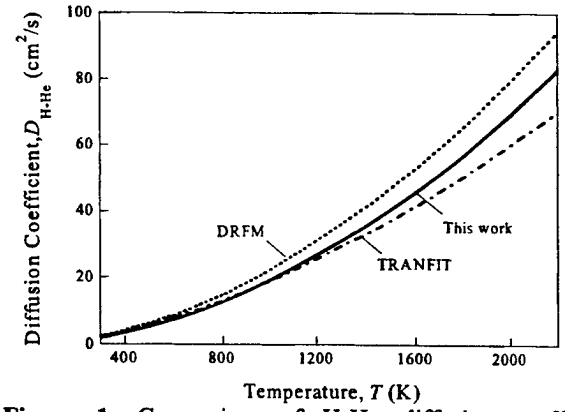

Figure 1. Comparison of H-He diffusion coefficient computed in the present work with those predicted by Sandia TRANFIT and DRFM.

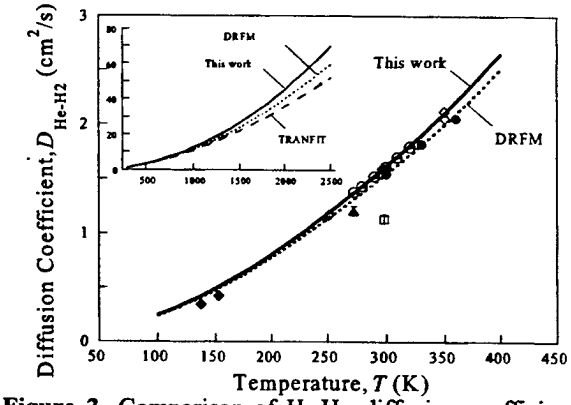

Figure 3. Comparison of H_2-He diffusion coefficient computed in the present work with experimental data and those predicted by Sandia TRANFIT and DRFM.

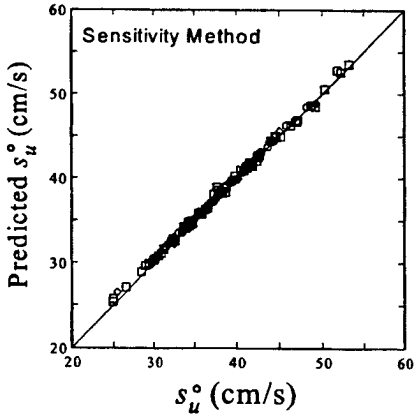

Figure 5. 45° angle diagonal plots of methane-air flame speeds (ϕ = 0.98) predicted by the response surfaces as a function of the flame speed values obtained from computational experiments.

THE CHEMISTRY CONTROLLING IGNITION OF HYDROCARBONS AND THEIR MIXTURES AT HIGH PRESSURES

Contract No. DAAG55-98-1-0286; 37699-EG
AASERT Award DAAG55-97-1-0196; 36910-EG-AAS

David L. Miller and Nicholas P. Cernansky

Department of Mechanical Engineering and Mechanics
Drexel University, Philadelphia, PA 19104

SUMMARY/OVERVIEW:

This research program investigates the chemistry controlling ignition of hydrocarbons and their mixtures at elevated pressures. The objective of this program is the development of kinetic and mechanistic information in the low and intermediate temperature regime (600-1000 K) at pressures up to 20 atm. These reaction conditions are representative of actual engine conditions prior to and during the ignition process. The methodology is to perform bench scale tests to generate reactivity maps and species evolution profiles for single component pure fuels; 2, 3, and 4 component mixtures of pure fuels; and full boiling range fuels. Results from these studies are being used to provide kinetic and mechanistic information, to formulate hypotheses on autoignition mechanisms, to determine the relative effects of the various classes of components within multi-component fuel mixtures, and to build combustion models that can be used in the design and evaluation of engine systems.

TECHNICAL DISCUSSION:

Recent efforts focused on four research areas, the first was the identification of the intermediate oxidation species of 1-pentene, n-heptane, iso-octane, toluene, and their mixture in the Pressurized Flow Reactor (PFR) at Drexel University. The second was the identification of negative temperature coefficient (NTC) behavior for representative distillate fuel components, including: n-dodecane, isocetane, methylcyclohexane, decalin, α-methylnaphthalene, and hexylbenzene. The third was the development of a chemical surrogate that closely matches the reactivity and ignition behavior of JP-8. The fourth was the continued refinement of a technique for the measurement of reactive radicals using Magneto-Optic Rotation (MOR) coupled to Cavity Ringdown Laser Absorption Spectroscopy (CRLAS).

ISF Surrogate Studies – Previously, we had shown that a blend of iso-octane, n-heptane, 1-pentene, and toluene, dubbed RON 92, exhibited a NTC behavior similar to that of more complicated Industry Standard Fuels (ISFs) and to the military standard fuel, JP-8. The NTC behavior occurs when the reactivity of a hydrocarbon species decreases with increasing temperature, something contrary to intuition. It can be characterized utilizing a CO reactivity mapping technique. Recent work focused on detailed speciation of the intermediates formed by the ISF surrogate, RON 92. Each of RON 92's components and the mixture were oxidized in the PFR. Two types of experiments were conducted for each fuel, Controlled Cool Down (CCD) and Constant Inlet Temperature (CIT). The CCD experiment generates a CO reactivity map and

the behavior of intermediate species over a range of temperatures, nominally 600 to 800 K. The CIT experiments allow for the examination of the behavior of intermediate species over a range of reaction times at a given temperature. For each experiment 15 gas samples were extracted from the reaction zone and rapidly quenched, the intermediate species were then identified using a Gas Chromatograph (GC) coupled to a Mass Spectrometer or quantified using a GC with a Flame Ionization Detector. Currently, identification of the major intermediate species has been completed. Species quantification for both CIT and CCD experiments is underway.

During the oxidation of n-heptane (99+% HPLC Grade), a clear NTC behavior was observed at 8 atm, equivalence ratio of 0.4, nitrogen dilution of 85%, and residence time of 100 ms. The temperature at which the reactivity peaked, referred to as the start of NTC, occurred at 705 K. The major species formed included: heptane, propene, 1-butene, 1-pentene, cis & trans 2-heptene, cis & trans 3-heptene, formaldehyde, acetaldehyde, 2-propenal, propanal, butanal, pentanal, 3-buten-2-one, 1-penten-3-one, methanol, and several cyclic ethers yet to be identified.

During the oxidation of 1-pentene (95%) a clear NTC behavior was observed at 8 atm, equivalence ratio of 0.6, nitrogen dilution of 70%, and residence time of 225 ms. The temperature at which the reactivity peaked was 716 K. The major species included: propene, 1,3-butadiene, 1-pentene, 2-pentene, cis & trans 1,3-pentadiene, formaldehyde, acetaldehyde, 2-propenal, propanal, 2-butenal, butanal, pentanal, 3-buten-2-one, and a few unidentified cyclic ethers.

During the oxidation of iso-octane (99.7% HPLC Grade), a weak NTC behavior was observed at 8 atm, equivalence ratio of 0.75, nitrogen dilution of 65%, and residence time of 250 ms. The temperature at which the reactivity peaked was 665 K. Several runs were conducted at this operating condition to identify the cause of this surprisingly low NTC temperature. The major species observed included: propene, 1-butene, 2,4,4-trimethyl-1-pentene, 2,4,4-trimethyl-2-pentene, formaldehyde, 2-methyl-2-propenal, 2-methyl-propanal, 2,2-dimethyl-propanal, acetone, 4,4-dimethyl-2-pentanone, and 2,2,4,4,tetramethyl-THF. All of these compounds are indicative of iso-octane oxidation, however, a definitive explanation for the low start of NTC has yet to be developed.

During the oxidation of toluene (99%), no NTC behavior was observed at 8 atm, equivalence ratio of 0.75, nitrogen dilution of 65%, and residence time of 250 ms. This operating condition is the maximum concentration at which fuel can be safely introduced. Hence, future oxidation studies of toluene will need to be conducted with a chemical initiator, such as DME.

During the oxidation of RON 92 (4.6% 1-pentene, 49.6% iso-octane, 14% n-heptane, and 31.8% toluene), a clear NTC behavior was observed at 8 atm, equivalence ratio of 0.6, nitrogen dilution of 65%, and residence time of 225 ms. The temperature at which the reactivity peaked was 695 K. The major species were: n-heptane, iso-octane, propene, 1-butene, 1-pentene, 4,4-dimethyl-1-pentene, 4,4-dimethyl-2-pentene, benzene, 2-heptene, 3-heptene, 2,4,4-trimethyl-1-pentene, 2,4,4-trimethyl-2-pentene, toluene, formaldehyde, acetaldehyde, 2-propenal, propanal, 2-methyl-2-propenal, 2-methyl-propanal, 2,2-dimethyl-propanal, butanal, pentanal, benzaldehyde, 3-buten-2-one, 4,4-dimethyl-2-pentanone, and 2,2,4,4,tetramethyl-THF.

Distillate Fuel Component Studies – In efforts with larger hydrocarbon species, the reactivity characteristics of several distillate fuel components were examined. Due to the high reactivity of these compounds, low fuel concentrations were necessary. This required updating the fuel delivery system with a high pressure syringe pump. The new system is capable of delivering flow rates between 0 to 200 ml/min in 0.001 ml/min increments and has greatly increased system

repeatability (CO mapping differences less then 5%) and decreased concentration variations during CIT and CCD experiments.

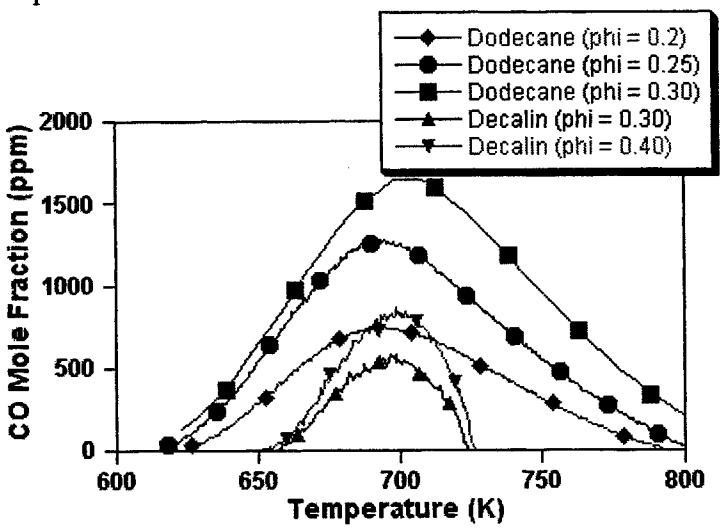

Figure 1: Reactivity map of n-dodecane and decalin.

Using the CO reactivity mapping technique, the oxidation of neat n-dodecane, isocetane, methylcyclohexane, decalin, α-methylnaphthalene, and hexylbenzene was examined at 8 atm (also 12 atm for α-methylnaphthalene) over a range of equivalence ratios and N2 dilutions. Both n-dodecane and decalin showed strong NTC behavior starting at 700 and 695 K, respectively, over all the conditions tested (Figure 1). However decalin reacted over a very narrow temperature range, approximately between 725 and 655 K, compared to the corresponding values for n-dodecane, 800 and 600 K. Methylcyclohexane either did not oxidize at lean conditions (equivalence ratio $\Phi = 0.30$, N2 dilution = 80%) or it became explosive at richer conditions ($\Phi =$ 0.70, N2 dilution = 65%), therefore, controlled oxidation of methylcyclohexane was not achievable. The other pure hydrocarbons tested (the aromatics and isocetane) were resistant to ignition, and no reactivity was observed.

JP-8 Surrogate Studies – Blends of distillate fuel components were used to develop a surrogate for JP-8. All mixtures were prepared with a Cetane Number of approximately 45, and they were oxidized at 8 atm, equivalence ratio of 0.30, nitrogen dilution of 80%, and residence time of 120 ms. A total of 3 binary, 2 ternary, and 6 larger mixtures were tested over a temperature range of 800 to 600 K and compared with the CO reactivity map of JP-8. All components, except methylcyclohexane, were blended together assuming linear blending. Methylcyclohexane behaved as if it was more reactive than the corresponding ideal linear blend and, as a result, a blended cetane number was determined using a linear correlation between the maximum CO production and the fuel (or mixture) Cetane Number. This correlation was developed and tested using the data obtained from the oxidation of both the pure hydrocarbons and binary mixtures.

The criteria used to determine the ability of each surrogate to match the reactivity map of JP-8 was the start and stop of reactivity, the start of the NTC region, the magnitude of overall reactivity, and a composition that matched JP-8's published values. Two examples of "bad" surrogates can be seen in Figure 2. The mixture that matched the JP-8 reactivity the closest was a five component mixture consisting of 26% n-dodecane, 36% isocetane, 14% methylcyclohexane, 6% decalin, and 18% α-methylnaphthalene . The reactivity map of this mixture and that of JP-8 is shown in Figure 3. During the process of developing the surrogate, a

cooperative effort to model the chemical kinetics of JP-8 and its components was begun with Politechnico di Milano (Dr. Eliseo Ranzi and Dr. Tiziano Faravelli).

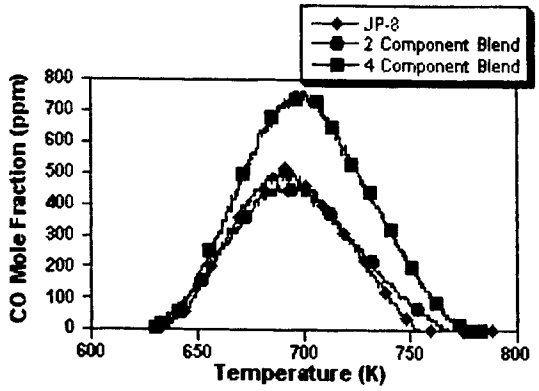

Figure 2: Reactivity map of two "bad" surrogate mixtures.

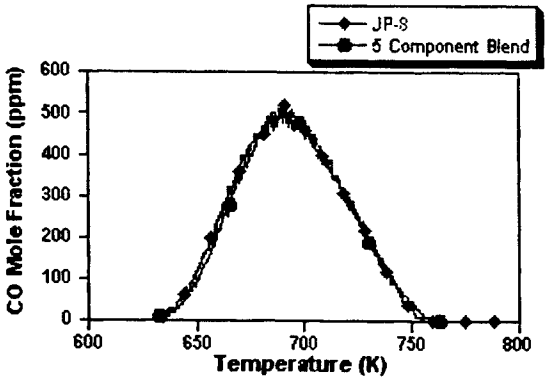

Figure 3: Reactivity map of final surrogate mixture.

Laser Diagnostics – Previously, we adapted the sensitive technique of Cavity Ringdown Laser Absorption Spectroscopy (CRLAS) and the selective technique of Magneto-Optic Rotation (MOR) to measuring highly reactive radicals in flame environments. The measurement of these unstable radical species will assist in the determination of the mechanisms that govern hydrocarbon combustion at elevated pressures. Currently, we are designing a system to use CRLAS coupled with MOR in conjunction with the PFR to measure HO2, and other reactive radicals.

We are continuing to refine combined MOR and CRLAS techniques, developing a methodology dubbed Cavity Enhanced Magneto-Optic Rotation (CEMOR). CEMOR combines the sensitivity of CRLAS with the selectivity of MOR, enabling selective detection of paramagnetic species even in extremely low concentrations. In studies performed using atomic gallium aspirated into an air-acetylene slot burner, CEMOR was shown to improve the detection limit by five orders of magnitude over standard atomic absorption. The CEMOR signal can be used for quantification of species concentration in one of two ways. The maximum intensity of the CEMOR signal was shown to have a quadratic dependence on species concentration as expected. Also, the time to maximum signal intensity can be correlated to concentration using a power curve fit. A better model of the rotation effects on signal coupled with the exponential signal decay characteristic of ringdown is necessary to clarify this time dependant behavior.

With funding from the DOD DURIP program (DAAD19-01-1-0438), we purchased a Nd:YAG pumped Optical Parametric Oscillator (OPO) laser system with a frequency doubler. The OPO is a solid state alternative to a dye laser system, and is continuously tunable from the UV (220 nm) to the near IR (1700 nm). In order to become familiar with this system and in preparation for efforts to detect HO2, we are currently using this system to study OH radical spectra in a flame in the 1380-1410 nm region. We plan to compare CRLAS and CEMOR detection sensitivities and optimize the CEMOR experimental configuration. However, high soot levels in our flame results in scattering of light within the cavity, adversely effecting ringdown, and deposition of a soot film on the ringdown mirrors, decreasing reflectivity and increasing maintenance of the cavity. To eliminate these problems, we are incorporating a graphite furnace atomizer to replace the flame. This should eliminate these effects and further increase sensitivity of the CEMOR technique.

CHEMICAL-KINETIC CHARACTERIZATION OF AUTOIGNITION AND COMBUSTION OF DIESEL AND JP-8

(Grant/Contract Number DAAD19-99-1-0259)

Principal Investigator: Dr. Kalyanasundaram Seshadri

Department of Mechanical and Aerospace Engineering
University of California at San Diego
La Jolla, California 92093

SUMMARY/OVERVIEW:

The principal objective of the research is to obtain a fundamental understanding of the mechanisms of autoignition and combustion of diesel and JP-8. Chemical-kinetic mechanisms describing autoignition and combustion of these fuels are not available. This research will address this deficiency by first developing surrogate diesel and surrogate JP-8 each preferably made up of three hydrocarbon compounds. Chemical-kinetic mechanisms will be developed for these hydrocarbon fuels. Experimental and numerical studies are in progress.

TECHNICAL DISCUSSION:

Diesel and JP-8 comprise hundreds of aliphatic and aromatic hydrocarbon compounds. The major components of these fuels are straight-chain paraffins, branched-chain paraffins, cycloparaffins, and aromatics. Detailed chemical-kinetic mechanisms describing autoignition and combustion of a number of these compounds are not available. In this research surrogate diesel and surrogate JP-8 each preferably made up of three hydrocarbon compounds will be developed. These surrogate fuels must reproduce various aspects concerning autoignition and combustion of diesel and JP-8. The aliphatic hydrocarbon fuels considered here are heptane, decane, and dodecane. The aromatic hydrocarbon considered here is toluene. Numerical and analytical studies were carried out to elucidate the extinction and autoignition characteristics of ethane (C_2H_4), ethene (C_2H_6), propene (C_3H_6), and propane (C_3H_8) in nonpremixed and premixed systems. It is of importance to obtain an improved understanding of the chemical-kinetic mechanisms of combustion of these fuels because they are considered to be subsets of chemical-kinetic mechanism of combustion of higher hydrocarbon compounds that include heptane, decane, and dodecane. An experimental and numerical study was performed to elucidate the chemical-kinetic mechanism of combustion of toluene.

Nonpremixed and Premixed Extinction and Autoignition of C_2H_4, C_2H_6, C_3H_6, and C_3H_8

Experimental studies were conducted on laminar nonpremixed and premixed flames stabilized in the counterflow configuration. The fuels tested were ethene (C_2H_4), ethane

(C_2H_6), propene (C_3H_6), and propane (C_3H_8). Studies on nonpremixed systems were carried out by injecting a fuel stream made up of fuel and nitrogen (N_2) from one duct and an oxidizer stream made up of air and N_2 from the other duct. Studies on premixed systems were carried out by injecting a premixed reactant stream made up of fuel, oxygen, and nitrogen from one duct, and an inert-gas stream of N_2 from the other duct. Critical conditions of extinction were measured by increasing the flow rates of the counterflowing streams until the flame extinguishes. Critical conditions of autoignition were measured by preheating the oxidizer stream of the nonpremixed system and the inert-gas stream of the premixed system. Experimental data for autoignition were obtained over a wide range of temperatures of the heated streams. In addition for premixed systems experimental data were obtained for a wide range of values of the equivalence ratio including fuel-lean and fuel-rich conditions. Numerical calculations were performed using a detailed chemical-kinetic mechanism and compared with measurements. This study highlights the influences of nonuniform flow field on autoignition in premixed systems that were not available from previous studies using shock tubes. For the premixed system considered in this study the changes in the strain rates at extinction with equivalence ratio were found to be similar to previous observations of changes in laminar burning velocities with equivalence ratio. The studies on autoignition in the premixed system show that the temperature of the inert-gas stream at autoignition reaches a minimum for a certain equivalence ratio. For premixed systems abrupt extinction and autoignition were not observed if the value of the equivalence ratio is less than some critical value. This critical value of the equivalence ratio was found to depend on the strain rate.

Chemical Kinetic Study of Toluene Oxidation

This study was performed in collaboration with W. J. Pitz and C. K. Westbrook from Lawrence Livermore National Laboratory, Livermore, California, J. W. Bozzelli and C.-J. Chen from New Jersey Institute of Technology, Newark, New Jersey, I. Da Costa, R. Fournet, F. Billaud, and F. Battin-Leclerc from CNRS-ENSIC, Nancy, France. The objective of this study was to elucidate the chemical-kinetic mechanism of combustion of toluene. A detailed chemical-kinetic mechanism for toluene was improved by adding a more accurate description of the phenyl + O_2 reaction channels, toluene decomposition reactions and the benzyl + O reaction. Results of the chemical kinetic mechanism were compared with experimental data obtained from premixed and nonpremixed systems. Under premixed conditions, predicted ignition delay times were compared with new experimental data obtained in shock tube. Also, calculated species concentration histories were compared to experimental flow reactor data from the literature. Under nonpremixed conditions, critical conditions of extinction and autoignition were measured in strained laminar flows in the counterflow configuration. In this configuration a fuel stream made up of prevaporized toluene and nitrogen was injected from one duct, and a mixture of oxygen and nitrogen from another duct. Numerical calculations were performed using the chemical-kinetic mechanism at conditions corresponding to those in the experiments. Critical conditions of extinction and autoignition were predicted and compared with the experimental data. Comparisons

between the model predictions and experimental results of ignition delay times in shock tube, and extinction and autoignition in nonpremixed systems show that the chemical-kinetic mechanism predicts that toluene/air is overall less reactive than observed in the experiments. For both premixed and nonpremixed systems, sensitivity analysis was used to identify the reaction rate constants that control the overall rate of oxidation in each of the systems considered. Under shock tube conditions, the reactions that influence ignition delay time were H + O_2 chain branching, the toluene decomposition reaction to give an H atom, and the toluene + H abstraction reaction. The reactions that influence autoignition in nonpremixed systems involve the benzyl + HO_2 reaction and the phenyl + O_2 reaction.

Autoignition of Heptane, Decane, and Dodecane

A new counterflow burner was built to carry out autoignition experiments on liquid hydrocarbon fuels. In this configuration a heated mixture of air and nitrogen is injected from a duct. This heated mixture flows against fuel evaporating from a liquid pool. The level of the liquid pool is accurately controlled. The temperature of the mixture of air and nitrogen is increased until autoignition takes place. The strain rate at autoignition is recorded.

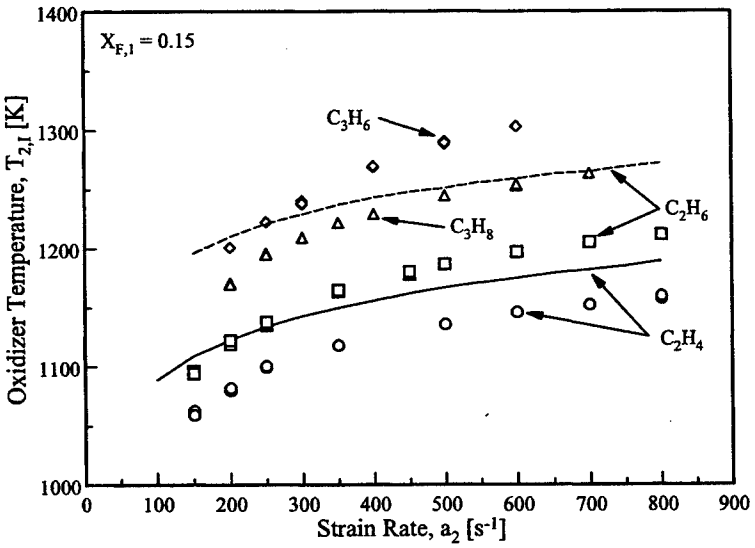

Figure 1: The oxidizer temperature at autoignition, $T_{2,I}$, as a function of the strain rate, a_2, for nonpremixed systems. The symbols represent measurements and the lines are results of numerical calculations. The oxidizer is air

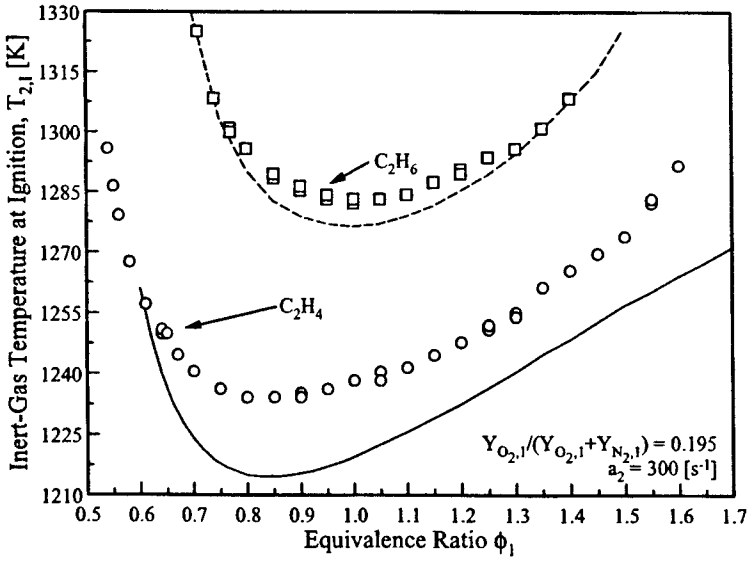

Figure 2: The temperature of the inert-gas stream at autoignition, $T_{2,\mathrm{I}}$, as a function of the equivalence ratio, ϕ_I, of the premixed reactant stream. The symbols represent measurements. The lines show results of numerical calculation. The strain rate is $300\,\mathrm{s}^{-1}$

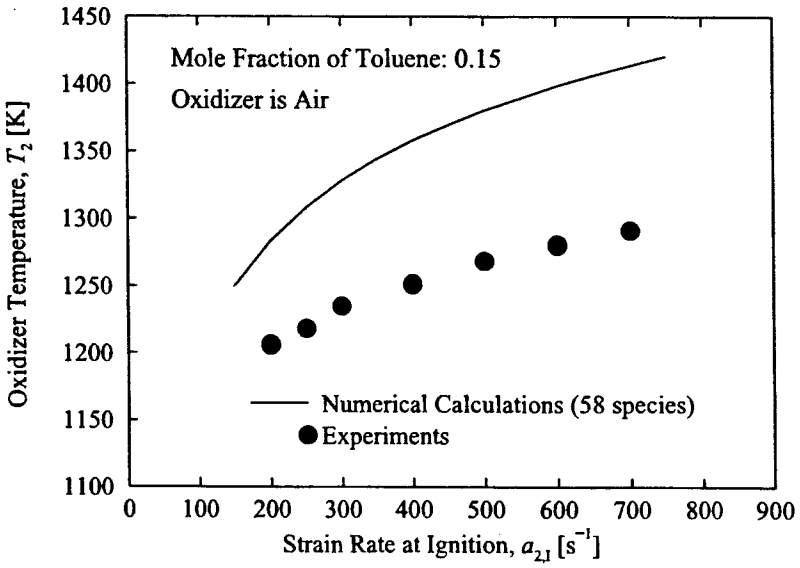

Figure 3: Oxidizer temperature at autoignition, T_2, as a function of the strain rate, $a_{2,\mathrm{I}}$. The symbols represent measurements. The solid line represents results of numerical calculations performed using a chemical-kinetic mechanism made up of 58 species.

SHOCK TUBE MEASUREMENTS OF IGNITION PROCESSES IN DIESEL-RELATED FUELS

ARO Contract No. DAAD19-01-1-0597

Principal Investigator: Ronald K. Hanson

Mechanical Engineering Department
Stanford University, Stanford CA 94305-3032

SUMMARY/OVERVIEW:

We report results from the first year of a three-year program of basic research aimed at improving knowledge of the combustion kinetics behavior of diesel-related fuels. The work is intended to support efforts underway in other laboratories to improve diesel engine performance. Research is being conducted in two Stanford shock tube facilities and focuses on two topics: (1) measurements of shock-induced ignition time and individual species concentration time-histories measurements during the combustion of diesel-related gas-phase fuels, and (2) fundamental studies of fuel sprays in a new aerosol shock tube using state-of-the-art optical diagnostic techniques.

TECHNICAL DISCUSSION:

Ignition Time and Species Concentration Time-History Measurements

Validation of hydrocarbon oxidation reaction mechanisms and development of new and improved reduced mechanisms require a reliable database of experimental combustion targets; such data are often drawn from experiments in shock tubes, flames or flow tube reactors. Though a limited amount of shock tube ignition time data presently exists for some fuels, these data exhibit substantial scatter and are of varying reliability. By contrast, data for stable species in flames or bench-top reactors have often been used to tune reaction mechanisms, but little or no data is available on transient radical species, such as OH or CH_3, that play an important role in ignition processes. To help remedy these deficiencies, we are currently working to establish a new database of ignition time and species (minor and major) concentration time-history measurements to be acquired in shock tube studies of the major components of practical fuels and for surrogate fuel mixtures [1-4]. This database will include studies of fuel components such as n-alkanes, branched alkanes, alkenes, aromatics, and diesel surrogate mixtures.

Thus far, we have measured shock tube ignition times for four n-alkanes, namely propane, n-butane, n-heptane and n-decane, and two branched alkanes, iso-octane and iso-butane. These ignition time delays were measured behind reflected shock waves over the temperature range of 1200–1700 K, pressure range of 1-6 atm, fuel concentration 100 ppm to 1%, and stoichiometric ratios of 0.25 to 2.0. Ignition delay times were measured through the shock tube endwall using CH emission at 431 nm. A parametric study of the n-alkane

experimental data reveals marked similarity of the ignition delay time characteristics among these four n-alkanes, and a correlation was developed in which the stoichiometric ignition time data for all four n-alkanes could be described in a single expression. Comparisons to past ignition time studies further validated this correlation.

OH radical concentration time histories were measured behind reflected shock waves in n-alkane/O_2/Ar and branched alkane/O_2/Ar mixtures. OH concentrations were measured using narrow-linewidth ring-dye laser absorption of the $R_1(5)$ line of the OH A-X (0,0) band at 306.5 nm. These OH concentration time history measurements were compared to model predictions performed with current detailed oxidation mechanisms. In the iso-octane mixtures, the rapid formation of OH coincident with the decomposition of iso-octane is evident in the first 10 μs, but the OH radicals are then rapidly scavenged and the intermediate plateau concentrations of OH are far lower than found, for example, in n-heptane mixtures. See Fig. 1. To our knowledge, these data provide the first extensive measurements of ignition times and OH concentration time histories for low-concentration iso-octane auto-ignition, and hence provide a critical contribution to the database needed for validation of a detailed mechanism for this primary reference fuel.

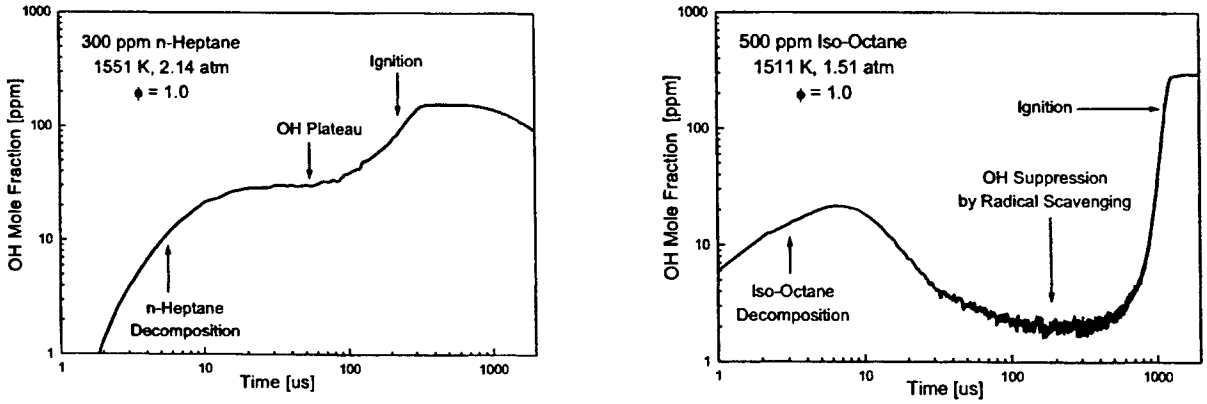

Figure 1. OH concentration time histories in these experiments were measured using narrow-linewidth ring-dye laser absorption at 306.5 nm in a shock tube. The OH concentration plateau is suppressed before ignition in the iso-octane experiments, but not in the n-heptane experiments.

Shock Tube Studies of Fuel Sprays

We have begun the study of two-phase flows in shock tubes.

Liquid fuels are predominant in mobile energy-conversion systems such as gas turbine combustors and internal combustion engines. While previous researchers have studied combustible sprays in shock tubes to learn about droplet breakup, evaporation, and ignition times, these studies generally have applied commercial injectors with wide droplet size distributions and relatively large droplets. Since the combustion of a two-phase mixture is strongly dependent on size-dependent droplet heating and evaporation rates, the results have largely been qualitative in nature, confused by the droplet size distribution, or quantitative only in specific situations. The objective in this aspect of our shock tube kinetics research is to

establish a method that produces a two-phase mixture with a narrow size distribution so that the behavior of droplets of a specific size class can be studied independently in a shock tube.

A survey of the literature demonstrated that a number of techniques are available to create monodisperse sprays. For the size of droplets that we are most interested in, 1-20 microns in diameter, condensation of droplets from a vapor appears to be the most promising technique. We have built a small spray/shock wave interaction facility (See Fig. 2) and are exploring various methods of aerosol formation including one based on vapor cooling using liquid nitrogen. We plan to inject a variety of aerosol/gas phase mixtures, both non-reactive and reactive, to with a goal of achieving a spatially uniform distribution in a test section adjacent to the reflected end of our shock tube. Subsequently, experiments will examine aerosol behavior over a wide range of shock strengths and initial conditions. This experimental format should permit study of the full range of spray/shock interactions from simple evaporation, through ignition, to detonation. Parallel to this, laser diagnostics will be developed to measure droplet size and loading, fuel vapor concentration, temperature, transient species concentration time-histories, and to image reactive flow structures (e.g., detonation waves). The first shock tube experiments will employ multi-wavelength, tunable diode lasers and fixed-frequency HeNe (632.8 nm and 3.39 μm) lasers for absorption and extinction measurements. Thus far we have observed the evaporation of an H_2O aerosol (r_{v50} = 2.7 μm, 10 ppm by volume) in a nitrogen bath gas behind M_s =1.6 shocks.

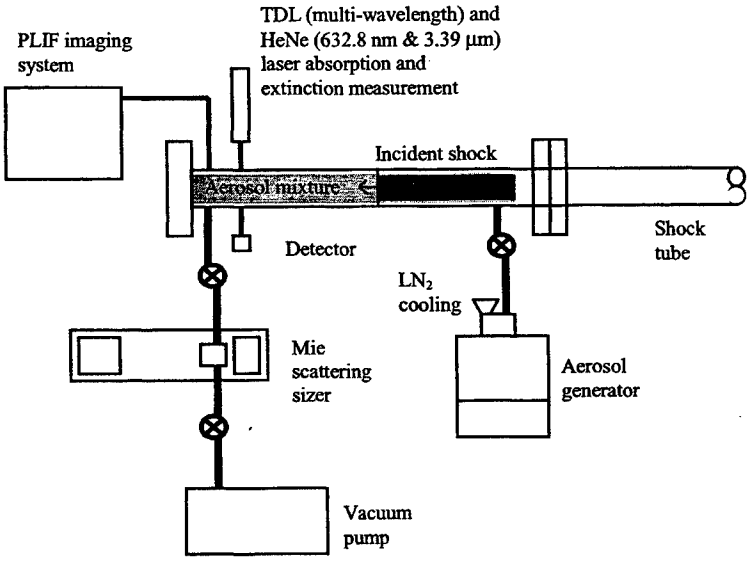

Figure 2. Aerosol spray/shock wave interaction facility.

ARO-SPONSORED PUBLICATIONS:

1. D. F. Davidson, M. A. Oehlschlaeger, J. T. Herbon, and R. K. Hanson, "Shock Tube Measurements of Iso-Octane Ignition Times and OH Concentration Time Histories," *Proceedings of the Combustion Institute* **29,** in press.
2. D. C. Horning, D. F. Davidson, and R. K. Hanson, "Study of the High-Temperature Autoignition of n-Alkane/O2/Ar Mixtures," *Journal of Propulsion and Power* **18**, 363-371 (2002).
3. D. C. Horning, D. F. Davidson, and R. K. Hanson, "Ignition Time Correlations for n-Alkane/O_2/Ar Mixtures," *Proceedings of the Symposium on Shock Waves* **23**, Texas (2001).
4. D. C. Horning, D. F. Davidson, and R. K. Hanson, "Shock Tube Study of the High-Temperature Thermal Decomposition of n-Alkanes," *Proceedings of the Symposium on Shock Waves* **23**, Texas (2001).

Autoignition and Burning Speeds of JP-8 Fuel at High Temperatures and Pressures

Grant No. DAAD19-01-1-0587
Hameed Metghalchi

Mechanical, Industrial and Manufacturing Engineering,
Northeastern University,
Boston, Massachusetts 02115

Summary

An experimental facility has been built to measure burning speed and study autoignition of JP-8 fuel at high temperatures and pressures. It includes two combustion chambers, spherical and cylindrical, optical set up and also a high temperature oven. Burning speed of fuel-oxidizer-diluent mixture is determined form the pressure rise during a combustion process using a thermodynamic model based on the conservation of mass and energy.

Technical Discussion

The experimental facility consists of two combustion chambers (spherical and cylindrical), charging apparatus and a data acquisition system. The cylindrical combustion chamber has been used to visualize the flame and investigate the existence of structural instabilities. The spherical chamber consists of two hemispheric heads made from SAE 4140 alloy steel that are bolted together to make a 15.24 cm (6 inch) inner diameter sphere [1]. The chamber is designed to withstand pressures up to 425 atm. The cylindrical chamber has been designed to be as nearly identical as possible to the spherical chamber, with an aspect ratio of one. The inner diameter of the cylindrical chamber is 13.33 cm (5.25 inch) [2]. Windows with 15.24 cm (6 inch) diameter are mounted in the end caps of the cylindrical chamber to provide optical observation of the flame using shadowgraph technique. A high speed CCD digital video camera, with variable speeds of up to 8000 frames/second, is used for flame visualization.

The chamber can be heated to 500 K in an oven. Thermocouples mounted at several locations are used to monitor the exterior temperature of the chamber and a thermocouple inserted through one of the chamber ports is used to check the initial temperature of the gas inside the chamber.

The theoretical model used to calculate burning velocity from the pressure rise in a constant volume chamber is based on one previously developed by Metghalchi and Keck [3] and [4] with some modifications [5], [6]. In this model, gases in the chamber are divided into three parts as shown in Figure 1. The first is the burned gas in the center of chamber, the second is the uniform temperature unburned gas around the burned gas, and the third is the portion of unburned gas contained in the thermal boundary layer at the wall, which conducts energy to the chamber wall, where temperature is a function of location and time. The temperature distribution throughout the gas has been shown in Figure 1 at two different times. It is assumed that:

The flame thickness is negligible for a flame radius greater than two or three centimeters. This condition will be achieved by the time that pressure begins to rise. Figure 2 shows the normalized flame thickness for lean methane-air mixture. In Figure 2 the mixture was initially at five atmosphere pressure, 5% diluent and equivalence ratio of 0.8. Flame front thickness can be calculated by using the Rallis and Garforth [7] derivation. It can be observed from Figure 2 that for radii larger than 2-3 cm the ratio of flame thickness to flame radius is negligible (on the order of 10^{-4}) and consequently the stretch corrections are small. As the pressure increases the flame thickness decreases and this ratio will be even smaller at large radii.

The flame front is smooth and spherical.

The burned and unburned gases are ideal gases.

The core unburned gas in the chamber is compressed isentropically from its initial condition.

The burned gases are divided into shells in which the temperature is uniform in each shell, but varies from shell to shell. Number of shells is proportional to combustion duration. A new shell is developed for every millisecond. Combustion duration varies between 50 to 150 milliseconds. The gases in each shell are assumed to be in chemical equilibrium and isentropically compressed as the pressure rises. As a result of this isentropic compression, gas temperature in each shell increases as flame propagates.

The burning speed is calculated by the equation

$$S_u = m\, \mathrm{v}_u \dot{x} / A_f \qquad (1)$$

Where S_u is burning speed, m is the mass of the gas mixture in the chamber, v_u is the specific volume of the unburned gas, $\dot{x}$ is the mass fraction burning rate and A_f is the flame area. The mass of the gas mixture is determined from the measured initial composition, temperature, and pressure. Properties of the unburned gas such as specific internal energy and

specific volume are determined using the JANAF Tables and pressure measurements. The properties of the burned gases are determined using the JANAF Tables and the STANJAN equilibrium code. Using the volume and energy equations, temperature and mass fraction of burned gas are determined iteratively:

$$\frac{V}{m} = \int_0^x v_b dx'' + \int_x^{x'} v_{u_s} dx'' + \int_{x'}^1 v_{b.l.} dx'' \qquad (2)$$

$$\frac{E}{m} - \frac{Q}{m} = \int_0^x e_b dx'' + \int_x^{x'} e_{u_s} dx'' + \int_{x'}^1 e_{b.l.} dx'' \quad (3)$$

Using this model burning speeds have been calculated for methane-air-diluent mixtures. The predictions of the GRI-Mech 3.0 model have been compared with flame speed measurements made in the spherical chamber for a wide range of conditions spanning both the high and low temperature regimes. The data used were limited to cases where corrections for stretch and curvature were negligible, i.e. flame radius much greater than flame thickness. The conditions under which significant "cracking" or wrinkling occurred, were observed and are reported.

Figure 3 shows a comparison between measured and calculated values of the burning speeds for stoichiometric methane-air mixtures at 1 atm pressure vs. unburned gas temperature. It can be seen that for these conditions, which are in the high temperature regime, the PREMIX calculations are in excellent agreement with results of this study. Previously measured values reported by Kurata et al. [8], Iijima et al. [9] and Sharma et al. [10] and Gottgens et al. [11] are also shown.

Figure 4 shows the burning speeds along isentropes for stoichiometric methane-air-diluent mixtures with initial pressures of 1 atm and diluent of 0-15%. Again the agreement is good with PREMIX calculations. Also in this figure the values of power law fit to the experimental data have been shown along with the actual data.

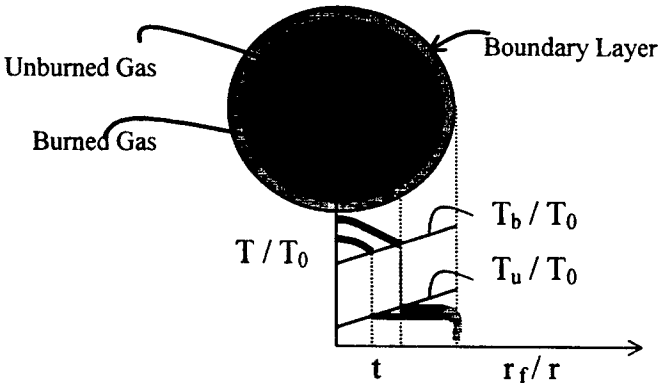

Figure 1. Three different regions of gas in the combustion chamber.

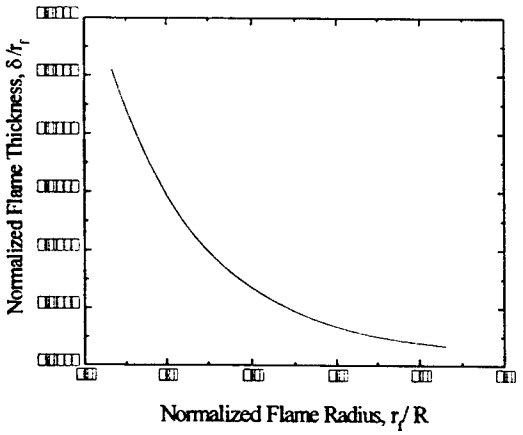

Figure 2. Normalized flame thickness vs. normalized flame radius of methane-air-diluent mixture

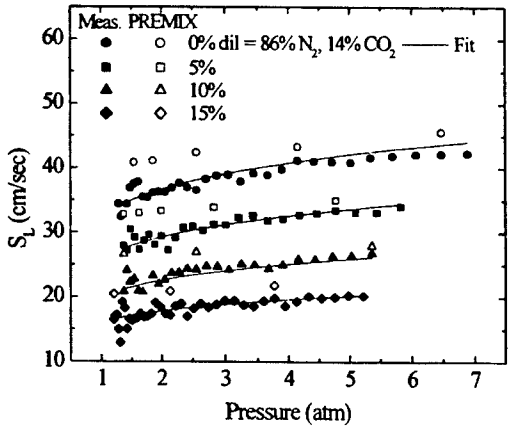

Figure 3- Comparison of burning speed of methane-air mixtures at atmospheric pressure.

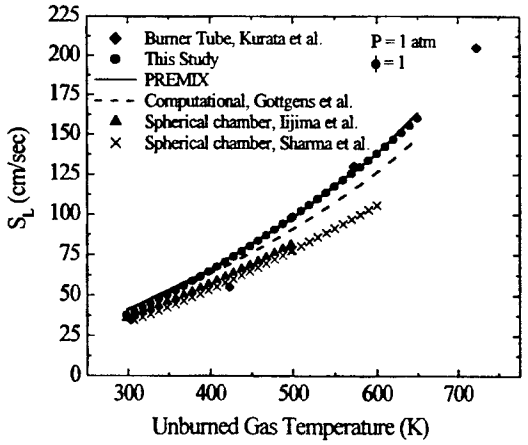

Figure 4. Comparison of burning speed of stoichiometric methane-air-diluent mixtures

Reference

1. Elia, M., M. Ulinski, and M. Metghalchi, ASME Journal of Engineering for Gas Turbines and Power, 2001. **123**: p. 190-196.
2. Rahim, F., et al., International Journal of Engine Research, in Press, 2002.
3. Metghalchi, M. and J.C. Keck, Combustion and Flame, 1980. **38**: p. 143-154.
4. Metghalchi, M. and J.C. Keck, Combustion and Flame, 1982. **48**: p. 191-210.
5. Rahim, F. and M. Metghalchi. *Combustion Institute*. 2001. North Carolina.
6. Rahim, F. and M. Metghalchi. *Western States Section/Combustion Institute*. 2002.
7. Rallis, C.J. and A.M. Garforth, Progress in Energy and Combustion Science, 1980. **6**: p. 303-329.
8. Kurata, O., S. Takahashi, and Y. Uchiyama, Journal of SAE, 1994: p. 119-125.
9. Iijima, T. and T. Takeno, Combustion and Flame, 1986. **65**: p. 35-43.
10. Sharma, S.P., D.D. Agrawal, and C.P. Gupta. *Eighteen Symposium (International) on combustion*. 1981.
11. Gottgens, J., F. Mauss, and N. Peters. *Twenty-Fourth Symposium (International) on Combsution Institute*. 1992.

STABILIZATION AND BLOWOUT OF GASEOUS- AND SPRAY-JET FLAMES

ARO Grant/Contract Number: AMSRL-RO-RI 40131-EG

Principal Investigator: Kevin M. Lyons

North Carolina State University
Department of Mechanical and Aerospace Engineering
Raleigh, NC 27695-7910

SUMMARY/OVERVIEW:

The focus of our efforts in this research program is to determine the underlying mechanisms that control lifted flame stabilization and blowout in spray flames. A significant amount of data exists for the characterization of gaseous diffusion flames as a result of past research performed by the combustion community. In these studies, mechanisms of stabilization, the role of premixing and scalar dissipation have been examined to varying degrees in systems such as lifted laminar and turbulent diffusion flames. One current priority is to experimentally analyze lifted spray flames and compare the mechanisms associated with spray flames to those observed in the gaseous diffusion flames. This report details the recent research performed in spray flames and describes the preliminary findings.

TECHNICAL DISCUSSION:

Description and quantification of the phenomena that control two-phase combustion processes are of great interest and importance, as most practical combustion devices initially introduce fuel in the liquid phase. Understanding what mechanisms are responsible for flame stabilization, propagation, and blowout will serve to aid in future combustor designs of higher efficiency and reduced emissions. In order to develop better combustion technology, experimental work must be performed which explores the fundamental aspects of spray flame behavior.

In comparison to gaseous diffusion flames, relatively few studies have been performed to analyze the stabilization mechanisms associated with lifted spray flames. Within the past decade, more emphasis has been placed on the study of spray combustion, but the wide variety of burner designs and fuel injection strategies has often produced results that differ greatly and are not easily correlated. The method of fuel injection has a significant effect on the flame characteristics. This effect arises due to the issue of fuel vaporization and its associated time scale, which is a strong function of

droplet size and distribution. The vaporization time scale now must be compared to the chemical and mixing time scales, and these relative comparisons will contribute to the different regimes observed in the flame. Two common choices for the injection of liquid fuel is to either utilize a spray nozzle similar to what is used in oil burning applications (i.e. an oil furnace) or to implement what is known as an air-blast injector. Our group has selected to examine spray nozzles because of the ability to adjust the spray pattern(droplet distribution) and fuel flow rate. In addition, the spray nozzles are representative of typical automotive fuel injectors, which provides a connection between the research and real-world applications. Therefore, the way in which the fuel is introduced into the oxidizer flow field becomes much more critical in spray flames than in gaseous flames, and this complicated aspect of spray combustion indicates that much more experimentation must be done in order to understand how the relationship between fuel and oxidizer flows affects flame stabilization. Developing a better understanding of spray flame stabilization will allow comparisons to be made to the better characterized phenomena associated with gaseous diffusion flames.

Sprays pose significant challenges to applying non-intrusive optical diagnostic techniques in combustion systems due to complicating factors such as attenuation and scattering of the probe beam, and interference from the droplets. Characteristics such as spray pattern, droplet size, velocity distribution, and oxidizer flow field play an important role in determining how the flame structures will exist [1]. Some previous experiments in spray flames [2,3,4] have reported that the flame can exhibit a double structure, originating at the leading edge, that diverges with increasing downstream location. This double flame structure is of interest with respect to both the nature of the flame and its effect on flame stabilization. Consequently, OH Planar Laser-Induced Fluorescence has been performed in the near field of an atmospheric ethanol spray flame. This laser diagnostic was selected by our group to map the reaction zones in order to gain insight to the flame characteristics. This planar imaging technique has been shown to satisfactorily mark the fuel-lean side of the flame front of hydrocarbon diffusion flames. It should be noted that in the case of premixed reacting flows, the OH radical can exist in the hot products of combustion and therefore will yield a signal which is indicative of post-combustion gases and not combustion. These premixed flame "false" signals, which can limit the ability to map reaction zones, can provide a distinction between areas which burn in either a diffusion or premixed mode. Typically, a diffusion flame will appear as a thin line of OH fluorescence, whereas a premixed flame will show "broad" regions of OH intensity which signifies both premixed reactions and hot products [5].

The burner utilizes an adjustable annular air co-flow surrounding an axisymmetric spray injector. Nozzles of varying flow rate, cone angle, and cone configuration supply the fuel spray. OH fluorescence from the flame is probed via the $R_1(8)$ transition (281.252 nm) and is captured with an ICCD digital camera. Particular attention has been focused on the double flame structure that is observed in these spray flames. Contrary to the single flame structure observed in lifted non-premixed gaseous flames [6], the double flame structure appears as two diverging flame fronts originating at the stabilization point, consisting of an outer diffusion flame and an inner structure that possesses premixed flame characteristics, especially at locations downstream of the leading edge.

The inner flame structure burns primarily in a diffusion mode near the leading edge and evolves into a region indicative of premixed burning by the relatively large blotches of OH observed in the experimental data (see Figure 1). The degree of premixedness varies with experimental conditions, with some nozzle/co-flow combinations displaying more premixed flame evidence than others. Local extinction at the lowest axial locations of the inner flame structure, caused primarily by the presence of large fuel droplets crossing the reaction zone, is thought to contribute to the premixing of reactants that ignite at downstream locations. It is believed the larger droplets feed the outer reaction zone while the smaller, easily vaporized droplets sufficiently mix with entrained or co-flow air to support premixed combustion in the inner reaction zone. One interesting observation was made for the two smallest fuel nozzles analyzed in the experiment. The case for no co-flow exhibited the "leading edge" phenomenon similar to that observed in lifted gaseous diffusion flames. The presence of a single flame structure with no inner flame zone indicates that there is not sufficient air entrainment to support combustion at the inner zone. Once co-flow is introduced, the flame is lifted enough to entrain oxidizer for inner zone combustion. In general, while low-speed co-flow simply enhances the double structure with a minimal effect on liftoff height, the higher co-flow velocities create a well-lifted flame that exhibits a highly fluctuating stabilization point and an unsteady double structure.

This phase of the research has provided insight into the nature of spray flames, and future efforts are aimed at quantifying these spray flame mechanisms in order to better understand how the observed structures affect spray flame stabilization. The issue of flame blowout is also under the scope of investigation. Work is currently under way to study flame blowout in both the gaseous and spray flames. Flame blowout is induced by exceeding either a critical fuel jet velocity or a critical co-flow velocity (where applicable). In either case, the flame base lifts to a downstream axial location beyond which the flame cannot sustain itself without an external ignition source. Considerable work has been done to enhance blowout limits, but there is still some question as to what mechanisms control blowout. The use of a high speed digital camera facilitates the analysis of these flames as they approach and achieve blowout. The evolution of the highly transient structures can be well documented with the camera, and a significant amount of insight can be obtained without relying upon a laser-based diagnostic technique. Future investigations may benefit from laser diagnostics in order to look at specific mechanisms or phenomena. As mentioned before, utilizing both spray and gaseous burners with similar co-flow configurations allow the best possible comparisons to be made given the innate differences between the two types of combustion. Understanding flame blowout will allow researchers to more efficiently design methods for enhancing blowout limits and thus optimize the heat release in the flame which can be converted into useful work.

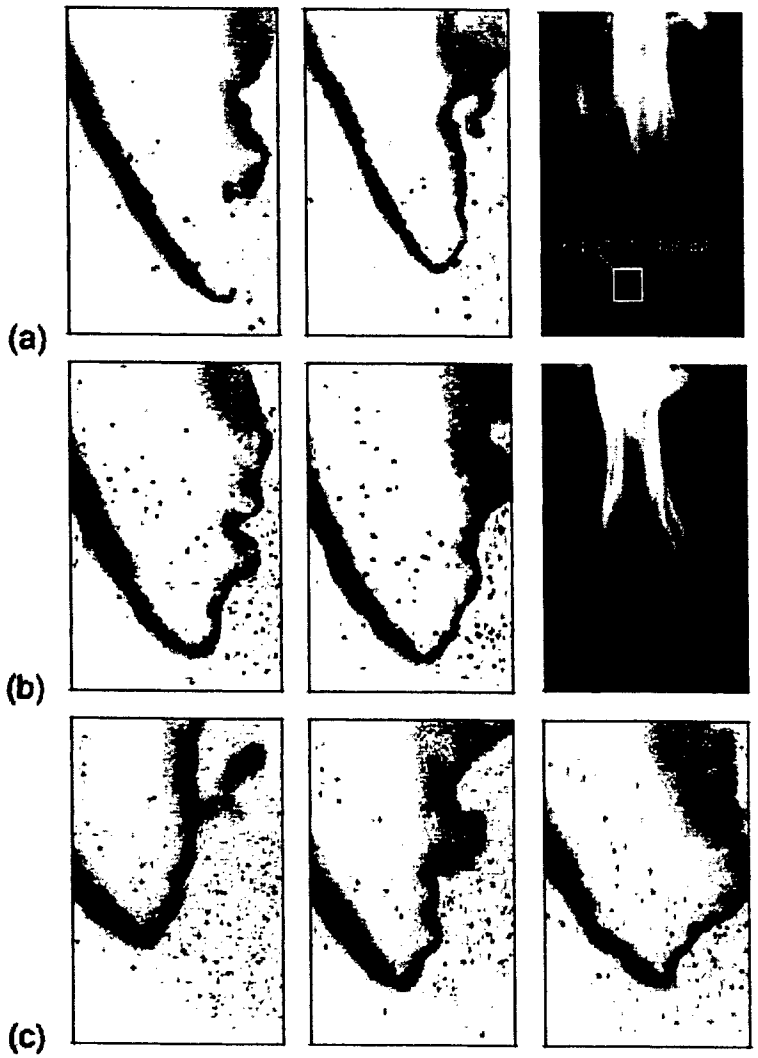

Figure 1. OH images and photographs for a typical spray nozzle with (a) no co-flow, (b) 0.29 m/s co-flow, and (c) 0.34 m/s co-flow. OH images display left half of flame base.

References

1. Friedman, J.A., and Renksizbulut, M., Investigating a Methanol Spray Flame Interacting With an Annular Air Jet Using Phase-Doppler Interferometry and Planar Laser-Induced Fluorescence. *Combust. Flame* **117** (1999) 661-684.
2. Cessou, A., and Stepowski, D., Planar Laser Induced Fluorescence Measurement of [OH] in the Stabilization Stage of a Spray Jet Flame. *Combust. Sci. Technol.* **118** (1996) 361-381.
3. Cessou, A., Goix, P., and Stepowski, D., Simple Description of the Combustion Structures in the Stabilization Stage of a Spray Jet Flame. *Atomization and Sprays* **9** (1999) 1-27.
4. Stepowski, D., Cessou, A., and Goix, P., Flame Stabilization and OH Fluorescence Mapping of the Combustion Structures in the Near Field of a Spray Jet. *Combust. Flame* **99** (1994) 516-522.
5. Kelman, J.B., and Masri, A.R., Simultaneous Imaging of Temperature and OH Number Density in Turbulent Diffusion Flames. *Combust. Sci. Technol.* **122** (1997) 1-32.
6. Watson, K. A., Lyons, K. M., Donbar, J. M. and C. D. Carter Observations on the Leading Edge in Lifted Flame Stabilization, *Combustion and Flame* **119**(1999) 199-202.

MIXING, CHEMICAL REACTIONS, AND COMBUSTION IN HIGH-SPEED TURBULENT FLOWS

AFOSR Grant F49620-01-1-0006

Paul E. Dimotakis
Graduate Aeronautical Laboratories
California Institute of Technology, Pasadena, CA 91125

Summary/Overview

This research focuses on fundamental investigations of mixing, chemical-reaction, and combustion, in turbulent, subsonic, and supersonic flows. It is comprised of an experimental effort; an analytical, modeling, and computational effort; and a diagnostics- and instrumentation-development effort. Computational studies are focusing on fundamental issues pertaining to the simulation of multi-dimensional flows and turbulent mixing, and hydrocarbon flames.

Technical discussion

Experiments in progress investigate laminar-flame properties of premixed methane- and ethane-air mixtures, at atmospheric pressure, over a range of equivalence ratios, Φ, with a current focus on extinction strain rates against low-temperature walls. These are important in the context of cold-wall quenching of hydrocarbon flames. The experiments utilize a stagnation-flow configuration, similar to counterflow flames, introduced by Law and coworkers (Wu & Law 1984, Law 1988, and Zhu *et al.* 1988), and rely on digital imaging of flame chemiluminescence, extensions to particle-streak velocimetry (PSV) for flow-field measurements, and independent jet-exit velocity measurements. Strained laminar flame-speed data, extrapolated to zero strain rate in the method of Law and coworkers (Wu & Law 1984), for both methane and ethane, show good agreement to previous data and validate the experimental methodology.

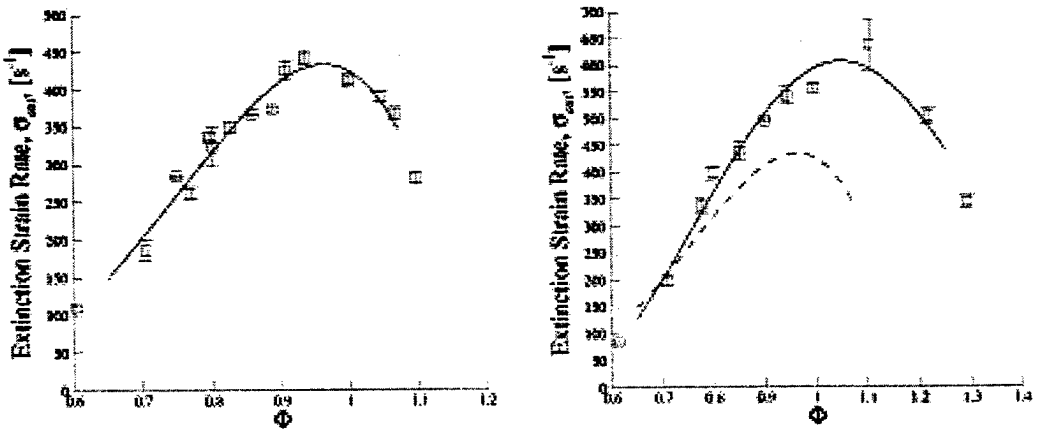

Fig. 1 Extinction strain rates against a room-temperature stagnation plate. Smooth curves are least-squares fits to the data. Left: Methane-air. Right: Ethane-air (dashed curve for methane-air).

Figure 1 plots the measured local extinction strain rates, σ_{ext}, for methane-air and ethane-air mixtures, against room-temperature stagnation plates. Extinction is induced through a gradual increase in jet velocity as a frame sequence was recorded. Extinction conditions are derived from the last frame that captures a flame in each sequence. Error estimates derive from ensemble statistics (repeated experiments), or slope-error estimates from a single run, depending on individual image-data and streak suitability. Smooth curves are least-squares fit to the data and drawn to aid the eye. Stable rich flames, $\Phi > 1$, are obtained with an inert surrounding ambient gas. Ethane-air extinction strain-rate values are somewhat higher than for methane-air mixtures, in accord with the higher flame speeds for this hydrocarbon-air mixture. The corresponding methane-air least-squares fit is included in the ethane-air figure for comparison purposes. The experimental work is part of the Ph.D. research of J. Bergthorson.

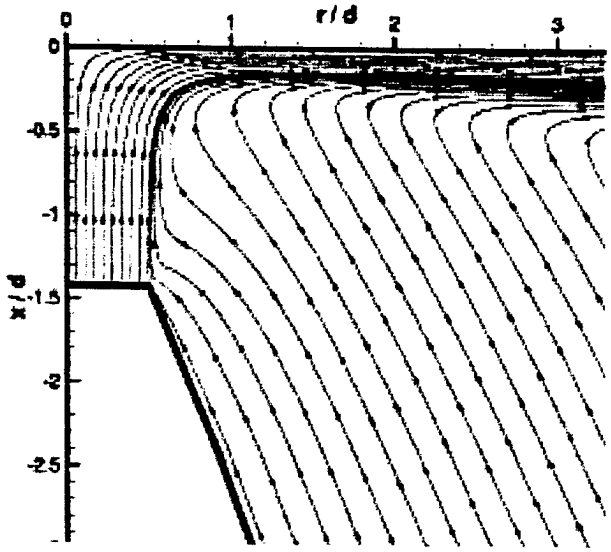

Fig. 2 Direct numerical simulation of the impinging jet and near-field streamline pattern for a cold jet impinging on a stagnation plate.

A numerical study of a cold jet impinging on a stagnation plate was performed to complement the experimental study. The code implemented a modification and extension of the PRISM spectral-element code (Henderson & Karniadakis 1995) adapted for axisymmetric flow and the accommodation of the complex inflow/outflow boundary conditions of the experimental geometry. Figure 2 plots the flow streamlines for a cold impinging jet on the stagnation plate, at Re = 700. Figure 3 compares the computed 2D (axisymmetric) centerline axial velocity for an impinging jet, at Re = 1400 and 700 (solid line) to experimental results obtained using Particle-Streak Velocimetry (PSV). Also plotted for this flow is the 1D stream function solution to the full equations, as used in standard stagnation flame codes (Kee *et al.* 1988), computed by D. Goodwin. The numerical simulations are part of the Ph.D. research of K. Sone, in collaboration with D. Meiron and D. Goodwin.

Experiments on flames presently in progress exploit the nearly completed KFS high-framing-rate digital-imaging system and focus on flame behavior and the associated flow field under conditions that result in transitions in flame behavior. The KFS Camera system is a custom camera system designed for high-speed, low-noise imaging applications, and is based on the KFS CCD image sensor, which has 1024×1024 pixels, 12 μm^2, and 32 output channels. This was developed and characterized at JPL by M. Wadsworth, S. A. Collins, and S. T. Elliott. The 32 output channels allow a 16-fold reduction in (readout time)×(noise figure)^2 compared to a CCD with only 2 output channels. Camera head control and processing electronics were developed by D. Lang, in collaboration with S. Kaye, with mechanical design by P. Svitek and G. Katzenstein. The camera head contains the CCD clock drivers, 32 output amplifiers and local power regulators. D/A converters allow programming of the CCD clock and bias voltages for optimum performance.

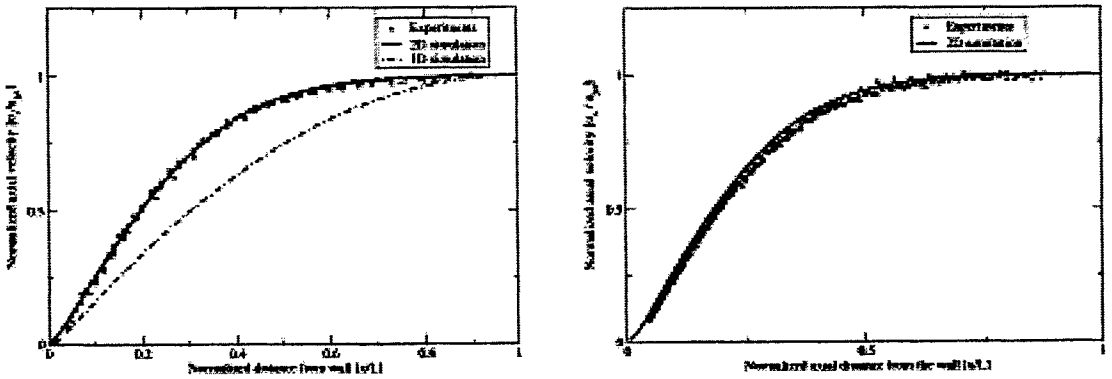

Fig. 3. Experimental data and numerical simulations of the centerline axial velocity for an impinging jet. L/d_j = 1.424. Solid lines: Axisymmetric (2D) simulation using Prism code. Dashed line: 1D streamfunction solution (D. Goodwin). Left: Re = 1400. Right: Re = 700.

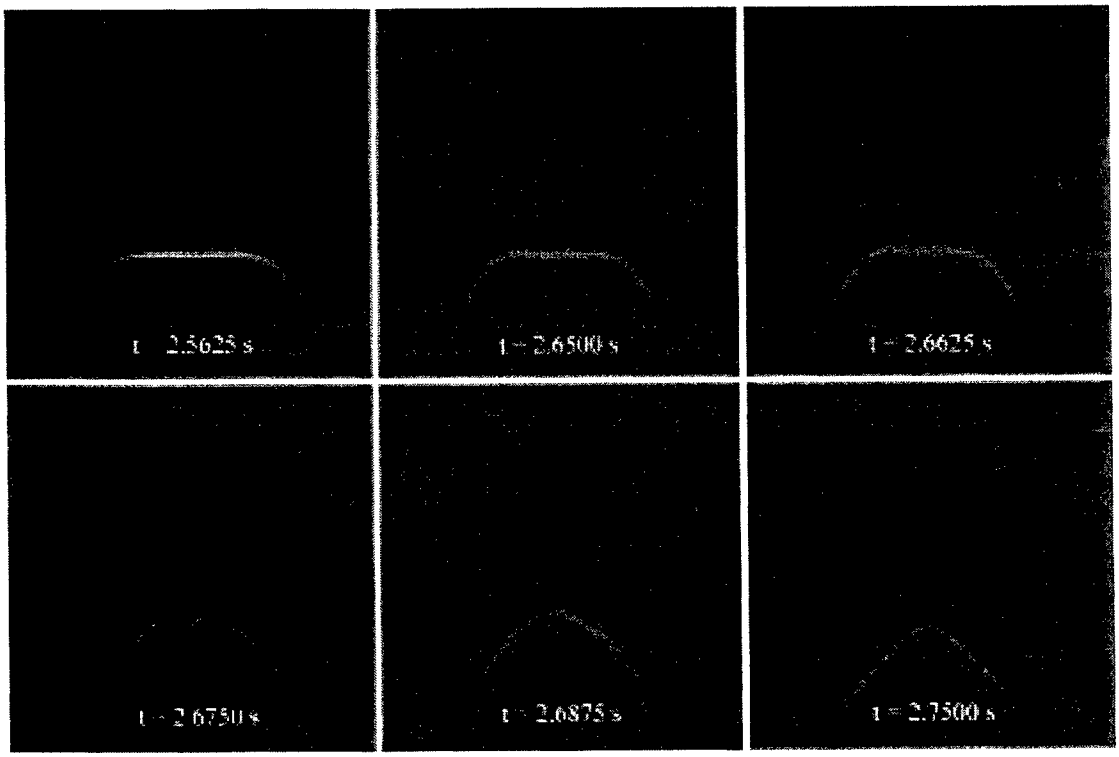

Fig. 4. Image sequence of a transitioning ethylene-18% O_2:(O_2 + N_2), Φ = 0.7 flame. Data acquired with the KFS system at 80 fps (12.5 ms framing period).

Eight 4-channel A/D converter boards accommodate the 32 KFS-CCD channels. Each A/D channel has programmable gain, offset, low-pass filters, and correlated double sampling (CDS). The latter is required if a readout noise below ~100 e^-/pixel is to be achieved. Each channel is digitized to 12 bits and compressed (lossless compression) before being stored in RAM. Each A/D converter board has 512 MB of RAM, for a total of 4 GB. Approximately 4000 frames can be stored in RAM, assuming a conservative 1.5:1 compression ratio. A timing board provides

master timing signals to the camera head, A/D converters, and other external devices (lasers & chopper wheels). A power board provides power and shutter-driver electronics for the camera head. A computer with National Instruments LabWindows CVI provides overall control, image display, and local disk storage. At a 10 ms readout time (100 fps with a pulsed light source), readout noise is in the range, 23.2 ± 2.5 e^-/pixel. At a 5 ms readout time (200 fps with a pulsed light source), noise is in the range 28.6 ± 3.5 e^-/pixel. These represent a considerable advance over alternative imaging devices (factor of 3-4); a significant difference given that noise is approximately proportional to the square root of detected light amplitude.

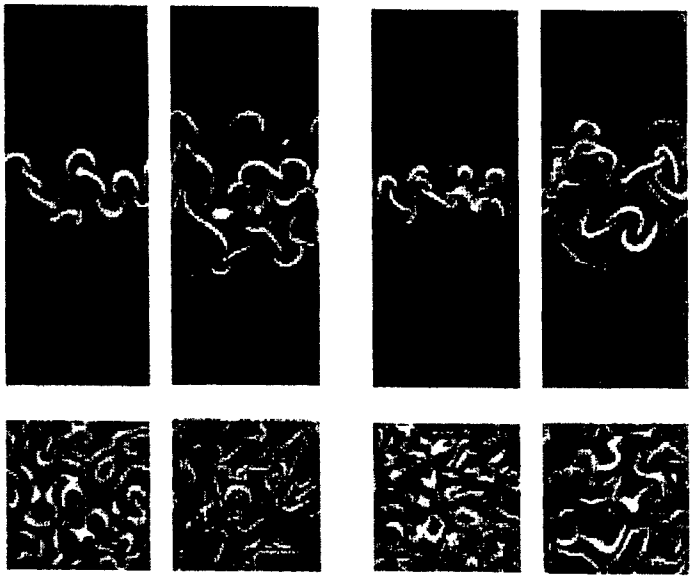

Fig. 5 Scalar dissipation rate field. Case A (left) at $t/\tau = 1.84, 2.69$. Case C (right): $t/\tau = 3.04, 4.01$. The grayscale values chosen such that 95% of the total dissipation rate is visible. Also shown are isoscalar contours: $X = 0.5$ (red) and $X = 0.1$ and 0.9 (blue).

Figure 4 depicts the first laboratory image sequence recorded with the KFS camera system. It is a premixed ethylene-O_2-N_2 flame transitioning from a stretched, approximately flat, flame to a Bunsen flame. The mixture is diluted with N_2 to a reduced oxygen content of 18% O_2:(O_2 + N_2) and an equivalence ratio of $\Phi = 0.7$. The frame sequence was acquired at 80 fps, with a 7.5 ms exposure and a 5 ms readout time per frame. The middle four frames are consecutive images, while the first and last are some time before and after the transition to show the two stable flame configurations for reference. Two new simulations of Rayleigh-Taylor (RT) instability were completed. The first (Case D) is a ($512^2 \times 2040$)-grid (0.56×10^9 nodes) calculation and achieved a Reynolds number of $Re = 5500$. It was performed on 1024 processors of Blue-Pacific at the Lawrence Livermore National Laboratory, requiring approximately twelve months to complete. The second simulation (Case C-) was run at a lower density ratio on a $256^2 \times 1024$ grid, and is the first of a series to explore density-ratio effects. Data from previous RT simulations (Cook & Dimotakis 2001: Cases A, B, and C) were used to study mixing. They differed only in their initial perturbation spectra, *i.e.*, $k_A < k_B < k_C$, where k_A, k_B, and k_C denote the peak-amplitude wavenumber, respectively. Figure 5 plots the logarithm of the scalar dissipation (mixing) rate, χ, for Cases A and C. Large values of χ are organized in sheets, as observed in other turbulent flows. In Case A, the sheets correlate with the caps of the ascending/descending plumes and with inter-vortex regions associated with secondary Kelvin-Helmholtz instabilities. In Case C, the structure of the flow is not as manifest. These visualizations and pdf's of χ show that mixing is distributed throughout the mixing zone.

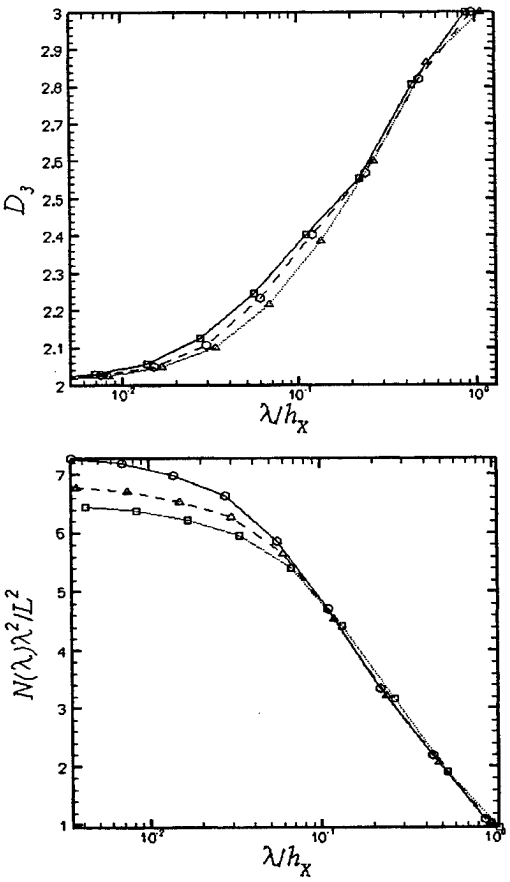

Fig. 6 Data analysis at $t/\tau = 4.16$ (dotted), 4.33 (dashed), 4.48 (solid). Top: coverage dimension. Bottom: normalized resolved surface area.

Three-dimensional isoconcentration surfaces in turbulent flow can be related to surface-to-volume ratio measures needed to quantify mixing. An issue in this study was their geometrical statistics. These were investigated in terms of the coverage dimension, defined as,

$$D_3(\lambda) = -\frac{\mathrm{d}\log N_3(\lambda)}{\mathrm{d}\log\lambda}$$

where $N_3(\lambda)$ is the number of cubes of size λ required to cover the 3D level sets. Figure 6 (top) shows the coverage dimension, $D_3(\lambda)$, for Case C for three, late-time 3D fields. The observed dependence of the coverage dimension on the scale λ is as expected for level sets transitioning from smooth geometry, at diffusion scales, to space-filling configurations at large scales, and is similar to that found experimentally in turbulent jets (Catrakis & Dimotakis 1996). Figure 6 (bottom) shows the isosurface surface area normalized by the initial interfacial area as a function of the coverage (resolved) scale, λ. The curves collapse at large scales and deviate from one another at inner (viscous) scales, indicating increasing surface area as time and Reynolds number increase.

The research on RT flow mixing is performed by T. Mattner and B.-E. Gurret, in collaboration with A. Cook (LLNL), and is cofunded by the Caltech DOE/ASCI center.

Experimental investigations are in progress on the aerodynamic control of internal flows, as occur, for example, in subsonic diffusers and scramjet combustors. Recent work has focused on subsonic flow over a backward-facing perforated ramp, using the $(H_2 + NO)/F_2$ chemical system to explore the effects of heat release and to measure mixing between the two streams. Diagnostics include upper- and lower-guidewall pressure measurements, total pressure and temperature measurements at the test-section exit, and schlieren images recorded on a 1024^2-pixel, 30 fps camera. Previous non-reacting work has demonstrated the ability to control various aspects of the flowfield, such as the pressure coefficient and exit velocity profile, via variable mass-injection through the perforated plate. Similar effects can be achieved with lower mass injection through heat release, *i.e.*, the dilatation from the chemical reaction. Figure 7, left, shows the variation of the upper-guidewall pressure coefficient with increasing mass injection for non-reacting flow. The freestream velocity for these runs is $U_1 \cong 120$ m/s. Figure 7, right, shows the results for chemically reacting flows, with variable heat release through increased reactant (H_2, F_2) concentrations, at the same U_1, and an injection velocity of $U_2 \cong 11$ m/s. Dilatation from the chemical reaction plays the same role as additional mass injection. Mass injection requirements are seen to lower (roughly, half) in the chemically reacting case (4% H_2/F_2), for the same

pressure coefficient. Similar effects are found in the downstream velocity profiles. As mass injection ratio is increased, the recirculation zone downstream of the ramp is pushed further downstream. Similar effects are seen with heat release at constant mass injection ratio. Work in progress is focusing on quantifying mixing, taking advantage of the $(H_2 + NO) / F_2$ chemical system. This work is part of the Ph.D. research of M. Johnson and is performed in collaboration with G. Katzenstein, E. Dahl, and D. Lang.

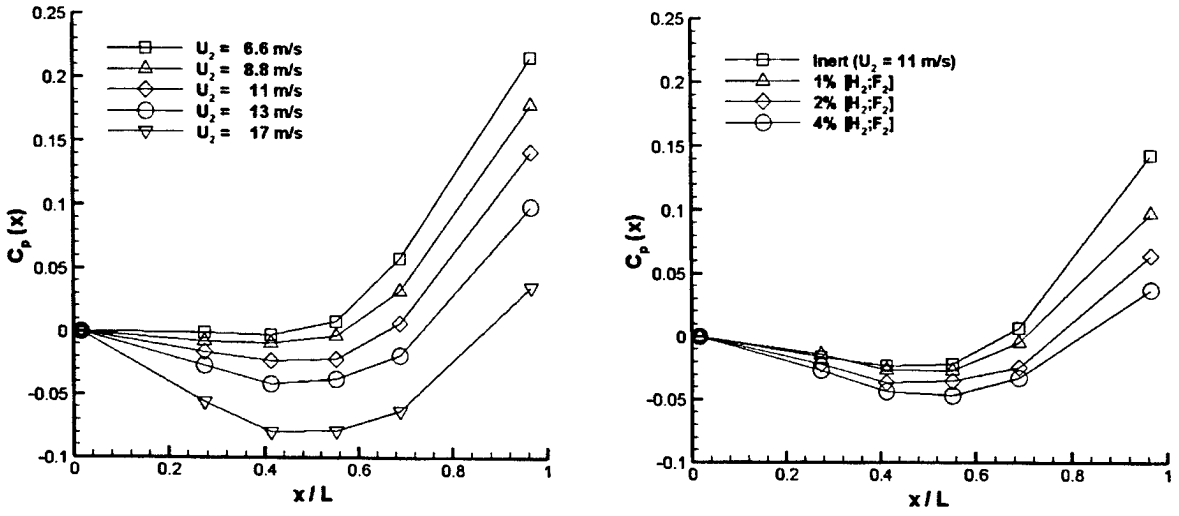

Fig. 7 Upper (high-speed) guidewall pressure coefficients for non-reacting (left) and reacting (right) flows over a perforated ramp.

References

Catrakis, H. J., & Dimotakis, P. 1996 Mixing in turbulent jets: scalar measures and isosurface geometry. *J. Fluid Mech.* **317**, 369-406.

Cook, A. W., & Dimotakis, P. E. 2001 Transition stages of Rayleigh-Taylor instability between miscible fluids. *J. Fluid Mech.* **443**, 69-99.

Henderson, R. D., & Karniadakis, G. E. 1995 Unstructured spectral element methods for simulation of turbulent flows. *J. Comp. Physics* **122**, 191-217.

Kee, R. J., Miller, J. A., Evans, G. H., & Dixon-Lewis, G. 1988 A computational model of the structure and extinction of strained, opposed flow, premixed methane-air flames. *Proc. Comb. Inst.* **22**, 1479-1494.

Law, C. K. 1988 Dynamics of stretched flames. *Proc. Comb. Inst.* **22**, 1381-1402.

Wu, C. K., & Law, C. K. 1984 On the determination of laminar flame speeds from stretched flames. *Proc. Comb. Inst.* **20**, 1941-1949.

Zhu, C. K., Egolfopoulos, F. N., & Law, C. K. 1988 Experimental and numerical determination of laminar flame speeds of methane/(Ar, N_2, CO_2)-air mixtures as a function of stoichiometry, pressure and flame temperature. *Proc. Comb. Inst.* **22**, 1537-1545.

FREQUENCY AND POWER DENSITY EFFECTS ON FREE-PISTON LINEAR ALTERNATOR SYSTEMS

Grant/Contract Number: DAAD19-01-1-041

Principal Investigators: Parviz Famouri, Nigel Clark

Department of Mechanical and Aerospace Engineering

Lane Department of Computer Science and Electrical Engineering

West Virginia University

Morgantown, WV 26506

SUMMARY/OVERVIEW

Research at West Virginia University has led to the construction of a prototype two-stroke, crankless, linear free-piston compression ignition engine, and an accompanying time-based mathematical model. The engine consists of two linked opposed pistons connected by a connecting rod with a permanent magnet alternator attached to the reciprocating shaft. The piston motion of the linear engine is not mechanically defined, but results from the balance of pressures, alternator loading, and frictional forces in the opposing cylinders. The model utilizes both thermodynamic and heat transfer models, as well as dynamic models to predict the effect of changing engine physical parameters, such as bore and stroke, as well as changing internal parameters

such as alternator loading and injection timing. Results from the laboratory and the model indicate that low translating mass and high reciprocating speeds are desirable to increase engine power densities, and to decrease engine inefficiencies. Since the linear engine possesses no crankshaft, the direct extraction of useful mechanical work is impossible, necessitating the use of an electrical or fluid-power device. The proposed linear engine will power a permanent magnet linear alternator, for use as compact, high power, electrical power generation.

TECHNICAL DISCUSSION

Research conducted at West Virginia University in both modeling and successfully operating a two-stroke linear engine have shown some operating characteristics for these type devices.

Several cases have been examined using various engine parameters. Table 1 shows engine parameter values used as a base control case.

Table 1. Base values used in model.

Bore (mm)	75
Stroke (mm)	71
Mass (kg)	4
Load, C_a (N-sec/m)	50
Lambda (λ)	4
Injection Position (mm)	3
Combustion Duration (s)	0.0035
Diffusive Burn, Qd (%)	80
Premixed Burn, Qp (%)	20

Lambda is the lambda ratio, or air/fuel ratio relative to stoichiometric air/fuel ratio. The premixed and diffusive burn percentages were taken to represent the ratio set for premixed to diffusive combustion. In most modeling 20% of the burn was assumed to be premixed, with 80% diffusive. Due to the physical configuration of the proposed

model, injection timing was position based. In the base case injection was set to occur 3mm before the piston reaches maximum stroke. The variable C_a was used to affect the amplitude of the sinusoidal load function applied to the model. An increase in C_a leads to an increase in the load applied to the alternator. The simulated alternator load is based on a permanent magnet machine with resistive load. A similar approach was used in previous modeling efforts at West Virginia University.

$$F_l = (C_a)\frac{dx}{dt}\sin^3\left(\frac{\pi x}{L_{st}}\right)$$

Equation 1

The equation form reflects that the voltage is influenced by the position and velocity of the translator in the stator. The equation yields a peak load for the highest product of velocity and proximity to the center point. Figure 1. illustrates the typical shape of the load modeled.

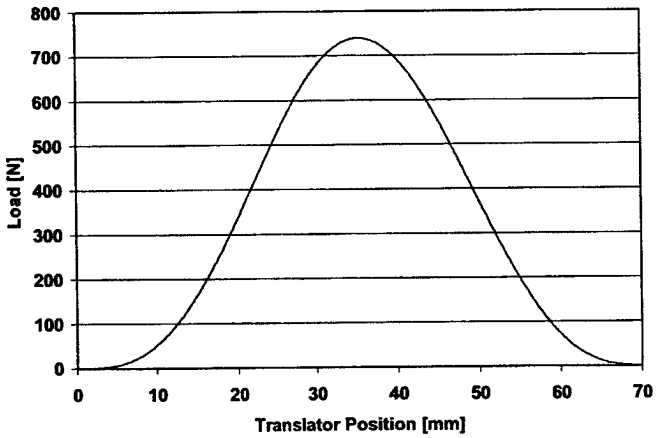

Figure 1. A typical load shape considered in the analysis

Table 2 contains output data for the base case. The effects of varying translator mass, changing premixed to diffusive burn ratio, earlier and later injection position, and varied load values were examined.

Table 2. Base case output data

Power Output (kW)	7.1
Reciprocating Frequency (Hz)	56.2
Friction (N)	60
Compression Ratio	36.6
Indicated Efficiency (%)	40.86

Increasing engine reciprocating mass has the effect of lowering the operating frequency while increasing the operating compression ratio and peak in-cylinder pressures. A further conclusion reached is that the amount of energy needed to reverse the piston motion for a heavier translator is greater, indicating lower efficiency. Since there is no "flywheel" effect from the translating mass the energy used in the previous cycle is mostly lost, except for the air spring effect after the intake port closes. It is therefore advantageous to operate the engine at high speeds with low translating mass, allowing for higher power densities and greater efficiency. The effect of increasing bore/stroke ratios for a given translating mass has also been shown to increase reciprocating speed, with the accompanying improvements in power density and efficiency. Other research has been conducted into the effects of injection timing, duration and shape, on piston motion reversal and energy efficiency.

The linear engine offers the potential to generate and deliver power without the need to convert linear piston motion to rotary crankshaft motion. An idealized model of a linear engine, consisting of two pistons linked by a solid rod has revealed the relationship

between stroke, compression ratio, heat input, operational frequency and other parameters. The diesel prototype showed successful characteristics in the testing performed, and it is the intent of the researchers to operate the linear engine-alternator combination and verify the model

Towards Lattice Boltzmann method for Turbulent Combustion

AFOSR GRANT Number F49620-01-1-0142
Principle Investigators: Sharath S. Girimaji [*], Li-Shi Luo [**]

[*]Aerospace Engineering Department, Texas A&M University,
College Station, TX 77843
[**]ICASE, Mail Stop 132C, NASA Langley Research Center,
3 West Reid Street, Building 1152, Hampton, Virginia 23681-2199

SUMMARY/OVERVIEW

The primary objective of this work is to investigate the ability of the lattice Boltzmann method to simulate scalar mixing, chemical reaction and ultimately turbulent combustion. Simulations of initially non-premixed binary mixtures yield scalar probability distribution functions that are in good agreement with direct numerical simulation (of Navier-Stokes equation) data. One-dimensional chemically-reacting flow simulation of a premixed mixture yields a flame speed that is consistent with experimentally determined value. These results serve to establish the feasibility of the lattice Boltzman method as a viable tool for computing turbulent combustion.

TECHNICAL DISCUSSION

In an effort to establish the suitability of lattice Boltzmann method (LBM) for turbulent combustion, two building block problems are considered: (i) scalar mixing and (ii) one-dimensional chemically reacting flow. The details are given in the reference by Yu, Luo and Girimaji (2002)[1]. A brief description of the study is now presented.

Two species (presumably fuel and oxidizer) generically labeled as black and white are initially segregated and randomly distributed in the computational domain which in the present case is a square box. Mesh size is set 500 x 500. The macroscopic velocity is set everywhere to zero corresponding to a pure diffusion problem. It should be mentioned here that the mesoscopic velocities are non-zero. At the continuum level, the mixing example considered appears as a pure diffusion problem without any advection velocities. However, at the mesoscopic level, each of the components is associated with non-zero velocities. Scalar mixing in a multi-component flow is truly more significant

than simple passive scalar mixing. Due to the kinetic nature of the LBM, the extension of this method to cases with non-trivial macroscopic velocity field is straight forward. This problem epitomizes the scalar mixing issues encountered in a typical non-premixed combustion application. The initial values for the number densities are $n^b = 1.0$, $n^w = 0.0$ in region of the black species and $n^w = 1.0$, $n^b = 0.0$ in region of white species. Simulations are performed for two different sets of relaxation time scales: $\tau^b = \tau^w = 1.0$ and $\tau^{bw} = \tau^{wb} = 30.0$. Citing homogeneity of the scalar field, periodic boundary conditions are used in all directions. The LBM methodology permits simulation of mixing between species of equal or unequal number and mass densities with equal facility. However, in continuum based methods, mixing between species of unequal mass densities is not straight-forward. This represents a fundamental advantage of the LBM over continuum-based methods. The equal mass case is particularly interesting as the results can be directly compared with directed numerical simulation (DNS) of Navier-stokes equation data of Eswaran and Pope[2]. In this case, the number density and mass density are equivalent since the molecular weight of the two species are identical. Figure 1(a) shows the time evolution of the probability density function (pdf) of scalar in which $\bar{\rho} = (\rho^b - \rho^w)\backslash(\rho^b + \rho^w)$. The corresponding DNS[2] data is shown in Figure 1(b). The LBM and DNS data show excellent agreement. In particular, the change of the pdf shape from the initial double-delta shape through a nearly uniform distribution to, finally, a Gaussian-like distribution is well captured by the LBM results. It deserves mention here that many other mixing models do not, even qualitatively, capture the form of pdf during evolution. The time evolution of the root-mean-square (rms) of scalar fluctuations obtained from LBM also compare well with that from DNS[2](figure not shown) for an appropriate choice of relaxation time scale. In Figure 2, the evolution of the pdf of the number density in unequal mass case is shown. (The initial distribution of the species is the same as in previous case.) This problem is not easily solved in the continuum-based methods. Since the average number density is identical for both species, the final pdf distribution is symmetric about the mean value for each species. However, the intermediate forms of the pdf are quite nonsymmetric, demonstrating that the mixing process in this case is quite different from the equal-mass case even if the final distributions are similar. In ongoing work, we attempt to accurately characterize the relationship between the time-constant and diffusion coefficient[3]. Here, it suffices to say that given the right time-constant, the LBM captures the DNS behavior well, qualitatively and quantitatively.

In a reacting flow, the state of the fluid at any given point in space and time can be completely specified in terms of fluid velocity, composition vector (either in terms of mass fraction or concentration) and temperature. We need to develop the LBM for all these variables. For generating a background flow, the conventional LBM substeps of relaxation and convection are used. However for the temperature and concentration fields, there is an extra substep between those substeps to account for reaction. This is identical to the time-splitting approach used in continuum methods for chemically reacting flows. The simplest non-trivial case when reaction can be studied without the complicating effects of mixing is the case of 1-D flame propagation through a homogeneous premixed mixture($C_3H_8 + 5O_2 \Rightarrow 3CO_2 + 4H_2O$). The background flow maintains both the pressure and velocity fields uniform in space and time. A heat source is placed at a location close to the inlet to ignite the mixture. Once ignition is achieved,

Figure 2 shows that JP-8 contains more puffins that have 7 to 0 carbon atoms. The model showed that these light compounds would start the engine in the first cycle, in spite of their low CN.

COMPARISON BETWEEN MODEL PREDICTIONS AND EXPERIMENTAL RESULTS

Cold Start experiments were conducted in a cold room, on a single-cylinder, direct-injection, 4-stroke-cycle, air-cooled diesel engine, using DF-2 and JP-8 fuels. The results of the cylinder gas pressure and instantaneous angular velocity of the engine are shown in Fig.3, for two ambient temperatures: 10°C and 0°C. In both cases the cranking period for JP-8 was shorter than that for DF-2. Results of tests at other ambient temperatures supported this trend.

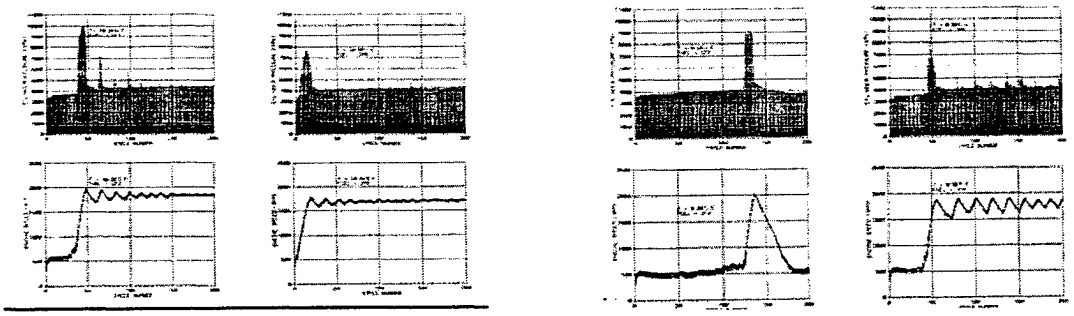

Figure 3. Comparison between the cranking cycles for DF-2 and JP-8

CONCLUSIONS

1.A first generation simulation model for the cold-start cranking-period has been developed. The model indicated: (a) CN alone is not a good indicator of the number of cranking cycles and (b) Fuel volatility is as important as CN in controlling the cranking period.
2.A new auto-ignition index (AI) is developed to predict the cranking period.
3.The model predictions indicated that the volatile paraffin components of the DF2 and JP8 are the initiators of the autoignition process at the end of cranking period.
4.The model predictions agreed with the results of experiments on a single-cylinder diesel engine.

RECOMMENDATIONS

1.Develop a second-generation model based on experimental data for the vapor pressure of the actual fuels as a function of temperature.
2.Combine the combustion instability model and the cranking prediction model to predict the HC (white smoke) emissions.
3.Extend the model to multi-cylinder heavy-duty diesel engines.
4.Apply the model to determine the electronic control strategies to reduce the cranking period, combustion instability and HC (white smoke) emissions.

the heat source is removed. At subsequent times the flame propagates to the right. Initial conditions are set as following: The values of pressure and velocity are set at $p = 1$, $u_x = u_{in} = 0.1$, $u_y = 0.0$. Both fields are maintained uniform at all times in this simple case. The temperature is set at $T = 300^0K$ everywhere except at $x = 50$ where a heat source is placed with $T_{source} = 1500^0K$ to ignite the mixture. The hot spot is removed after the mixture ignites. The mass ratio of nitrogen is $Y_{N2} = 0.7375$. The well-premixed mixture consists of propane and oxygen with the mass ratios of $Y_{C3H8} = 0.2252$, $Y_{O2} = 0.0373$. The mass fractions of the products are initially set to zero: $Y_{CO2} = Y_{H\_2O} = 0.0$. Periodic boundary conditions are used at the top and bottom boundaries and the fully developed boundary condition is applied at the outlet. At the inlet, the initial conditions are maintained. In Figure 3, the flame position is shown as a function of time. The flame location is identified as the position with the highest reaction rate at any given time. The linear variation of flame location with time (in Figure 3) indicates that the flame propagates at a nearly constant rate. This flame speed can be easily estimated from knowing the flame position at initial ($t_i = 0$; $x_{fl} = 50$) and final ($t_f = 4000$; $x_{fl} = 406$) times. The flame speed thus calculated is $vf = [x_{fl}(t_f)-x_{fl}(t_i)]\(t_f-t_i) = 0.0089$ in lattice units. Knowing the flame speed, the burning velocity can be easily determined: $S_L = u_{in}-v_f$. In the above, u_{in} is the reactant velocity at the inlet (which is maintained uniform throughout the flow-field). The burning velocity thus obtained will be in lattice units. This can be converted into metric units as follows: $S_L = u_p(u_{in} - v_f)\(u_{in})$.The resulting burning velocity is $S_L = 0.11$ m/s which compares extremely well with the value obtained from experiments for a propane-air flame[4]. Figure 4 shows that the reaction rate profile in the reaction zone as time evolves. Simulations indicate that flame behavior is sensitive to the magnitude of the heat source.

Based on these simulations, we conclude that LBM can perform adequately for more complicated turbulent combustion simulations.

References

[1]. H. D. Yu, L.-S. Luo and S. Girimaji, Scalar Mixing and Chemical Reaction Simulations Using Lattice Boltzmann Method, International Journal of Computational Engineering Science, in press.

[2].V. Eswaran and S.B. Pope, Direct Numerical Simulations of the Turbulent mixing of a Passive Scalar, Physics of Fluids, **31**,506(1988).

[3]. L.-S. Luo, H. D. Yu and S. Girimaji, Binary Mixing Simulations Using Lattice Boltzmann Method, being prepared.

[4].Yamaoka and H. Tsuji, *Twentieth Symposium(International) Combustion*, The Combustion Institute, Pittsburgh, 1883(1982).

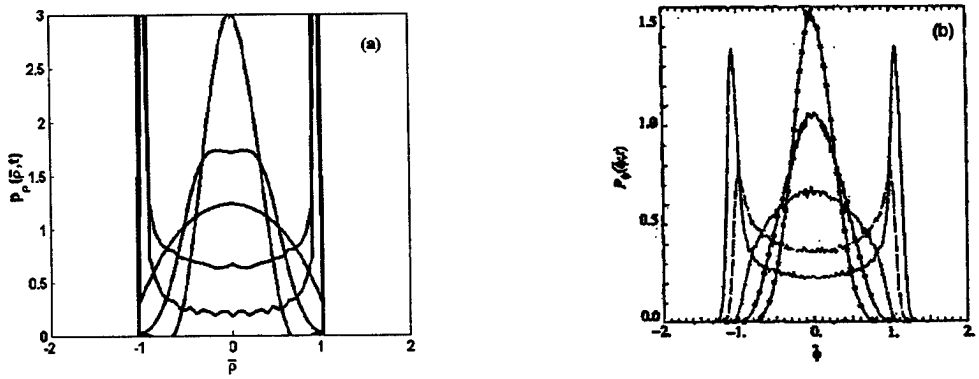

Fig 1: Pdf evolution of number density with time in equal mass case
(a) LBM; (b) DNS

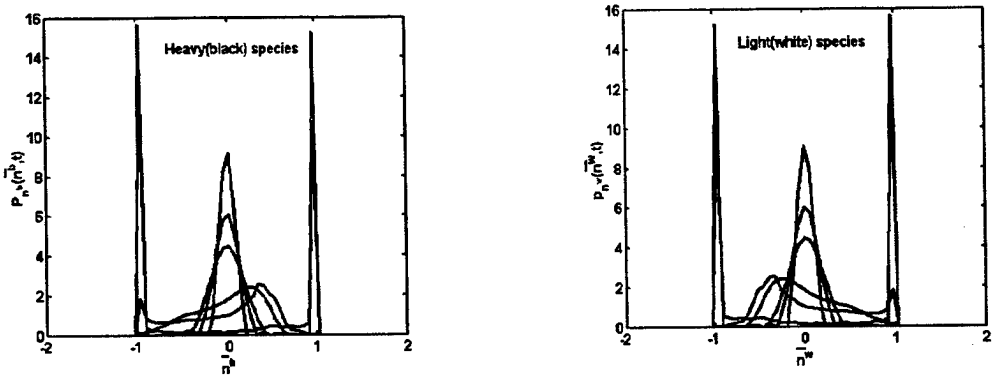

Fig2 : Pdf evolution of number density with time in unequal mass case
$m^b : m^w = 2 : 1$

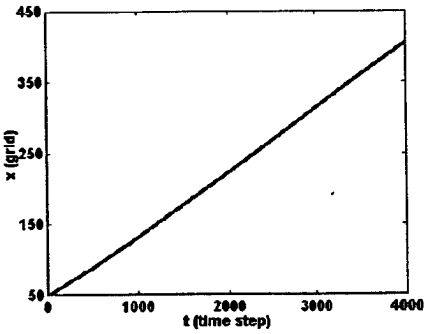

Fig 3: The flame position evolution with time

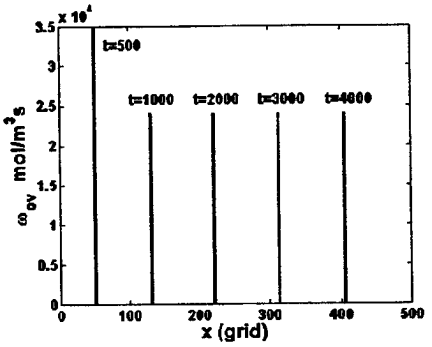

Fig 4: Reaction rate profile at different times

FILTERED MASS DENSITY FUNCTION FOR SUBGRID SCALE MODELING OF TURBULENT DIFFUSION FLAMES

Grant Number F49620-00-1-0035

Principal Investigator(s): Peyman Givi and Farhad A. Jaberi*

Department of Mechanical and Aerospace Engineering
University at Buffalo, SUNY
Buffalo, NY 14260-4400

SUMMARY/OVERVIEW:

The specific objectives of this work are:

(i) To further develop and improve the ``filtered density function" (FDF) methodology for closure of the subgrid scales (SGS) in turbulent reacting flows.

(ii) To implement the resulting SGS closure for large eddy simulation (LES) of turbulent diffusion flames.

TECHNICAL DISCUSSION

The filtered density function (FDF) [1] methodology has proven effective for large eddy simulation (LES) of turbulent reacting flows. The fundamental property of the FDF methods is exhibited by the closed form nature of the chemical source term appearing in the transport equation governing the FDF. This property is very important as evidenced in several applications of FDF for LES of a variety of turbulent reacting flows; see Ref. [2] for a recent review. The encouraging results attained thus far warrant further improvements and implementations of LES/FDF for a wider class of reacting flows. Our efforts within the past year have been concentrated on doing exactly that. Specifically, we have been working on:

(I) Development of the FDF methodology for SGS modeling of the velocity field.

(II) Development of the joint velocity-scalar FDF methodology.

(III) Implementation of our previously developed FDF for LES of turbulent methane jet flames.

Our efforts pertaining to (I) are summarized in Ref. [3]. In this work, a methodology termed the ``velocity filtered density function" (VFDF) is developed. The exact transport equation governing the evolution of the VFDF is derived. It is shown that the effects of SGS convection in this equation appear in a closed form. The unclosed terms are modeled similar to that in PDF methods in Reynolds averaged simulation (RAS) procedures [1]. In this way, the VFDF is at least equivalent to a second-order moment SGS closure. The modeled VFDF transport equation is solved numerically via a Lagrangian Monte Carlo scheme in which the solutions of the equivalent stochastic differential equations (SDEs) are obtained. The numerical scheme preserves the Itô-Gikhman nature of the SDEs [4] and provides a reliable solution for the

VFDF. The consistency of the VFDF formulation and the convergence of its Monte Carlo solutions are assessed. This is done via comparisons between the results obtained by the Monte Carlo procedure and the finite difference solution of the transport equations of the first two filtered moments of VFDF (LES-FD). With inclusion of all of the third moments from the VFDF into the LES-FD, the consistency and convergence of the Monte Carlo solution is demonstrated by good agreements of the first two SGS moments of VFDF with those obtained by LES-FD.

The efforts pertaining to (II) are documented in Ref. [5]. In this work, a methodology termed the ``velocity-scalar filtered density function" (VSFDF) is developed. Compared to conventional LES, this approach has the advantage of treating chemical reaction in a closed form; and compared to scalar FDF, has the advantage of treating convective transport (of momentum and species) in closed form. These modeling advantages have an associated computational penalty. An exact transport equation is derived for the VSFDF in which the effects of the SGS convection and chemical reaction appear in closed form. The unclosed terms in this transport equation are modeled. Again, a system of stochastic differential equations, which yields statistically equivalent results to the modeled VSFDF transport equation, is constructed. These SDEs are solved numerically by a Lagrangian Monte Carlo procedure in which the Itô character of the SDEs is preserved. The consistency of the proposed SDEs and the convergence of the Monte Carlo solution are assessed. The VSFDF results are also compared with those obtained via existing SGS closures. It is expected that VSFDF will not be much more expensive than the scalar FDF, at least for multi-species turbulent flame simulations.

In efforts pertaining to (III), we have used our previously developed scalar filtered mass density function (SFMDF) [6,7] methodology for LES of a piloted jet flame configuration as considered in the experiments of the Combustion Research Facility at the Sandia National Laboratory [8,9]. This flame has been the subject of broad investigations by other computational/modeling methodologies [10]. In the experiments, three basic flames are considered, identified by Flames D, E, and F. The geometrical configuration in these flames is the same, but the jet inlet velocity is varied. In Flame D, the fuel jet velocity is the lowest and the flame is close to equilibrium. The jet velocity increases from flames D to E to F, with noticeable non-equilibrium effects in the latter two.

So far, we have only considered Flame D. For LES of this flame, combustion is modeled via the equilibrium methane-oxidation model. This model is enacted via flamelet simulations, which consider a laminar counterflow (opposed jet) flame configuration [11]. The full methane oxidation mechanism of the Gas Research Institute (GRI) [12] is employed. At low strain rates, the flame is close to equilibrium. Thus, the thermo-chemical variables are determined completely by the ``mixture fraction." This flamelet library is coupled with our LES/SFMDF solver in which transport of the mixture fraction is considered. It is useful to emphasize here that the FDF of the mixture fraction is not ``assumed" *a priori* (as done in almost all other flamelet based LES; *e.g.* Refs. [13-17]). Rather, it is calculated explicitly via the SFMDF.

With the equilibrium chemistry model, the results obtained by LES/SFMDF are compared with Sandia's experimental data [8-10] for Flame D. The preliminary agreements are encouraging, but more work is needed for reliable conclusions.

WORK IN PROGRESS

Our current work is concentrated on the following issues:

(1) Documenting the results of our work on LES/VSFDF for a journal publication.

(2) Fine-tuning and further implementation of the LES/SFMDF methodology for prediction of Sandia's Flame D.

(3) Further assessment of a new computational methodology, termed the "Spectral/hp Element" method [18]. The advantage of this methodology is that it contains spectral accuracy and it also allows for utilization of "unstructured" grids. This assessment is needed for possible replacement of our current mean flow solver with this methodology, so that we can consider a larger computational domain for our simulations of jet flames.

(4) Consideration of the reduced kinetics mechanism of methane-air oxidation [19] in conjunction with the ISAT routine [20] in our scalar LES/SFMDF for predictions of non-equilibrium methane jet flames.

ACKNOWLEDGMENT

We are indebted to Professor Stephen B. Pope (Cornell University) for his valuable collaboration on various aspects of this work.

References

[1] Pope, S. B., *Turbulent Flows*, Cambridge University Press, Cambridge, UK, 2000.

[2] Givi, P., A Review of Modern Developments in Large Eddy Simulation of Turbulent Reacting Flows, in Liu, C., Sakell, L., and Herklotz, R., editors, *DNS/LES-Progress and Challenges*, pp. 81-92, Greyden Press, Columbus, OH, 2001.

[3] Gicquel, L. Y. M., Givi, P., Jaberi, F. A., and Pope, S. B., Velocity Filtered Density Function for Large Eddy Simulation of Turbulent Flows, *Phys. Fluids*, **14** (3): 1196-1213 (2002).

[4] Arnold, L., *Stochastic Differential Equations: Theory and Applications*, Krieger Publishing Co., Malabar, FL, 1974.

[5] Drozda, T. G., Consistency Assessment of Velocity-Scalar Filtered Density Function for Large Eddy Simulation of Turbulent Flows, M.S. Thesis, Department of Mechanical and Aerospace Engineering, University at Buffalo, State University of New York, Buffalo, NY, 2002.

[6] Jaberi, F. A., Colucci, P. J., James, S., Givi, P., and Pope, S. B., Filtered Mass Density Function for Large Eddy Simulation of Turbulent Reacting Flows, *J. Fluid Mech.*, **401**:85-121 (1999).

[7] James, S. and Jaberi, F. A., Large Scale Simulations of Two-Dimensional Nonpremixed Methane Jet Flames, *Combust. Flame*, **123**: 465-487 (2000).

[8] Nooren, P. A., Versiuis, M., Van der Meer, T. H., Barlow, R. S., and Frank, J. H., Raman-Rayleigh-LIF Measurements of Temperature and Species Concentrations in the Delft Piloted Turbulent Jet Diffusion Flame, *Applied Physics*, **B71**: 95 (2000).

[9] Sandia National Laboratory, Combustion Research Facility website, http://www.ca.sandia.gov/tdf/, 2002.

[10] Barlow, R. S., Sandia National Laboratories, TNF Workshop website, http://www.ca.sandia.gov/tdf/Workshop.html, 2002.

[11] Peters, N., *Turbulent Combustion*, Cambridge University Press, Cambridge, UK, 2000.

[12] Smith, G. P., Golden, D. M., Frenklach, M., Moriarty, N. W., Eiteneer, B., Goldenberg, M., Bowman, C. T., Hanson, R., Song, S., Gardiner, W. C., Lissianski, V., and Qin, Z., http://www.me.berkeley.edu/gri-mech

[13] De Bruyn Kops, S. M., Riley, J. J., Kosály, G., and Cook, A. W., Investigation of Modeling for Non-Premixed Turbulent Combustion, *Combust. Flame*, **60**:105-122 (1998).

[14] DesJardin, P. E. and Frankel, S. H., Two-Dimensional Large Eddy Simulation of Soot Formation in the Near-Field of a Strongly Radiating Nonpremixed Acetylene-Air Turbulent Jet Flame, *Combust. Flame* **119**:121-132 (1999).

[15] Pitsch, H. and Steiner, H., Large Eddy Simulation of a Turbulent Piloted Methane/Air Diffusion Flame (Sandia Flame D), *Phys. Fluids*, **12**(10): 2541-2554 (2000).

[16] Ladeinde, F., Cai, X., Sekar, B., and Kiel, B., Application of Combined LES and Flamelet Modeling to Methane, Propane, and Jet- A Combustion, AIAA Paper 2001-0634, 2001.

[17] Kempf, A., Forkel, H., Chen, J. Y., Sadiki, A., and Janicka, J., Large-Eddy Simulation of a Counterflow Configuration With and Without Combustion, *Proc. Combust. Inst.*, **28**:35-40 (2000).

[18] Karniadakis, G. E. and Sherwin, S. J., *Spectral/hp Element Methods for CFD*, Oxford University Press, New York, NY 1999.

[19] Sung, C. J., Law, C. K., and Chen, J. Y., An Augmented Reduced Mechanism For Methane Oxidation with Comprehensive Global Parametric Validation, *Proc. Combust. Inst*, **27**:295-303 (1998).

[20] Pope, S. B., Computationally Efficient Implementation of Combustion Chemistry using *in situ* Adaptive Tabulation, *Combust. Theo. Modeling*, **1**:41 (1997).

AUTIGNITION, COMBUSTION INSTABILITY AND WHITE SMOKE UNDER TRANSIENT CONDITIONS WITH JP-8 FUEL

DAAG55-98-1-0285

Naeim A. Henein

Wayne State University
College of Engineering
Center for Automotive Research
Detroit, Michigan, 48202

SUMMARY

A better understanding of the autoignition and combustion processes of JP-8 in diesel engines is essential for the development of electronic controls needed for reliable cold starting of military diesel engines and reduced white smoke signature in the field.
JP-8 has a lower Cetane Number (CN), but a higher volatility than the commercial DF-2 fuel. A mathematical model has been developed to predict the length of the cranking period considering the combined effects of fuel volatility and C.N. The model predictions agreed with the experimental data obtained on a single cylinder diesel engine over a wide range of ambient temperatures.

BACKGROUND

Military vehicles may be required, to operate on JP-8 instead of the commercial DF-2 fuel. Research sponsored by ARO, conducted at the Center for Automotive Research at Wayne State University, indicated that currently produced heavy-duty diesel engines have difficulty in starting on JP-8, particularly at low ambient temperatures. It is important to find out the reason behind this behavior and if it related to the lower CN of JP-8. The starting process can be divided into two major parts: the cranking and acceleration periods. The instability during acceleration has been investigated earlier. This investigation is limited to the cranking period.

THEORETICAL ANALYSIS

A detailed analysis is made to find out the properties of the cylinder gas in each cycle during the cranking period. The concentration of the fuel vapor [F] is calculated considering droplet evaporation, wall-liquid film evaporation, recycled fuel vapor, and the effect of accumulated fuel on the compression ratio.

AUTOIGNITION INDEX (AI):

An autoignition index is developed to account for the effects of fuel vapor concentration [F], cylinder gas temperature T and the activation energy for the global autoignition reactions E. The model assumes that autoignition would start if AI reaches a certain value, determined from experiments at one ambient temperature. As the cranking goes on, AI increases to a critical value above which autoignition and firing would occur.

$$AI = \int_{t_{inj}}^{t_{end}} k_0[F]\exp(-\frac{E}{RT})dt$$

Because of the difficulty in determining the physical properties of distillates such as DF-2 and JP-8, the computations are made for n-paraffins. Paraffins having 7 to 19 carbon atoms are the major components of these fuels.

The predicted number of cranking cycles and CN are shown in figure(1). Paraffins having 7 to 9 carbon atoms would start in the first cycle. This is in spite the fact that the CN for these light hydrocarbons is lower than the CN for the heavier hydrocarbons.

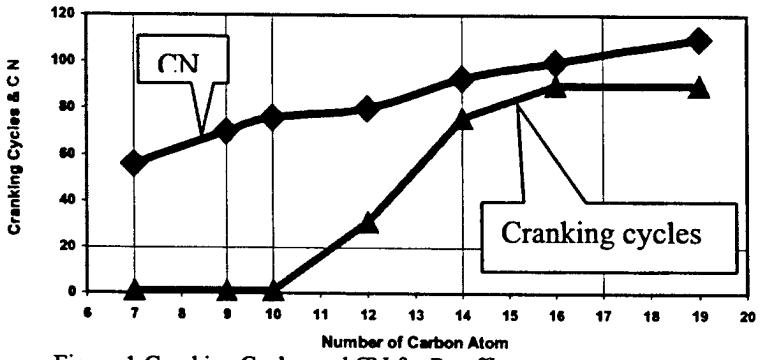

Figure 1 Cranking Cycles and CN for Paraffins

COMPOSITION BETWEEN THE COMPONENTS OF DF-2 AND JP-8

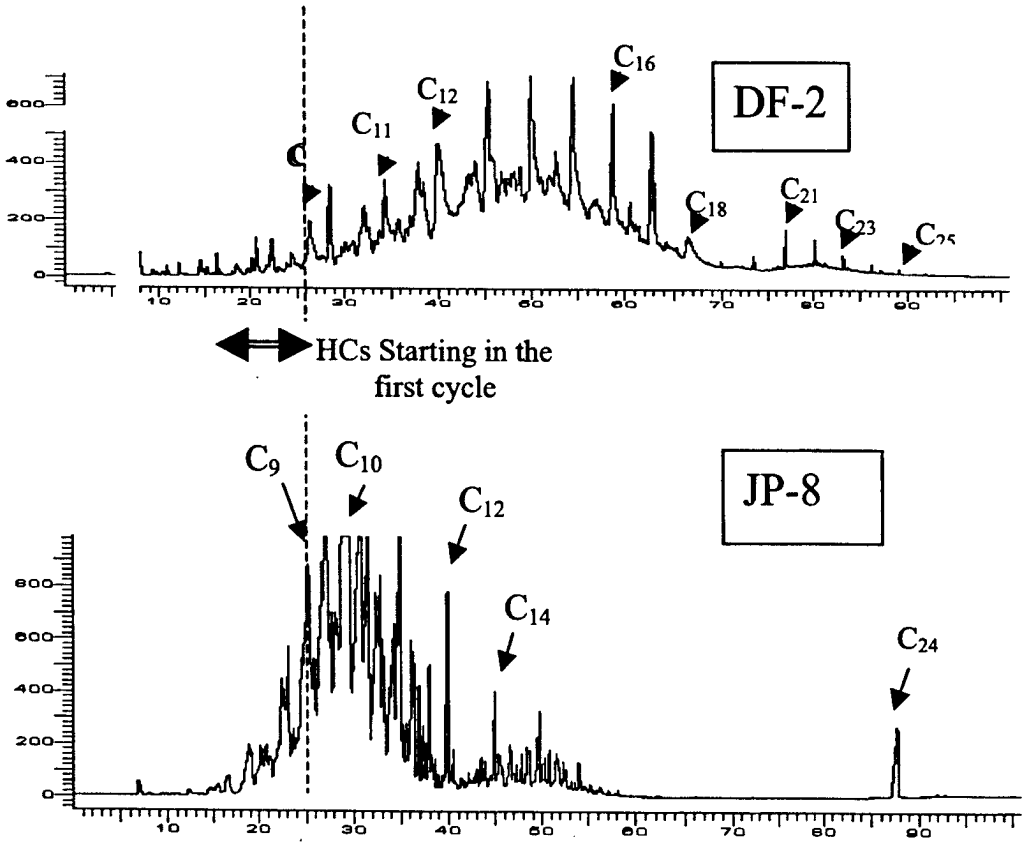

Figure 2. GC analysis of DF-2 and JP-8

TRANSIENT BURNING CHARACTERISTICS OF JA2 PROPELLANT USING EXPERIMENTALLY DETERMINED ZEL'DOVICH MAP*

K. K. Kuo, S. Kumar, and B. Zhang
Department of Mechanical and Nuclear Engineering
The Pennsylvania State University
140 Research Bldg East
University Park, PA 16802, USA
Tel: 814-863-6270 fax 814-863-3203
email: kenkuo@psu.edu

ABSTRACT

Combustion characteristics of JA2 propellant were studied both experimentally and theoretically. Its steady-state burning behavior was investigated using a constant-pressure optical strand burner. The parameters measured were the regression rate, sub-surface temperature profile, and burning surface temperature for different initial propellant temperatures ($-40 < Ti < 60^{\circ}C$) and chamber pressures ($0.1 < P < 62$ MPa). The burning rate data of PSU and US Army for an even broader range of pressure were used in the correlation development. The burning rates were correlated as a function of initial temperature and pressure up to 300 MPa. The temperature sensitivity (σ_p) was found to decrease as pressure increases, reaching an asymptotic value of 0.0024 K^{-1} at very high pressures. Surface temperature data for JA2, determined from the subsurface temperature profile of the JA2 propellant samples, were correlated as a linear function of pressure with coefficients dependent on initial temperature. The two Novozhilov stability parameters were obtained for the operating range in which the surface temperature could be measured using fine-wire thermocouples. Based upon Novozhilov's stability criteria, JA2 propellant was found to have stable burning behavior for the range of operating conditions studied. The Zel'dovich map of JA2 propellant was constructed from the experimental data. This map was then used in a computer simulation to investigate the transient burning characteristics of JA2 propellant under different pressurization rates. From the simulation results, it was found that JA2 propellant only exhibit a mild transient burning effect, which is consistent with the observations obtained from a previous study at PSU using an interrupted burner coupled with a real-time X-ray radiography. The reason for relatively mild transient burning effect of JA2 propellant is the low value of the temperature sensitivity (σ_p) at high pressures and the rapid decay of σ_p as the pressure increases at low pressures ($P < 20$ MPa).

---

*The authors would like to thank Dr. David M. Mann of ARO for his support and encouragement of this work as a part of the research activities under the Grant No. DAAD19-01-1-0573.

STATISTICAL INTERPRETATION OF POWER SPECTRAL DENSITIES MEASURED BY PICOSECOND TIME-RESOLVED LASER-INDUCED FLUORESCENCE IN TURBULENT NONPREMIXED FLAMES

AFOSR Grant Number F49620-00-1-0017

Principal Investigators: Normand M. Laurendeau, Galen B. King and Jay P. Gore

School of Mechanical Engineering, Purdue University, West Lafayette, IN 47907-1288

SUMMARY/OVERVIEW

This research is concerned with measurements of hydroxyl time series using picosecond time-resolved laser-induced fluorescence (PITLIF) in a Re = 10,000 turbulent H_2/N_2 jet diffusion flame. Radial profiles and temporal statistics were obtained, including autocorrelation functions, power spectral densities (PSDs) and integral time scales, for a range of axial locations, x/D = 10-40. Temporal statistics at the jet centerline were also obtained for the axial range x/D = 20-40. The autocorrelation functions were found to be self similar and can be fully characterized by their integral time scales. The time-series statistics were compared to previous data for other non-premixed jet flames. The integral time scales ranged from 0.7 to 2.1 ms at peak [OH] locations and from 0.7 to 1.7 ms along the jet centerline. At the jet centerline, time scales were found to decrease somewhat within the flame and to increase rapidly downstream of the flame tip. This behavior was similar to that observed for previous radial profiles of integral time scales in $CH_4/H_2/N_2$ flames.

TECHNICAL DISCUSSION

Measurements of minor-species concentrations in turbulent flames are of interest owing to their importance in pollutant chemistry and to their use as markers of instantaneous flame structure. Time-scale information can be provided by scalar time series when measurement repetition rates are sufficiently fast to resolve turbulent fluctuations. This approach has been demonstrated for many scalars, including the concentrations of CH[1] and OH[2]. These time series of minor-species concentrations can be recovered by use of picosecond time-resolved laser-induced fluorescence (PITLIF), which directly accounts for potential variations in both the electronic quenching rate coefficient and the background flame emission.

In the previous report, a stochastic simulation was presented to predict some of the measured statistics, including the scalar integral time scale. Recent work involved measurements in nonpremixed swirling flames and the H3 flame. In the present report, time series measurements in a single turbulent (Re = 10,000) hydrogen/nitrogen jet diffusion flame (H3) are reported in an effort to compare measured [OH] time series statistics with those predicted by large eddy simulation (LES)[3]. The chosen fuel mixture and flame geometry have been studied previously by Meier *et al.*[4] using single-pulse spontaneous Raman scattering. The measurements

[1] Renfro, M. W., King, G. B. and Laurendeau, N. M., *Combust. Flame* 122:139-150 (2000).
[2] Renfro, M. W., Guttenfelder, W. A., King, G. B. and Laurendeau, N. M., *Combust. Flame* 123:389-401 (2000).
[3] Dreizler, A., Technische Universität Darmstadt, Personal Communication (2001).
[4] Meier, W., Prucker, S., Cao, M.H., Stricker, W., *Combust. Sci. and Tech.* 118:293 (1996).

reported here represent an ongoing effort to characterize scalar time series for this specific flame, which complements the data provided by Meier *et al.*[4]. Species concentrations and time-series measurements were also obtained in similar flames for a range of Reynolds numbers and fuel mixtures; these will be reported at a later date. Temperature and NO time-series measurements are also planned for the same set of flames in the near future. Concentration measurements were made in a single jet flame with a fuel composition of 50% H_2 and 50% N_2 (by volume). The burner was identical to that used by Meier *et al.*[4] and consisted of a straight stainless steel tube (i.d. 8 mm, length 350 mm) with a thinned rim at the exit. Coflowing dry air was provided by a contoured nozzle (i.d. 140 mm) at an exit velocity of 0.3 m/s. The burner could be translated in the axial and radial directions to change the position of the measuring location. Radial profiles of time-averaged [OH] were obtained at x/D= 10, 20, 30, and 40 in the flame by using a sampling rate of 10 Hz and an averaging time of five seconds. At each height, time-series measurements were obtained at a sampling rate of 12 kHz. Fifty time series of 4096 points each were collected to obtain clean statistics at each measurement location. Time-series measurements were also obtained at the burner centerline for an axial range of x/D = 20-40 with a 16 mm step-size. PDFs, PSDs, autocorrelation functions, and integral time scales were computed from these time series in the same manner as reported by Renfro *et al.*[5,6], including a correction for the measured contribution of shot noise. The signal-to-noise ratio (SNR) for these measurements was about 5 at peak [OH] locations when using an average laser power of 7-8 mW.

Figure 1 shows relative radial profiles, measured for time-averaged [OH] at each height in the flame. For each individual radial profile measurement, a Gaussian function was fit to the data using a least-squares algorithm to determine the time-averaged normalized [OH] peak, profile full-width at half-maximum (FWHM), and peak radial location. The numerical values of the three normalization parameters are given in Table 1, along with time-averaged fluorescence lifetimes, and intermittency parameters which were determined from time-series measurements at the peak [OH] locations. The axial locations x/D = 10 and x/D = 20 display two separate [OH] peaks on either side of the jet centerline. At x/D = 30, a partially formed unimodal [OH] peak can be observed at the centerline, which becomes fully developed farther downstream at x/D = 40.

A representative time series measurement at the peak radial location for x/D = 10 is shown in Fig. 2. The trace represents the first 10 ms of data collected and visually demonstrates fluctuations in the [OH] fluorescence as the [OH] layer moves with respect to the fixed laser beam. The time-series fluctuations as observed in Fig. 2 can be quantified in terms of time-series statistics, i.e., the power spectral density and the autocorrelation function.

Figure 3(a) shows autocorrelation functions for the peak [OH] locations at four different heights in the flame, normalized by their respective integral time scales. A technique developed by Renfro *et al.*[5] utilizing the measured PSDs was employed to eliminate the effects of shot noise. Integral time scales, τ_I, were calculated by numerically integrating each autocorrelation function over 100 data points. This corresponds to about 3 times the integral time scale for the x/D = 10 location, about 7-8 times the integral time scale for the x/D = 20, 30 locations, and about 4.5 times the integral time scale for the x/D = 40 location. A normalized autocorrelation function from a previous H_2/Ar flame (x/D = 20, Re = 9000)[5] and an exponential fit is also plotted for the sake of comparison in Fig. 3(a). Each curve is plotted to a maximum of 5 times its integral time scale. The normalized curve for the previous H_2/Ar flame and those for the present study at axial heights x/D = 20, 30, 40 essentially collapse to a single curve while that for

[5] Renfro, M. W., King, G. B., and Laurendeau, N. M., *Appl. Opt.* 38:4596 (1999).
[6] Renfro, M. W., Gore, J. P., King, G. B., and Laurendeau, N. M., *AIAA J.*, 38:1230 (2000).

x/D = 10 displays a slightly larger decay time. At x/D = 10, the flame sits outside the shear layer and thus the fuel-flow fluctuations do not affect the OH concentrations as strongly. The decay at x/D = 10 is faster than the exponential fit until $t/\tau_I = 1.3$, after which it decays considerably slower than the exponential fit. At all other locations, the decay of the autocorrelation functions is much faster as compared to the exponential fit until $t/\tau_I = 2.5$, after which the overlap with the exponential fit is nearly perfect. Figure 3(b) shows normalized autocorrelation functions at the jet centerline for 11 different axial locations in the range x/D = 20 to x/D = 40; they clearly display a much better collapse when compared to that observed in Fig. 3(a). Since a PSD is the Fourier transform pair to the autocorrelation function, this collapse is observed equally in the frequency-domain statistics. Such collapses of two-time statistics for OH were first shown by Renfro *et al.*[5] in their measurements of H_2/Ar flames, and is also observed in the PSDs of this study, as shown in Figs. 4(a) and 4(b). The collapse implies that the relative distribution of fluctuation rates at a single point in a turbulent flow is the same as that at a different point. Thus, the integral time scale is a good representation of temporal variations in [OH] for the two cases.

Since the two time-series statistics are self-similar when normalized by τ_I, the [OH] fluctuations throughout the single flame of this investigation can be fully described by their variation in integral time scale. Renfro *et al.*[5] found that τ_I increases for OH as the axial height or radial location increases, and as the Reynolds number decreases for their hydrogen/argon flames. Figure 5(a) shows integral time scales as a function of radial location (r/x) for three different axial heights. For these heights, the time scales range from 0.7 to 2.1 ms. At x/D = 10, the time scales are much greater as compared to those at other heights because of the near-field effects of laminarization[2]; hence, that location is not included in Fig. 5. The dashed vertical lines in Fig. 5 mark the peak OH locations at the corresponding heights. The integral time scales at peak locations for x/D = 20 and x/D = 30 are almost equal and that for x/D = 40 is almost twice as large. At x/D = 40, the peak OH concentration occurs at the jet centerline and thus mixing of the combustion products with ambient air is prominent, as this location is past the flame tip. For x/D = 20 and x/D = 30, the integral time scales on the fuel side are nearly constant until the peak OH location and increase rapidly towards the air-side into the mixing regime. Figure 5(b) shows integral time scales and mean [OH] concentrations as a function of axial height along the jet centerline. The τ_I values range from 0.8 to 1.7 ms and dip to their minimum value at x/D = 34. This axial location corresponds to the peak in mean [OH] concentration. This correspondence might be related to thermally-induced flow below the flame tip, followed by air entrainment beyond the flame tip. The time scales, τ_I, are nearly constant in the x/D = 20 to 25 range, decrease somewhat until x/D = 34, and then increase rapidly to significantly higher values farther downstream of the flame tip. This behavior is approximately similar to the trend observed in the τ_I radial profiles. Nevertheless, it clearly demonstrates a significant drop in [OH] concentration fluctuations downstream of the flame tip.

Renfro *et al.*[7] have recently developed a simulation that relates a synthetic mixture fraction time series to one for a reactive scalar, such as OH, using a one-dimensional laminar flamelet approximation. Since the 1-D state relationships for species such as OH do not extend over all mixture fractions, significant scalar intermittency occurs caused by large fluctuations of the instantaneous mixture fraction. This scalar intermittency leads to lower integral time scales for OH as compared to mixture fraction and thus to convoluted time scale profiles. Renfro *et al.*[6] have shown that this simulation accurately captures the radial variation in OH time scales, which reflect a minimum near the location of maximum OH. The reduction in time scale near the tip of the flame in the present measurements possibly reflects a similar dependence on the underlying mixture fraction statistics and the OH state relationship. Hence, future work on this flame will

[7] Renfro, M. W., Gore, J. P., and Laurendeau, N. M., *Combust. Flame* 129:120-135 (2002).

consider extrapolation of mixture fraction time scales using iterative flamelet calculations[6] and comparisons of measured [OH] time-series statistics with those predicted by large eddy simulation (LES)[3].

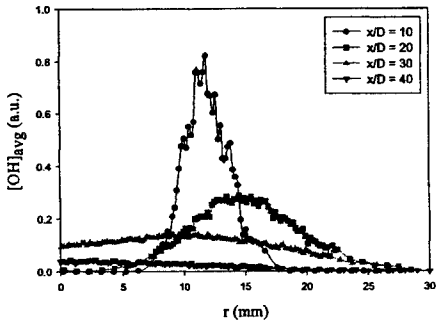

Figure 1: Mean OH radial profiles for x/D = 10-40.

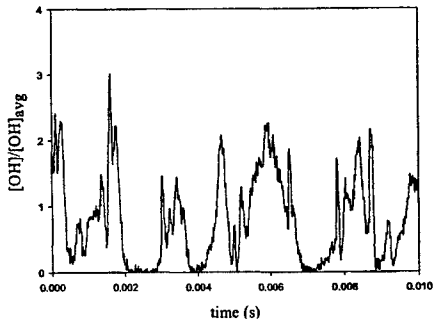

Figure 2: Representative time series at peak for x/D = 10.

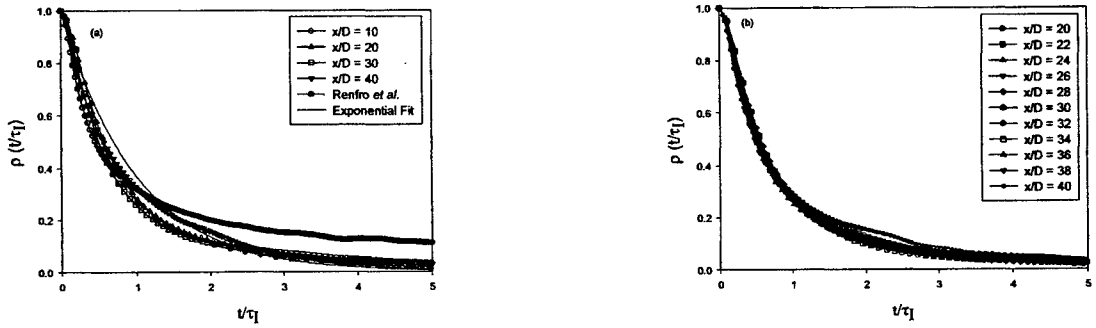

Figure 3: Autocorrelation functions: (a) at peak OH locations, and (b) along the jet centerline.

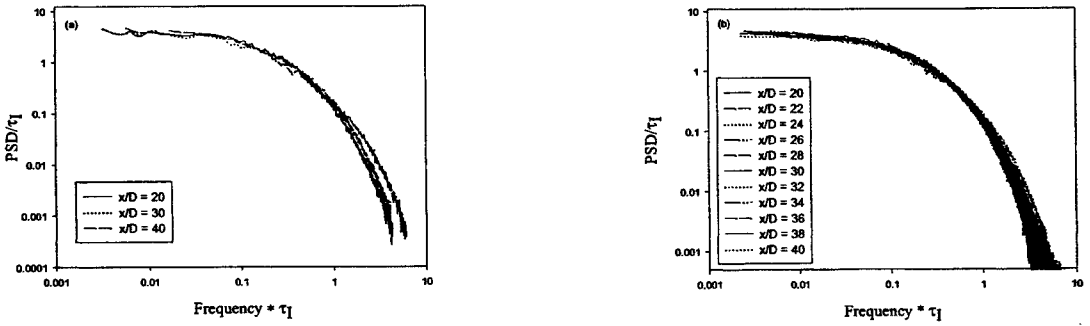

Figure 4: Normalized PSDs: (a) at peak OH locations, and (b) along the jet centerline.

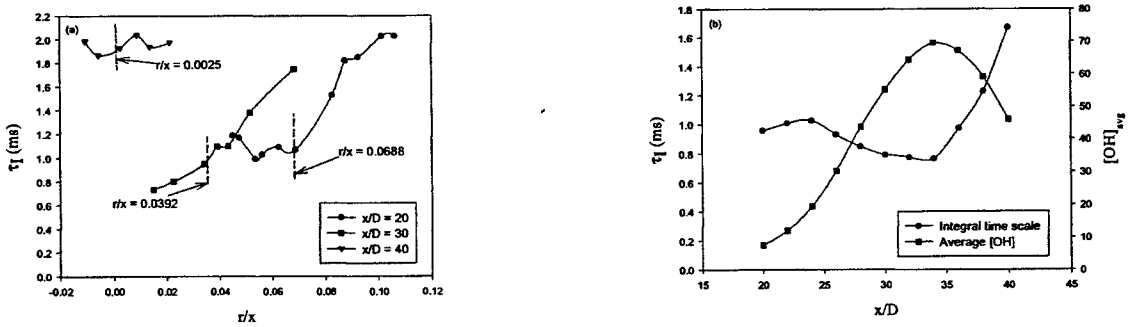

Figure 5: (a) Integral time scales at different axial heights, and (b) Integral time scales and average [OH] along the jet centerline.

Table 1: Normalized [OH] and fluorescence lifetime statistics for radial locations of peak [OH].

Re	x/D	r/x	$[OH]/[OH]_{max}$	FWHM (mm)	Fluor. Lifetime (ns)	I (%)
10000	10	0.15	1	4.35	1.42	14.3
10000	20	0.09	0.35	10.27	1.52	33.0
10000	30	0.04	0.17	22.98	1.60	41.8
10000	40	0.00	0.056	27.02	1.49	63.2

PHYSICAL AND CHEMICAL PROCESSES IN FLAMES

(AFOSR Grant No. F49620-01-1-0029)

Principal Investigator: Chung K. Law

Department of Mechanical and Aerospace Engineering
Princeton University, Princeton, NJ 08544

SUMMARY/OVERVIEW

The objectives of the present program are to develop detailed and simplified chemical kinetics models for hydrocarbon combustion, and to understand and quantify the dynamics of flames. During the reporting period progress were made in the following projects: (1) Laminar flame speeds of mixtures of ethylene, *n*-butane, and toluene at atmospheric pressure were determined using DPIV. Results agree well with calculations based on a detailed kinetic mechanism. A semi-empirical correlation for the mixture flame speed was also developed. (2) Laminar flame speeds of methane/air and methane/oxygen/inert mixtures were determined for pressures up to 60 atmospheres. Comparison with calculations based on GRI-Mech shows increasing disagreement as pressure exceeds 20 atmospheres. The global kinetic parameters governing flame propagation exhibit similarity with those of the second and third explosion limits of the homogeneous hydrogen/oxygen system. (3) Stretch effects on premixed flame pulsation were experimentally studied for the counterflow system. Results substantiate previous computational and analytical findings that positive stretch promotes pulsating instability and consequently flame extinction. (4) Pulsating instability of diffusion flames was experimentally observed, in the spherically symmetric configuration, hence substantiating previous computational and analytical predictions of its existence. Both transport-induced and radiation-induced extinction limits were also demonstrated to occur.

TECHNICAL DISCUSSION

1. Laminar Flame Speeds of Mixtures of Ethylene, *n*-Butane, and Toluene with Air

The atmospheric laminar flame speeds of mixtures of air with ethylene, *n*-butane, and toluene were experimentally determined using DPIV and computationally simulated using a detailed kinetic model over an extended range of equivalence ratios. Binary fuel blends with 1-to-1, 1-to-2, and 2-to-1 molar ratios were examined. Comparison of experimental and computed flame speeds shows generally good agreement (Figs. 1.1 and 1.2). A semi-empirical mixing rule, which requires only knowledge of the flame speeds and flame temperatures of the individual fuel constituents, is shown to provide accurate estimates for the laminar flame speeds of binary fuel blends under the conditions tested. Results are reported in Publication No. 4.

2. Laminar Flame Speeds of Methane/Air Mixtures up to 60 Atmospheres

Using a specially designed high- and constant- pressure combustion chamber, the propagation and morphology of spark-ignited expanding spherical methane flames were imaged using schlieren cinematography and a high-speed digital camera. Stretch-free laminar flame speeds were then determined for methane/air flames up to 20 atm. (Fig. 2.1) and methane/oxygen/helium flames up to 60 atmospheres (Fig. 2.2). Simulations using GRI-Mech 3.0 show moderate deviations for pressures above the range of 20-40 atmospheres.

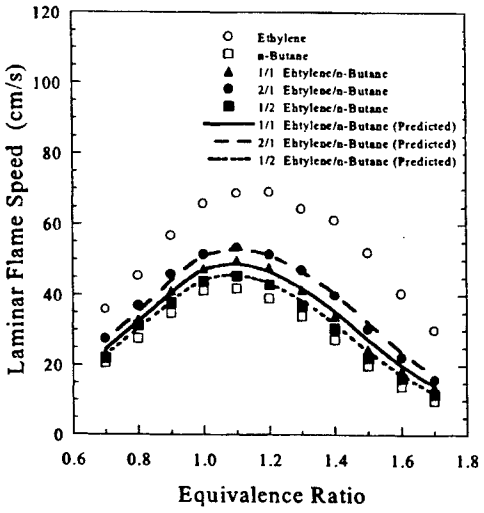

Figure 1.1

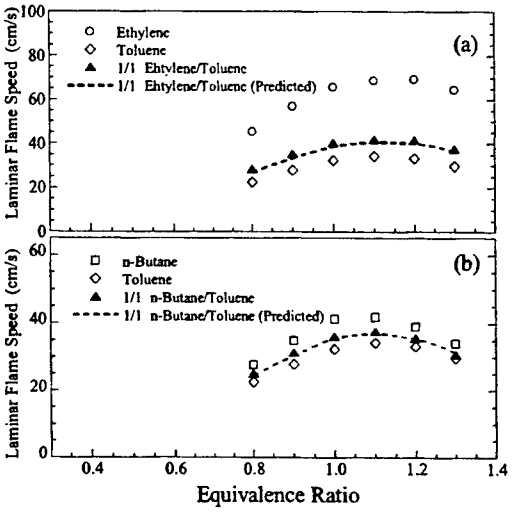

Figure 1.2

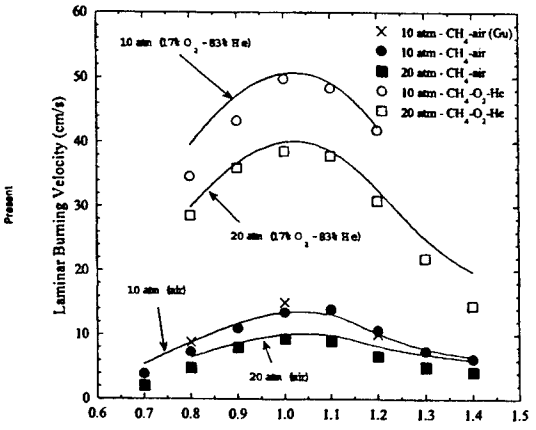

Figure 2.1

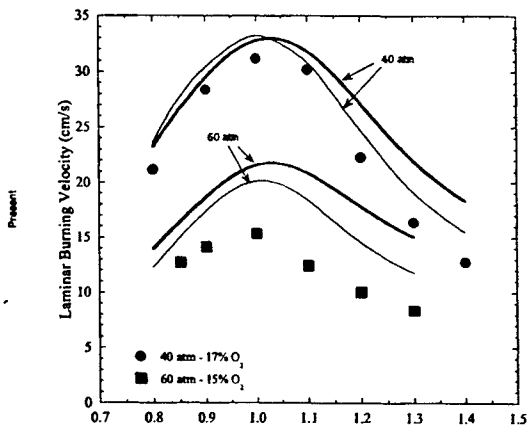

Figure 2.2

Based on the extracted global reaction orders (Fig. 2.3), it was demonstrated that methane/air flames exhibit the same second and third explosion limit behavior commonly associated with homogeneous hydrogen/oxygen mixtures. In particular, with increasing pressure and for certain mixtures, the global activation energy can increase and then decrease, while the overall reaction order can decrease and then increase. The changeover in behavior for methane/air flames occurs at the relatively low pressures of a few

atmospheres. The need to consider intricate chemistry in the simulation of practical phenomena is therefore again demonstrated. This work is reported in Publication No. 5.

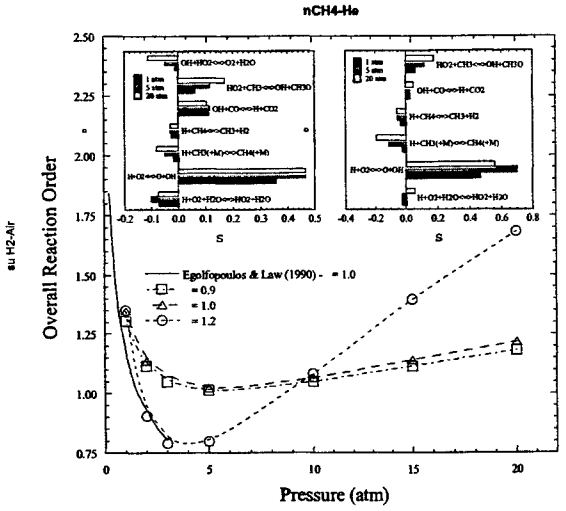

Figure 2.3

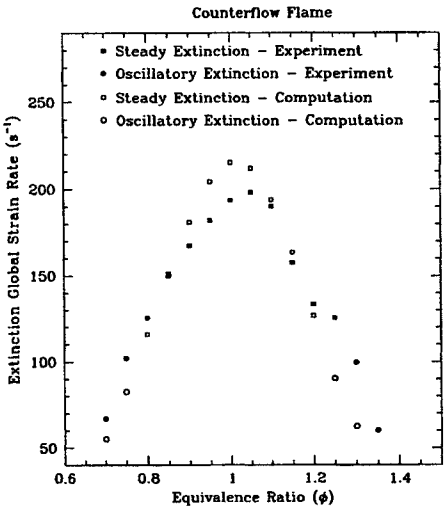

Figure 3.1

3. Pulsating Instability and Extinction of Stretched Premixed Flames

Effects of stretch on the pulsating instability of rich hydrogen/air premixed flames, which are characterized by large Lewis numbers, were first analytically and computationally investigated via the negatively stretched inwardly propagating spherical flame (IPF) and the positively stretched counterflow flame (CFF). Results for the IPF show that the flame initially propagates at the laminar flame speed when the flame radius is large. Oscillation subsequently develops, and is then amplified, damped, and eventually suppressed when the flame is still sufficiently far away from the center. Thus negative stretch tends to suppress the occurrence of pulsating instability, and thereby extend the flammable range of rich hydrogen/air flames beyond that of their unstretched, planar counterpart. Results for the CFF show that oscillation is initiated at an equivalence ratio much smaller than the one-dimensional rich threshold, and that the critical strain rate leading to pulsation is smaller than the corresponding static extinction limit. The pulsating flames are also quasi-steady in nature in that the period of oscillation is larger than the characteristic flame time. As such, the unsteady flame cannot recover once the instantaneous flame temperature is reduced below the corresponding steady-state extinction temperature. Since pulsating extinction occurs at a smaller strain rate than the steady extinction limit, the flame extinguishes in the pulsating instead of the steadily propagating mode, and the flammable range is accordingly narrowed. This work is reported in Publication No. 6.

Experiments were subsequently conducted on CFFs of lean and rich mixtures of methane in $15\%O_2/(O_2+He)$ such that the mixture Lewis number uniformly exceeds unity. Results on the flame luminosity and position showed that these flames do exhibit pulsating instability as the strain rate is increased beyond a critical value, that pulsation develops for sufficiently off-stoichiometric ($\phi \leq 0.80$ and $\phi \geq 1.30$) flames while steady burning and extinction are associated with near-stoichiometric flames, and that the amplitude of the oscillatory flames increases with increasing strain rate until the flame extinguishes. Computations with detailed chemistry and transport showed qualitative and

quantitative agreement with the experimental results (Fig. 3.1), including the oscillation frequency. The calculation further reveals that during the course of large amplitude oscillation, when the instantaneous flame temperature falls below its value at the steady-state extinction limit, the flame cannot revive itself and extinction occurs. This work is reported in Publication No. 7.

4. Oscillatory Extinction of Spherical Diffusion Flames

In the last reporting period the transient behavior of spherical diffusion flames was computationally studied in the transport- and radiation-induced limit of the isola response of flame extinction. Oscillatory instability was observed near both extinction limits, with the oscillation amplitude growing until it becomes large enough to extinguish the flame.

For the present reporting period, experimental verification of the numerical results were conducted for near-limit spherical diffusion flames. Near spherical symmetry of burner-generated diffusion flames were obtained by conducting the experiments in reduced pressures. Various inert gasses (N_2, CO_2, He) were used to dilute the oxidizer in order to change the Lewis number and radiation properties of the mixture so that both the transport- and radiation-induced limits could be achieved. Extinction was triggered by gradually decreasing the fuel concentration. Results show that, at the transport induced limit, extinction is characterized by sudden quenching of the flame as demonstrated by a rapid decrease of the radiometer signal voltage. However, at the radiation-induced limit extinction is preceded by oscillations in the flame luminosity that grows in amplitude before extinction. The observations qualitatively agree well with the computation, although quantitative difference exists. These differences could be due to the neglect of radiation re-absorption in the calculation. This work is reported in Publication No. 8.

JOURNAL PUBLICATIONS

1. "Theory of complex CSP for chemistry reduction and analysis," by T. Lu, Y. Ju, and C. K. Law, *Combustion and Flame*, Vol. 126, pp. 1445-1455 (2001).
2. "Steady and pulsating propagation and extinction of rich hydrogen/air flames at elevated pressures," by E. W. Christiansen, C. J. Sung, and C. K. Law, *Combustion and Flame*, Vol. 124, pp. 35-49 (2001).
3. "Augmented reduced mechanisms for NO emission in methane oxidation," by C.J. Sung, C.K. Law, and J.-Y. Chen, *Combustion and Flame*, Vol 125, pp. 906-919 (2001).
4. "Determination of laminar flame speeds of fuel blends using digital particle image velocimetry: ethylene, n-butane, and toluene mixtures," by T. Hirasawa, C.J. Sung, A. Joshi, H. Wang, and C.K. Law, *Proc. Combust. Inst.*Vol. 29, in press.
5. "Outward propagation, burning velocities, and chemical effects of methane flames up to 60 atmospheres," *Proc. Combust. Inst.*, Vol. 29, in press.
6. "On stretch-affected pulsating instability in rich hydrogen/air flames: asymptotic analysis and computation," by C.J. Sung, A. Makino, and C.K. Law, *Combustion and Flame*, Vol 128, pp. 422-434 (2002).
7. "Pulsating instability and extinction of stretched premixed flames," by E.W. Christiansen and C.K. Law, *Proc. Combust. Inst.*, Vol. 29, in press.
8. "Oscillatory extinction of spherical diffusion flames," by S.W. Yoo, E.W. Christiansen, and C.K. Law, *Proc. Combust. Inst.*, Vol. 29, in press.

Acoustic Sensing and Actuation in Gaseous Flows

Contract # DAAD19-01-0571

Principal Investigator: Tim Lieuwen

School of Aerospace Engineering
Georgia Institute of Technology
Atlanta, GA 30332-0150

SUMMARY/OVERVIEW:

This program is developing acoustic techniques for non-intrusive sensing and actuation of gas flows. Work performed to date has focused on the use of acoustic absorption measurements for gas mixture characterization. During the first year of the program, a facility was designed, fabricated and tested for making these absorption measurements. Measurements of the absorption characteristics of air, carbon dioxide, and various mixtures containing carbon monoxide and nitric oxide were obtained. Practical procedures for reducing these data into more fundamental values of absorption coefficient that account for the effects of reverberation and diffraction were developed. Data obtained from carbon dioxide mixtures shows good agreement with that found in the literature using much more sensitive, but industrially impractical methods. Although not the primary focus of this study, these data suggest a low cost method for making sensitive measurements of low levels (on the order of 0.01%) of water vapor. Plans are underway for using these measurements to characterize the level of mixing between multi-component gas mixtures.

TECHNICAL DISCUSSION:

Background

The objectives of this program are to develop acoustic techniques for 1) sensing and 2) actuation in gas flows. Work performed in this first year focused on the former item. Specifically, this work focused on the use of acoustic absorption measurements to characterize gas mixtures. The objective of this work is two fold: 1) determine the accuracy and sensitivity with which acoustic absorption can be measured in practical environments, and 2) demonstrate the use of acoustic absorption measurements to infer the level of molecular mixedness between constituents in a multi-component gas media.

Technical Approach

Acoustic waves propagating through a gaseous media are damped by absorption processes. Absorption arises from viscosity, thermal conductivity and the relatively slow relaxation of the vibrational modes of gas molecules[1]. Such vibrational relaxation processes damp acoustic waves through the following mechanism: the isentropic gas compression

occurring in an acoustic perturbation cause perturbations in the gas temperature and, thus, local translational energy. Through molecular collisions, the translational energy is redistributed to the rotational and vibrational degrees of freedom. Thus, in very low frequency acoustic perturbations, energy is fed from the translational to the vibrational energy modes of the gas during the compressive phase of the acoustic cycle. This energy is then returned from the vibrational to the translational energy modes during the rarefaction phase of the cycle. While gas translational and rotational modes equilibrate very quickly, the vibrational mode requires extensively longer. Thus, even at relatively low frequencies the internal energy exchange processes cannot respond sufficiently quickly to acoustic fluctuations, with the affect that energy is not removed from or returned to the acoustic wave in phase with its oscillations. These nonequilibrium affects cause the acoustic wave to be damped. Maximum acoustic damping occurs at the "relaxation frequency", f_v (the inverse of the characteristic vibrational relaxation time), whose exact value depends upon the molecular species. The damping of acoustic waves by these vibrational relaxation processes is *generally the dominant damping mechanism in gaseous media over a wide range of frequencies*.

These results suggest that the amount of acoustic energy absorbed at certain frequencies can be used to infer the rate of vibrational relaxation in a gaseous mixture and, in turn, as a diagnostic of various gas properties

Facility Development

A facility for measuring the absorption characteristics of gaseous media was designed, fabricated, and tested. It consists of a 96 cm long, 30.5 cm diameter plexiglass tube that is capped at both ends. The length of the chamber can be varied by moving one wall in a piston like arrangement. A ½", type 4191 Bruel and Kjaer microphone is situated at the fixed end of the tube. Acoustic disturbances were generated with a 38 mm diameter, type 616341 electrostatic Polaroid transducer which is situated at the movable end of the wall. These transducers were biased with 150 VDC, and driven at 9 VAC peak-peak with a Hewlett Packard type 33120A function generator. The chamber is sealed so that various gas mixtures can be interrogated with minimal contamination from the ambient environment. A vacuum pump is used to evacuate the chamber so that a gas mixture with the desired concentration can be placed inside the chamber. To achieve high degrees of purity, a procedure of multiple evacuations and fills was employed.

Carbon Dioxide Absorption Measurements

Carbon dioxide was chosen as the primary gas to use in the remainder of these tests for characterization of gas mixedness. It was chosen because of its prominence as a species in combustion applications, as well as its relatively low vibrational temperature, resulting in high levels of absorption at room temperatures.

Tests performed to date have concentrated on determining the accuracy with which absorption in carbon dioxide can be measured. Because the relaxation frequency of carbon dioxide is strongly dependent upon the ambient level of water vapor, tests were conducted with high purity gases. The chamber was evacuated to a pressure of 0.1 bar and filled to atmospheric pressure with high purity carbon dioxide. This procedure was repeated several times so that the concentration of ambient gases was reduced to very low levels. By monitoring the change in absorption with time, it was then possible to observe the changing level of water vapor in the chamber due to diffusion from the ambient atmosphere into the test chamber. Figure 1 plots the dependence of the amplitude of 50 kHz pulses at several instants in time from

the initiation of the test. As clearly shown in the figure, the amplitude changes by a factor of eight over a four hour period.

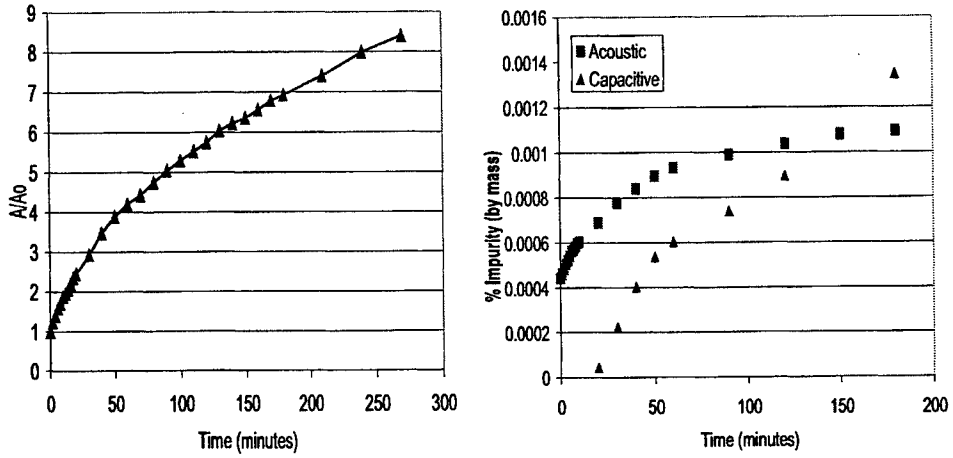

Figure 1. (Left) Variation of amplitude of 50 kHz acoustic signal with time. (Right) Comparison of calculated dependence of water vapor concentration upon time, using measured absorption values and humidity sensor.

The change in concentration of water vapor in the chamber can be inferred from these measurements and using theory for acoustic absorption and published measurements of the dependence of the relaxation frequency of carbon dioxide upon water vapor concentration. Figure 1 also plots the temporal evolution of the water vapor concentration that was calculated using absorption measurements obtained at 40 and 50 kHz. As can be seen in the figure, this simple analysis suggests that the initial water vapor concentration was around 0.02% (by mass) and monotonically increased to 0.07% after four hours.

These predicted values were compared to measurements of the water vapor concentration using a capacitive dielectric type humidity sensor. It should be emphasized that this sensor is not designed for such low level humidity measurements and thus its results have a high uncertainty. As can be seen, the measurements give reasonable results at the "higher" humidity levels, but not at lower values. It is difficult at this point to assess how much of this deviation is due to shortcomings in the acoustic absorption technique because of the factors 1) large uncertainties in humidity sensor readings, particularly at low values, 2) spatial nonuniformity of the water vapor concentration in the chamber. However, as can be seen from Figure 2, there is nearly a linear relation between the water vapor concentration from these two techniques. The two curves were obtained on different days, indicating the repeatability of the measurement.

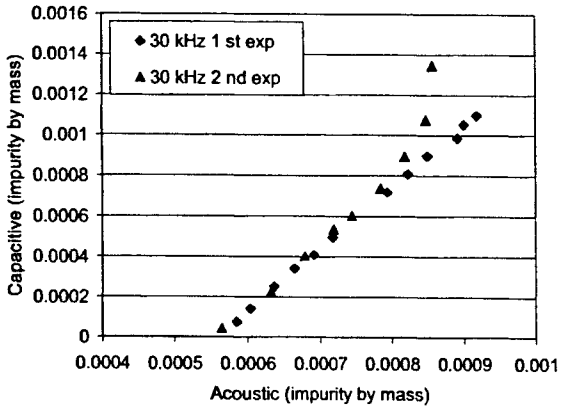

Figure 2. Comparison of humidity ratios determined from acoustic absorption and capacitive dielectric sensor.

In addition, Figure 3 plots a comparison of the measured and predicted acoustic amplitudes at frequencies from 10-40 kHz. The figure shows that the agreement is excellent.

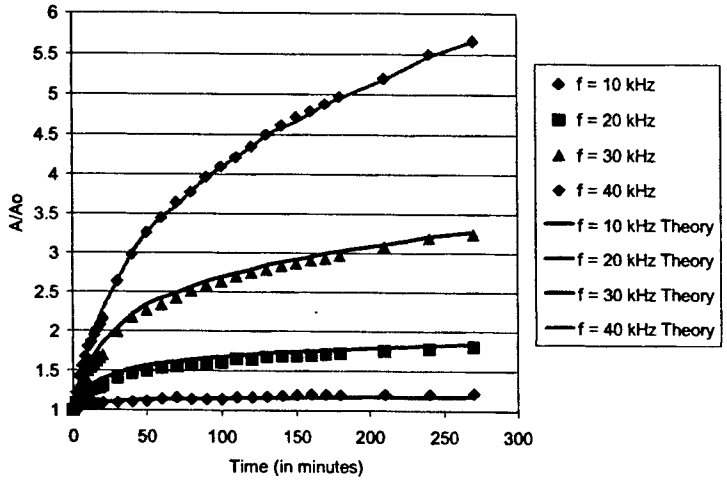

Figure 3. Comparison between predicted and measured values of acoustic signal at frequencies of 10, 20, 30, and 40 kHz.

Ongoing and Future Work

Work performed to date suggests that acoustic absorption can be measured with reasonable accuracy and sensitivity to be used as a diagnostic in practical geometries. The objective of our ongoing and future work is to utilize these measurements as a diagnostic. Specifically, we plan to first assess the feasibility of using acoustic absorption to characterize the degree of mixing between two gases. The basic idea of this approach is the following: the vibrational relaxation frequency of a particular molecule and, thus, the amount of absorption, depends upon what other molecules it is in contact with. Thus, the absorption characteristics of a multi-component gas mixture should vary depending upon the relative degree of mixing among its constituents.

References

[1] Pierce, A., *Acoustics: An Introduction to its Physical Principles and Applications*, Acoustical Society of America: New York, 1991.

A PHENOMENOLOGICAL MODEL FOR AUTOIGNITION IN DIRECT INJECTION DIESEL ENGINES

(Grant/Contract Number DAAG55-98-I-0433)

Principal Investigators: A. M. Mellor*, S. L. Plee, R. J. Tabaczynski

*Vanderbilt University, VU Station B 351592
2301 Vanderbilt Place, Nashville, TN 37235-1592

SUMMARY/OVERVIEW:

The focus of the program is developing engineering models for direct injection (DI) diesel performance and emissions. To date emissions of oxides of nitrogen (NO_x) have received primary emphasis. A quasi-steady NO_x model, intended for use as a preliminary design tool, has been developed and used to examine the effects of in-cylinder mixing, exhaust gas recirculation (EGR), and multiple fuel injections. Insight gained from the quasi-steady NO_x model lead to the development of a NO_x model for use in cycle simulation and CFD codes which has been shown to correlate emissions for four heavy-duty diesel engines. Present work is focused on development of phenomenological DI diesel ignition, combustion, NO_x, and soot models for inclusion in cycle simulation type codes that predict engine performance and emissions. The proposed phenomenological ignition model and data acquired for model validation are discussed below.

TECHNICAL DISCUSSION:

The objective of the present work is to develop and validate a DI diesel phenomenological ignition model. The model will include the effects of charge temperature, charge pressure, exhaust gas recirculation (EGR), mixing between fuel and cylinder charge, wall impingement, and work done on the ignition site by surrounding charge. Ignition delay data acquired from a single-cylinder DI diesel research engine will be used for model validation.

Ignition delay models used in cycle simulation codes typically lump mixing and chemical processes into a term that has the form of an inverse reaction rate coefficient.

$$\tau_{id} = AP_{ch}^{-n} \exp\left(\frac{E_A}{RT_{ch}}\right) \quad (1)$$

where P_{ch} and T_{ch} are the cylinder charge pressure and temperature, respectively. Because the chemical and physical processes are lumped together, the model constants can not be determined a priori and experimental calibration data are required for each test setup. The proposed model includes both the physical and chemical processes governing ignition and thus may allow for more accurate prediction and for model constant determination from test setup conditions, not experimental data.

Description of the Ignition Process: In the DI diesel engine fuel is injected in the liquid phase, typically at temperatures between 400 and 450 K. As the spray progresses through the

combustion chamber it entrains high temperature cylinder charge causing the liquid fuel to evaporate. The liquid fuel will reach a steady-state length, which in DI diesel engines is typically in the range of 15 to 40 mm dependent upon operating conditions [1-3]. Beyond the liquid fuel penetration length, only fuel vapor exists. The vapor fuel will continue to penetrate across the cylinder entraining more charge.

By the time of ignition the DI diesel fuel plume will look similar to that shown in Fig. 1. The works of Dec [1] and Higgens and Siebers [2] indicate that ignition occurs volumetrically throughout the dashed line region in Fig. 1 and that this region is very well mixed with the equivalence ratio being between 2 and 4 for typical DI diesel operating conditions.

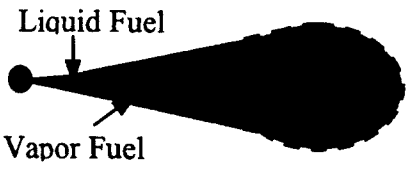

Figure 1: Schematic of a single DI diesel spray plume at the time of ignition based on work of Dec [1] and Higgens et al. [2].

One might argue that ignition should occur along the periphery of the spray plume where conditions are near stoichiometric. However, laser diagnostic images of the spray plume show that the shear layer, where conditions are near stoichiometric, is very thin [1,2] indicating that it is highly strained. These results suggest that the strain rate in the shear layer is such that ignition can not be supported and that conditions inside the fuel plume are more conducive for ignition.

Model Formulation: To determine the ignition timing, a potentially ignitable eddy is examined. At the time of injection the eddy is composed entirely of liquid fuel at the fuel injection temperature. As the eddy penetrates into the cylinder it entrains charge and the fuel evaporates. The fuel eddy will continue to entrain charge, thereby increasing its temperature and oxygen concentration, until it eventually reaches conditions favorable for ignition.

Theoretically, the first eddy to be injected will be the first to ignite as it has the longest time to evaporate and mix with charge. This theoretical result is supported by experiments which show that ignition occurs near the tip of the fuel spray, as discussed above [1-3]. Further, these experiments show that by the time of ignition all of the fuel in the ignition region has evaporated. Therefore the heat required for evaporation must be included in the model, but the evaporation process or rate is not of importance since it is known that the eddy will contain only vapor fuel at the time of ignition.

The first law of thermodynamics for the potentially ignitable eddy in which all of the fuel has evaporated is

$$\dot{\omega}_f Q_{LHV} + h_{ch}\frac{dm_e}{dt} = \frac{d}{dt}\left(m_e C_{v,e} T_e\right) + P_{ch}\frac{dV_e}{dt} \qquad (2)$$

where the subscripts e and ch indicate eddy and charge, respectively . The heat addition term is given by the rate of fuel consumption, $\dot{\omega}_f$, multiplied by the lower heating value of the fuel, Q_{LHV}. The internal energy of the eddy is calculated using the eddy mass, constant volume specific heat, and temperature of the eddy. The work term is the result of work being done on the eddy by the surrounding charge. Note that the eddy entrainment rate, (dm_e/dt), is always positive because eddy mass loss is not considered.

For this preliminary formulation of the ignition model, the fuel consumption rate is calculated using a one-step reaction of the fuel with oxidizer. For the relatively small range of temperatures and pressures encountered in diesel engines prior to ignition, a one-step reaction mechanism is typically adequate. In the event that this work reveals that a one-step reaction mechanism is inadequate then skeletal kinetic models may be explored.

Assuming that pressure is uniform throughout the cylinder, the volume of the eddy can be written in terms of the bulk charge conditions using the ideal gas law (note that the charge volume is equivalent to cylinder volume).

$$V_e = V_{ch}\frac{m_e R_e T_e}{m_{ch} R_{ch} T_{ch}} \tag{3}$$

The charge mass and molecular weight are assumed to be constant. Including the fuel reaction rate, expanding the internal energy term, and substituting for the pressure using the ideal gas law, Eq. (2) can now be solved for the rate of eddy temperature change.

$$\frac{dT_e}{dt} = \frac{A[fuel]^a[oxid]^b \exp(-E/RT_e)Q_{LHV}}{\rho_e C_{p,e}} - \frac{T_e}{C_{p,e}}\frac{dC_{P,e}}{dt} - \frac{C_{P,e}T_e - C_{P,ch}T_{ch}}{\tau_{mix} C_{P,e}} - \frac{R_e T_e}{C_{p,e} V_{ch}}\frac{dV_{ch}}{dt} + \frac{R_e T_e}{C_{p,e} V_{ch} T_{ch}}\frac{dT_{ch}}{dt} \tag{4}$$

where A is the pre-exponential factor, ρ is density, and a and b are the fuel and oxidizer orders of reaction, respectively. The characteristic mixing time, τ_{mix}, is defined as

$$\frac{1}{\tau_{mix}} = \frac{1}{m_e}\frac{dm_e}{dt} \tag{5}$$

and is discussed in more detail below. The eddy fuel and oxidizer concentrations are determined from species conservation equations and the temperature of the eddy is given by

$$T_e = T_f + \int_{SOI}^{t} \frac{dT_e}{dt} dt - \frac{m_f h_{fg}}{m_e C_{p,e}} \tag{6}$$

where dT_e/dt is given by Eq. (4). Though Eq. (6) can be solved for the temperature of the eddy from SOI to ignition, the temperature given by Eq. (6) is not representative of that found in the eddy until the time at which all of the fuel in the eddy has evaporated.

Ignition will occur when the first term on the right of Eq. (4) (reaction rate term) becomes large. Once ignition occurs, combustion models will be initiated to predict the rate of heat release.

The laser diagnostic results reviewed above indicate that ignition occurs in the head of the spray plume and that the mixture within this plume appears well mixed. Therefore, the eddy entrainment rate, and thus τ_{mix}, may be determined from the entrainment rate into the plume head. Using an idealized spray plume model, like that presented by Naber and Siebers [4], in which the spray cone angle is assumed to remain constant as the spray penetrates into the cylinder, an expression for this entrainment rate can be derived. Evaluation of such an expression is presently underway.

A method of accounting for wall effects on the ignition process will be part of future work as well. Wall impingement is expected to influence the ignition process through the eddy entrainment rate and also by heat transfer. Experimental results and phenomenological wall impingement models already presented in the literature will be the starting point for this research.

Experimental: Tests are conducted using a 0.75 L single-cylinder research engine equipped with a piezo-electric controlled common rail injection system and operating with a low sulfur research grade #2 diesel fuel. The injector current signal, needle lift, and cylinder pressure are measured throughout the cycle at a resolution of 0.1 CAD and averaged over 300 cycles to obtain data representative of each steady-state operating condition. The air and fuel flow rates to

the engine, the percent exhaust gas recirculated into the intake charge, and the intake manifold temperature and pressure are also measured.

The injection characteristics of the experimental injector have been studied using injection rate data provided by the injector manufacturer. From these data, correlations for the start of injection (SOI) timing and injection rate profile have been developed in terms of the injector current signal and injector needle lift.

Ignition timing is determined from the apparent rate of heat release, which is calculated from a first law analysis of the cylinder contents. Ignition in this study is defined as the time at which the heat release rate reaches 5% of its peak value. The ignition delay is the ignition time minus the SOI time.

The test matrix is designed to study the effects of temperature, pressure, charge composition, and mixing on the ignition process in the DI diesel engine. The effects of temperature and pressure are examined by varying the temperature and pressure of the intake charge. The effect of charge composition is investigated using EGR. To study the effect of mixing on the ignition process, injection pressure, mass of fuel injected, and engine speed sweeps are conducted. Each portion of the test has been designed to keep constant for each sweep as many operating parameters affecting ignition as possible. Sample results are shown in Fig. 2.

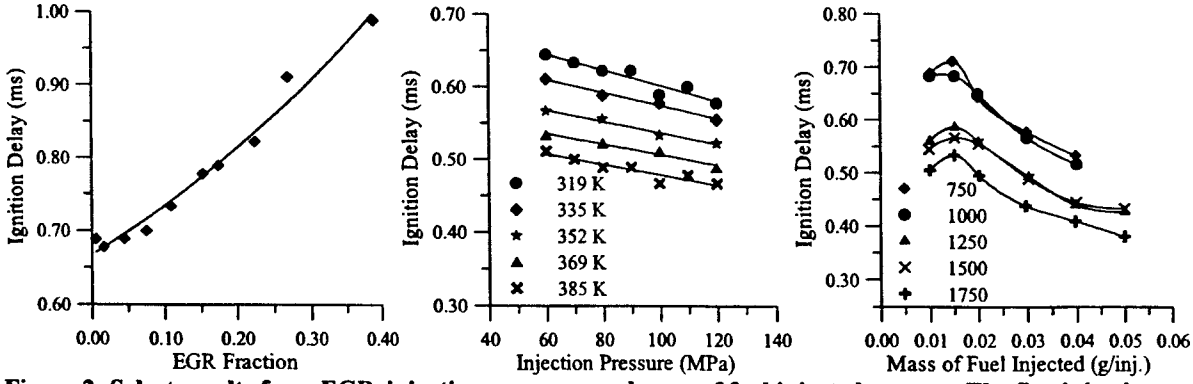

Figure 2: Select results from EGR, injection pressure, and mass of fuel injected sweeps. The five injection pressure sweeps shown are for the five intake manifold temperatures shown in the legend. The five fuel injection quantity sweeps are for the five engine speeds shown in the legend.

Future Efforts: Future efforts will be focused on evaluation of the proposed mixing time and study of the effects of wall impingement on the ignition process. Work is also underway on development of phenomenological DI diesel combustion and soot models. A combustion model obtained from the U.S. Army Tank and Automotive Command (TACOM) [5] is the starting point for the combustion model work. A NO_x model developed previously at Vanderbilt will then be included with the other models to provide a simulation package for the prediction of DI diesel engine performance and emissions of NO_x and soot.

References:

1. Dec, J. E. (1997), "A conceptual model of DI Diesel combustion based on laser-sheet imaging," SAE Paper 970873.
2. Higgins, B., Siebers, D., and Aradi, A. (2000), "Diesel-spray ignition and premixed-burn behavior," SAE Paper 2000-01-0940.
3. Siebers, D. L. (1999), "Scaling liquid-phase fuel penetration in diesel sprays based on mixing-limited vaporization," SAE Paper 1999-01-0528.

4. Naber, J. D. and Siebers, D. L. (1996), "Effects of gas density and vaporization on penetration and dispersion of diesel sprays," SAE Paper 960034.
5. Schihl, P. J. (1998), "Development of global mixing, combustion, and ignition models for quiescent chamber direct-injection diesel engines", Ph.D. Dissertation, Dept. Mech. Eng. University of Michigan, Ann Arbor.

PDF MODELLING OF TURBULENT COMBUSTION

AFOSR Grant F-49620-00-1-0171
Principal Investigator: Stephen B. Pope

Mechanical & Aerospace Engineering
Cornell University
Ithaca, NY 14853

SUMMARY

Significant advances have been made in three different aspects of the modeling of turbulent combustion. First, the rate-controlled constrained equilibrium method (RCCE, Keck 1990) has been combined with the *in situ* adaptive tabulation algorithm (ISAT, Pope 1997) to produce a unified dimension-reduction/storage-retrieval methodology for the computationally-efficient implementation of combustion chemistry (Tang & Pope 2002). Second, ideas from the conditional moment closure (CMC, Klimenko & Bilger 1999) and the mapping closure (Chen et al. 1989) have been combined to produce a new approach for modeling molecular mixing in turbulent reactive flows (Klimenko & Pope 2002). And third, a methodology has been developed for obtaining accurate stochastic models for Lagrangian velocity (Pope 2002a) and acceleration (Pope 2002b) based on DNS data from homogeneous turbulent shear flow. These three developments are described further in the following sections. In addition, in collaboration with the group at Buffalo, progress has been made on combining the PDF and LES methodologies (Gicquel et al. 2002).

EFFICIENT IMPLEMENTATION OF COMBUSTION CHEMISTRY

It is computationally prohibitive to use detailed hydrocarbon chemistry directly in turbulent combustion calculations. Two separate approaches have been taken to reduce the computational burden: dimension reduction; and, storage/retrieval. Tang & Pope (2002) have combined these two approaches into a unified methodology. Dimension reduction is achieved through rate-controlled constrained equilibrium (RCCE Keck, 1990); and storage/retrieval through the ISAT algorithm (Pope 1997). In this context, RCCE is preferred over other reduction methodologies (e.g., QSSA, ILDM), because of the guaranteed existence and continuity of the implied low-dimensional manifold.

The combined ISAT-RCCE methodology is tested for a pairwise-mixing stirred reactor (PMSR) using the 31-species GRI 1.2 mechanism for methane. Three different tests (referred to as *C1*, *C2* and *C3*) are performed. In *C1* the constrained species are H_2O, CO_2, O_2, CH_4 and CO. Three more species (H_2, OH, and O) are added to form the constraint subspace in *C2*, and in *C3* another three species (CH_3, C_2H_2 and C_2H_4) are included. Additional constraints are imposed on all 4 elements and enthalpy, and hence the dimension reductions are from 32 to 10, 13 and 16 for the three cases, respectively. To test the accuracy of the algorithm, we solve the entire ODE system (32-dimensional) by direct integration (DI) to get the accurate solution. Figure 1 shows the relative error in species compositions, temperature and density against their reference values for one particle (advanced over 2000 time steps in the statistically stationary state). It can be observed that, as the number of constraints increases, the error in the constrained species decreases. For *C3*, the relative errors in major species (including CO and H_2) are under 3% with the errors of other constrained species being less than 10%.

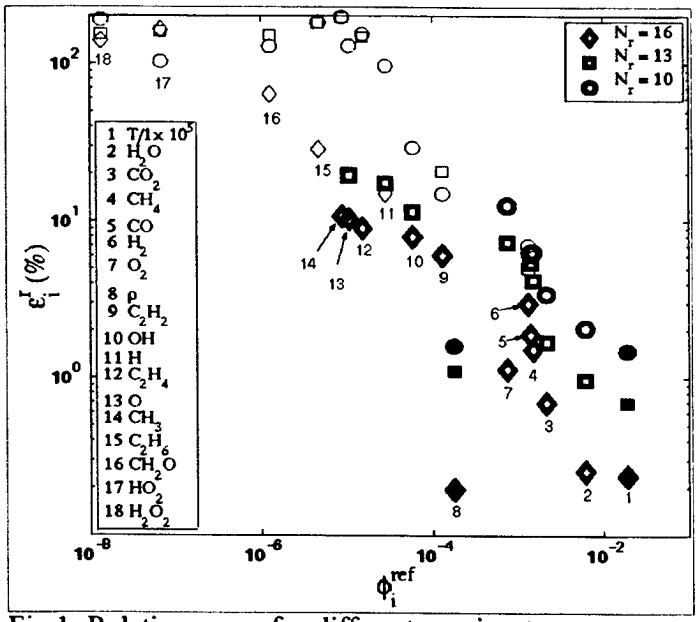

Fig.1: Relative errors for different species, temperature and density, against the reference value for each quantity, for different numbers of represented species in ISAT-RCCE. From the PMSR test case of Tang & Pope (2002).

In Figure 2, the accuracy of ISAT-RCCE is compared to that of the augmented reduced mechanism of Sung et al. (1998)—which is based on the same detailed mechanism and which has the same number of degrees of freedom. It may be seen that the two methods have comparable accuracy.

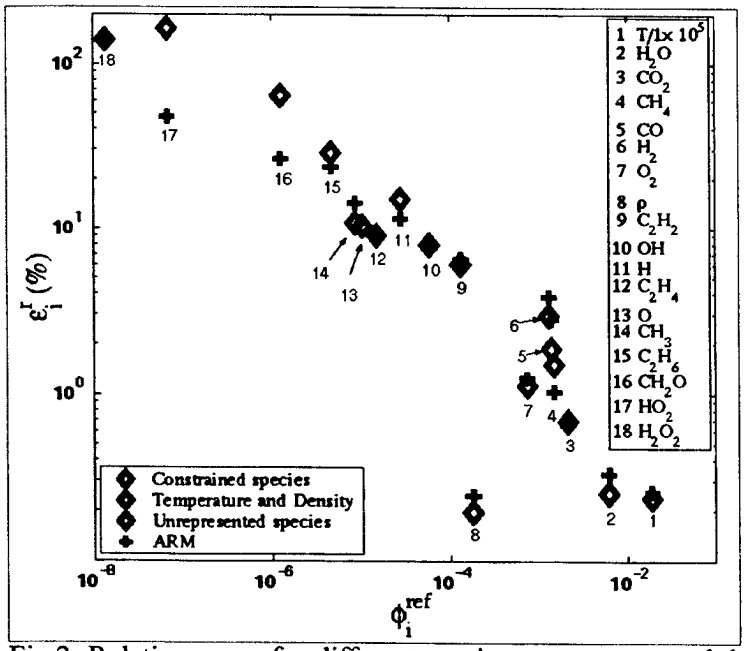

Fig.2: Relative errors for different species, temperature and density, against the reference value for each quantity, from the PMSR test case: comparison of ISAT-RCCE (Tang & Pope 2002) with the augmented reduced mechanism (Sung et al. 1998).

MODELLING TURBULENT MIXING

In PDF methods for turbulent combustion, the modeling of molecular diffusion is both crucial and difficult. In Klimenko & Pope (2002) a new methodology is developed—multiple mapping conditioning (MMC)—which combines ideas from the mapping closure (Chen et al. 1989), and from the conditional moment closure (Klimenko & Bilger 1999). In part, this approach extends the particle implementation of the mapping closure to multiple scalars.

Remarkably, the MMC model admits an analytic solution for the case of two passive scalars evolving from a triple-delta-function initial condition. This case was studied using DNS by Juneja & Pope (1996), with the three delta functions located at the vertices of an equilateral triangle in the two-dimensional composition space. The evolution predicted by MMC (Fig. 3) is in excellent agreement with the DNS. No other mixing model has been shown to be even qualitatively correct for this case.

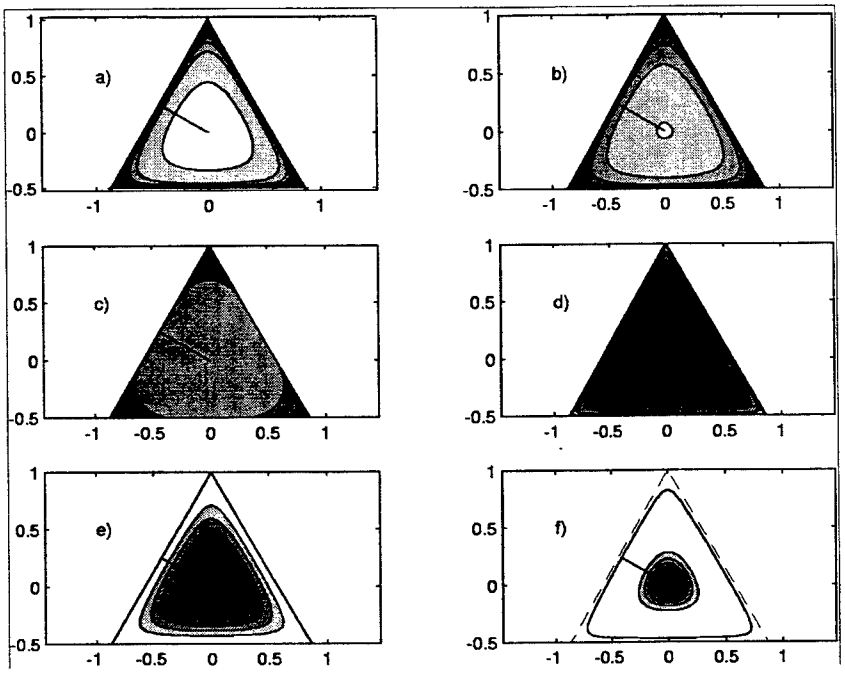

Fig.3: Temporal evolution (a-f) of the joint PDF of two passive scalars from a triple-delta-function initial condition according to the MMC closure of Klimenko & Pope (2002).

STOCHASTIC MODELLING OF VELOCITY AND ACCELERATION

In PDF methods, the turbulence modelling is embodied in a stochastic model for the velocity following a fluid particle (see e.g., Pope 2000). The standard model—the generalized Langevin model—involves tensor coefficients. In Pope (2002a) a methodology is developed to determine these coefficients from DNS data. In Pope (2002b) this methodology is extended to a stochastic model for acceleration, which is a natural way to incorporate Reynolds-number effects.

Figure 4 shows the velocity-acceleration autocovariances predicted by the model compared to the DNS data of Sawford & Yeung (2000). As may be seen, the model is able to provide an accurate representation of these fundamental statistics.

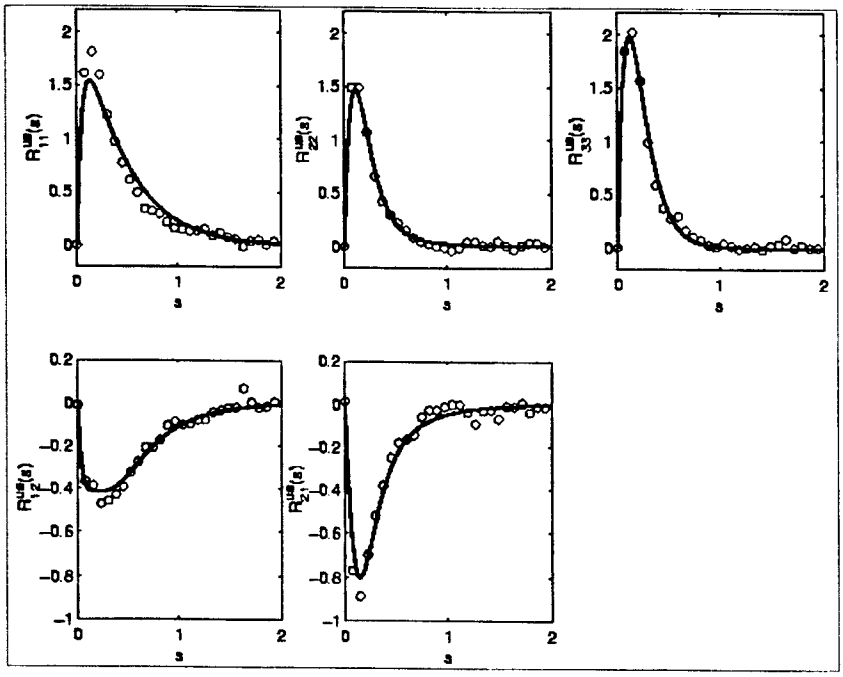

Fig.4: Velocity-acceleration Lagrangian covariances: symbols, from the DNS data of Sawford & Yeung (2001); lines, from the stochastic model of Pope (2002b).

REFERENCES

H. Chen, S. Chen & R.H. Kraichnan (1989). *Phys. Rev. Lett.* 63:2657.

L.Y.M. Gicquel, P. Givi, F.A. Jaberi & S.B. Pope (2002). *Phys. Fluids* 14:1196

.A. Juneja & S.B. Pope (1996). *Phys. Fluids* 8:2161.

J.C. Keck (1990). *Prog. Energy Combust. Sci.* 16:125.

A. Klimenko & R.W. Bilger (1999). *Prog. Energy Combust.* Sci. 25:595.

A. Klimenko & S. B. Pope (2002). "A model for turbulent reactive flow based on multiple mapping conditioning" *Phys. Fluid* (submitted).

S.B. Pope (2000a). *Turbulent Flows*, Cambridge University Press.

S.B. Pope (1997). *Combust. Theo. Modelling* 1:41-63.

S.B. Pope (2002a). *Phys. Fluids* 14: 1696.

S.B. Pope (2002b) "A stochastic Lagrangian model for acceleration in turbulent flows" *Phys. Fluids* (to be published).

B.L. Sawford & P.K. Yeung (2000). *Phys. Fluids* 12:2033.

C.J. Sung, C.K. Law and J.-Y. Chen (1998). *Proc. Combust. Inst.*, Vol. 27, pp. 295-304.

Q. Tang & S.B. Pope (2002). *Proc. Combust. Inst.* 29 (to be published).

Study of In-cylinder Reactions of
High Power-density Direct-injection Diesel Engines

(DAAD19-01-1-0766)

Principal Investigator (s): KT Rhee

98 Brett Road, Piscataway, NJ 08855 / Rutgers University

SUMMARY/OVERVIEW

Development of high power-density (HPD) direct-injection compression-ignition (DI-CI) or Diesel engines is explored by employing low air-fuel-ratio combustion, high-speed, two-cycle operation, low heat-rejection (LHR), and others. These strategies for HPD engine design become more promising when melded, in the conventional CI-engine-base, with high-performance fuel injection (HPFI), advanced design and materials, and tribology improvement.

Among the problems faced in this challenging work is clearly *control of the combustion process*. For example, a high-speed operation and LHR result in both a shortened physical time for mixing and increased intake air temperature. They necessitate an enhanced induction air management (e.g. cooling and turbocharging) and better fuel delivery (by using an HPFI). Those measures would help lead to a low-smoke-emission high-efficiency HPD by implementing a better control of fuel-air distribution and preflame reactions prior to the onset of an abrupt combustion stage.

In-cylinder DI-CI reaction processes, are often significantly altered when even a seemingly simple design parameter is changed, affecting both engine output and emissions. A better understanding of the impacts of HPD system basics, therefore, would be a precondition for achieving successful engine development. Desirably, since the cut-and-try development approach is costly, it necessitates a more realistic model to predict the behavior of Diesel flames in turbulent, high-speed, high-temperature and high-pressure environments subject to the *wide range of operating parameters* experienced by vehicle powerplants. There is a pressing need for *a tool capable of validating* any proposed combustion model by *observing realistic combustion in details* consistent with new engine design strategies.

In order to help achieve the above goals, four main work tasks have been carried out during the reporting period. They include: (1) construction of a new CI-DI engine apparatus with optical access; (2) advancement of Rutgers Super Imaging System (SIS); (3) development of a new operating system for the SIS; and (4) development of data reduction methods.

PROGRESS ACHIEVED DURING REPORTING PERIOD

New CI-DI Engine with Optical Access. There are several reasons motivated construction of this new apparatus. First of all, the optical access in an existing single-cylinder Cummins 903 engine (hereafter, called Engine-I) via one of two intake-valves permits observation of progressive reactions around only one spray plume (out of eight), which seemed to limit investigation of in-cylinder reactions. For example, after discovering some unusual phenomena earlier from this apparatus using the Rutgers Super Imaging System (SIS), which will be discussed more, simultaneous observation of reactions in multiple

plumes was expected to help understand the phenomena better. The new apparatus (hereafter, called Engine-II) has been designed/constructed by modifying a V-2 Cummins 903 engine. Unlike the optical access in Engine-I looking down through the cylinder head, the access in Engine-II is made through a hollow extended piston, which is mounted on the existing reciprocating unit with a new piston-top where an infrared optical window is mounted. The window is mounted in such a way to observe reaction in several plumes at the same time. This approach in Engine-II is expected to complement that from Engine-I. Among the special features of Engine-II is an inornel-made piston-top in order to overcome high stress over the components when the engine is operated as an HPD system. (The accumulated cost for completing this apparatus is about $75K.)

Advancement of Rutgers Super Imaging System (SIS). Several work tasks are being carried out for advancing the SIS, including: (a) fabrication of new camera boards; (b) incorporation of the SIS for massive data processing; and (c) Six-camera SIS.

The electronic packages driving the digital cameras in the SIS designed/fabricated in the Rutgers IC Engines Laboratory are proven to meet the requirements for our research, but their reliability is limited to exhibit occasionally erratic performance. In order to achieve more consistent experiment and quantitative imaging (determination of distributions of temperature and species concentration in the reaction volumes), at this time the electronic boards are being fabricated by outside professionals.

At the same time, the SIS has been incorporated with modern fast-data processing hardware-packages in order to achieve an unprecedented goal in high-speed imaging area. Recall that previous high-speed imaging of events in the engine cylinder has been done by taking sequential images in high rates only from a single combustion cycle at once. There are a couple of reasons for such limitations, including that the massive data handling has not been well supported by other technological area (e.g. speed and capacity of data storage) and that the optical window is rapidly fouled by soot deposit. The advanced SIS system was to overcome such limitations, which is now capable of *high-speed imaging from* (as many as 100) *consecutive cycles (HSI-CC)* opposed to from a single cycle at a time. The data handling ability of this system may be illustrated by the fact that loading a set of data from a single HIS-CC experiment to a laptop computer via a direct hard-wire takes approximately 25 minutes.

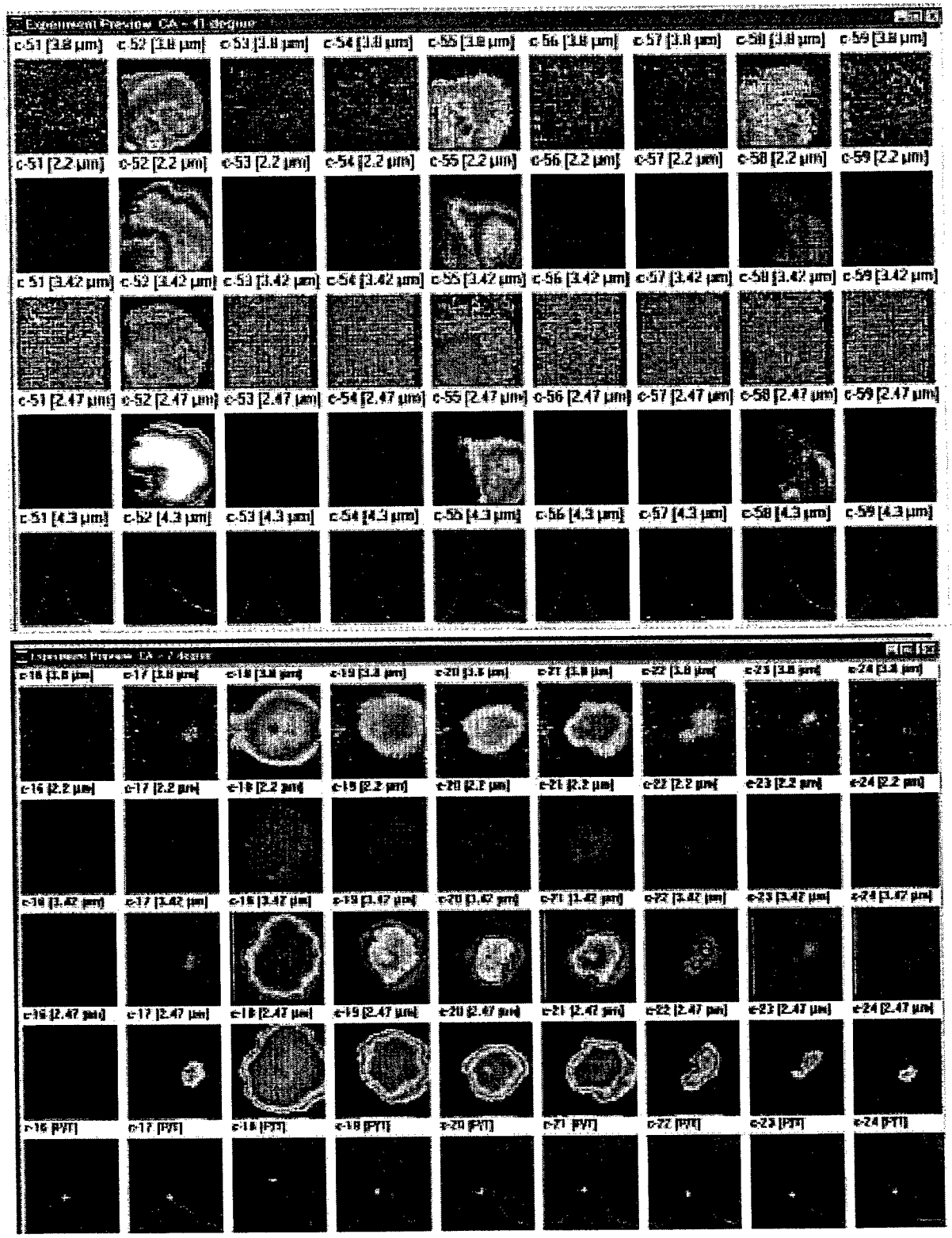

Fig. 1. High-speed Spectral Imaging (plus p-t History) from Consecutive Cycles Obtained from: (Top) Diesel Engine and (Bottom) SI Engine.

Six-Camera SIS. While four geometrically identical images in respective spectral bands are simultaneously captured at successive instants of time by using the SIS, it came to wonder if we could concurrently obtain distributions of spectra within the band width of the individual (spectral) images.

In this approach, two additional IR digital cameras are mated with a newly designed separate optical arrangement in the SIS: One is to display spectra distribution over the entire imaging band (2-5μm) and other is to obtain the same within the spectral bands of one of the said four spectral images. After lengthy analysis and design of this method, optical components are being purchased.

Development of a New Operating System (OS) for the SIS. When vast amounts of data are captured by via the HIS-CC method using the SIS, it was necessary to develop a new operating system (OS-HIS-CC) for the SIS for both data acquisition and review/analysis. Note that a part of such performance was achieved by using the Rutgers Animation Program (RAP) earlier when relatively small-scale results were obtained from a single cycle at the time. Development of this new OS is in progress, which is, again, basically to perform both data acquisition and similar goals by the RAP.

Development of Data Reduction Methods. Among the main purposes of developing the SIS and other data handling methods as described above is to achieve "quantitative imaging," which is to determine distributions of species and temperature in reacting flows. Recall that the SIS obtains four identical sets of digital data matrixes from corresponding pixels covered with respective spectral filters. The incipient undertaking of this work was based on a concept of "solving four simultaneous equations for four unknowns." For this, several spectral methods were developed in the past as reported earlier.

Because of tremendous advancements in the digital data handling technology, which is made use of in our present research endeavor, it was decided to develop our earlier and new band methods by melding them all together in a Window-based data processing method. This work is also in progress: The performance of the initial result is considered to be very promising.

Sample Results. In order to demonstrate some of results being obtained by using the HIS-CC, two sets of images are shown in Fig. 1. They are copies of a PC screen exhibited by using the above-mentioned new OS-HIS-CC, which illustrates the engine crank angle when the images were taken from consecutive cycles as shown on the same. In the p-t history, (+)-mark indicates the matching crank angle of imaging.

Such sets of images are successively displayed on the PC screen (i.e., movies). Note that the images from the next sets of cycles are readily examined by using the new OS-HIS-CC. Without detailed elaboration, note that the first set was obtained from Engine-I (DI-CI engine), showing reactions around a single spray plume during the start at room temperature. The second was from a spark-ignition engine also during the cold start. Note that "C-" in the photos represents cycle number from the start of imaging.

CONCURRENT RESEARCH ON HIGH GRAVITY (G) COMBUSTION AND ENABLING MATERIALS

(LRIR: 99PR12ENT)

Principal Investigator(s): Dr. W. M. Roquemore (PR) and Dr. R. J. Kerans (MLLN)

AFRL/PR, Bldg 490
1790 Loop Road North
WPAFB OH 45433-7103

SUMMARY/OVERVIEW:

This is a joint program between MLLN and PRTS. Fundamental combustion and materials science issues are being investigated that will lead to the development of a revolutionary propulsion system that operates on a highly efficient near-constant temperature (CT) cycle instead of the constant pressure cycle of today's engines. A key technology essential for the development of a propulsion system that operates on a CT cycle is an ultra-compact inter-turbine burner (ITB) that will efficiently add heat between the turbine stages and is constructed of advanced, lightweight ceramic-matrix composites (CMC) materials.

TECHNICAL DISCUSSION

A revolutionary gas turbine engine is proposed that uses a near constant temperature (CT) cycle and an Inter-Turbine Burner (ITB) to provide large amounts of power extraction from the low-pressure turbine. This level of energy is achieved with a modest 533 K temperature rise across the ITB. The excess energy can be used to power a large fan for a high bypass ratio transport aircraft, to drive a generator for electrical power extraction, or to power unconventional weapons systems. Conventional gas turbine engines cannot meet these power demands without a loss of engine thrust, and would ultimately lead to a second power source to provide energy for these applications, adding considerable cost and weight to the system. This paper will describe efforts that focus on Ultra-Compact Combustor (UCC) technology to serve as an ITB or main combustor in the CT engine, since reducing the size of the main combustor and ITB is essential to reducing overall engine weight and size.

Computational Fluid Dynamics (CFD) is used to guide combustor design modifications. The modified combustor hardware was tested in the Atmospheric Combustion Research Test Complex (ACRTC) at WPAFB. Experimental results indicate that the combustion system operated at 99+ combustion efficiency over a wide range of operating conditions. Flame lengths were extremely short at about 50% that of conventional systems. High heat release rates were seen while maintaining high combustion efficiencies. Combustor cavity g-loading enhanced reaction rates by increasing the combustion efficiency.

To meet the conflicting requirements of higher compression ratio, high heat release rates, reduced weight and low emissions require revolutionary combustion systems. For example, advanced combustors are becoming shorter and utilize non-metallic materials to meet the required thrust-to-weight ratio goals. Shorter residence times in the combustion chamber may reduce the NOx emissions, but the CO and UHC emissions may increase due to inadequate reaction time. Also, the unburned fuel could escape the combustion chamber and continue to burn in the turbine machinery, which could pose a series of rotating component challenges such as vane and blade durability.

Recently, Sirignano and Liu (1997) have proposed the idea of a turbine burner gas turbine engine to operate on a CT cycle. The efficiency of a CT cycle approaches that of a Carnot cycle. The cycle analysis indicates that additional work can be gained with CT cycle engine without large performance penalties. Key to this cycle is that sufficient heat is added in the turbine to compensate for the work extracted to drive the compressor. Combustion in the inter-turbine duct has two major requirements. First, the ITB must be short enough to successfully accomplish its function without resulting in an increase in overall engine length. Second, the ITB must achieve the required heat release without introducing a large loss in total pressure. If a successful ITB can be devised with these attributes, then the combustion concept becomes a candidate for the main combustor of the engine. Incorporation of a UCC as a main combustor would provide sufficient length savings as to guarantee that a quasi-constant temperature cycle could be achieved without any increase in overall engine length. If an ITB was not included for some reason, adoption of a UCC would allow a reduction in overall engine weight.

The ITB concept is clearly attractive, but a conventional combustor is much too large to fit between the stages of a turbine. A UCC is needed in order to implement the ITB concept without significantly increasing the engine length and thereby negating much of its benefit. In this work, we present preliminary experimental results of a UCC concept that utilizes high "g" swirl to shorten the overall flame length.

The effects of acceleration on combustion, specifically centrifugal acceleration, have been previously studied by Lewis (1973). He found that flame speed increases with increasing acceleration up to approximately 800g. Above this limit, flame speed abruptly decreased prior to being extinguished. He found that for regions of increasing flame speed, the laminar flame speed follows the relation:

$$S_L \propto g^{1/2} \qquad \text{Eq. 1}$$

Yonezawa et al. (1991) applied this concept to design and analyzed a jet-swirled combustor. This concept looks very much like a conventional annular combustor, but with a series of injection ducts inclined both axially and circumferentially to drive a swirling flow within the combustor liner. A qualitative flow analysis was undertaken to optimize the angles of the injection duct and a prototype was developed to test the concept. It was shown that a much higher loading factor could be obtained in this combustor design with high efficiency, and for a given loading factor, the jet swirl combustor had a higher efficiency over a conventional combustor. This work demonstrated that the rate of combustion could be sufficiently enhanced so that the length of a combustor could be reduced by ~33% while maintaining high combustion efficiency. Combustion is enhanced because the pressure gradient associated with the centrifugal acceleration of a rotating flow causes rapid mixing

and transport of the hot gases towards the central axis of the flow. The accumulation of the hot gases near the central axis becomes a source of high temperature that promotes rapid combustion.

Here, we have proposed and begun experiments on a UCC which will combine turning vanes to the rotor with the combustor and eliminate the stator leading to the combustor. A trench, or cavity, will run around the outer circumference of the vanes (Fig. 1). Aligned with this cavity, within each vane, will be a radial cavity. The idea is to burn rich in the circumferential cavity, allowing much of the required combustion residence time to take place in the circumferential direction of the engine, rather than the axial as is done conventionally. The flow within this cavity will be swirled to generate high "g" loading and reduce the chemical residence time. Flame stabilization occurs as combustion products are recirculated in the cavity. The intermediate products of combustion will be transported into the radial cavity in the vane where combustion will continue. Finally, across the leading edge of the vanes, again in a circumferential orientation, there will be a flame holder where products will be entrained into the main flow and complete the combustion process. Swirl from either the compressor (if used as a main combustor) or the turbine stage ahead of the ITB may be used to drive the swirl in the cavity. This will negate the need for a stator ahead of the combustor, further shortening the system. The increased residence time of the combustion products in the cavities will contribute significantly to achieving complete combustion in a short distance. The cavities are a folded combustion system so that the quick-quench, lean-burn process actually starts at the inlet of the combustor with the rich burn process taking place in parallel in the cavities, and is accomplished without extending the length of the combustion system. We estimate that an ultra-compact combustor, of design as described above, would be at least 66% shorter than a conventional combustion system defined as the diffuser, combustor, and the turbine inlet guide vanes.

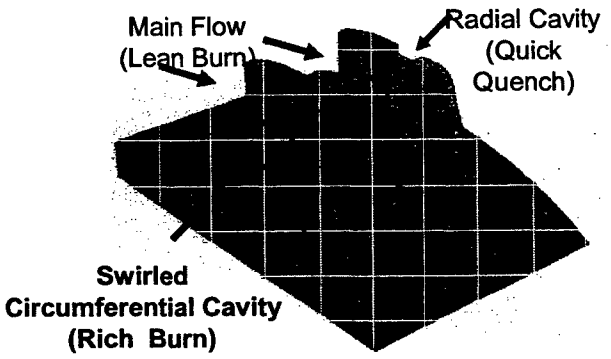

Figure 1: UCC/ITB Concept for Advanced

Sirignano, W.A., Delplanque, J.P., and Liu, F., "Selected Challenges in Jet and Rocket Engine Combustion Research," *33rd AIAA/ASME/SAE/ASEE Joint Propulsion Conference*, Seattle, WA AIAA-97-2701 (1997).

Sirignano, W.A., and Liu, F., "Performance Increases for Gas-Turbine Engines Through Combustion Inside the Turbine," *Journal of Propulsion and Power,* **15**:1 pp.111-118 (1999).

Liu, F., and Sirignano, W.A., "Turbojet and Turbofan Engine Performance Increases Through Turbine Burners," *38th Aerospace Sciences Meeting & Exhibit,* Reno, NV, AIAA-2000-0741 (2000).

Lewis, G.D., "Centrifugal-Force Effects on Combustion," *14th Symposium (International) on Combustion,* The Combustion Institute, pp.413-419 (1973).

Yonezawa, Y., Toh, H., Goto, S., and Obata, M., "Development of the Jet-Swirl High Loading Combustor," *26th AIAA/SAE/ASME/ASEE Joint Propulsion Conference,* Orlando, FL, AIAA-90-2451 (1990).

Roquemore, W.M., Shouse, D., Burrus, D., Johnson, A., Cooper, C., Duncan, B., Hsu, K.Y., Katta, V.R., Sturgess, G.J., and Vihinen, I., "Trapped Vortex Combustor Concept for Gas Turbine Engines," *39th AIAA Aerospace Sciences Meeting & Exhibit,* Reno, NV, AIAA-2001-0483 (2001).

PULSE DETONATION PHYSIOCHEMICAL AND EXHAUST RELAXATION PROCESSES

LRIR 01PR02COR

Principal Investigator: Dr. Fred Schauer (AFRL/PRTS)

AFRL/PRTS
1790 Loop Road North, Building 490
Wright-Patterson AFB OH 45433-7103

SUMMARY/OVERVIEW:

The objective of this program is to establish the scientific knowledge of detonation initiation, propagation, and blow-down needed to develop a pulse detonation engine (PDE) that will function on hydrocarbon fuels. The complex interaction of chemistry, gas dynamics, turbulent mixing, and geometry are responsible for the success or failure of the detonation phenomena required to operate a PDE. Detonation tube exhaust blow-down conditions, which are predicted to have a significant impact upon performance, will be explored in order to achieve basic understanding of the relationships between detonations, nozzles, and multiple detonation tube interactions.

TECHNICAL DISCUSSION

The technological motivation for this program is the need to develop low-cost high-performance PDE's that can operate on hydrocarbon fuels. PDE's rely upon detonation combustion to produce a pressure rise in the combustion chamber instead of the expensive rotating machinery used in gas turbine engines. Consequently, the most expensive and maintenance-intensive components of a conventional turbine engine, namely the compressor and turbine stages, will not be necessary in PDE's. PDE's operates on a near-constant-volume heat addition cycle as opposed to the constant-pressure cycle employed in nearly all conventional aero-propulsion systems. The constant volume cycle offers improvements to specific thrust, specific fuel consumption, and specific impulse at a greatly reduced cost. In theory, the PDE can efficiently operate at Mach numbers from zero to above four without using a combined cycle/rocket approach. However, there are some major technical problems that must be resolved before the full potential of PDE's can be realized.

Foremost among the hurdles for a practical PDE system are the requirements for initiation and successful propagation of a detonation with hydrocarbon fuels in air. Although this has not been achieved in 60 years of PDE research, modern computational fluid mechanics (CFD), laser diagnostics, and high-speed instrumentation have not been applied to this challenge until recently. CFD and experimental studies of deflagration-to-detonation transition (DDT) and

propagation are being carried out in order to explore the parameters controlling detonation initiation including: geometry effects, plasma ignition, hybrid fueled pre-detonators, and endothermic fuels. In addition to existing high-frequency instrumentation, an optically accessible test section will be coupled with our high-framing rate cameras to observe the deflagration to detonation transition processes and compare with models. The imaging and laser diagnostics experience obtained from our AFOSR Combustion Research program will also be used to study the detonator tube blow down. High-frequency Schlieren, PLIF, and/or planar Raman imaging will be used to investigate the exit boundary conditions influence on thrust. Two-dimensional nozzles are used in these investigations, and an optical test section will be employed to study both the nozzle flow conditions and multi-tube interactions. CFD calculations are used to gain an understanding of the mechanisms whereby the thrust is influenced by the conditions established when the detonation wave reaches the exit plane. For example, our Chin detonation spiral was developed recently because modeling of the detonation initiation processes indicated a new mechanism for starting detonations. The insight gained from discovering these phenomena resulted in propane/air detonations with no oxygen enrichment.

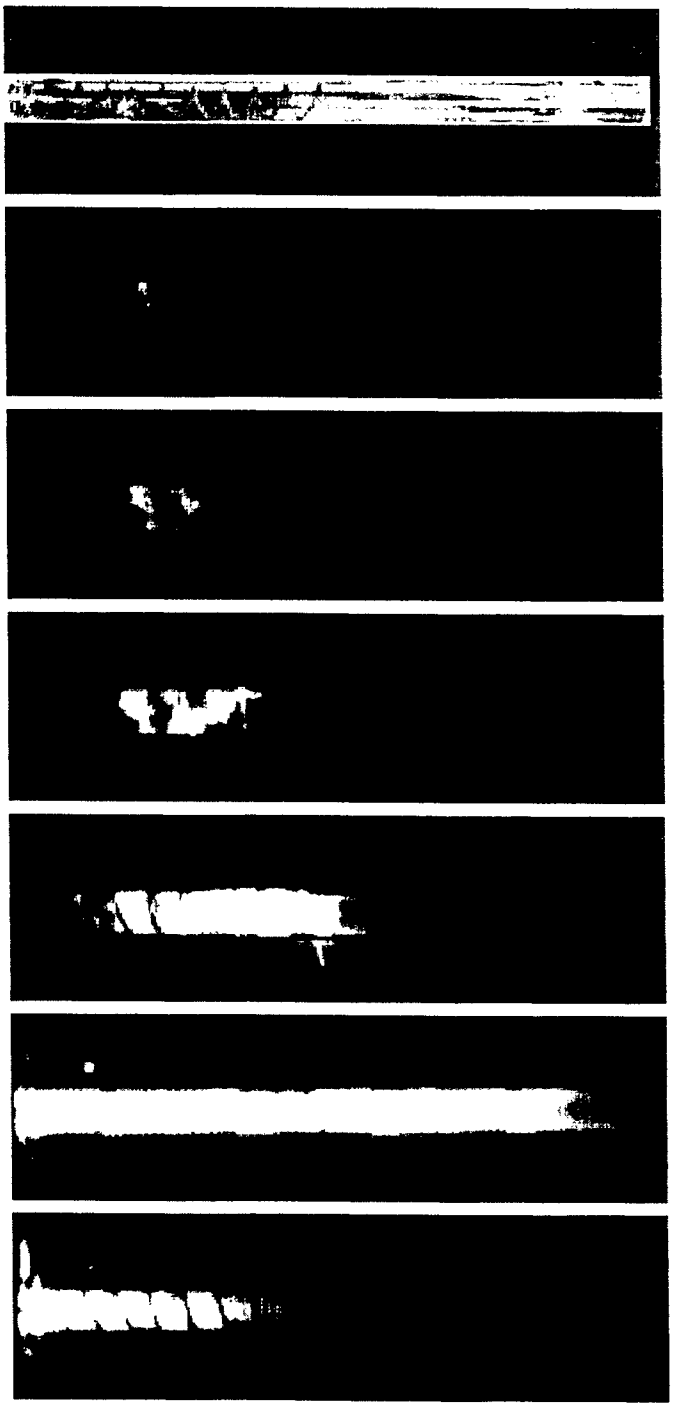

Figure 1. High speed imaging of DDT processes. From top to bottom: still of polycarbonate tube with Shelkin spiral, formation of hot spot, formation of multiple hot spots, micro explosion, DDT event, subsequent right running detonation and left running retonation, and in the last frame: left running expansion wave during blow down process.

This research couples the Combustion Science Branch's extensive basic combustion research experience with the pulse detonation engine in-house research program and high-fidelity detonation modeling capabilities in order to gain the understanding required to overcome the fundamental technological hurdles bracketing the PDE tube: detonation initiation and blow down conditions. Prior 6.2 studies conducted by AFRL/PRTS have made tremendous progress, but we lack understanding of the mechanisms enabling this progress. The techniques developed under this research effort

are producing this understanding and then applied to the challenges of detonation initiation and tube blow down.

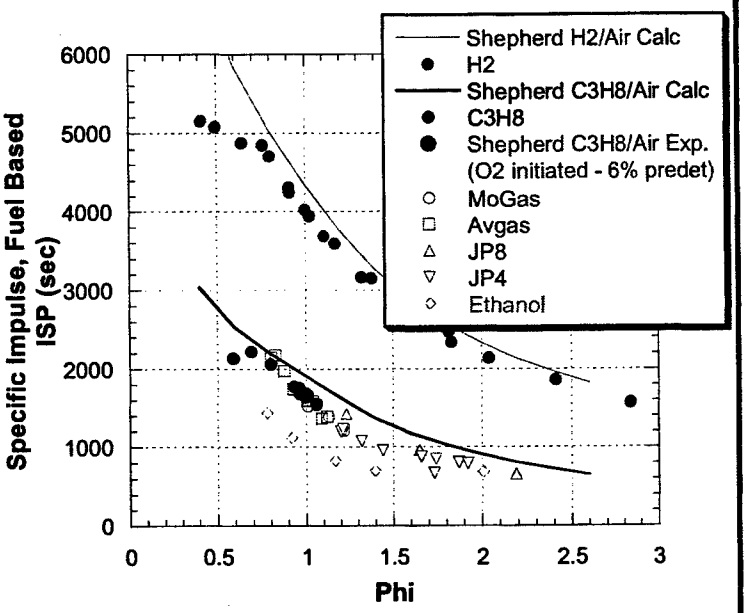

Figure 2. Variation of thrust versus equivilance ratio for various fuel-air mixtures.

Computational modeling and experiments have been conducted in order to understand the mechanisms required for deflagration-to-detonation-transition (DDT). The complex interaction of chemistry, gas dynamics, and geometry was found to play a key role in the generation of coalescing compression waves that were ultimately responsible for the creation of 'hot spots' required for successful DDT. Mechanisms studied by this research for DDT include: obstructions such as classical Shelkin spirals which create compression wave reflections while increasing flame speed through turbulence and flame mixing enhancement (see high speed imaging results in Fig. 1); 'Smirnov' type cavities which generate compression waves that subsequently interact with the flame front; and flame propagation in small detonator tube to cell width ratios which result in increased transverse wave reflection events.

The understanding gained of these complex mechanisms through CFD, DDT is experimentally achieved in complex hydrocarbon-air mixtures that did not previously achieve DDT in a practical configuration. Furthermore this work has been extended from detonation of vapor fuel/air mixtures, to the detonation of liquid fuel/air mixtures. Sample results of specific impulse versus a wide range of equivilance ratios are shown in figure 2 with hydrogen, propane, and liquid gasoline fuels. The mechanisms described above have subsequently been applied towards successful detonation initiation in motor gasoline, av-gas, JP4, JP8, and ethanol with stoichiometries ranging from 0.7 to over 4. Data is compared to analytical predictions by Shepard. The heating values for the complex hydrocarbon fuels shown are all similar, except for ethanol, which has a lower heating value and a resultant lower specific impulse.

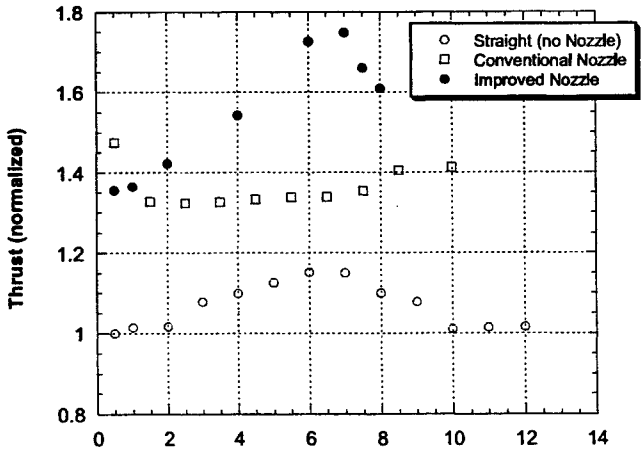

Figure 3. Variation of specific impulse (fuel) versus detonator tube fill fraction for tubes of varying area.

Exhaust relaxation processes have also been studied both numerically and experimentally. The detonator tube blow down process had previously been found to have a significant impact

on the resulting PDE performance and is also the source of much controversy as small changes in the exit conditions may impact the pressure relaxation portion of each detonation cycle. The effects of nozzles, bleeding off detonation pressure, ejectors, and other detonator geometry's which impact the sensitive tube exit boundary conditions are being examined. Some sample results depicting the impact of changing detonator tube shape and operating conditions are contained in figure 3. Axial variations in tube area, combined with the coupling of detonations with expansion and compression waves, were found to produce variations in efficiency as high as 75%. The changing operating condition result in much different blow down mechanisms as seen in the images of figure 4.

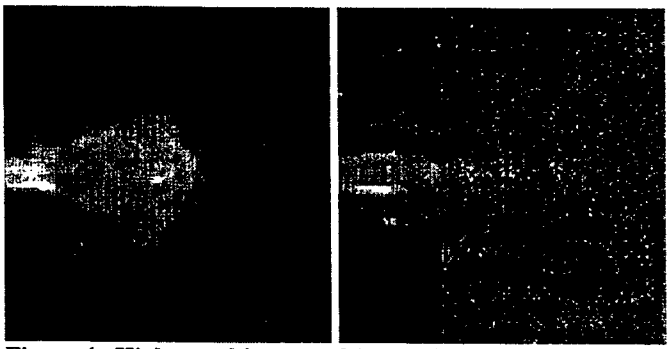

Figure 4. High speed images of detonation blow down. On the left blow down event, a spherical compression wave and vortex roll up is evident. On the right, a much different process has occurred.

CATALYTIC IGNITION AS A TOOL FOR CONVERTING SMALL ENGINES TO EFFICIENT JP-8 OPERATION

DAAD 19-00-1-0134 / P-40953-EG-DPS

Judi Steciak, Ph.D., P.E., Mechanical Engineering
Steve Beyerlein, Ph.D., Mechanical Engineering
Don Blackketter, Ph.D., Mechanical Engineering
David McIlroy, Ph.D., Physics

University of Idaho – Boise
800 Park Boulevard
Boise, Idaho 83712-7742

SUMMARY/OVERVIEW:

Catalytic ignition permits small engines to operate efficiently with heavy fuels. The technology advances the Army towards its goal of a 'one-fuel' military and can improve the performance of heavy fuel engines operating under part-load conditions. Findings discussed below include: 1) design of a small genset evaluation protocol including acquisition of baseline performance data; 2) development of a first-order model to predict igniter ignition timing; 3) changing the catalytic igniter design for JP-8 operation in a small genset.

Portable Genset Platform Baseline Test Protocol

A prior visit to Army CECOM at Ft. Belvoir established the need for 500 W to 1 kW gensets. The Army currently has no gensets with this power output that operate on diesel or JP-8. Commercially available gensets in this size range – for example, Honda models 1800 and 2000 – meet the weight requirement (these gensets weigh less than 20 lbs) but run on gasoline.

Conversion of a small genset, like the Honda eu-1000i (Figure 1), to operation with heavy fuels (D1, D2, JP-5 and/or JP-8) meets a need the military has today. This genset has a nominal 1,000W output.

Tests were done to determine the Brake Specific Fuel Consumption (BSFC) and Brake Specific Emissions (BSE) of a Honda eu-1000i gasoline generator to within a 95% confidence interval. The Brake Specific Fuel Consumption is calculated using the following values: mass of the fuel consumed by the generator (m), power output (P), and running generator time (t). The emissions included in this analysis are hydrocarbons (HC), nitrogen oxides (NO_x), carbon monoxide (CO), and carbon dioxide (CO_2). The Brake Specific Emissions is determined similarly to the BSFC except that the mass of the emission produced is used instead of the fuel consumed. The tests established a set of baseline data for use as a comparison when the generator is converted to a catalytic ignition system using JP-8.

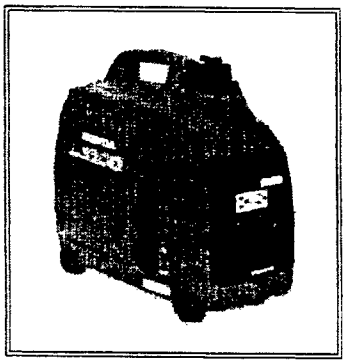

Figure 1. Honda EU1000iA2 genset

To determine the BSFC and BSE values, a load cell (light bar) was attached to the generator and ran multiple, 3-minute time intervals for loading conditions of 1, 3, 5, 7 and 9 100W light bulbs. The values from these tests were used to determine the BSFC and BSE at each load condition. For the BSE, a 5-gas analyzer was attached to the exhaust of the generator for the same loading conditions as the BSFC. Additionally, the generator was tested with the economy throttle on and off for each load condition. Both the BSFC and BSE were taken simultaneously. The following results were obtained: For the economy throttle setting on the generator, the range of BSFC values was 581.00 ± 21.2 g/kW-hr for 10 bulbs and 1710.80 ± 255.55 g/kW-hr for 1 bulb. For the maximum throttle setting, the BSFC ranged from 588.21 ± 12.71 g/kW-hr for 10 bulbs and 2750.88 ± 192.26 g/kW-hr for 1 bulb. For the emissions data, the values ranged from 250 PPM to 362 PPM for HC, 153 PPM to 202 PPM for NO_x, 3.21 % to 7.44 % for CO, and 8.5 % to 12.23 % for CO_2. After taking this data and analyzing, it was found that the mass measurement was the biggest contributor to error with between 60 and 80 percent of error being contributed by the mass. A fuel mass metering system was developed to correct this.

First-Order Catalytic Ignition Timing Model

Until recently, timing the ignition of the SmartPlug® has been strictly empirical. To better understand the behavior of catalytic ignition, a first-order combustion model was created. The model balances mass and energy, uses a two-step global combustion model with diesel fuel parameters, and involves 24 ordinary differential equations that are solved simultaneously with Matlab®. This model was originally used to predict the behavior of aqueous fuels, but was modified to suit heavy fuels. This model is used to establish trends, gain a better understanding of the physics behind this type of ignition, and determine the design parameters that have the largest impact on ignition timing.

In order to represent the Smartplug®, the igniter was divided into three zones for a lumped-parameter model. Each zone is assumed to be perfectly stirred (i.e. characterized by a single temperature and fuel concentration) and situated as in Figure 2 below. Zone I is the main chamber, and part of the pre-chamber without core; Zone II is the region of the pre-chamber that surrounds the catalytic portion of the igniter core. This is the only zone where catalytic surface reactions take place. Also note that electrical heating is possible in this zone. Zone III is the region of the pre-chamber that surrounds the non-catalytic portion of the igniter core. This is the only region where gas-phase reactions take place. Pressure is assumed to be constant across all zones and determined by piston position. Mass is progressively transferred from Zone I to Zone III as the piston moves upward. The temperature and fuel concentrations in each zone are governed by equations of mass and energy conservation.

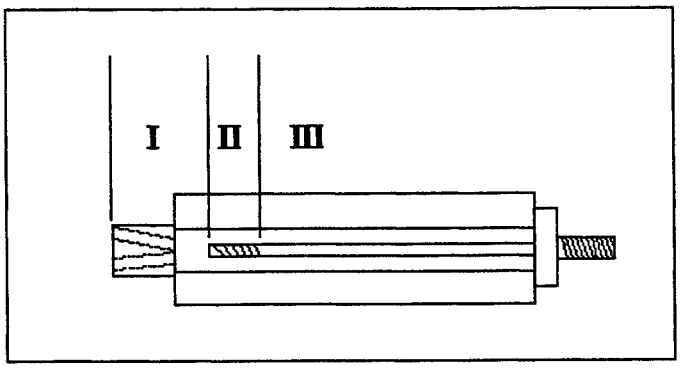

Figure 2. Igniter cutaway showing zones used in ignition calculations.

Catalytically assisted ignition in internal combustion engines has two distinct phases. The first phase is catalytic oxidation of the fresh mixture entering the pre-chamber. Provided that the catalyst is above the surface ignition temperature for a given fuel, this begins as soon as the interface between the fresh charge and the residual gas from the previous cycle contacts the catalyst. The second phase is the auto-ignition of the unburned mixture that accumulates in the rear of the pre-chamber.

By plotting the ratio of heat release rates as a function of crank angle, it is possible to detect departure from a motoring trace. Ignition is defined when the homogeneous energy generation rate exceeds the heterogeneous rate (Figure 3).

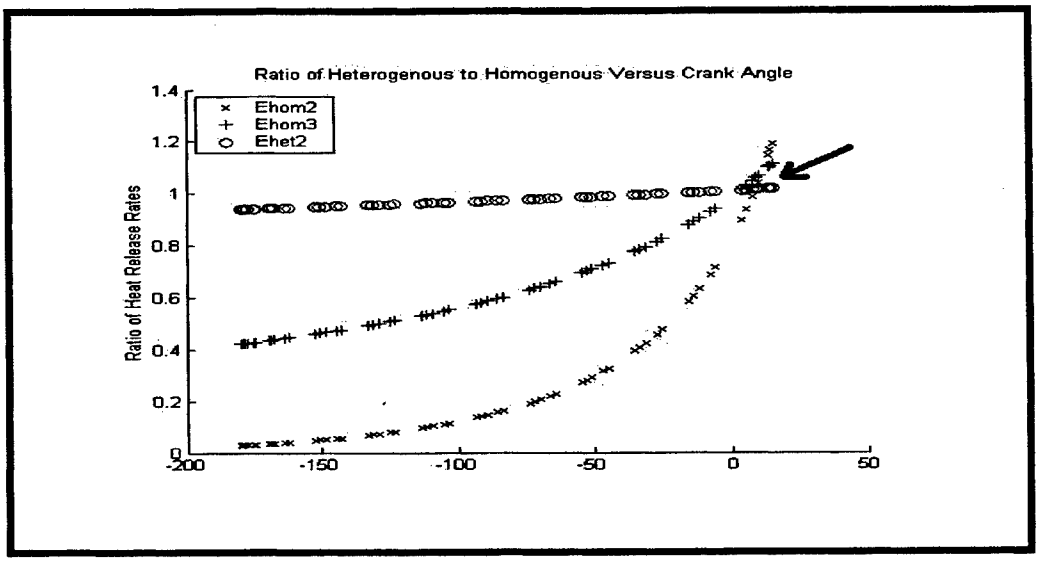

Figure 3. Catalytic ignition of the prechamber is defined when the homogeneous energy generation rate exceeds the heterogeneous energy generation rate (indicated by the arrow).

The results of a parametric study using the model illustrates the impact of igniter length and surface temperature on ignition timing (Figures 4 and 5).

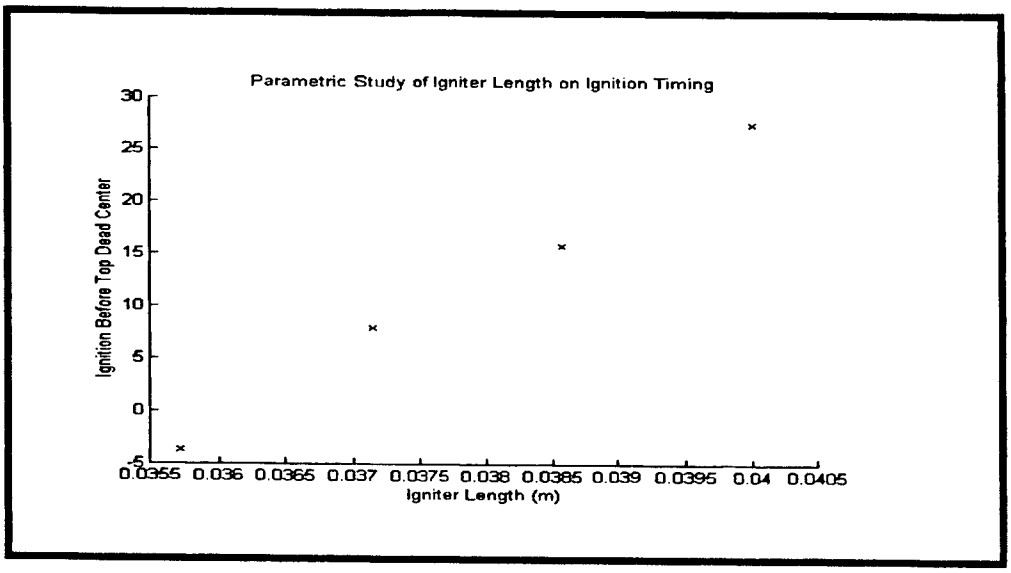

Figure 4. Impact of igniter length on ignition timing.

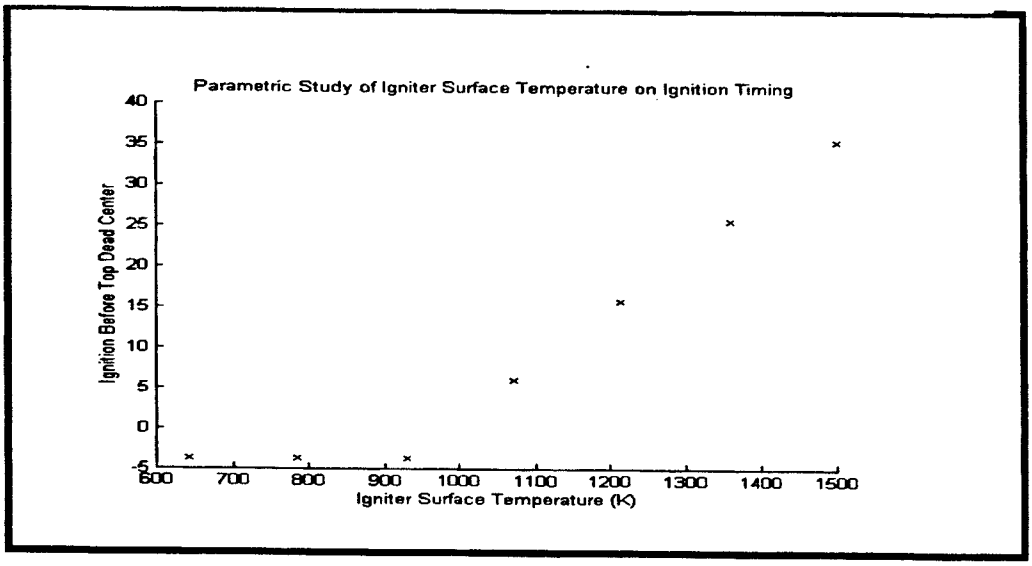

Figure 5. Impact of igniter surface temperature on ignition timing.

Igniter Design for Honda Genset Conversion

Igniters were designed to convert a Honda eu-1000i gasoline-fueled to jet fuel operation with catalytic ignition. The design requires downsizing the igniter prechamber to accommodate the existing sparkplug access and avoid changes to the head. Other changes will include replacing the main carburetor jet with a variable needle valve to accommodate JP-8 fuel viscosity and air-fuel ratio and replacing the choke plate with a plate that has improved sealing for producing fuel-rich mixtures for cold start.

EXPERIMENTAL STUDY OF VELOCITY FILTERED JOINT DENSITY FUNCTION AND ITS TRANSPORT EQUATION

AFOSR Grant F-49620-02-1-0130
Principal Investigator: Chenning Tong

Department of Mechanical Engineering
Clemson University
Clemson, SC 29634-0921

SUMMARY

Velocity filtered joint density function (VFJDF) and its transport equation used in PDF-based large eddy simulation (LES) of turbulent combustion are studied experimentally in an axisymmetric turbulent jet. The statistical characteristics of the VFJDF and the unclosed terms in its transport equation are analyzed using their conditional averages. The VFJDF is found to have qualitatively different characteristics for small and large subgrid-scale (SGS) kinetic energy. The characteristics under the latter conditions suggest that the SGS turbulence is under rapid distortion and is in non-equilibrium. Therefore the velocity-wave-vector PDF model of Van Slooten and Pope (1997), capable of treating rapid distortions, may be very useful as a model for SGS turbulence.

TECHNICAL DISCUSSION

PDF-based LES approaches for computing turbulent combustion have shown great promise (Gicquel et al. 2002). A method currently being established by Peyman Givi's group solves the velocity-scalar FJDF transport equation. This approach treats the SGS scalar transport exactly and has the potential to provide a more realistic description of the SGS mixing. Gicquel et al. (2002) has developed a stochastic VFJDF model based on the Generalized Langevin Model for PDF methods. Here we study the VFJDF and its transport equation for improving VFJDF models. The results also provide a basis for studying the velocity-scalar FJDF.

The velocity FJDF is defined as

$$f_u(\mathbf{V};\mathbf{x},t) = \int \prod_{i=1}^{3} \delta[u_i(\mathbf{x}',t) - V_i] G(\mathbf{x}'-\mathbf{x}) d\mathbf{x}', \tag{1}$$

where $\mathbf{V}$, δ, and G are the sample-space variable for $\mathbf{u}$, the Dirac delta function, and the filter function, respectively. The integration is over all physical space. The FJDF represents the weighted joint distribution of the velocity components in a grid cell, and for a top-hat (box) filter $f_u(\mathbf{V})d\mathbf{V}$ is the fraction of fluid in the grid cell whose velocity components are between V_i and $V_i + dV_i$. The transport equation of the FJDF is obtained using the Navier-Stokes equations:

$$\frac{\partial f_u}{\partial t} + V_j \frac{\partial f_u}{\partial x_j} = \frac{\partial \langle p \rangle_L}{\partial x_i} \frac{\partial f_u}{\partial V_i} + \frac{\partial}{\partial V_i}\{\langle \frac{\partial p'}{\partial x_i} | \mathbf{u} = \mathbf{V} \rangle_L f_u\} - \frac{\partial}{\partial V_i}\{\langle \nu \frac{\partial^2 u_i}{\partial x_j \partial x_j} | \mathbf{u} = \mathbf{V} \rangle_L f_u\}, \tag{2}$$

where $\langle \cdot \,|\mathbf{u} = \mathbf{V}\rangle_L$ denotes a conditionally filtered variable conditional on the velocity vector. The left hand side represents the time rate of change of the FJDF and transport of FJDF

in physical space. The terms on the right hand side are transport of the FJDF in velocity space by the resolvable-scale pressure gradient, by the SGS pressure gradient, and by the viscous acceleration. An alternative term to the conditionally filtered viscous acceleration is the conditionally filtered energy dissipation $\langle \epsilon_{ik} | \mathbf{u} = \mathbf{V} \rangle_L$, where $\epsilon_{ik} = \nu \frac{\partial u_i}{\partial x_j} \frac{\partial u_k}{\partial x_j}$ is the energy dissipation tensor.

The FJDF is a random process and requires statistical descriptions. Here we employ conditional sampling and averaging techniques. Previous studies of conserved scalar FDF and its transport equation using these techniques (Tong 2001, Wang and Tong 2002) have shown that the SGS scalar is in equilibrium and non-equilibrium for small and large SGS scalar variance respectively, and the two regimes have qualitatively different characteristics. For equilibrium SGS scalar the FDF is on average near Gaussian, indicating that the SGS scalar is well mixed. For non-equilibrium SGS scalar the FDF is bimodal, thus the SGS scalar is poorly mixed. These results for the SGS scalar suggest that similar distinctions may also exist in the SGS velocity field. Thus we investigate the VFJDF and the SGS terms in the FJDF transport equation by analyzing their conditional means with the SGS kinetic energy, $K_L = (\langle u''^2 \rangle_L + \langle v''^2 \rangle_L)/2$ as a conditioning variable.

Our measurements were made in an axisymmetric turbulent jet at 80 jet nozzle diameters (D =15 mm) downstream. The jet Reynolds number UD/ν is 40000. A sensor array consisting of three hot-wire probes is used to obtain data for performing filtering operations in both the streamwise (x) and transverse (y) directions. The filter size is 20 mm. This technique enables us to acquire a large amount of data (10^7 samples) necessary to achieve statistical convergence. Because the filter in the x direction is a true box filter whereas that in the y direction is an approximation by three discrete points, some subgrid-scale fluctuations are excluded from the computed subgrid-scale velocity. It is easily shown that this aliasing effect is stronger for the u component. To faithfully capture the structure of the SGS velocity field, equal contributions to K_L from the two velocity components are needed. Thus, a weighting coefficient a is used in obtaining the conditioning variable: $K'_L = 1/2(a\langle u''^2 \rangle_L + \langle v''^2 \rangle_L)$. We also use different a values to capture structures with different levels of anisotropy.

A. The velocity FJDF

The mean FJDF conditional on the SGS energy and the resolvable-scale velocity is shown in Fig. 1. For small SGS energy the conditional FJDF is close to joint-Gaussian, similar to the JPDF in a fully developed turbulent jet, which is in quasi-equilibrium. For large SGS energy ($K'_L/\langle K'_L \rangle = 4.2$) the FJDF has an approximately uniform region, beyond which the FJDF decreases rapidly (faster than joint-Gaussian). The existence of the uniform region suggests that the SGS velocity field under this condition contains structures in which the velocity varies approximately linearly in physical space. Examples of such structures include axisymmetric contraction and expansion, plane strain, and plane strain plus plane shear. Since these local structures occur at large K'_L, the strain rate imposed by them is larger than the average turbulent strain rate near the filter scale. As a result, the production of the SGS energy increases, and when the strain rate is sufficiently large, the "background" SGS turbulence (the SGS turbulence minus the structure) may be undergoing local rapid distortion. This suggests that the SGS velocity field is in non-equilibrium, because rapid

distortion is a linear process, and spectral transfer is not effective in responding to the increased SGS energy production. Therefore the dissipation lags behind the production, resulting in local non-equilibrium.

Since wavenumber information is needed to describe turbulence under rapid distortion, conventional one-point PDF model is not sufficient. To overcome this difficulty, Van Slooten and Pope (1997) developed a velocity-wave-vector PDF model which gives exact Reynolds stress under the rapid distortion limit. The present study suggests that local rapid distortion might exist even when the mean strain rate is not large. Thus it may be beneficial to adopt this model to LES so that the local rapid distortion effects can be taken into account.

B. The conditionally filtered viscous acceleration and dissipation

In the present study two components of the viscous acceleration vector are measured. The conditionally filtered viscous acceleration vector is shown in Fig. 2 as streamline plots. The magnitude of the vector field, normalized by $8\nu K_L^{1/2}/\Delta^2$, is given as gray scale isocontours. The streamlines generally flow towards a stagnation point, which is approximately at the peak of the VFJDF. The magnitude of the acceleration increases with the magnitude of the velocity. This dependence is similar to that of the scalar diffusion on the value of the scalar. However, for large SGS energy the normalized magnitude is smaller. This is because the velocity in the local structures varies approximately linearly in the physical space and contributes little to viscous acceleration. This behavior further suggests that the "background" SGS turbulence is undergoing rapid distortion.

The conditionally filtered energy dissipation (one component) $\nu(\frac{\partial u_1}{\partial x_1})^2$ normalized by $8\nu K_L/\Delta^2$ is given in Fig. 3 as surface plots. This normalization gives the ratio of the total dissipation to the contributions from the strain rate at the filter scale. For small SGS variance the surface is concave with moderate dependence on the velocity vector. For large SGS energy the dissipation increases somewhat with u, but the surface is flatter and the overall dependence on the velocity is weaker. In addition the normalized dissipation values are smaller than those for the small SGS energy. This is because the local structure (rapid distortion) contributes significantly to the total dissipation. Thus the local rapid distortion also modifies the dissipation scales. The results show that the state of the SGS turbulence ranges from equilibrium and non-equilibrium to rapid distortion, providing strong support for adopting the velocity-wave-vector model to LES.

REFERENCES

Gicquel, L. Y. M., Givi, P., Jaberi, F. A., and Pope, S. B. (2002) Velocity filtered density function for large eddy simulation of turbulent flows. Phys. Fluids **14,** 1196–1213.

Tong, C. (2001) Measurements of conserved scalar filtered density function in a turbulent jet. Phys. Fluids **13,** 2923–2937.

Van Slooten, P. R. and Pope, S. B. (1997) PDF modeling for inhomogeneous turbulence with exact representation of rapid distortions. Phys. Fluids **9,** 1085–1105.

Wang, D. and Tong, C. (2002) Conditionally filtered scalar dissipation, scalar diffusion, and velocity in a turbulent jet. Phys. Fluids **14,** In press.

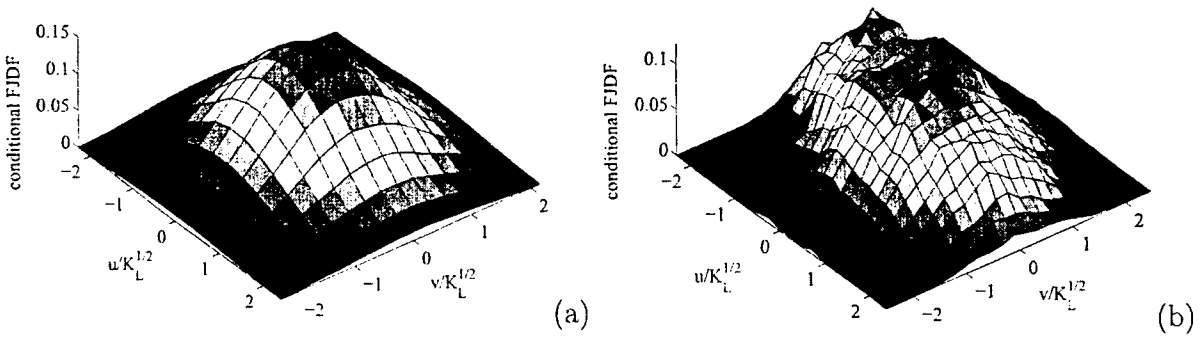

Figure 1: Mean FJDF conditional on the SGS energy and the resolvable-scale velocity: (a) $K'_L/\langle K'_L\rangle = 0.33$, $\langle u\rangle_L = \langle u\rangle$ (3 m/s), $\langle v\rangle_L = 0$. The FJDF is close to joint-Gaussian; (b) $K'_L/\langle K'_L\rangle = 4.2$, $\langle u\rangle_L = \langle u\rangle$ (3 m/s), $\langle v\rangle_L = 0$. The FJDF has an approximately uniform region.

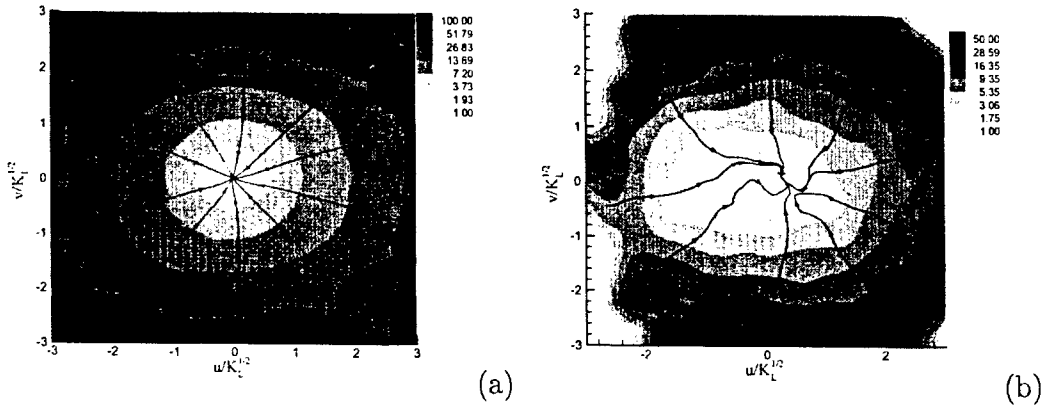

Figure 2: Normalized mean conditionally filtered viscous acceleration vector $\langle\langle\nu(\frac{\partial^2 u}{\partial x^2}, \frac{1}{2}\frac{\partial^2 v}{\partial x^2})|u,v\rangle_L|K'_L,\langle u\rangle_L,\langle v\rangle_L\rangle$. The conditions are the same as in Fig. 1. The diffusion is smaller for large SGS energy.

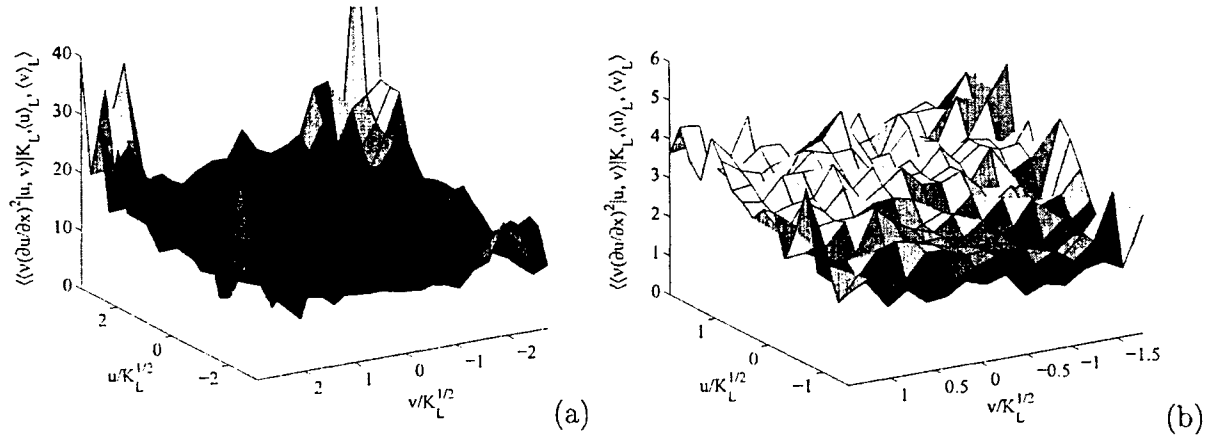

Figure 3: Normalized mean conditionally filtered dissipation. The conditions are the same as in Fig. 1. The dissipation is smaller for large SGS energy.

Invitees

John Abraham
School of Mechanical Engineering
Purdue University
West Lafayette, IN 47907
(765) 494-1505
FAX: 494-0530
jabraham@ecn.purdue.edu

Mukund Acharya
Allied Signal Engines
M/S 301-125
111 South 34th Street
P.O. Box 52181
Phoenix, AZ 85072-2181
(602) 231-2808
Mukund.Acharya@alliedsignal.com

M. S. Anand
Rolls-Royce Corporation
P.O. Box 420
Speed Code T14
Indianapolis, IN 46206-0420
(317) 230-2828
FAX: 230-3691
m.s.anand@rolls-royce.com

William Anderson
AMSRL-WT-PC
U.S. Army Research Laboratory
Aberdeen Proving Ground, MD 21005-5066
(410) 278-9992
DSN 298-9992
FAX: 278-7333
willie@arl.army.mil

Kurt Annen
Aerodyne Research, Inc.
45 Manning Road
Manning Park Research Center
Billerica, MA 01821-3976
(978) 663-9500 Ext.234
FAX: 663-4918
kannen@aerodyne.com

Chris Atkinson
Dept. of Mechanical & Aerospace Engineering
West Virginia University
P.O. Box 6106
Morgantown, WV 26506-6106
(304) 293-4111
FAX: 293-2582

Steve Beckel
Pratt and Whitney
M/S 715-83
P.O. Box 109600
West Palm Beach, FL 33410-9600

Josette Bellan
Jet Propulsion Laboratory
M/S 125-109
4800 Oak Grove Drive
Pasadena, CA 91109
(818) 354-6959
FAX: 393-5011
josette.bellan@jpl.nasa.gov

Michael Berman
AFOSR/NL
801 North Randolph Street, Room 732
Arlington, VA 22203-1977
(703) 696-7781
DSN 426-7781
FAX: 696-8449
michael.berman@afosr.af.mil

William Berry
Director for Research
Defense Research & Engineering
3040 Defense Pentagon
Washington, DC 20301-3040

Thomas Beutner
AFOSR/NA
801 North Randolph Street, Room 732
Arlington, VA 22203-1977
(703) 696-6961
DSN 426-6961
FAX: 696-8451
thomas.beutner@afosr.af.mil

Robert Bill
Propulsion Directorate
Army Research Laboratory
NASA Glenn Research Center, M/S 77-12
21000 Brookpark Road
Cleveland, OH 44135-3191
(216) 433-3703
FAX: 433-3000
Robert.C.Bill@lerc.nasa.gov

Mitat Birkan
AFOSR/NA
801 North Randolph Street, Room 732
Arlington, VA 22203-1977
(703) 696-7234
DSN 426-7234
FAX: 696-8451
mitat.birkan@afosr.af.mil

Kevin Bowcutt
North American Aircraft Division
Rockwell International Corporation
P.O. Box 3644
Seal Beach, CA 90740-7644

Andreja Brankovic
Flow Parametrics, LLC
15 Debra Drive
Bear, DE 19701
(302) 838-7368
FAX: 838-7369
brankov@flowparametrics.com

R. C. Brown
Aerodyne Research, Inc.
45 Manning Road
Manning Park Research Center
Billerica, MA 01821-3976
(978) 663-9500
FAX: 663-4918

Walter Bryzik
Propulsion Systems Division
ATTN: AMSTA-TR-R, MS 121
USA Tank-Automotive Command
Warren, MI 48397-5000
(810) 574-6461
FAX: 574-5054
bryzik@cc.tacom.army.mil

John D. Buckmaster
Department of Aeronautical and
Astronautical Engineering
University of Illinois at Urban-Champaign
306 Talbot Laboratory
104 S. Wright Street
Urbana, IL 61801
(217) 333-1803
FAX: 244-0720
limey@uiuc.edu

T. D. Butler
Theoretical Division, M/S B-210 T-DO
Los Alamos National Laboratory
Los Alamos, NM 87545
(505) 667-4401
FAX: 665-4055
tdbutler@lanl.gov

H. F. Calcote
ChemIon Inc.
159 Philip Drive
Princeton, NJ 08540
(609) 921-6891
FAX: 921-6891
calcote@alumni.princeton.edu

George Caledonia
Physical Sciences, Inc
20 New England Business Center
Andover, MA 01810
(508) 689-0003
FAX: 689-3232

Donald Campbell
NASA Glenn Research Center
21000 Brookpark Road
M/S 3-2
Cleveland, OH 44135
(216) 433-2929
FAX: 433-5266

Herb Carlson
AFOSR/CA
801 North Randolph Street, Room 732
Arlington, VA 22203-1977
(703) 696-7550
DSN 426-7550
FAX: 696-9556
herb.carlson@afosr.af.mil

Len Caveny
13715 Piscataway Drive
Ft. Washington, MD 20744
(301) 292-5319
FAX: 292-3724
Lcaveny@compuserve.com

Nicholas Cernansky
Department of Mechanical Engineering
Drexel University
32nd and Chestnut Streets
Philadelphia, PA 19104-2884
(215) 895-2284
Nicholas.Peter.Cernasky@drexel.edu

Chine I. Chang
Director
U.S. Army Research Office
P.O. Box 12211
Research Triangle Park, NC 27709-2211
(919) 549-4203
DSN 832-4203
FAX: 549-4348
jchang@aro-emh1.army.mil

Harsha Chelliah
Dept. of Mechanical, Aerospace
and Nuclear Engineering
University of Virginia
Charlottesville, VA 22903-2442
(804) 924-6037
FAX: 982-2037
harsha@virginia.edu

Jacqueline Chen
M/S 9051
Sandia National Laboratories
P.O. Box 969
Livermore, CA 94551-0969
(510) 294-2586
FAX: 294-1012
jhchen@sandia.gov

S. Y. Cho
Dept. of Mechanical and Aerospace Engineering
Princeton University
Princeton, NJ 08544-5263

M. B. Colket
United Technologies Research Center
411 Silver Lane, M/S 129-29
East Hartford, CT 06108
(860) 610-7481
(860) 658-9502
FAX: 610-7593
colketmb@utrc.utc.com

S. M. Correa
GE Corporate Research & Development
P.O. Box 8, K1ES112
Schenectady, NY 12301
(518) 387-5853
FAX: 387-7258
correa@crd.ge.com

Werner Dahm
Department of Aerospace Engineering
3056 FXB 2140
The University of Michigan
Ann Arbor, MI 48109-2140
(734) 764-4318
(734) 761-2026
FAX: 763-0578
wdahm@umich.edu

Eugene Danielson
U.S. Army Tank-Automotive and
Armaments Command
ATTN: AMSTA-TR-R - MS 121
Warren, MI 48397-5000

Ron Davis
Process Measurements Division (836)
National Institute of Standards & Technolgy
100 Bureau Drive, Stop 8360
Gaithersburg, MD 20899-8360
(301) 975-2739
ronald.davis@nist.gov

Peter A. DeBarber
MetroLaser
2572 White Road
Irvine, CA 92614
(949) 553-0688
FAX: 553-0495
debarber@deltanet.com

Paul Dimotakis
California Institute of Technology
1201 East California Boulevard
M/C 301-46
Pasadena, CA 91125
(626) 395-4456
(626) 794-2594
FAX: 395-4447
dimotakis@caltech.edu

Glenn Diskin
NASA Langley Research Center
M/S 197
Hypersonic Airbreathing Propulsion Branch
Hampton, VA 23681-2199
(757) 864-6268
FAX: 864-7923
g.s.diskin@larc.nasa.gov

Gregory Dobbs
United Technologies Research Center
M/S 90
Silver Lane
East Hartford, CT 06108
(860) 610-7145

James F. Driscoll
Department of Aerospace Engineering
3004 FXB Building
University of Michigan
Ann Arbor, MI 49109-2118
(734) 936-0101
FAX: 763-0578
jamesfd@umich.edu

J. Philip Drummond
NASA Langley Research Center
M/S 197
Hampton, VA 23681-0001
(757) 864-2298
FAX: 864-7923
j.p.drummond@larc.nasa.gov

C. Dutton
Dept. of Mechanical and Industrial Engineering
University of Illinois at Urban-Champaign
140 Mechanical Engrg. Building, M/C 244
1206 West Green Street
Urbana, IL 61801
(217) 333-8883
FAX: 244-6534
j-dutton@uiunc.edu

J. T. Edwards
AFRL/PRTG
Building 490
1790 Loop Road, N
Wright-Patterson AFB, OH 45433-7103
(937) 255-3524
DSN 785-3524
FAX: 255-1125
james.edwards@wpafb.af.mil

Fokion N. Egolfopoulos
Department of Mechanical Engineering
University of Southern California
Olin Hall 400B
Los Angeles, CA 90089-1453
(213) 740-0480
FAX: 740-8071
egolfopo@almaak.usc.edu

G. M. Faeth
Department of Aerospace Engineering
3000 FXB Building
University of Michigan
Ann Arbor, MI 48109-2140
(734) 764-7202
FAX: 936-0106
gmfaeth@umich.edu

Parviz Famouri
Dept. of Computer Science & Electrical Engineering
West Virginia University
P.O. Box 6109
Morgantown, WV 26506
(304) 293-0405 Ext. 2530
pfamouri@wvu.edu

Gregory W. Faris
Molecular Physics Laboratory
SRI International
333 Ravenswood Avenue
Menlo Park, CA 94025-3493
(650) 859-4131
FAX: 859-6196
faris@mplvax.sri.com

Partick Farrell
Engine Research Center
1500 Engineering Drive
University of Wisconsin
Madison, WI 53706
(608) 263-1686
farrell@engr.wisc.edu

Farley Fisher
National Science Foundation
CTS/Room 525
4201 Wilson Boulevard
Arlington, VA 22230
(703) 306-1371
FAX: 306-0319
ffisher@nsf.gov

David E. Foster
Engine Research Center
1500 Engineering Drive
University of Wisconsin
Madison, WI 53706
(608) 263-1617
foster@engr.wisc.edu

Bish Ganguly
AFRL/PRPE
2645 Fifth Street, Suite 13
Wright-Patterson AFB, OH 45433-7919
(937) 255-2923
DSN 785-2923
FAX: 656-4095
biswa.ganguly@pr.wpafb.af.mil

Richard G. Gann
Building and Fire Research Laboratory
National Institute of Standards & Technology
100 Bureau Drive, MS 8650
Gaithersburg, MD 20899-8650
(301) 975-6866
FAX: 975-4052
rggann@nist.gov

Alan Garscadden
AFRL/PR
1950 Fifth Street, Building 18A
Wright-Patterson AFB, OH 45433-7251
(937) 255-2246
DSN 785-2246
FAX: 986-4657
alan.garscadden@pr.wpafb.af.mil

Kresimir Gebert
BKM, Inc.
5141 Santa Fe Street
San Diego, CA 92109
(858) 270-6760
bkm-inc@worldnet.att.net

R. Giffen
General Electric Company
Aircraft Engine Group
Neumann Way
Cincinnati, OH 45215

Sharath Girimaji
Department of Aerospace Engineering
Texas A&M University
College Station, TX 77843-3141
(979) 845-1674
FAX: 845-6051
girimaji@aero.tamu.edu

Peyman Givi
Dept. of Mechanical and Aerospace Engineering
State University of New York
Buffalo, NY 14260-4400
(716) 645-2593 Ext. 2320
FAX: 645-3875
givi@eng.buffalo.edu

Irvin Glassman
Dept. of Mechanical and Aerospace Engineering
Princeton University
Princeton, NJ 08544-5263
(609) 258-5199
(813) 442-1118
FAX: 258-5963
glassman@princeton.edu

George Gogos
Department of Mechanical Engineering
University of Nebraska-Lincoln
Lincoln, NE 68588-0656
(402) 472-3006
ggogos1@unl.edu

Judah Goldwasser
Office of Naval Research
Mechanics Division, Code 333
800 North Quincy Street
Arlington, VA 22217-5660
(703) 696-2164
DSN 426-2164
FAX: 696-2558
goldwaj@onr.navy.mil

James Gord
AFRL/PRTS
Building 490
1790 Loop ,
Wright-Patterson AFB, OH 45433-7103
(937) 255-7431
DSN 785-7431
FAX: 656-4570
james.gord@pr.wpafb.af.mil

Jay P. Gore
School of Mechanical Engineering
Purdue University
1003 Chaffee Hall
West Lafayette, IN 47907-1003
(317) 494-1500
FAX: 494-0530

Larry Goss
Research Applications Division
Systems Research Labs, Inc.
2800 Indian Ripple Road
Dayton, OH 45440-3696
(513) 252-2706

Richard Gould
Dept. of Mechanical and Aerospace Engineering
Box 7910
North Carolina State University
Raleigh, NC 27695-7910
(919) 515-5236
FAX: 515-7968
gould@eos.ncsu.edu

Frederick Gouldin
Dept. of Mechanical and Aerospace Engineering
Cornell University
Ithaca, NY 14853-5692
(607) 255-5280
fcg2@cornell.edu

Mark Gruber
AFRL/PRA
1790 Loop Road, N
Wright-Patterson AFB, OH 45433-7251
(937) 255-2175
DSN 785-2175
FAX: 656-4659
Mark.Gruber@afrl.af.mil

Brian K. Gullett
U.S. Environmental Protection Agency
National Risk Management Research Laboratory
Air Pollution Technology Branch (MD-65)
Research Triangle Park, NC 27711
(919) 541-1534
FAX: 541-0290
gullett.brian@epa.gov

Rajendra Gupta
Department of Physics
226 Physics Building
University of Arkansas
Fayetteville, AK 72701
(501) 575-5933
rgupta@comp.uark.edu

Mark A. Hagenmaier
AFRL/PRA
Building 18
1950 Fifth Street, Suite 10
Wright-Patterson AFB, OH 45433-7251
(937) 255-5210
DSN 785-5210
FAX: 476-4659
hagenma@possum.appl.wpafb.af.mil

Nabil S. Hakim
Director, Advanced Engineering
Detroit Diesel Corporation
13400 W. Outer Drive, R03-B
Detroit, MI 48239-4001
(313) 592-7455
FAX: 592-5906

Robert D. Hancock
AFRL/PRTS
Building 490
1790 Loop Road, N
Wright-Patterson AFB, OH 45433-7103
(937) 255-6814
DSN 785-6814
FAX: 255-1125
hancockr@ward.appl.wpafb.af.mil

Ronald Hanson
Department of Mechanical Engineering
Stanford University
Building 530, Room 112
Stanford, CA 94305-3030
(650) 723-4023
FAX: 725-4862
hanson@me.stanford.edu

Naeim Henein
Department of Mechanical Engineering
Wayne State University
2121 Engineering Building
Detroit, MI 48201
(313) 577-3887
FAX: 577-8789
henein@me1.eng.wayne.edu

Cecil F. Hess
MetroLaser
2572 White Road
Irvine, CA 92614
(949) 553-0688
FAX: 553-0495
chess@metrolaserinc.com

Robert Holland
United Technologies Chemical Systems Division
P.O. Box 49028
San Jose, CA 95161-9028
(408) 224-7656

Lawrence Hunter
Applied Physics Laboratory
Johns Hopkins University
Johns Hopkins Road
Laurel, MD 20707-6099
(301) 953-5000 Ext. 7406

Frank Hurley
U.S. Army Research Office
P.O. Box 12211
Research Triangle Park, NC 27709-2211
(919) 549-4432
DSN 832-4432
FAX: 549-4310
hurley@aro-emh1.army.mil

Farhad Jaberi
Dept. of Mechanical and Nuclear Engineering
Kansas State University
Manhattan, KS 66506
(785) 532-5619
FAX: 532-7057
jaberi@mne.ksu.edu

Thomas Jackson
AFRL/PRSC
Building 18
1950 Fifth Street
Wright-Patterson AFB, OH 45433-7251
(937) 255-2175
DSN 785-2175
FAX: 656-4659
thomas.jackson@afrl.af.mil

Jay Jeffries
Department of Mechanical Engineering
Thermophysics Division, Building 520
Stanford University
Stanford, CA 94305-3032
(650) 736-0007
FAX: 723-1748
Jeffries@Navier.Stanford.edu

Gordon Jensen
United Technologies Chemical Systems Division
P.O. Box 49028
San Jose, CA 95161-9028
(408) 365-5552

Jeff Jensen
Kaiser-Marquardt
16555 Staycoy Street
Van Nuys, CA 91406

William Johnson
BKM, Inc.
5141 Santa Fe Street
San Diego, CA 92109
(619) 270-6760

Craig Johnston
Lockheed Advanced Dev. Company
Lockheed-Martin Corporation
1011 Lockheed Way
Palmdale, CA 93599-7212

Walter Jones
AFOSR/NA
801 North Randolph Street, Room 732
Arlington, VA 22203-1977
(703) 696-8457
DSN 426-8457
FAX: 696-8451
walter.jones@afosr.af.mil

John Kelly
Altex Technologies Corporation
650 Nuttman Road
Suite 114
Santa Clara, CA 95054
(408) 980-8610
G. B. King
Department of Mechanical Engineering
Purdue University
West Lafayette, IN 47907-1288
(765) 494-6518
kinggb@ecn.purdue.edu

Merrill K. King
NASA Headquarters
Code UG
300 E Street, SW
Washington, DC 20546
(202) 358-0817
FAX: 358-3091
mking1@mail.hq.nasa.gov

David E. Klett
Department of Mechanical Engineering
North Carolina Agricultural
and Technical State University
Greensboro, NC 27401-3209

Charles Kolb
Aerodyne Research, Inc.
45 Manning Road
Manning Park Research Center
Billerica, MA 01821-3976
(978) 663-9500
FAX: 663-4918

Kenneth Kuo
Department of Mechanical Engineering
Pennsylvania State University
University Park, PA 16802
(814) 865-6741
FAX: 863-3203

Ming-Chia Lai
Department of Mechanical Engineering
Wayne State University
2129 Engineering Building
Detroit, MI 48202
(313) 577-3893
lai@mel.eng.wayne.edu

John Larue
Department of Mechanical & Aerospace Engineering
S3226 Engineering Gateway
Zot Code: 2750
University of California, Irvine
Irvine, CA 92717
(949) 824-6724
FAX: 824-8585
Jclarue@uci.ecu

Allan Laufer
Office of Energy Research
U.S. Department of Energy
19901 Germantown Road
Germantown, MD 20874
(202) 903-5820
Allan.Laufer@oer.doe.gov

Normand Laurendeau
School of Mechanical Engineering
Purdue University
West Lafayette, IN 47907-1288
(765) 494-2713
FAX: 494-0539
Laurende@ecn.purdue.edu

C. K. Law
Dept. of Mechanical and Aerospace Engineering
Princeton University
Princeton, NJ 08544-5263
(609) 258-5271
FAX: 258-6233
cklaw@princeton.edu

C. C. Lee
Environmental Protection Agency
26 West Martin Luther King Drive
Cincinnati, OH 45268
(513) 569-7520
FAX: 569-7471
lee.chun@pamail.epa.gov

Anthony Leonard
Graduate Aeronautical Labs
California Institute of Technology
Pasadena, CA 91125
(626) 395-4465

Arthur Lewis
University of Dayton Research Institute
Aerospace Mechanics Division
300 College Park
Dayton, OH 45469-0110
(937) 229-4235
FAX: 229-4251

Goang Liaw
Department of Civil Engineering
Alabama A&M University
P.O. Box 367
Normal, AL 35762
(205) 851-5565

Timothy Lieuwen
School of Aerospace Engineering
Georgia Institute of Technology
Atlanta, GA 30332-0150
(404) 894-3041
FAX: 894-2760
tim.lieuwen@aerospace.gatech.edu

Charles L. Liotta
Department of Chemical Engineering
Georgia Institute of Technology
Atlanta, GA 30332-0100
(404) 853-9344
FAX: 894-6956

Lyle N. Long
Department of Aerospace Engineering
233 Hammond Building
Pennsylvania State University
University Park, PA 16802
(814) 865-1172
FAX: 865-7092
lnl@psu.edu

Kevin Lyons
Dept. of Mechanical and Aerospace Engineering
North Carolina State University
P.O. Box 7910
Raleigh, NC 27695
(919) 515-5293
FAX: 7968
lyons@eos.ncsu.edu

Bruce MacDonald
Research Applications Division
Systems Research Labs, Inc.
2800 Indian Ripple Road
Dayton, OH 45440-3696
(513) 252-2706

Nick Makris
SA-ALC/SFT
Kelly AFB, TX 78241-5000
AV945-8212
FAX: 945-9964

David Mann
U.S. Army Research Office
P.O. Box 12211
4300 South Miami Boulevard
Research Triangle Park, NC 27709-2211
(919) 549-4249
DSN 832-4249
FAX: 549-4310
dmann@aro-emh1.army.mil

Nagi Mansour
Computational Fluid Mechanics
Branch, RFT 202A-1
NASA Ames Research Center
Moffett Field, CA 94035
(415) 604-6420

John Marek
NASA Glenn Research Center
M/S 5-11
21000 Brookpark Road
Cleveland, OH 44135-3127
(216) 433-3584
FAX: 433-3000
cecil.j.marek@lerc.nasa.gov

Jay Martin
University of Wisconsin-Madison
Engine Research Center
1500 Engineering Drive
Madison, WI 53706
(608) 263-9460
FAX: 262-6707
martin@engr.wisc.edu

James McDonald
Code 6110
Naval Research Laboratory
Chemistry Division
Washington, DC 20375-5342
(202) 767-3340
DSN 297-3340

Keith McManus
Physical Sciences, Inc
20 New England Business Center
Andover, MA 01810
(508) 689-0003
FAX: 689-3232

A. M. Mellor
Dept. of Mechanical & Materials Engineering
512 Kirkland Hall
Vanderbilt University
Nashville, TN 37240
(615) 343-6214
FAX: 343-6687

Lynn Melton
Programs in Chemistry
University of Texas, Dallas
P.O. Box 830688
Richardson, TX 75083-0688
(972) 883-2913
(972) 680-2163
FAX: 883-2925
melton@utdallas.edu

Suresh Menon
School of Aerospace Engineering
Georgia Institute of Technology
270 Ferst Drive
Atlanta, GA 30332-0150
(404) 894-9126
FAX: 894-2760
suresh.menon@aerospace.gatech.edu

Hameed Metghalchi
Dept. of Mechanical, Industrial and
Manufacturing Engineering
334SN
Northeastern University
360 Huntington Avenue
Boston, MA 2115
(617) -373-2973
FAX: 373-2921
metghal@coe.neu.edu

Michael M Micci
Department of Aerospace Engineering
233 Hammond Building
Pennsylvania State University
University Park, PA 16802
(814) 863-0043
(814) 692-8751
FAX: 865-7092
micci@henry2.aero.psu.edu

Andrzej Miziolek
AMSRL-WT-PC
Army Research Laboratory
Aberdeen Proving Gnd, MD 21005-5066
(410) 278-6157
FAX: 278-6094
miziolek@arl.army.mil

H. C. Mongia
Manager, Combustion Technology
GE Aircraft Engines
One Neumann Way, M/D A404
Cincinnati, OH 45215-6301
(513) 243-2552
FAX: 243-2538
Hukam.Mongia@ae.ge.com

Arje Nachman
AFOSR/NM
801 North Randolph Street, Room 732
Arlington, VA 22203-1977
(703) 696-8427
DSN 426-8427
FAX: 696-8450
arje.nachman@afosr.af.mil

Herbert Nelson
Code 6110, Chemistry Division
Naval Research Laboratory
4555 Overlook Avenue, SW
Washington, DC 20375-5342
(202) 767-3686

Michael Nusca
AMSRL-WT-PC
U.S. Army Research Laboratory
Aberdeen Proving Ground, MD 21005-5066
(410) 278-6108
DSN 298-6108
FAX: 278-7333
nusca@arl.army.mil

Elaine Oran
LCP&FD, Code 6404
U.S. Naval Research Laboratory
4555 Overlook Avenue, SW
Washington, DC 20375-5344
(202) 767-2960
FAX: 767-4798
ORAN@lcp.nrl.navy.mil

T. E. Parker
Engineering Division
Colorado School of Mines
Golden, CO 80401-1887
(303) 273-3657
FAX: 273-3602
tparker@mines.colorado.edu

Phillip H. Paul
MS 9051
Sandia National Laboratories
P.O. Box 969
Livermore, CA 94551-9051
(510) 294-1465
FAX: 294-1012
phpaul@sandia.gov

Lisa Pfefferle
Department of Chemical Engineering
Yale University
New Haven, CT 06520-8286
(203) 432-2222
FAX: 432-7232
pfefferle@htcre.eng.yale.edu

Emil Pfender
Department of Mechanical Engineering
125 Mechanical Engineering
The University of Minnesota
Minneapolis, MN 55455

Robert Pitz
Dept. of Mechanical and Materials Engineering
Vanderbilt University
Nashville, TN 37235
(615) 322-0209
FAX: 343-8730
pitzrw@ctrvan.vanderbilt.edu

S. B. Pope
Dept. of Mechanical and Aerospace Engineering
Cornell University
Ithaca, NY 14853-7501
(607) 255-4314
FAX;255-1222
pope@mae.cornell.edu

David Pratt
AFRL/VAS
Building 45 Annex
2130 Eighth Street, Suite 1
Wright-Patterson AFB, OH 45433-7542
(937) 255-5042
DSN 785-5042
FAX: 656-7915
David.Pratt@va.afrl.af.mil

Martin J. Rabinowitz
M/S 5/10
NASA Glenn Research Center
21000 Brookpark Road
Cleveland, OH 44135-3191
(216) 433-5847
FAX: 433-5588
marty@lerc.nasa.gov

Larry Rahn
Sandia National Laboratories
7011 East Avenue
M/S 9056
Livermore, CA 94551-0969
(510) 294-2091
FAX: 294-2276
rahn@sandia.gov

Mohan K. Razdan
Rolls-Royce Corporation
P.O. Box 420
Speed Code T10B
Indianapolis, IN 46206-0420
(317) 230-6404
FAX: 230-3691
mohan.razdan@rolls-royce.com

Robert Reed
Sverdrup Technology, Inc.
AEDC
1099 Avenue C
Arnold AFB, TN 37389-9013
(615) 454-4648
DSN 340-4648
(615) 454-6317

Rolf D. Reitz
Department of Mechanical Engineering
University of Wisconsin
1500 Johnson Drive
Madison, WI 53706
(608) 262-0145
FAX: 262-6717

Steven Reznick
AFOSR/CD
801 North Randolph Street, Room 732
Arlington, VA 22203-1977
(703) 696-7555
DSN 426-7555
FAX: 696-9556
steven.reznick@afosr.af.mil

Kyung T. Rhee
Dept. of Mechanical and Aerospace Engineering
Rutgers, The State Univ of New Jersey
Piscataway, NJ 08854-0909
(732) 445-3651
KTRhee@jove.rutgers.edu

James Riley
Department of Mechanical Engineering
University of Washington
Seattle, WA 98195
(206) 543-5347
73671.737@Compuserve.com

William Roberts
Dept. of Mechanical and Aerospace Engineering
Box 7910
North Carolina State University
Raleigh, NC 27695-7910
(919) 515-5294
FAX: 515-7968
wrobert@eos.ncsu.edu

Gerald A. Roffe
GASL
77 Raynor Avenue
Ronkonkoma, NY 11779

W. M. Roquemore
AFRL/PRTS
Building 490
1790 Loop Road, N
Wright-Patterson AFB, OH 45433-7103
(937) 255-6813
DSN 785-6813
FAX: 656-4570
melr@ward.appl.wpafb.af.mil

Daniel Rosner
Department of Chemical Engineering
Yale University
New Haven, CT 06520-8286
(203) 432-4391
FAX: 432-7232
daniel.rosner@yale.edu

John Ross
Department of Chemistry
Stanford University
Stanford, CA 94305-3032
(650) 723-9203

Gabriel Roy
Office of Naval Research
Mechanics Division, Code 1132
800 North Quincy Street
Arlington, VA 22217-5660
(703) 696-4406
DSN 426-4406
FAX: 696-0934
roy@ocnr-hq.navy.mil

Robert C. Ryder
Flow Parametrics, LLC
15 Debra Drive
Bear, DE 19701
(302) 838-7368
FAX: 838-7369
rryder@flowparametrics.com

Kurt Sacksteder
NASA Glenn Research Center
M/S 500-217
21000 Brookpark Road
Cleveland, OH 44135
(216) 433-2857

Michael Salkind
President
Ohio Aerospace Institute
22800 Cedar Point Road
Cleveland, OH 44142
(440) 962-3001
FAX: 962-3120
MichaelSalkind@oai.org

Mohammad Samimy
Ohio State University
Department of Mechanical Engineering
206 West 18th Street
Columbus, OH 43210-1107
(614) 422-6988
(614) 848-9439
FAX: 292-3163
msamimy@magnus.acs.ohio-state.edu

G. S. Samuelsen
Dept. of Mechanical and Aerospace Engineering
University of California
Irvine, CA 92697-3975
(949) 824-5468

Lakshmi Sankar
School of Aerospace Engineering
Georgia Institute of Technology
Atlanta, GA 30332
(404) 894-3014

Domenic Santavicca
Propulsion Engineering Research Center
Pennsylvania State University
106 Research Building East - Bigler Road
University Park, PA 16802-2320
(814) 863-1863

R. J. Santoro
Department of Mechanical Engineering
Pennsylvania State University
University Park, PA 16802-2320
(814) 863-1285
FAX: 865-3389
rjs2@email.psu.edu

Sutanu Sarkar
Dept. of Applied Mechanical and
Engineering Science, M/C 0411
University of California
La Jolla, CA 92093-0411
(858) 534-8243
FAX: 534-7599
ssarkar@ucsd.edu

John Schaefer
Energy and Environmental Division
Acurex Corporation
555 Clyde Avenue
P.O. Box 7555
Mountain View, CA 94039

Frederick Schauer
AFRL/PRTS
Building 490, Room 104
1790 Loop Road, N
Wright-Patterson AFB, OH 45433-7103
(937) 255-6462
DSN 785-6462
FAX: 255-1125
frederick.schauer@wpafb.af.mil

Peter Schihl
Propulsion Systems Division
ATTN: AMSTA-TR-R, MS 121
USA Tank Automotive Command
Warren, MI 48397-5000
FAX: 574-5054
schihlp@tacom.army.mil

Lyle Schwartz
AFOSR/CC
801 North Randolph Street, Room 732
Arlington, VA 22203-1977
(703) 696-8457
DSN 426-7551
lyle.schwartz@afosr.af.mil

Ernest Schwarz
Propulsion Systems Division
ATTN: DRSTA-RGD
USA Tank-Automotive Command
Warren, MI 48397-5000
(810) 574-5656
FAX: 574-5054
schwarze@cc.tacom.army.mil

Lee Scuderi
McDonnell Douglas Aerospace
P.O. Box 516
St. Louis, MO 63166-0516

Jerry Seitzman
School of Aerospace Engineering
Georgia Institute of Technology
Atlanta, GA 30332-0150
(404) 894-0013
FAX: 894-2760
jerry.seitzman@ae.gatech.edu

Kalyanasundaram Seshadri
Center for Energy and Combustion Research, 0407
University of California
La Jolla, CA 92093-0407
(619) 534-4876
seshadri@ames.ucsd.edu

Robert Shaw
Division of Chemical and Biological Sciences
U.S. Army Research Office
Research Triangle Park, NC 27709-2211
(919) 549-0641

Adam Siebenhaar
Aerojet Propulsion Division
P.O. Box 13222
Sacramento, CA 95813-6000

Gupreet Singh
U.S. Department of Energy
1000 Independence Avenue, S.W.
Washington, DC 20585
(202) 586-2333
FAX: 586-4166
GUPREET.SINGH@hq.doe.gov

William Sirignano
Dept. of Mechanical and Aerospace Engineering
University of California
Irvine, CA 92697-3975
(949) 824-3700
FAX: 824-3773
sirignan@uci.edu

Davey Smith
Northrop Grumman Corporation
B-2 Division Dayton Office
2850 Presidential Dr., Ste 100
Fairborn, OH 45324

Gregory Smith
Department of Chem Kinetics
SRI International
333 Ravenswood Avenue
Menlo Park, CA 94025-3493
(415) 859-3496

Kenneth A. Smith
Department of Chemical Engineering
Room 66-540
Massachusetts Institute of Technology
Cambridge, MA 02139
(617) 253-1973
FAX: 253-2701
kas@mit.edu

Judi Steciak
University of Idaho-Boise
800 Park Boulevard
Boise, ID 83712-7742
(208) 364-4080
FAX: 387-1246
jsteciak@uidaho.edu

David Stewart
Dept. of Theoretical and Applied Mechanics
University of Illinois at Urban-Champaign
216 Talbot Laboratory, M/C 262
104 South Wright Street
Urbana, IL 61801-2983
(217) 333-7947
FAX: 244-5707
dss@uiuc.edu

Geoffrey J. Sturgess
Innovative Scientific Solutions, Inc.
2786 Indian Ripple Road
Dayton, OH 45440-3638
(937) 252-2706
FAX: 656-4652
gsturgess@aol.com

B. Sturtevant
Department of Engineering and Applied Science
California Institute of Technology
Pasadena, CA 91125

G. Sullins
Applied Physics Laboratory
Johns Hopkins University
Johns Hopkins Road
Laurel, MD 20707-6099
(301) 953-5000

Rodney Tabacyznski
Director, Power Train Research Lab
Ford Motor Research Laboratory
3623 Scientific Research Lab, P.O. Box 2053
Dearborn, MI 48121-2053
(313) 322-8930

Douglas Talley
AFRL/PRSA
10 East Saturn Boulevard
Edwards AFB, CA 93524-7660
(661) 275-6174
DSN 525-6174
FAX: 275-6245
Douglas.Talley@ple.af.mil

Jefferson W. Tester
M.I.T. Energy Laboratory
Room E40-455
Massachusetts Institute of Technology
Cambridge, MA 02139
(617) 253-3401
FAX: 253-8013
testerel@mit.edu

Julian Tishkoff
AFOSR/NA
801 North Randolph Street, Room 732
Arlington, VA 22203-1977
(703) 696-8478
DSN 426-8478
FAX: 696-8451
julian.tishkoff@afosr.af.mil

Chenning Tong
Department of Mechanical Engineering
Clemson University
248 Fluor Daniel EIB
Clemson, SC 29634-0921
(864) 656-7225
FAX: 656-4435
ctong@ces.clemson.edu

Michael Trenary
Department of Chemistry, M/C 111
5324 SES
The University of Illinois
Chicago, IL 60680
(312) 996-0777
FAX: 996-0431
mtrenary@uic.edu

James Trolinger
MetroLaser
2572 White Road
Irvine, CA 92614
(949) 553-0688
FAX: 553-0495
jtrolinger@vmsa.oac.uci.edu

Timothy Troutt
Department of Mechanical Engineering
Washington State University
Pullman, WA 99164-2920

Gretar Tryggvason
Dept. of Mechanical Engineering & Applied Mech.
2350 Hayward, Room 2250
The University of Michigan
Ann Arbor, MI 48109-2125
(734) 763-1049
FAX: 764-4256
gretar@umich.edu

A. D. Vakili
University of Tennessee Space Institute
M/S 26
B.H. Goethert Parkway
Tullahoma, TN 37388
(931) 393-7483
avakili@utsi.edu

Mark Valco
Propulsion Directorate
Army Research Laboratory, MS 49-1
NASA Glenn Research Center
Cleveland, OH 44135-3127
(216) 433-3717
FAX: 433-2182
aamark@lims01.lerc.nasa.gov

David Van Wie
The Johns Hopkins University
Applied Physics Laboratory
11100 Johns Hopkins Road
Laurel, MD 20723-6099
(240) 228-5194
FAX: 228-5850
David.VanWie@jhuapl.edu

John Vanderhoff
Ballistic Research Laboratory
DRSMC-BLI(A)
Aberdeen Proving Ground, MD 21005
(410) 278-6642

Paul Waltrup
The Johns Hopkins University
Applied Physics Laboratory
11100 Johns Hopkins Road
Laurel, MD 20723-6099
(240) 228-5626
Paul.Waltrup@jhuapl.edu

Joe Wander
AFRL/MLQL
139 Barnes Drive, Suite 2
Tyndall AFB, FL 32403-5323
(904) 283-6240
DSN 523-6240
FAX: 283-6064
Jwander@mlq.afrl.af.mil

Hai Wang
Department of Mechanical Engineering
University of Delaware
Newark, DE 19716
(302) 831-2421
FAX: 831-3619
hwang@me.udel.edu

Zhicheng Wang
Clark Atlanta University
223 James P. Brawley Drive, S.W.
Atlanta, GA 30314
(404) 880-6125
FAX: 880-6615
zhicheng_wang@hotmail.com

Charles Westbrook
Lawrence Livermore National Laboratories
P.O. Box 808
Livermore, CA 94551
(925) 422-4108
FAX: 422-2644
westbrook1@llnl.gov

Phillip R. Westmoreland
Department of Chemical Engineering
University of Massachusetts
Amherst, MA 01003
(413) 545-1750
(413) 545-2507
(413) 545-1647
westm@ecs.umass.edu

James Whitelaw
Department of Mechanical Engineering
Imperial College of Science, Technology & Medicine
University of London
Exhibition Road
London SW7 2BX, UK
+44 (0) 20 7594 7028
FAX: +44 (0) 20 7598 3905
j.whitelaw@ic.ac.uk

Forman Williams
Center for Energy and Combustion Research, 0310
University of California
La Jolla, CA 92093-0310
(858) 534-5492
(858) 534-4285
FAX: 534-7720
fwilliams@ucsd.edu

Skip Williams
AFRL/VSBXT
29 Randolph Street
Hanscom AFB, MA 01731
(781) 377-2076
FAX: 377-7091
skipw@plh.af.mil

Bernard T. Wolfson
Wolfson Associates International
4797 Lake Valencia Boulevard, West
Palm Harbor, FL 33563
(813) 786-3007

Mary J. Wornat
Dept. of Mechanical and Aerospace Engineering
D238 Engineering Quadrangle
Princeton, NJ 08544-5263
(609) 258-5278
FAX: 258-6109
mjwornat@princeton.edu

J. M. Wu
University of Tennessee Space Institute
B.H. Goethert Parkway
Tullahoma, TN 37388-9700

Vigor Yang
Propulsion Engineering Research Center
The Pennsylvania State University
111 Research Building, East
University Park, PA 16802-2320
(814) 863-1502
FAX: 865-4784
vigor@arthur.psu.edu

Richard Yetter
Dept. of Mechanical and Nuclear Engineering
Pennsylvania State University
State College, PA 16802
(814) 863-6375
rayetter@psu.edu

Michael Zachariah
Department of Mechanical Engineering
University of Minnesota
111 Church Street, S.E.
Minneapolis, MN 55455
(612) 626-9081
zacha008@umn.edu

Ben Zinn
School of Aerospace Engineering
Georgia Institute of Technology
Atlanta, GA 30332-0150
(404) 894-3033
FAX: 894-2760
ben.zinn@aerospace.gatech.edu